3rd International Conference on Structural Engineering Research (iCSER2022)

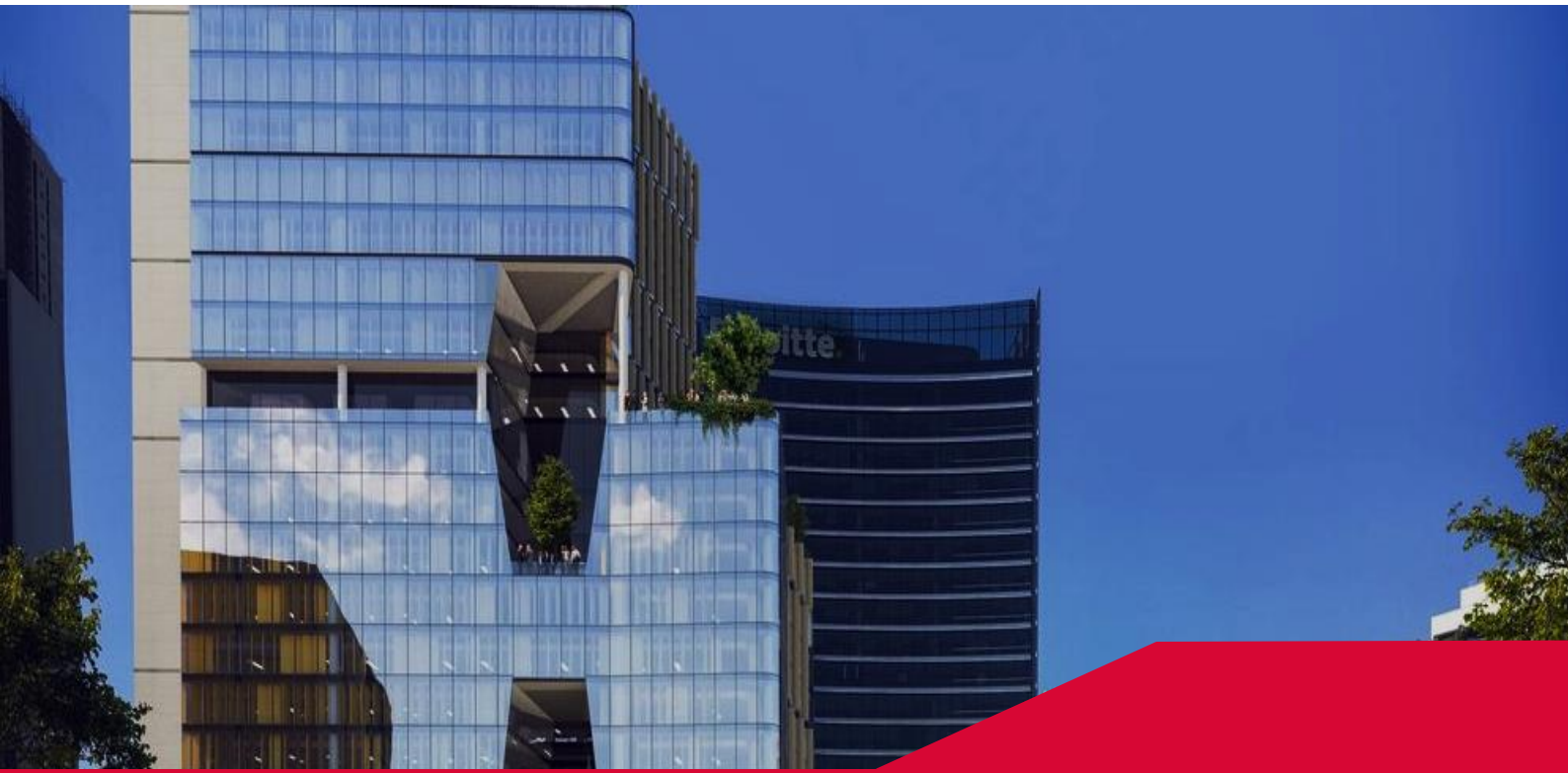

ISBN: 978-0-6456692-1-3

Proceedings

Md Kamrul Hassan, Fidelis R. Mashiri, Zhong Tao, Eds.

ISBN: 978-0-6456692-1-3

Proceedings of the 3rd International Conference on Structural Engineering Research (iCSER2022), 6th GCSTMR World Congress

27-30 November 2022

Western Sydney University, Sydney, Australia

Organised By

ISBN: 978-0-6456692-1-3

Md Kamrul Hassan, Fidelis R. Mashiri, Zhong Tao, Eds.

ISBN: 978-0-6456692-1-3

Editors:

Md Kamrul Hassan
School of Engineering, Design and Built Environment
Western Sydney University, Australia

Fidelis Rutendo Mashiri
School of Engineering, Design and Built Environment
Western Sydney University, Australia

Zhong Tao
Centre for Infrastructure Engineering,
School of Computing, Engineering and Mathematics
Western Sydney University, Australia

Date published: 26 Nov 2022

Publisher:
Science Technology and Management Crescent Australia Limited
12 Boyer Pl, Minto, New South Wales 2565, Sydney, Australia

This book proceeding can be cited as:

Hassan MK, Mashiri F, Tao Z. (2022). Proceedings of the 3rd International Conference on Structural Engineering Research (iCSER2022), edited by Hassan et al., 27-30 Nov 2022, Sydney, Australia, ISBN: 978-0-6456692-1-3.

ISBN: 978-0-6456692-1-3

Copyright

Published by Science Technology and Management Crescent Australia Limited in association with Global Circle for Scientific, Technological and Management Research, Sydney, Australia

ISBN: 978-0-6456692-1-3

We thank our generous sponsors

GEOTESTA

OMRON
Automation
+ Robotics

GDS
www.gdsinstruments.com

ISBN: 978-0-6456692-1-3

Table of Contents

ISBN: 978-0-6456692-1-3

Welcome by Conference Chairs

The International Conference on Structural Engineering Research aims to provide an international platform for effective exchange of ideas, reaffirming the existing collegial contacts, provide opportunities for establishing new ones as well as provide a forum for academics and researchers to present and share the results and findings of their latest research and practice on a wide range of topics relevant to structural engineering.

As the General Co-Chairs of the 3rd International Conference on Structural Engineering Research, 27-30 November 2022, Sydney (iCSER2022), we would like to thank the Plenary Speakers, Keynote Speakers, Invited Speakers, Authors, Sponsors, Secretaries, IT Team Members, Conference Advisory Committee Members, Organising Committee Members, Technical Committee Members, Reviewers and Volunteers for making this conference successful.

Associate Professor Fidelis Rutendo Mashiri and Professor Zhong Tao
General Co-Chairs
3rd International Conference on Structural Engineering Research (iCSER2022)

ISBN: 978-0-6456692-1-3

CONFERENCE ORGANISING COMMITTEE

Chair:

Associate Professor Fidelis Rutendo Mashiri and Professor Zhong Tao (General Co-Chairs)
Western Sydney University, Australia

General Secretary:

Dr Md Kamrul Hassan (Conference Secretary), Western Sydney University, Australia

Conference Management Coordinator:

Ms Jenis Islam, Western Sydney University, Australia

Treasurer:

Dr Md Hasan Hafizur Rahman, Director, Science, Technology and Management Crest Australia (STAMCA), New South Wales, Australia

IT Team Leader:

Dr. Rezaul Bashar, Science, Technology and Management Crest Australia (STAMCA), New South Wales, Australia

ISBN: 978-0-6456692-1-3

CONFERENCE TECHNICAL COMMITTEE

TECHNICAL COMMITTEE CHAIRS

Associate Professor Fidelis Rutendo Mashiri and Professor Zhong Tao
Western Sydney University, Australia

CONFERENCE SECRETARY

Dr. Md Kamrul Hassan, Western Sydney University, Australia

TECHNICAL COMMITTEE MEMBERS

Prof Dennis Lam, University of Bradford, UK
Prof Richard Liew, National University of Singapore, Singapore
Prof Takeshi Mori, Hosei University, Japan
Prof Lewei Tong, Tongji University, China
Prof Xiao-Ling Zhao, The Hong Kong Polytechnic University, Hong Kong, China
Prof Riadh Al-Mahaidi, Swinburne University of Technology, Australia
Prof Scott Smith, Southern Cross University, Australia
Prof Emad Gad, Swinburne University of Technology, Australia
Prof Muhammad Hadi, University of Wollongong, Australia
Prof Yan Zhuge, University of South Australia, Australia
Prof Wei Wang, Tongji University, China
Prof Huanjun Jiang, Tongji University, China
Prof Yang Xiang, Western Sydney University, Australia
Prof Bijan Samali, Western Sydney University, Australia
Prof Sarah Zhang, Western Sydney University, Australia
Prof Morgan Dundu, University of Johannesburg, South Africa
Prof Raquib Ahsan, Bangladesh University of Engineering and Technology, Bangladesh
Prof Mahbuba Begum, Bangladesh University of Engineering and Technology, Bangladesh
Prof Muhammad Fauzi Mohd Zain, Universiti Kebangsaan Malaysia, Malaysia
Prof Anna Paradowska, University of Sydney and ANSTO, Australia
Prof Mahmud Ashraf, Deakin University, Australia
Associate Prof Maslina Jamil, Universiti Kebangsaan Malaysia, Malaysia
Associate Prof Jiting Qu, Dalian University of Technology, China
Associate Prof Neaz Sheikh, University of Wollongong, Australia
Associate Prof Gokhan Ozdemir, Anadolu University, Turkey
Associate Prof Prabir Sarker, Curtin University, Australia
Associate Prof Wei Li, Tsinghua University, China
Associate Prof Olivia Mirza, Western Sydney University, Australia
Associate Prof Baolin Wang, Western Sydney University, Australia

ISBN: 978-0-6456692-1-3

ISBN: 978-0-6456692-1-3

REVIEWER LIST

Associate Professor Fidelis Mashiri, Western Sydney University, Australia
Associate Professor Xinqun Zhu, University of Technology Sydney, Australia
Associate Professor Baolin Wang, Western Sydney University, Australia
Dr Md Kamrul Hassan, Western Sydney University, Australia
Dr Tilak Pokharel, Swinburne University of Technology
Dr Ee Loon Tan, Western Sydney University, Australia
Dr Mohamed Ghannam, Mansoura University, Egypt
Dr Pezhman Sharafi, Western Sydney University, Australia
Dr Won Hee Kang, Western Sydney University, Australia
Dr Maria Rashidi, Western Sydney University, Australia
Dr Kamyar Kildashti Komsari, Western Sydney University, Australia
Dr Sameera Pathirana, Western Sydney University, Australia
Dr Jason Jiang, Western Sydney University, Australia
Dr Utsab Katwal, Western Sydney University, Australia
Mr Bulbul Ahmed, PhD Student, Western Sydney University, Australia
Mr Masoud Mohammadi, PhD Student, Western Sydney University, Australia
Md Ibrahim Mostazid, PhD Student, University of New South Wales, Australia
Ms Bahareh Nikmehr, PhD Student, Deakin University, Australia
Ms Dayani Kahagala Hewage, PhD Student, Western Sydney University, Australia

ISBN: 978-0-6456692-1-3

Paper Peer Review Process:

All full length papers included in the Proceedings of the 3rd International Conference on Structural Engineering Research, 27-30 November 2022 have been independently peer reviewed. The submitted abstracts were reviewed by the Technical Committee, and if the abstract was accepted, the author was invited to submit full papers. The full papers were then reviewed by two or more Reviewers as listed in the reviewer list (Page-xvi), and the review comments were sent to the authors to address the comments in updating the papers. The revised papers submitted by the authors were then checked by the Editors and accepted once the papers satisfied the requirements of the 3rd International Conference on Structural Engineering Research.

Disclaimer

The papers published in this Conference Proceedings have been reviewed, edited and proofread to the best of our ability within the timeframe permitted. We acknowledge that there may be further proofing errors.

ISBN: 978-0-6456692-1-3

Keynote Speaker

****

Professor Brian Uy, Professor of Structural Engineering, Head of School of Civil Engineering, The University of Sydney, Australia.

Title of Presentation: Structural Engineering Research in High Performance Steel And Composite Structures.

Biography: Professor Brian Uy commenced as Professor of Structural Engineering and Head of the School of Civil Engineering at the University of Sydney in November 2016. He was previously Professor of Structural Engineering and Director of the Centre for Infrastructure Engineering and Safety (CIES) in the School of Civil and Environmental Engineering at The University of New South Wales from 2013-2016 and was awarded a Scientia Professorship from 2017-2022. Brian also holds an Adjunct Professor role within the School of Engineering and Information Technology at UNSW, Canberra (Australian Defence Force Academy (ADFA)). More detail about the speaker is available on https://www.sydney.edu.au/engineering/about/our-people/academic-staff/brian-uy.html

ISBN: 978-0-6456692-1-3

Keynote Speaker

****

Professor Xiao-Ling Zhao, Chair Professor of Civil Infrastructure, The Hong Kong Polytechnic University, Hong Kong, China.

Title of Presentation: Fatigue of High Strength and Ultra-High Strength Steel.

Biography: Professor Zhao is a Fellow of the Australian Academy of Engineering and Technology. He held the Chair of Civil Engineering from 2001 to 2019 and then the Head of Department of Civil Engineering from 2008 to 2011 at Monash University, Australia. Before joining PolyU, Professor Zhao was the Associate Dean (International) in the Faculty of Engineering at the University of New South Wales, Australia. His current research focuses on high-performance sustainable materials in civil engineering applications, steel-concrete-FRP hybrid construction and floating structure technology. Professor Zhao has published 9 books and 400 refereed journal papers with an H-index over 80. He has supervised more than 50 PhD students. Professor Zhao was selected as Australia's Top Researcher in the fields of Structural Engineering and Civil Engineering in the Australian's Research Magazine in 2019 and 2021 respectively. He was listed among the World's Top 2% Scientists in the field of Civil Engineering by Stanford University in 2020 and 2021. Professor Zhao has also received a number of prestigious fellowships More detail about the speaker is available on https://www.polyu.edu.hk/cee/people/academic-staff/prof-zhao-xiao-lin/

ISBN: 978-0-6456692-1-3

Keynote Speaker

****

Professor Hong Hao, ARC Laureate Fellow and John Curtin Distinguished Professor Curtin University, Australia.

Title of Presentation: Metaconcrete Structure to Resist Impulsive Loads.

Biography: Professor Hong Hao is the Foundation Director of the Centre for Infrastructural Monitoring and Protection. His research focuses on earthquake engineering, blast and impact engineering and structural health monitoring. His work aims to develop both new and upgraded structures that can withstand short-duration, high-impact blast loads. Professor Hao is also investigating newer materials, including Carbon FRP, Glass FRP and various polymers to increase the strength, ductility and energy absorption capability of structures. More detail about the speaker is available on http://structuraldynamics.curtin.edu.au/

ISBN: 978-0-6456692-1-3

Keynote Speaker

****

Professor Jin-Guang Teng, President and Chair Professor of Structural Engineering, The Hong Kong Polytechnic University, Hong Kong, China.

Title of Presentation: Structural Engineering Innovations with Emerging Materials for a Carbon-Neutral Future.

Biography: Professor Jin-Guang Teng, President and Chair Professor of Structural Engineering of The Hong Kong Polytechnic University (PolyU), is a Member of the Chinese Academy of Sciences, a Corresponding Fellow of the Royal Society of Edinburgh and a Fellow of the Hong Kong Academy of Engineering Sciences. He received his BEng Degree from Zhejiang University in 1983 and his PhD degree from the University of Sydney in 1990. His main research areas include the structural use of fiber-reinforced polymer (FRP) composites in construction and steel structures. Many of his research findings have been adopted by relevant design codes/guidelines in China, Australia, Europe, the United Kingdom and the United States. The research awards he has received include the State Natural Science Award of China (Second Class) and the inaugural IIFC Medal from the International Institute for FRP in Construction (IIFC). More detail about the speaker is available on https://www.polyu.edu.hk/ppoffice/senior-management-team/president/

ISBN: 978-0-6456692-1-3

Keynote Speaker

****

Professor Riadh Al-Mahaidi, Professor of Structural Engineering and Director, Smart Structures Laboratory, Swinburne University of Technology, Australia.

Title of Presentation: Enhancement of Safety of Structures under Extreme Events through Innovative Materials and Advanced Testing Techniques.

Biography: Dr Riadh Al-Mahaidi is a Professor of Structural Engineering and Director of the Smart Structures Laboratory at Swinburne University of Technology. Prior to joining Swinburne in January 2010, he was the Head of the Structures Group at Monash University. Over the past 20 years, he focused his research and practice on the lifetime integrity of bridges, particularly in the area of structural strength assessment and retrofitting using advanced composite materials. He currently leads a number of research projects on strengthening of bridges using fibre reinforced polymers combined cement-based bonding agents, fatigue life improvement of metallic structures using advanced composite systems, and shape memory alloys. He recently started some projects on hybrid testing of structures. He received a BSc (Hon 1) degree in civil engineering from the University of Baghdad and MSc and PhD degrees in structural engineering from Cornell University in the United States. To date, Riadh published over 250 journal and 270 conference papers. He was awarded the 2012 Vice Chancellor's Internationalization Award, the WH Warren Medal 2017 for the best paper published by Engineers Australia in civil engineering in 2016, the RW Chapman Medals in 2005 and 2010 for best journal publication in Engineers Australia Structural Journal, best paper awards at ACUN-4 (2002) and ACUN-6 (2012) Composites conferences. Prof Al-Mahaidi and his research group won the 2016 Engineers Australia Excellence Award for Innovation, Research and Development (High Commendation) for the $2.1mil Multi-Axis Substructure Testing (MAST) System they built at Swinburne. For further information, visit: https://www.swinburne.edu.au/research/our-research/access-our-research/find-a-researcher-or-supervisor/researcher-profile/?id=ralmahaidi

ISBN: 978-0-6456692-1-3

Keynote Speaker

****

Professor Rebecca Gravina, TMR Chair and Professor of Structural Engineering, The University of Queensland, Australia.

Title of Presentation: Durability of FRP Strengthened Reinforced Concrete Structures.

Biography: Professor Rebecca Gravina is the Queensland Government Department of Transport and Main Roads (TMR) Chair and Professor of Structural Engineering, in the School of Civil Engineering at the University of Queensland in Brisbane, Australia. She also held the position Professor of Civil and Infrastructure Engineering at RMIT University in Melbourne. Professor Gravina has over 25 years of experience in academia and consulting engineering. Her research field concerns the long-term performance and durability of reinforced concrete (RC) and prestressed concrete (PC) structures, sustainability of infrastructure, rehabilitation of existing structures with Fibre Reinforced Polymers (FRP), recycled materials in concrete, and engineering education. Professor Gravina is the Editor in Chief of the Australian Journal of Civil Engineering, President of the American Society of Civil Engineers (ASCE) Australian Section (2020-2022), and Executive Committee Member of the International Institute for FRP in Construction (IIFC). https://civil.uq.edu.au/profile/3657/rebecca-gravina

ISBN: 978-0-6456692-1-3

Invited Speaker

****

Professor Yan Zhuge, Professor of Structural Engineering, University of South Australia, Australia.

Title of Presentation: Recent Research Progress on FRP/Fibre Textile-reinforced UHPC Composites.

Biography: Dr Yan Zhang is a Professor in Structural engineering and the Professorial leads in Research Education, UniSA STEM, University of South Australia (UniSA). She was appointed as the Australian Research Council (ARC) College of Expert since 2019. Yan has lectured in several Australian universities for more than 25 years. Her main research interests include green concrete materials, fibre composite materials and structures. She has published more than 200 SCI technical papers in the referred international journals and conferences and has been invited as a keynote speaker at Australia and international conferences. Yan has won several Australian government awards and fellowships and attracted funding from Australian Research council (ARC) and industry. She was the winner of 2018 South Australia Winnovation award in Engineering category. https://people.unisa.edu.au/yan.zhuge

ISBN: 978-0-6456692-1-3

Invited Speaker

****

Associate Professor Xinqun Zhu, School of Civil and Environmental Engineering, University of Technology Sydney, Australia.

Title of Presentation: Recent Developments on Vehicle-Assisted Bridge Structural Health Monitoring.

Biography: Dr Xinqun Zhu obtained his PhD at the Hong Kong Polytechnic University in 2001. Currently, he is an Associate Professor in Structural Engineering at University of Technology Sydney (UTS). His research interests include structural health monitoring and condition assessment, Steel-Concrete Composite Structures, physics-informed machine learning, and advanced signal processing and sensor technology. Dr Zhu has been a Chief Investigator (CI) of over 20 research projects including three ARC Discovery Grants (DP110101328, DP160103197, DP220102045). He has published over 200 articles including two research books and 147 referred journal papers. His journal papers have been well-cited with a Google Scholar h-index of 39. He is a member of the American Society of Civil Engineers (ASCE), the Executive Committee of Australian Network of Structural Health Monitoring and the Structural Health Monitoring and Control Committee in Engineering Mechanics Institute of ASCE. He is also an Associate Editor of international Journal of Advances in Structural Engineering. https://profiles.uts.edu.au/Xinqun.Zhu

ISBN: 978-0-6456692-1-3

Invited Speaker

****

Associate Professor Dr Siti Aminah Osman, School of Civil and Environmental Engineering, Universiti Kebangsaan Malaysia, Malaysia.

Title of Presentation: Experimental Behavior of Twin-Layer Flat Steel-Sheet Composite Wall System (TFSCWs) with Opening under In-Plane Lateral Cyclic Loading.

Biography: Dr Siti Aminah Osman (S. A. Osman) graduated from Universiti Teknologi Malaysia in 1992 with BEng (Hons) in Civil Engineering, MSc in Structural Engineering from Unversity of Bradford, United Kingdom (1995) and PhD in Civil & Structural Engineering from Universiti Kebangsaan Malaysia (2006). She is an Associate Professor in the Department of Civil Engineering, Faculty of Engineering & Built Environment, Universiti Kebangsaan Malaysia (UKM) and is actively involved in research on structural dynamics for earthquake and wind loading, industrial building systems (IBS) and engineering education as well. She has more than 20 years of experience in teaching, training, research, publication and administration. She has published many papers related to her work internationally and locally. Currently, she is the Deputy Dean of Networking and Alumni of the faculty and is quite active in the activities with the industries and communities which is in line with her portfolio. She is also a member of the Board of Engineers Malaysia (BEM) and the Society of Engineering Education Malaysia (SEEM). https://www.ukm.my/jurutera/staff-directory/prof-madya-dr-siti-aminah-hj-osman/

ISBN: 978-0-6456692-1-3

List of Full Papers

Paper Title/Author Name/Paper ID — Page

STEEL AND COMPOSITE STRUCTURES

ISBN: 978-0-6456692-1-3

EXTREME EVENTS AND STEEL STRUCTURES

IMPULSIVE LOADS AND WALL BEHAVIOUR

FIBRE REINFORCED POLYMERS

ISBN: 978-0-6456692-1-3

CONCRETE TECHNOLOGY

ISBN: 978-0-6456692-1-3

STRUCTURAL HEALTH MONITORING

Proc. 3rd International Conference on Structural Engineering Research (iCSER 2022)
27-30 Nov 2022, Sydney, Australia
ISBN: 978-0-6456692-1-3

Experimental Behavior of Twin-Layer Flat Steel-Sheet Composite Wall System (TFSCWs) with Opening under In-Plane Lateral Cyclic Loading

Mustafa M. Ali[1], S. A. Osman[2] & M. Y. M. Yatim[3]

[1]Project Manager, Al Quds Land Engineering Co. for Trade and Constructions Ltd., 56001 Karbala, Province of Karbala, Iraq.

[2]Associate Professor, [3]Senior Lecturer, Department of Civil Engineering, Faculty of Engineering & Built Environment, Universiti Kebangsaan Malaysia (UKM), Bangi 43600, Selangor, Malaysia.

Corresponding author's E-mail: saminah@ukm.edu.my

Abstract

A composite twin-layer steel-sheet frame concrete infill wall, in which these materials integrally interact, provides significant advantages as a cyclic load resistant and dissipative energy structural element. Concrete-filled steel plate shear walls system has been investigated by other researchers concentrating on solid unframed walls which experienced severe failure at the wall's toe. However, the presence of the opening can deteriorate the performance of the wall significantly. This study aims to investigate the structural behaviour of half-scale specimens of a Twin-layer Flat Steel-sheet Composite Wall (TFSCW) system with an opening, infilled with recycled lightweight concrete (with polystyrene), in the presence of the opening and strengthened by the perfobond diagonal steel plate stiffeners under in-plane lateral cyclic loading. The experimental parameters were the existence of the recycled lightweight concrete core, the application of a central circular opening, and the implementation of the perfobond diagonal steel plate stiffeners. The results show that using recycled-lightweight concrete as a concrete core in the TFSCW system can improve the ultimate cyclic capacity and the cumulative dissipated energy by more than 60% and 43%, respectively. Also, the opening in the TFSCW deteriorated the TFSCW cyclic load capacity and energy dissipation by around 16%. However, adopting the strengthening method of perfobond diagonal steel plate stiffeners in the TFSCW with the opening has managed to increase the lateral shear strength by 19% and the cumulative dissipated energy by 13%. In conclusion, the composition of recycled lightweight concrete-filled twin-layer of SSP with opening and the perfobond diagonal stiffeners can be considered a reliable choice for double-skinned composite walls.

Keywords: *Concrete-filled steel plate shear walls, cyclic load, opening, energy dissipation, recycled lightweight concrete.*

1. INTRODUCTION

Composite wall systems (CWs) could be defined as a combined arrangement of different types of materials bonded together with different characteristics and properties, such as a twin steel sheet plate (SSP) and filled with concrete to behave as one new characteristic member. Such arrangements are used perfectly as lateral load-resisting systems in structures to resist earthquake or wind loads, as well as an axial load resistance member. For more than three decades, researchers such as Wright & Gallocher (1995), Hu et al. (2014), Epackachi et al. 2014, Rahnavard et al. (2016), Terranova et al. (2019), and professional structural designers are given more attention to the importance of CWs. Many studies have explored the use of CWs and infilled concrete to improve the structural behavior of CWs. However, less number of studies have examined the effect of opening on CWs behavior. Prior studies on the application of opening in a shear wall structure have observed a capacity deterioration occurred due to opening presence. Hossain (2000), has examined the opening effect on twin profiled steel composite walls (TPSCWs). Meanwhile, no previous study observed in the literature has determined

the opening impact on TFSCWs' performance yet.

Recent studies by Alavi & Nateghi (2013), and Ali et al. (2018) have shown that the diagonal steel plate stiffener improves the structural response of the wall and reduces the undesired effects of the openings. In composite infilled elements, this type of stiffener could be used as an SSP embedded linkage, and simultaneously as a steel-concrete shear connector by generating a number of through holes on the stiffeners plate allowing the infill concrete to flow through, and named as perfobond steel-plate stiffeners as studied by Oguejiofor & Hosain (1992) and Liu et al. (2019). Based on that, it is deemed that using the perfobond diagonal stiffening concept to overcome known challenges of opening on shear walls would behave effectively. However, to date, no data is available on the combination of an opening with perfobond diagonal stiffeners in the TFSCWs system. Meanwhile, due to the rapid development of the construction industry, demolition waste has increased significantly. Hence, concrete waste recycling matter become necessarily required to preserve natural resources and meet the current global toward a green environment. Moreover, using recycled waste concrete rather than regular coarse aggregate will considerably reduce the overall concrete cost. Therefore, this study aims to investigate the cyclic behavior of TFSCWs with openings strengthened by perfobond diagonal stiffeners and infilled with recycled-lightweight concrete. The structural response and performance of the TFSCWs with central circular opening and perfobond diagonal steel plate stiffeners under in-plane lateral cyclic loading were tested under cyclic load.

2. EXPERIMENTAL PROGRAM

Four innovative half-scale specimens of TFSCWs were examined and tested in the experimental program under cyclic load. The adopted specimens were labeled as TFSSW-E, TFSCW-F, TFSCW-FO, and the last, TFSCW-FOD as defined in Table 1. The boundary frame, twin-layer flat SSP and stiffener plate, which were employed in the TFSCW assembly, was made of steel as shown in Figure 1. The referred steel components were fabricated by the hot-rolling process. The specimens were built with a 1.16 (length/ height) aspect ratio corresponding to 3.5 m length and 3.0 m high conventional walls. The adopted aspect ratio was fixed for all specimens to allow other significant parameters to be varied after analyzing several configurations numerically. For instance, concrete panel thickness, SSP thickness, steel part yielding strength and wall aspect ratio, 102 mm total thickness including, twin-layer flat SSP of 1.0 mm thickness, and infill recycled-lightweight concrete were selected. Due to the specimen's scale, the specimen's shear connectors' design was limited to the perfobond diagonal stiffeners.

Table 1. Specimens' notation's definition

Specimen Designation	Specimens notation	Meaning of notations
TFSSW-E	E	Empty core
TFSCW-F	F	Filled core
TFSCW-FO	FO	Filled core with opening
TFSCW-FOD	FOD	Filled core with Opening and Diagonal stiffeners

The geometry description of the four half-scale specimens is summarized and presented in Table 2. The cyclic experimental tests were conducted at the structural laboratory of the Faculty of Civil Engineering, UiTM, Shah Alam Malaysia. The "Interface" lateral cyclic actuator jack was used for the lateral cyclic load test. The hydraulic jack loading capacity was 500 kN (pushing and reloading), including the attached loading cell. The lower beam of the boundary frame of the specimens was clamped down to the rigid concrete floor of the structural lab by a 30 mm thick plate bolted to the ground, which achieved a fixed support condition, as depicted in Figure 2. Generally, the same boundary conditions were applied for all tested specimens before and during the experimental test. In order to determine the specimens' behavior, 3 LVDTs were used to monitor the ground support, mid-height frame and ultimate lateral displacement. Whilst 12 and 14 strain gauges were used and installed on one side of perforated and solid specimens, respectively. Figure 3 exhibited all specimens after

finalizing the installation and before starting the experiment.

Table 2. The component schedule of the specimens

Specimen designation	Dimensions of specimen (mm)	Aspect ratio L/H	Diameter of opening (mm)	Stiffeners single-piece dimensions (mm)	Infill RLC grade (Mpa)	Effective height (mm)
TFSSW-E	1750×1504	1.16	x	x	x	1440.5
TFSCW-F	1750×1504	1.16	x	x	17	1440.5
TFSCW-FO	1750×1504	1.16	500	x	17	1440.5
TFSCW-FOD	1750×1504	1.16	500	720×100×4	17	1440.5

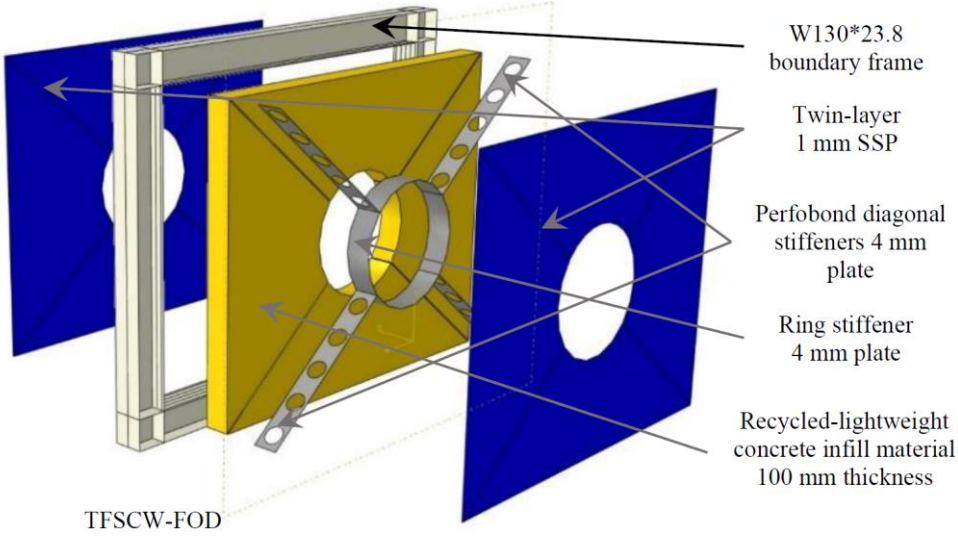

Figure 1. Sketch of TFSCW-FOD specimen

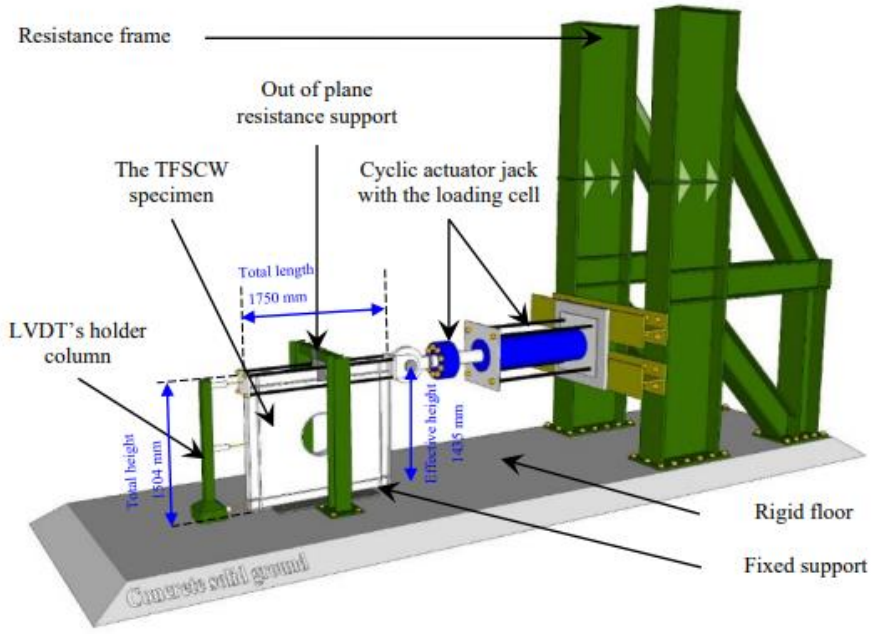

Figure 2. A 3D view of the experimental test setup

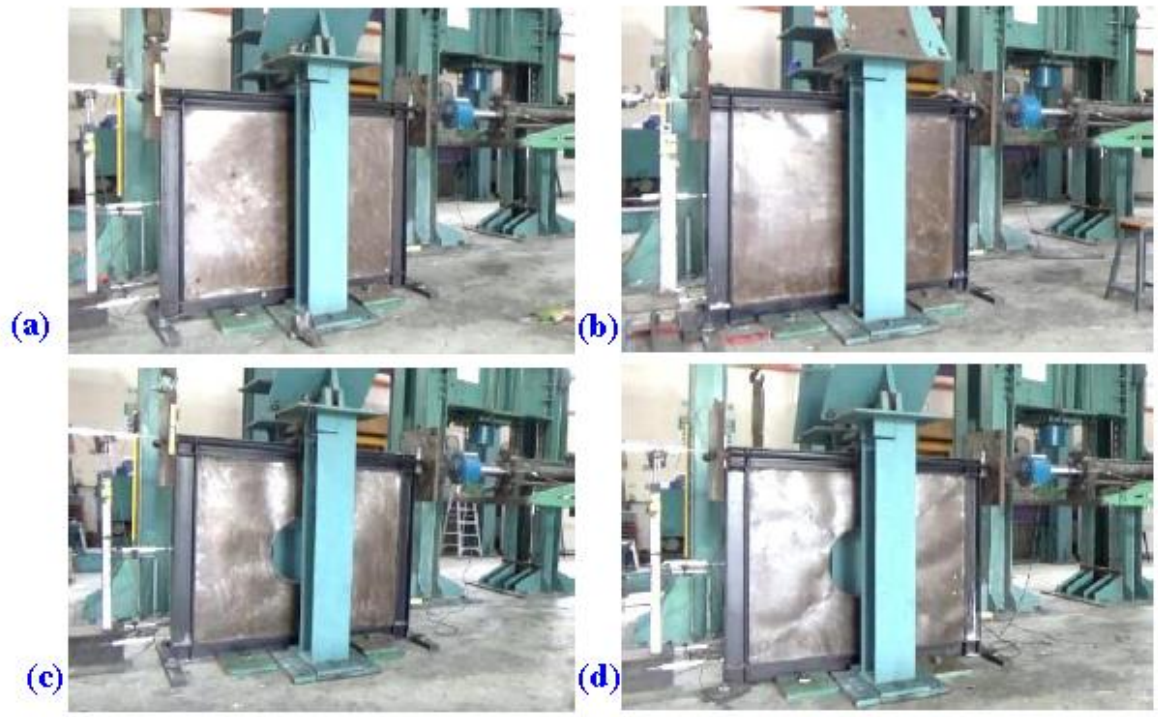

Figure 3. The specimens before the test initiation: (a) TFSSW-E, (b) TFSCW-F, (c) TFSCW-FO and (d) TFSCW-FOD

3. EXPERIMENTAL RESULTS

The initial stiffness, ultimate cyclic load, drift ratio at the ultimate load, cyclic load improvement ratio, cumulative energy dissipation and energy dissipation improvement are observed and discussed to describe the structural response of the four twin-layers flat steel-sheet and composite walls specimen under cyclic load.

The tested wall specimens' initial stiffness was calculated at less than 0.02% drift ratio, as shown in Table 3. The findings revealed that the initial stiffness of TFSSW-E was less than the other specimens due to the absence of filler material since this specimen was limited to steel parts (steel plate shear wall). The initial stiffness for specimen TFSCW-F was less than the equivalent of the TFSCW-FO specimen, which was unexpected, and that was probably attributed to unrecognizable initial flexibility at the specimen base support. In other words, a slight looseness at the base fixed support. Logically, the TFSCW-FOD specimen registered the highest initial stiffness, which was attributed to the presence of the perfobond diagonal stiffeners and/or connectors.

Table 3. The initial stiffness of the specimens

	Specimen designation			
Drift ratio (%)	**TFSSW-E**	**TFSCW-F**	**TFSCW-FO**	**TFSCW-FOD**
	Initial stiffness (kN/mm)			
less than 0.02%	107.42	109.89	146.89	295

Meanwhile, Table 4 shows that the ultimate capacity for a cyclic load of the specimens TFSSW-E and TFSCW-FOD was achieved at a 3.35% peak drift ratio. However, TFSCW-F and TFSCW-FO, with

the presence of infill concrete, registered the peak load at a 2.79% drift ratio. The results indicate that perfobond diagonal stiffeners influenced the peak shear resistance in the TFSCW-FOD specimen by extending the capacity progression to a 3.35% peak drift ratio.

The specimen infilled with the recycled lightweight concrete (TFSCW-F) achieved an improvement of +60% corresponding to the equivalent unfilled reference specimen (TFSSW-E), while specimen TFSCW-FO registered an improvement of +45% in the presence of opening, indicating that deterioration of -15% occurred corresponding to the equivalent solid specimen (TFSCW-F) attributed to opening existence. Last, specimen TFSCW-FOD, with the presence of the opening, recorded an enhancement of +64% compared to specimen TFSSW-E, indicating a +4% more capacity in reference to the TFSCW-F specimen to prove the efficiency of the adopted strengthening method. From the result, it can be demonstrated three key findings. First, the recycled-lightweight concrete greatly contributed to the increase in the walls' ultimate cyclic load capacity, presence, or absence of opening. Second, the application of opening diminishes the strength of the wall and influences the wall's behavior. Third, in the presence of an opening, the perfobond diagonal stiffeners significantly increased the ultimate lateral cyclic load and overcame strength decline efficiently.

Table 4. Test results of the specimens

Specimen designation	Ultimate cyclic load (kN)	Drift ratio at the ultimate load	Cyclic load improvement ratio (%)	Cumulative energy dissipation	Energy dissipation improvement (%)
TFSSW-E	247.97	3.35%	Reference specimen	79145 kN.mm	Reference specimen
TFSCW-F	398.11	2.79%	+ 60	113579 kN.mm	+ 43
TFSCW-FO	341.11	2.79%	+ 45	95418 kN.mm	+ 20
TFSCW-FOD	405.15	3.35%	+ 64	105708 kN.mm	+ 33

As for the cumulative energy dissipation shown in Table 4, +43% improvement occurred for the TFSCW-F specimen compared with the TFSSW-E specimen attributed to the influence of implementing the recycled-lightweight concrete as infill core material. Moreover, the findings demonstrated that the cumulative dissipated energy of the perforated specimen (TFSCW-FO) declined by -16%, compared with the unperforated specimen (TFSCW-F). As was expected, the opening application deteriorated the energy dissipation capacity of the wall. However, through the TFSCW-FOD specimen's outcome, it was clearly noted that the adopted technique of strengthening through perfobond diagonal stiffeners has proven its efficiency and restrained the deterioration of the energy dissipation capacity to +13% with the presence of opening.

Furthermore, it should be highlighted that the strengthening method with the perfobond diagonal stiffeners in the TFSCW-FOD specimen, has improved the lateral cyclic capacity and recorded a little higher lateral cyclic capacity than TFSCW-F. However, the comparison of the tested specimens' cumulative dissipated energy capacities demonstrates that the TFSCW-FOD specimen showed a negligible reduction in the cumulative dissipated energy capacity compared with the unperforated specimen (TFSCW-F). Even though the TFSCW-FOD specimen was strengthened by the diagonal perfobond stiffeners and achieved higher lateral cyclic capacity. Accordingly, the diagonal perfobond stiffeners have a higher impact on the lateral cyclic strength than the impact shown on the cumulative dissipated energy capacity.

4. CONCLUSIONS

A cyclic lateral-load experimental program of four twin-layers flat steel sheet and composite walls specimens is presented in this paper to determine the structural behavior and response. Based on the experimental results, the following conclusions can be drawn:

- Implementing the recycled lightweight concrete as a core infill material, all the strengthened and tested specimens achieved significant enhancement on the cyclic load capacity compared with the

equivalent un-filled specimen.

- Applying a central opening with a diameter of 1/3 of the steel sheet plate layer length in the TFSCW-FO specimen has led to a substantial deterioration in wall cyclic load capacity and dissipated energy ability, where both declined by -15% and -16%, respectively. However, the TFSCW-FO specimen still has a higher cyclic capacity than the empty-core specimen (TFSSW-E) by +45%.

- The perfobond diagonal plate stiffeners were proposed as a method of strengthening to overcome the challenges of applying an opening in the wall. On that matter, the perfobond diagonal plate stiffeners have shown a significant enhancement in the capacity, energy dissipation, and stiffness of the wall in the presence of the opening.

ACKNOWLEDGMENTS

The authors are grateful for the financial support from the Ministry of Higher Education through grant FRGS/1/2018/TK01/UKM/02/1.

REFERENCES

Alavi, E. & Nateghi, F. (2013). Experimental study on diagonally stiffened steel plate shear walls with central perforation. *Journal of Constructional Steel Research* 89, 9-20.

Ali, M. M., Osman, S. A., Husam, O. A. & Al-Zand, A. W. (2018). Numerical study of the cyclic behavior of steel plate shear wall systems (SPSWS) with differently shaped openings. *Steel and Composite Structures* 26(3), 361-373.

Epackachi, S., Nguyen, N. H., Kurt, E. G., Whittaker, A. S. & Varma, A. H. (2014). Numerical and experimental investigation of the in-plane behavior of rectangular steel-plate composite walls. *Structures Congress* 2014, 2478-2487.

Hossain, K. A. (2000). Axial load behaviour of pierced profiled composite walls. *The Institution of Professional Engineers New Zealand*, 1-7.

Hu, H.-S., Nie, J.-G. & Eatherton, M. R. (2014). Deformation capacity of concrete-filled steel plate composite shear walls. *Journal of Constructional Steel Research* 103, 48-158.

Liu, S., X., D., X., L., Y., L. & S., Z. (2019). Behavior of rectangular-sectional steel tubular columns filled with high-strength steel fiber reinforced concrete under axial compression. *Materials - mdpi* 12(2716): 1-15.

Oguejiofor, E. C. & Hosain, M. U. (1992). Behaviour of perfobond rib shear connectors in composite beams: full-size tests. *Canadian Journal of Civil Engineering* 19(2), 224-235.

Rahnavard, R., Hassanipour, A. & Mounesi, A. (2016). Numerical study on important parameters of composite steel-concrete shear walls. *Journal of Constructional Steel Research* 121, 441-456.

Terranova, B., Bhardwaj, S., Whittaker, A., Varma, A. & Orbovic, N. 2019. An experimental investigation of the effects of out-of-plane loading on the in-plane seismic response of sc wall piers. *Engineering Structures* 190, 380-388.

Wright, H. & Gallocher. 1995. The behaviour of composite walling under construction and service loading. *Journal of Constructional Steel Research* 35,3, 257-273.

Proc. 3rd International Conference on Structural Engineering Research (iCSER 2022)
27-30 Nov 2022, Sydney, Australia
ISBN: 978-0-6456692-1-3

Monotonic and Cyclic Behaviour of Q620 Structural Steels After Exposure to High Temperature

Hao Chen[1], Wei Li[2]

[1] PhD student, Tsinghua University, Beijing, 100084, China

[2] Associate Professor, Tsinghua University, Beijing, 100084, China

Corresponding author's E-mail: iliwei@tsinghua.edu.cn

Abstract

The mechanical properties of structural steel after fire exposure are important for the assessment of structural damage after a fire incident. In this study, quasi-static monotonic tensile and cyclic loading tests are carried out for the Q620 structural steel after high temperature exposure. The test parameters include the highest temperature experienced by specimens, the cooling method and the loading protocol. The stress-strain relationships of steels are recorded in the tests. The change of material properties and energy consumption capacity of Q620 steel after fire exposure are summarized. It is found that the material properties are significantly affected by the highest temperature experienced and the cooling method. When the highest temperature experienced by the specimen is more than 800°C, the ultimate strength and the energy consumption capacity decrease significantly. The yield and ultimate strength of specimens cooled in the air are lower than those cooled in the water.

Keywords: high-strength structural steel; high temperature exposure; cooling method; hysteretic behaviour

1. INTRODUCTION

The mechanical performance of steel after exposure to fire is important for the post-fire evaluation process. For those structures located in the seismic-prone zone, the hysteretic behaviour of steel needs to be clarified, as the material properties change after the heating and cooling process. In the past, numerous investigations have been carried out for the mechanical properties of steel under and after fire. The elastic modulus, yield strength, Poisson's ratio, and stress-strain relationship of steel under fire and after fire have been investigated by many researchers, e.g. Ding et al. (2006), Zhang et al. (2009), Qiang et al. (2012), Li et al. (2017) and Wang et al. (2020). The results showed that the post-fire yield strength decreased when the highest temperature experienced increased, while the elastic modulus and Poisson's ratio were moderate. However, studies on the hysteretic properties of steel after fire remain scarce. On the other hand, high-strength steel, i.e., steel with a yield strength higher than 460MPa, has developed rapidly in practice. In this paper, the quasi-static tensile and cyclic loading tests are conducted for the Q620 structural steel after high temperature exposure. The mechanical properties of Q620 steel after high temperature exposure are compared with those at ambient temperature.

2. EXPERIMENTAL INVESTIGATION AND RESULTS

2.1. Specimen design

The nominal yield strength of the Q620 steel is 620MPa. The test specimens were cut in the rolled direction of a Q620 steel sheet with a nominal thickness of 15mm. The profile of monotonic tensile specimens was designed in accordance with NSPRC (2010), as shown in Fig. 1(a), and the dimensions of cyclic specimens were prepared in accordance with NSPRC (2021), as shown in Fig. 1(b).

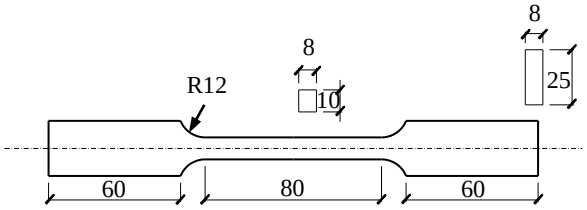

(a) Tensile specimens (unit: mm)

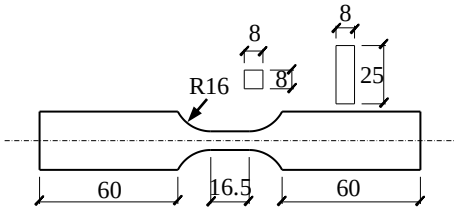

(b) Cycle loading specimens (unit: mm)

(c) Instron8801 test machine

Fig. 1 Dimensions of tests specimens

2.2. Test procedure

The heating and cooling procedure is shown in Fig. 2(a). The heating of specimens was conducted in a temperature-controlled electrical furnace. The specimens were heated from ambient temperature to a designated temperature with a heating rate of 2~10℃/min. When the designated temperature was reached, the specimens were placed in the furnace for more than 30 minutes in order to have enough time for phase transformation. Then the specimens were cooled down to ambient temperature in either air or water. The specimens cooled in the air were immediately taken out of the furnace when the soak time was reached and cooled down to ambient temperature naturally. For the specimens cooled in the water, they were immediately dunked in sufficient ambient-temperature water.

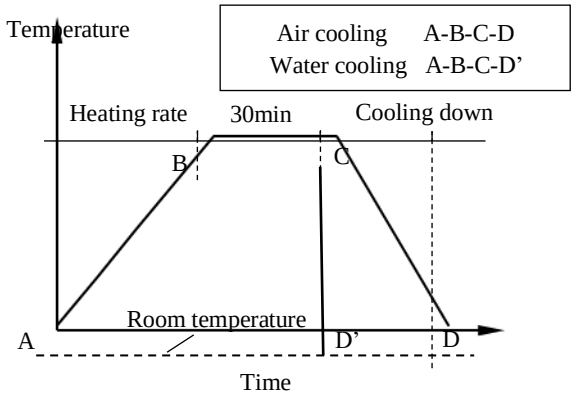

(a) Heating-cooling protocol

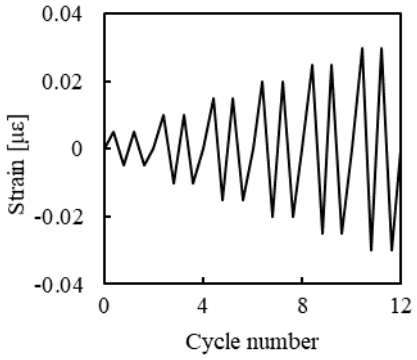

(b) Cyclic loading protocol

Fig. 2 Testing protocol

The monotonic tensile tests were conducted for the specimens after high temperature exposure on a universal testing machine. The specimens without thermal treatment were also tested for comparison. The cyclic tests were conducted using an Instron 8801 testing machine, as shown in Fig. 1(c). the elongation of the specimen was monitored by an extensometer with a gauge length of 12.5 mm and a measuring range of ± 35%. Fig. 2(b) shows the cyclic loading protocol, where each strain amplitude was repeated for two cycles to achieve a fair saturation. The specimens were loaded with a constant strain rate of 0.1%/s.

3. RESULTS AND ANALYSIS

3.1. Stress-strain relationship of monotonic tensile test

The measured mechanical properties of Q620 steel are summarized in Table 1, where the label T represents the maximum temperature experienced by specimens; A represents the specimens cooled in the air; W represents the specimens cooled in the water; MT represents the monotonic tensile test. The typical stress-strain relationships of the monotonic tensile test are presented in Fig. 3.

Table. 1 Mechanical properties of Q620 steel after high temperature exposure

No.	Specimen	Cooling method	Highest temperature experienced	Modulus of elasticity / MPa	Yield strength / MPa	Ultimate strength / MPa	Elongation after fracture
1	25T-MT	-	Ambient	2.02×10^5	656	731	13.6%
2	400T-A-MT	Air	400°C	2.13×10^5	637	717	12.7%
3	400T-W-MT	Water	400°C	2.15×10^5	679	764	12.7%
4	600T-A-MT	Air	600°C	2.16×10^5	666	737	13.8%
5	600T-W-MT	Water	600°C	2.17×10^5	673	754	12.5%
6	800T-A-MT	Air	800°C	1.87×10^5	366	622	16.7%
7	800T-W-MT	Water	800°C	1.91×10^5	480	752	10.7%

The results showed that when the highest temperature experienced by the specimens was no more than 600°C, the change of yield strength, the ultimate strength and the elongation of Q620 steel were moderate when compared with the counterparts at ambient temperature. The yield strength decreased by 2.9% when specimens were exposed to 400°C, while it increased by 1.5% when specimens were exposed to 600°C. The ultimate strength decreased by 1.9% when specimens were exposed to 400°C, while it increased by 0.8% when specimens were exposed to 600°C. When the highest temperature experienced was 800°C, the yield strength and ultimate strength decreased by 44.2% and 14.9%, respectively. The change of modulus of elasticity ranged from 5.4% to 7.4% for these specimens. The elongation after fracture decreased by 6.6% when specimens were exposed to 400°C, while it increased by 1.5% when specimens were exposed to 600°C. The elongation after fracture also increased by 22.8% when the highest temperature experienced was 800°C.

The cooling methods had a significant impact on the static mechanical properties. The specimens cooled in the water had a higher modulus of elasticity, yield strength and ultimate strength when compared to those cooled in air. However, the elongation after fracture was significantly reduced when the specimens were cooled down in the water. For the specimens exposed to 800°C, the elongation after fracture was 16.7% and 10.7% when they were cooled in the air and the water, respectively.

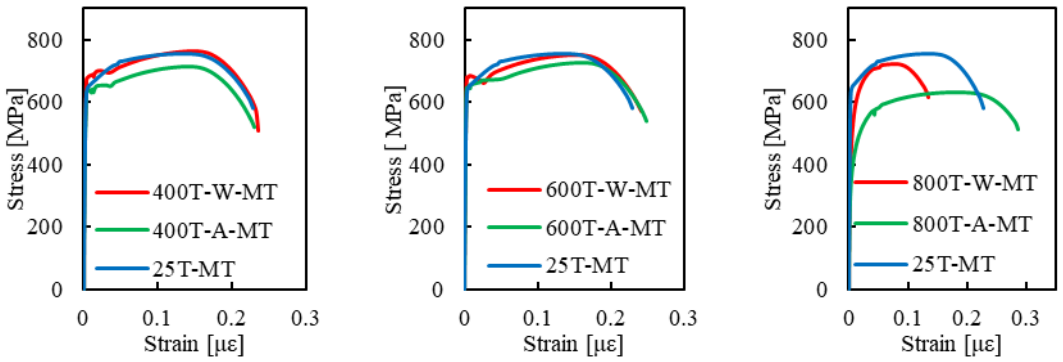

(a) 400°C (b) 600°C (c) 800°C

Fig. 3 Typical monotonic tensile stress-strain curves

3.2. Stress-strain relationship of cyclic loading test

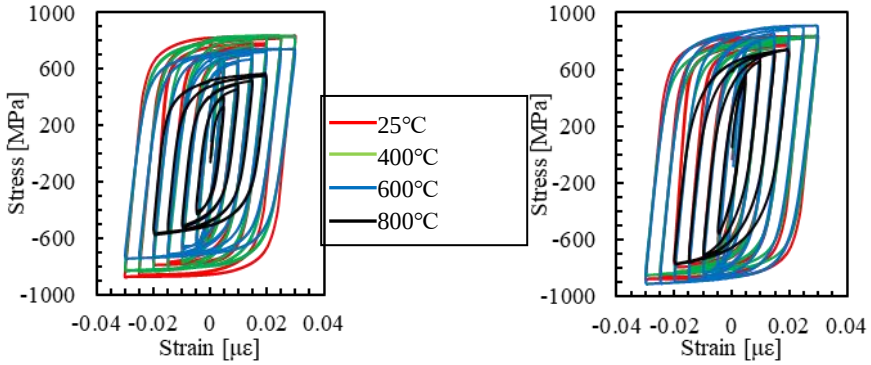

(a) Cooled in the air (b) Cooled in the water

Fig. 4 Typical cyclic loading stress-strain curves

The stress-strain relationships of the cyclic loading test after high temperature exposure are presented in Fig.4. For the specimen with the highest temperature was 800°C, obvious out-of-plane buckling occurred when the strain exceeded ±4% in the cyclic loading test, so only the data with the strain within ±4% was retained. In general, the hysteretic loops of specimens after fire exposure were plump.

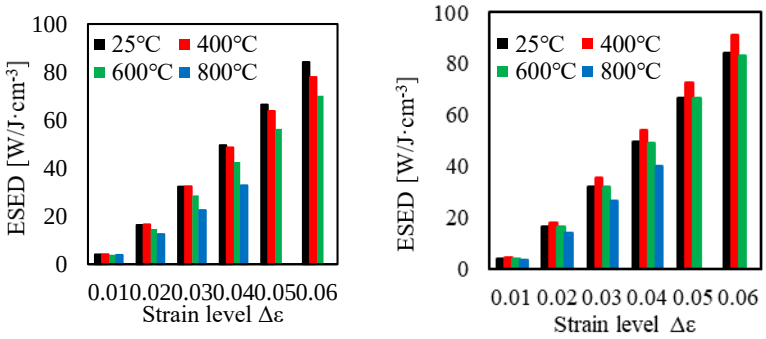

(a) Cooled in air (b) Cooled in water

Fig. 5 Comparison of ESED of steels after high temperature

The elastoplastic strain energy density (ESED) consumed by a single hysteretic loop can be obtained by the area of the stress-strain loop. In general, a larger ESED represents a better energy dissipation capacity. The calculated ESED for specimens are shown in Fig.5 and Table 2, where W is the ESED value, and Δε is the strain level.

Table. 2 Elastoplastic strain energy density (ESED) (Unit: J·cm^{-3})

No.	Specimen	Cooling method	Maximum temperature	Strain level Δε					
				0.01	0.02	0.03	0.04	0.05	0.06
1	25T	-	Ambient	4.008	16.276	32.295	49.535	66.391	84.132
2	400T-A	Air	400°C	4.131	16.588	32.414	48.589	63.773	77.854
3	600T-A	Air	600°C	3.964	14.649	28.644	42.574	56.362	70.109
4	800T-A	Air	800°C	3.779	12.263	22.759	33.445	-	-
5	400T-W	Water	400°C	3.991	16.126	31.091	47.093	62.859	78.847
6	600T-W	Water	600°C	4.044	16.207	31.405	47.748	63.462	78.719
7	800T-W	Water	800°C	3.371	13.765	26.640	39.875	-	-

It can be seen that both the highest temperature experienced and the cooling method affect the ESED of specimens. For the specimens cooled in the air, the energy dissipation capacity gradually decreased as the highest temperature increased. At the strain level of 0.04, the ESED values of the specimens

exposed to 600°C and 800°C decreased by 14% and 33%, respectively. For the specimens cooled in the water, when the highest temperature experienced by the specimens was less than 400°C, the post-fire energy dissipation capacity increased slightly. The capacity decreased when the temperature was more than 400°C. For instance, at the strain level of 0.04, ESED values of the specimens exposed to 600°C and 800°C decreased by 3% and 20%, respectively.

3.3. Metallographic analysis

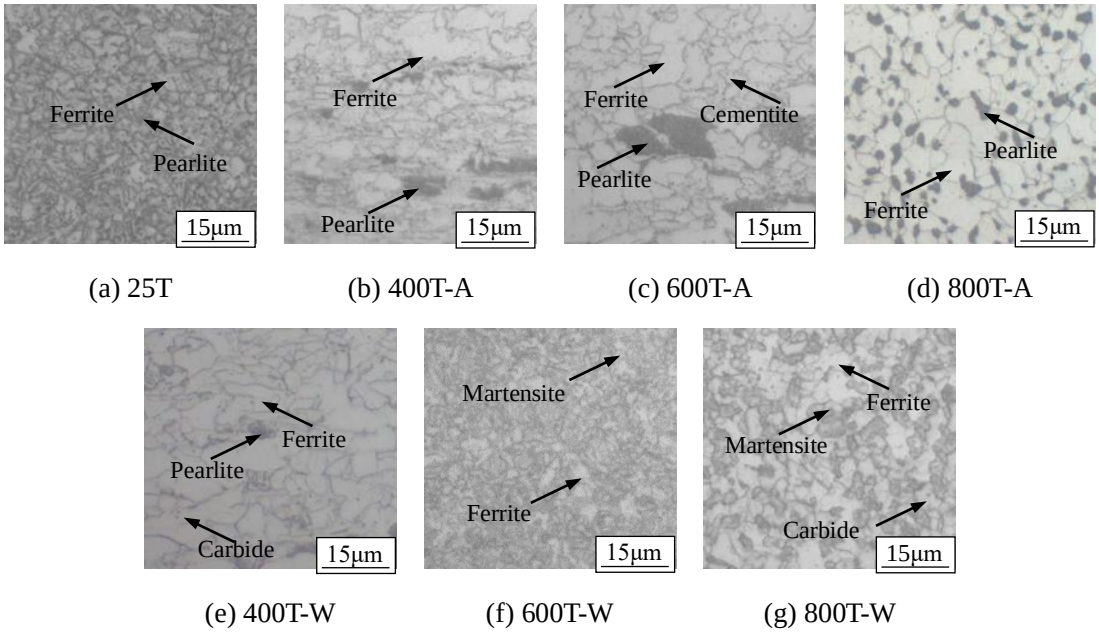

(a) 25T (b) 400T-A (c) 600T-A (d) 800T-A

(e) 400T-W (f) 600T-W (g) 800T-W

Fig. 6 Microstructure of specimens

Fig. 6 shows the metallographic structure of Q620 steel. The components of the metallographic structure at ambient temperature are mainly the ferrite (white) and the lamellar pearlite (black). The strength and hardness of pearlite are significantly higher than those of ferrite, while the plasticity and toughness are worse than those of ferrite. For Q620 steels cooled in the air, when the highest temperature experienced exceeded 400°C, the proportion of pearlite decreased. At around 800°C, the pearlite was in the form of spheroidal pearlite (the dark area in Fig. 6), which reduced the steel strength and enhanced the ductility. For the Q620 steel cooled in the water, the martensite appeared in the cooling products when the temperature was high, which enhanced the steel strength and reduced the ductility.

4. CONCLUSIONS

In this study, monotonic tensile and cyclic loading tests were carried out for Q620 steels after exposure to high temperatures. The main conclusions drawn were as follows:

- The yield strength, the ultimate strength and ultimate elongation of Q620 steel exposure to high temperature changed moderately when the highest temperature experienced was 600°C. The yield strength and ultimate strength decreased by 44.2% and 14.9% when the specimens were exposed to 800°C, respectively. However, the elongation after fracture increased by 22.8% when the highest temperature experienced was 800°C. For water-cooled specimens, the yield strength and the ultimate strength were higher than for air-cooled specimens, while the elongation after fracture was lower.

- The hysteretic curves of the specimens exposed to high temperatures were plump and stable. When the highest temperature experienced by the specimen was 800°C, for the specimens cooled in air, the energy consumption capacity of the Q620 specimen decreased by 33% when the strain level was 4%. For the specimens cooled in the water, the energy consumption capacity decreased by

20% when the strain level was 4%.

- The change of metallographic structure of Q620 steel was moderate when the highest temperature experienced was less than 600°C. The martensite was formed for the specimens exposed to around 600°C and cooled in the water.

REFERENCES

Ding, F. X., Yu, Z. W., & Hai, H. L. (2006). Experimental research on mechanical properties of Q235 steel after high temperature treatment, *Jianzhu Cailiao Xuebao* (*Journal of Building Materials*), *9*, 245-249. (in Chinese).

Li, G. Q., Lyu, H. B., & Zhang, C. (2017). Post-fire mechanical properties of high strength Q690 structural steel, *Journal of Constructional Steel Research, 132*, 108-116.

National Standard of the People's Republic of China. (2010). Metallic materials-tensile testing-Part 1: method of test at room temperature, *Standards Press of China, GB/T 228.1*.

National Standard of the People's Republic of China. (2021). Metallic materials-Fatigue testing-Axial-strain-controlled method, *Standards Press of China, GB/T 26077-2021*.

Qiang, X. H., Bijlaard, F. S. K., & Kolstein, H. (2012). Post-fire mechanical properties of high strength structural steels S460 and S690. *Engineering Structures, 35*, 1-10.

Wang, X. Q., Tao, Z., & Hassan, M. K. (2020) Post-fire behavior of high-strength quenched and tempered steel under various heating conditions, *Journal of Constructional Steel Research, 164*, 1-17.

Zhang, Y. J., Zhu, Y., Zhao, S., & Hu, K. X. (2009). Experimental research on mechanical properties of steel cooled in different modes after high temperature treatment, *Structural Engineers, 25*, 104-109.

Proc. 3rd International Conference on Structural Engineering Research (iCSER 2022)
27-30 Nov 2022, Sydney, Australia
ISBN: 978-0-6456692-1-3

Effect of Bolt Thread on Ultimate Capacity and Failure Mode of Structural Bolts Under Tension and Compression

Md Kamrul Hassan[1*], Bulbul Ahmed[1], Mohamed Ghannam[2], Swapan Saha[1]

[1]School of Engineering, Design and Built Environment, Western Sydney University, Penrith, NSW 2751, Australia

[2]Faculty of Engineering, Mansoura University, Mansoura, Dakahlia 35516, Egypt

Corresponding author's E-mail: k.hassan@westernsydney.edu.au

Abstract

Structural bolts have widely been used in prefabricated construction to connect the top and bottom steel columns. In recent years, normal structural bolts have been used to connect two concrete-filled steel tubular (CFST) columns to make efficient construction for prefabricated CFST columns and noticed that such bolts are under compression. Although extensive research has been conducted under tension, there is limited research on structural bolts under compression. Even, the effect of bolt thread under compression has not been investigated. The main aim of this study is to investigate the effect of bolt thread on the ultimate capacity and failure mode under tension and compression. The results indicate that the ultimate capacity of the bolts under compression is higher compared to the bolts under tension. Furthermore, the failure mode of the bolt under compression is also different compared to the tensile one.

Keywords: Structural bolts, Compression behaviour, Tension behaviour, Bolt thread, Finite element analysis.

1. INTRODUCTION

Conventional structural bolts have widely been used in composite construction to connect one component to another component (Shemshadian et al., 2019; Wang et al., 2019; Yang et al., 2022; Mumtaz and Yue, 2022; Paghaleh et al., 2022). Concrete-filled steel tubular (CFST) columns have been paid high attention in civil engineering construction. In construction with CFST column, blind bolts are suitable to connect one column to another column and column to beam connection instead of conventional structural bolts (Wu et al., 2005; Zhou et al., 2012; Tao et al., 2017; Li et al., 2018; Debnath and Chan, 2021; Li et al., 2021). Demountable CFST column-to-column connections are being used recently in on-site construction. But the demountable CFST column-to-column connection is complex and blind bolts are required. In contrast, prefabricated construction with CFST columns have been increased day by day for the higher capacity and fire resistance (Uy et al., 2017; Hassan et al., 2018). In prefabricated CFST column-to-column connection, conventional structural bolts can be used to minimise the cost compared to blind bolts.

To avoid the complexity of demountable CFST column-to-column connection, recently, Hassan et al. (2021) developed a prefabricated CFST column-to-column (PCC) connection system. This system uses locally available conventional structural bolts and couplers instead of blind bolts, which makes the construction economical. It is noted that the structural bolts experience compression in the PCC connection system. However, structural bolts under compression have not been investigated separately. Thus, there is a strong need to investigate the behaviour of bolts under compression. Much research on structural bolts under tension, shear and combined tension and shear has been conducted in the past studies (Grimsmo et al., 2016; Hu et al., 2016; Kawohl and Lange, 2016; Hedayat et al., 2017; Elliott et al., 2019; Li et al., 2020a; Song et al., 2020). However, there is no scientific research evidence on the effect of bolt thread on the ultimate capacity and failure modes of bolts under compression. Therefore, the effect of bolt thread on the ultimate capacity and failure modes under tension and compression needs to be investigated. In the present study, the effect of bolt thread on the ultimate capacity and failure

modes under tension and compression is investigated based on finite element (FE) analysis. FE model is developed and verified with the test data of structural bolts under tension and compression. Data was generated with different bolt sizes and grades by FE analysis. Based on the numerical data, design capacity has also been checked for the different number of bolt threads.

2. FE MODELLING AND VERIFICATION

2.1. Model building

The present study modelled the structural bolts, bolt head and top and bottom loading plate using 3D10 element. For the thread of the bolts, Fukuoka and Nomura (2008) proposed a helical thread model used in this study. The thread angle is constant as 60° for all bolts size, but the pitch is different for different diameters of bolts. Two loading plates having a thickness of 25 mm are used to apply the load at the top and bottom ends. For the M16 bolt, the pitch is 2.0 mm. On the other hand, this value is 2.5 mm and 3.0 mm for M20 and M24 bolts, respectively. The thickness of the bolt head is 10.07 mm, 12.47 mm, and 15.12 mm for M16, M20 and M24 bolts, respectively. The length of the bolt shank varies from 59.76 mm to 60.08 mm for bolts having a diameter of 16 mm to 24 mm. The diameter of the bolt shank is used as 24 mm, 30 mm, and 36 mm for M16, M20 and M24 bolts, respectively, in the FE model. From the sensitivity analysis, C3D8R elements were used for both loading plates.

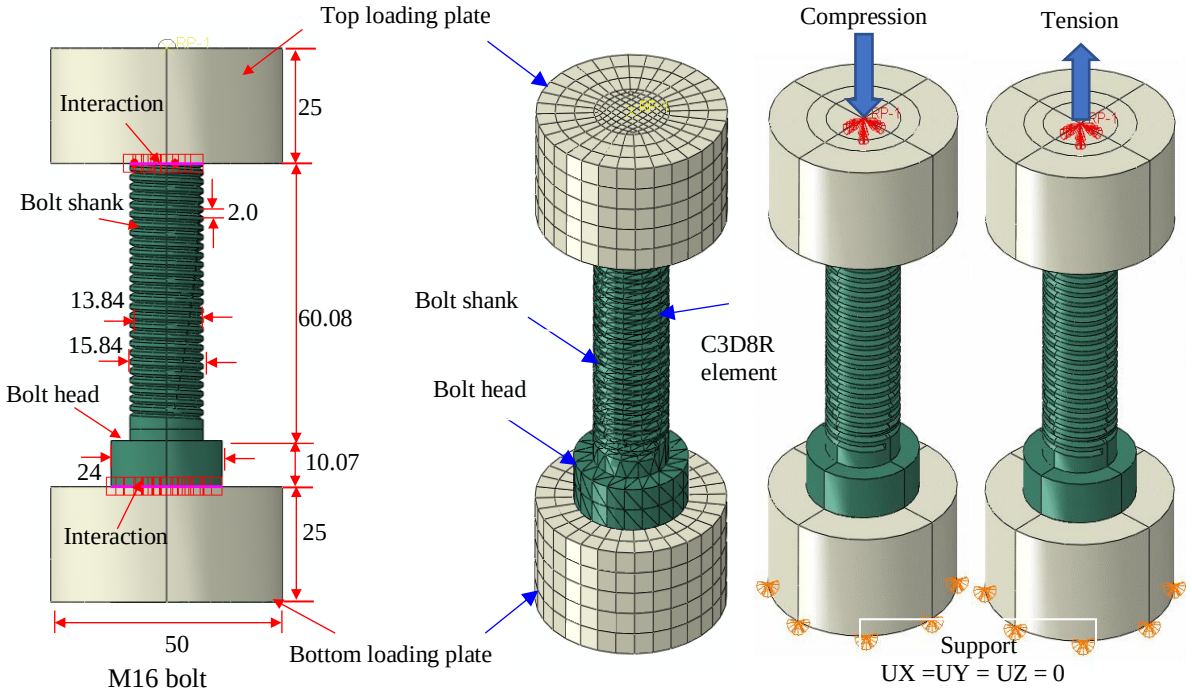

Figure 1. Model building for structural bolts under compression

The efficiency of the computational capacity is increased by selecting mesh sizes 5 mm and 10 mm for bolts and loading plates, respectively. Fixed end boundary conditions are used at the bottom end, and all the degrees of freedom except axial displacement are restrained at the top end. The loading is applied using the displacement control loading method. A reference point was created at the center of the loading plate, and all nodes are tied to this point. The axial load was applied in a downward direction through this reference point. All dimensions of M16 bolts used in FE model and the boundary conditions are presented in Figure 1. The full-range stress-strain material model proposed by Hassan (2016) is used to assign the elastic and plastic behaviour with strain hardening.

2.2. Verification

The developed FE model is verified with the 12 test results under compression. The dimensions of all

bolts are described in Table 1. Where, outer thread diameter (*D*1), inner thread diameter (*D*2), bolt length (*L*), thickness of bolt head (*H*), across corners of bolt head (*C*), across the flats of bolt head size (*F*), pitch (*P*) and thread angle. In this study, FE model results of 10.9 grade M20 bolt under compression is showed only for comparison purpose. The predicted curve can accurately represent the full range curve load-axial deformation curve, as depicted in Figure 2(a). From the comparison. It is seen that the initial stiffness, ultimate capacity, and the post-peak behaviour is well agreed. FE model is further validated with the test results of bolts under tension. For instance, 12.9 grade M20 fully threaded bolts was tested by Li et al. (2020b) under tension is used for the comparison. From the comparison it is observed that FE model can accurately reflect the full range curve load-axial deformation curve, as depicted in Figure 2(b).

Table 1. Dimension details of structural bolts

Bolt type and grade	*D* (mm)	*D*1 (mm)	*D*2 (mm)	*H* (mm)	*C* (mm)	*F* (mm)	*L* (mm)	Pitch, *P* (mm)	Thread angle (°)
CB16-8.8	16	15.84	13.84	10.07	27.20	23.81	60.08	2.00	60
CB16-10.9	16	15.86	13.86	10.18	27.26	23.83	59.91	2.00	60
CB20-8.8	20	19.82	17.30	12.47	34.12	29.91	60.02	2.50	60
CB20-10.9	20	19.82	17.26	12.48	34.21	29.92	60.02	2.50	60
CB24-8.8	24	23.76	20.72	15.12	40.93	35.63	59.76	3.00	60
CB24-10.9	24	23.74	20.74	15.24	40.83	35.61	59.43	3.00	60

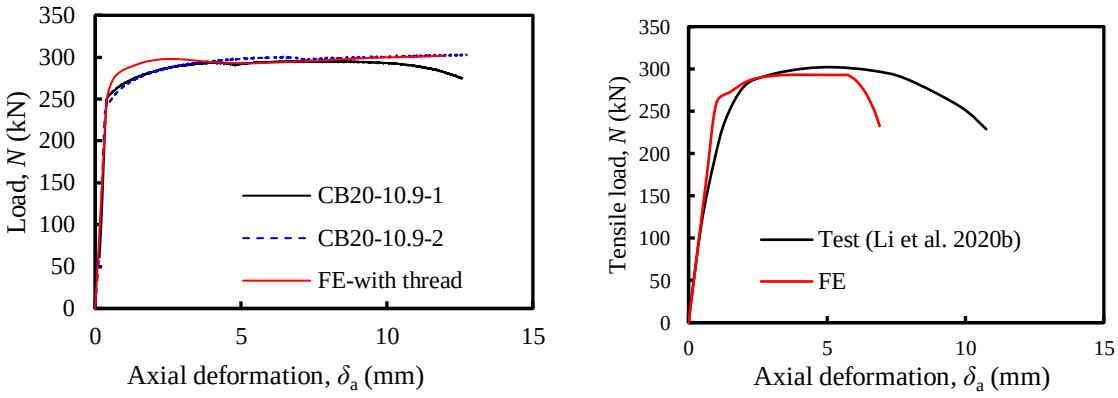

(a) Bolt under compression (b) Bolt under tension

Figure 2. Comparison between the test and FE results under compression and tension

3. BOLTS UNDER TENSION AND COMPRESSION

Structural bolts under tension and compression are discussed in this section. The failure modes of structural bolts under tension and compression are completely different. When the bolt is under compression, the global buckling failure mode is observed. However, when the bolt is under tension, axial elongation occurs, and it experiences necking under tension. The comparison of failure modes bolts under tension and compression is shown in Figure 3. Failure mode under tension is collected from Li et al. (2020a) for 12.9 grade M20 bolt, while global buckling failure mode is found from the test.

The ultimate capacity of the bolt under tension is less compared to compression. This is due to the necking of bolts which reduces cross-sectional, and the bolt is elongated, while the treads of the bolts are compressed, which increases the cross-sectional area of a bolt and increases its ultimate load capacity in the compression test. For instance, the ultimate capacity of a 10.9 grade M20 bolt is 270.55 kN (Li et al., 2020a) and 304 kN (test) under tension and compression, respectively. In contrast, the ultimate capacity of a 12.9 grade M20 bolt under tension is 302 (Li et al., 2020b), which is the same as a 10.9 grade M20 bolt under compression.

The structural behaviour is also investigated for 8.8 grade M20 bolt under tension and compression, as shown in Figure 4. From the comparison, load-deformation curves and failure modes are completely different. In compression, the bolt shows strain hardening behaviour, while sudden failure has been observed after reaching peak strength. In addition, necking at mid-height and global deformation failure are observed under tension and compression, respectively.

(a) Bolt under tension (Li et al., 2020a) **(b) Bolt under compression**

Figure 3. Failure modes of bolts under tension and compression

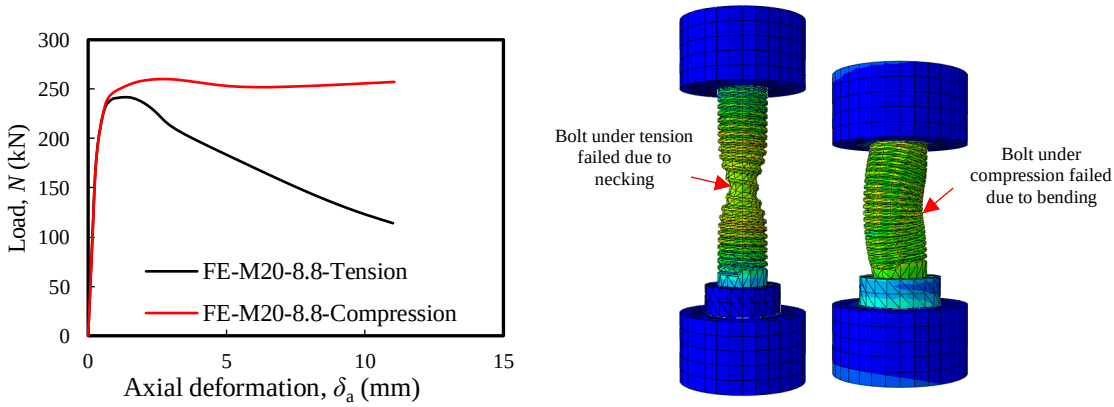

(a) Load-deformation curves **(b) Failure modes**

Figure 4. Behaviour of M20-8.8 grade bolt under tension and compression

4. EFFECT OF BOLT THREAD IN COMPRESSION AND TENSION

In the existing AS4100 design code, the ultimate capacity of the structural bolt is determined under tension by $N_{\mathrm{AS4100}} = A_{\mathrm{s,b}} f_{\mathrm{u}}$ equation. Where, ($A_{\mathrm{s,b}}$) is the effective cross-section of the bolt as expressed in Eq. (1). Effective diameter of bolt was used and the value of β is used as 0.9382. When β is used as 0.9382 the effective cross-sectional area of a bolt under tension is smaller and shows very conservative prediction.

$$A_{\mathrm{s,b}} = \frac{\pi}{4}(d_o - \beta P)^2 \tag{1}$$

Parametric analysis has been conducted for M20 bolt under compression with the defined effective diameter of AS4100 (E). The results are compared with the test results and found that prediction accuracy is very conservative, as depicted in Figures 5(a-b). Therefore, the ultimate capacity of bolt under compression is proposed based on the increased effective cross-sectional area. The measured cross-sectional area ($A_{\mathrm{s,b}}$) is determined from the average diameter D = ($D1$+$D2$)/2, where $D1$ is outer thread diameter and $D2$ is inner thread diameter. The value of β is considered as 0.58 to determine the effective cross-sectional area of the bolt and the ultimate capacity of the bolt under compression, as expressed in Eq. (2).

$$A_{s,b} = \frac{\pi}{4}(d_o - 0.58P)^2 \quad (2)$$

Based on proposed (P) effective cross-sectional area the FE results of the similar grade of bolts are shown in Figures 5(a-b). As can be seen from the figures, the ultimate capacity can achieve accurately. The failure modes are also observed and found that failure modes cannot predict properly when thread is not considered in the bolt shank. On the other hand, the failure mode can represent properly when thread is presented in bolt shank, as shown in Figures 6(a-c).

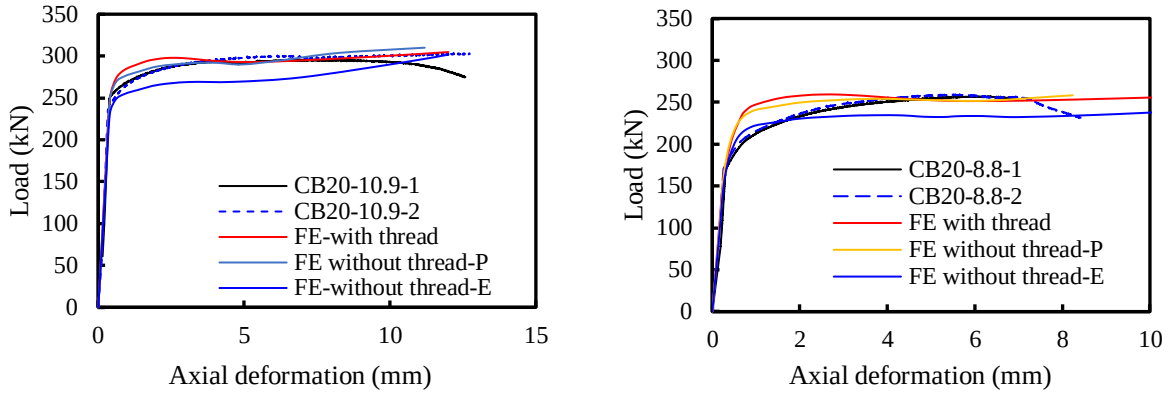

(a) M20 bolt with 10.9 grade **(b) M20 bolt with 8.8 grade**

Figure 5. Effect of bolt diameter on the ultimate load capacity of M20-8.8bolt

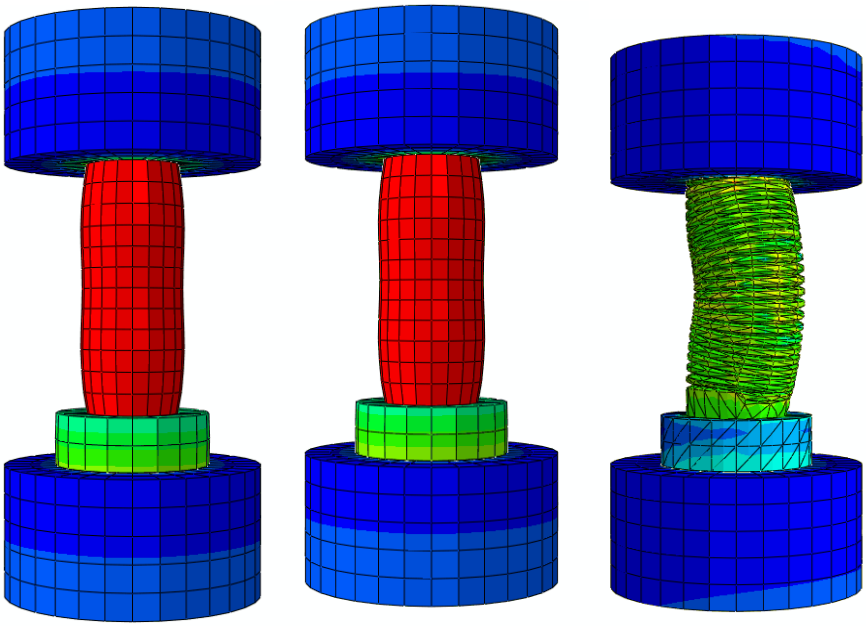

(a) With thread-E **(b) With thread-P** **(c) With thread**

Figure 6. Effect of bolt diameter on failure modes of M20-8.8 bolt

The ultimate capacity of the bolt under compression based on the proposed effective cross-sectional area using Eq.(2), is determined. It found that proposed equation of ultimate capacity of bolt under compression is significantly improved. The mean and standard deviation of the AS4100 code is 0.855 and 0.0253, respectively. On the other hand, these values are 0.927 and 0.0274, respectively based on the proposed approach.

CONCLUSIONS

This paper presents the effect of bolt thread under tension and compression to determine the ultimate capacity. FE modelling has been conducted and verified the test data under tension and compression. Parametric analysis has been performed based on the verified FE model and found that the ultimate capacity and failures modes are significantly affected under compression and tension. Also, bolt thread has large influence in ultimate capacity and the failure modes. Finally, the ultimate capacity equation is proposed with considering bolt thread and the proposed equation is compared with test data and observed a very good agreement between test and predicted results.

ACKNOWLEDGMENTS

The authors are grateful to the experimental and computational supports for numerical study provided by Western Sydney University. The authors would also like to extend immense thanks to Western Sydney University for providing the research platform. Finally, we would also like to express our gratitude to the laboratory staff for providing support during experimental tests.

REFERENCES

Debnath, P. P., Chan, T. M. (2021). A comprehensive numerical approach for modelling blind bolted CFST connections. *Structures*, 33, 2208-2225.

Elliott, M. D., The, L. H., Ahmed, A. (2019). Behaviour and strength of bolted connections failing in shear. *J Constr Steel Res*, 153, 320-329.

Fukuoka, T., Nomura, M. (2008). Proposition of helical thread modelling with accurate geometry and finite element analysis. *J Press Vessel Technol*, 130: 011204-011204-6.

Grimsmo, E. L., Aalberg, A., Langseth, M., Clausen, A. H. (2016). Failure modes of bolt and nut assemblies under tensile loading. *J Constr Steel Res*, 126: 15-25.

Hassan, M. K. (2016). Behaviour of hybrid stainless-carbon steel composite beam-column joints. *PhD Thesis, Institute for Infrastructure Engineering, Western Sydney University, Australia*.

Hassan, M. K., Sheikh, M. N., Saha, S. (2021). Behaviour and design of prefabricated CFST stub columns with PCC connections under compression. *Thin Walled Struct*, 166:108041.

Hassan, M. K., Tao, Z., Liao, L. (2018). Numerical study of column-column connections for prefabricated concrete filled steel columns. *25th Australasian Conference on Mechanics of Structures and Materials, Australia*.

Hedayat, A. A., Afzadi, E. A., Iranpour, A. (2017). Prediction of the bolt fracture in shear using finite element method. *Structures*, 12, 188-210.

Hu, Y., Shen, L., Nie, S., Yang, B., Sha, W. (2016). FE simulation and experimental tests of high strength structural bolts under tension. *J Constr Steel Res*, 126:174-186.

Kawohl, A. K., Lange, J. (2016). Tests on 10.9 bolts under combined tension and shear. *Acta Polytechnica*, 56(2), 112-117.

Li, D., Uy, B., Patel, V., Aslani, F. (2018). Behaviour, and design of demountable CFST column-column connections subjected to compression. *J Constr Steel Res*, 141, 262-274.

Li, D., Uy, B., Wang, J., Song, Y. (2020b). Behaviour, and design of high-strength Grade 12.9 bolts under combined tension and shear. J Constr Steel Res 2020b; 174: 106305.

Li, D., Uy, B., Wang, J., Song, Y. (2021a). Behaviour, and design of Grade 10.9 high strength bolts under combined actions. *Steel and Compos Struct*, 35(03): 327-341.

Li, B., Yang, Y., Liu, J., Liu, X., Cheng, Y., Chen, Y. F. (2021). Behaviour of T-shaped CFST column to steel beam connection with U-shaped diaphragm. *J Build Struct Eng*, 43, 102518.

Mumtaz, H., Yue, F. (2022). Numerical study of intermeshed steel beam-column connections. *J Constr Steel Res*, 189, 107079.

Paghaleh, F. J., Hadianfard, M. A., Saffari, H. (2022). Seismic behaviour of through beam connection to steel box-column. *J Constr Steel Res*, 193, 107261.

Shemshadian, M. E., Le, J. L., Schultz, A. E., Getrick, P. M., Al-Sabah, S., Laefer, D. F. (2019). Numerical study of the behaviour of intermeshed steel connections under mixed-mode loading. *J Constr Steel Res*, 160, 89-100.

Song, Y., Wang, J., Uy, B., Li, D. (2020). Experimental behaviour, and fracture prediction of austenitic stainless-steel bolts under combined tension and shear. *J Constr Steel Res*, 166: 105916.

Tao, Z., Hassan, M. K., Song, T. Y., Han, L. H. (2017). Experimental study on blind bolted connections to concrete-filled stainless-steel columns. *J Constr Steel Res*, 128, 825-838.

Uy, B., Patel, V., Li, D., Aslani, F. (2017). Behaviour, and design of connections for demountable steel and composite structures. *Structures*, 9, 1-12.

Wang, J., Wang, W., Lehman, D., Roeder, C. (2019). Beam-column connection under a column removal scenario. *J Constr Steel Res*, 153, 55-70.

Wu, L. Y., Chung, L. L., Tsai, S. F., Shen, T. J., Huang, G. L. (2005). Seismic behaviour of bolted beam-to column connections for concrete filled steel tube. *J Constr Steel Res*, 61, 1387-410.

Yang, F., Liu, Y., Jiang, Z., Xin, H. (2018). Shear performance of a novel demountable steel-concrete bolted connector under static push-out tests. *Eng Struct*, 160, 133-146.

Yang, Y., Xu, L., Feng, S., Sun, D., Xue, Y., Yu, Y. (2022). Experimental study on the seismic performance of a prefabricated steel column-column connection. *J Constr Steel Res*, 194, 107303.

Zhou, P., Xue, J. Y., Chen, X. (2012). Experimental study on seismic performance of joints between concrete-filled square steel tubular special-shaped columns and steel beams. *J Build Struct*, 33(8), 44-50.

Proc. 3rd International Conference on Structural Engineering Research (iCSER 2022)
27-30 Nov 2022, Sydney, Australia
ISBN: 978-0-6456692-1-3

Experimental Study on Tensile Behavior of Slip-Critical Blind Bolts Anchored in Concrete-Filled Steel Tubes

Xing Gao[1], Wei Wang[2] and Lip Teh[3]

[1]PhD candidate, State Key Laboratory of Disaster Reduction in Civil Engineering, Dept. of Structural Engineering, Tongji University, Shanghai, China
[2]Professor, State Key Laboratory of Disaster Reduction in Civil Engineering, Dept. of Structural Engineering, Tongji University, Shanghai, China
[3]Professor, School of Civil, Mining & Environmental Engineering, University of Wollongong, Wollongong, Australia

Corresponding author's E-mail: gussiegao@tongji.edu.cn

Abstract

This paper presents an experimental study on a Concrete-Anchored Slip-Critical Blind Bolt (CASCBB) system, which can be used to connect a steel beam to a concrete-filled steel tube column to form a rigid moment connection, with varying parameters such as types of bolts, tube thickness and bolt edge distance. A series of pull-out tests of CASCBBs embedded in concrete-filled steel square hollow section (SHS) was conducted to investigate the potential of the CASCBB connections. It was found that a concrete cone failure could be followed by a bolt pull-out or tube corner fracture, depending on the bolt edge distance and the tube thickness. A connection with a sufficiently thick flange of the SHS can benefit from the contribution of the flange to the tensile capacity, which can be of the same order as that of the concrete anchorage. The relative contribution of the tube flange to the connection's resistance was found to be a function of the ratio of the tube's thickness to its flange width. Placing the anchored bolt close to the SHS web doubled the stiffness compared to placing it in the middle of the flange due to the greater contribution of the steel tube. It also increased the load-carrying capacity significantly.

Keywords: Anchored connection, blind bolt, bolted tubular moment connection, slip-critical blind bolt.

1. INTRODUCTION

One of the most important advantages of hollow steel section is that it provides confinement to the concrete infill, increasing the concrete strength (Knowles and Park 1969). However, traditional bolting techniques are often not applicable to connections involving hollow sections. So blind bolting technology is, therefore, an attractive development as it allows the bolt to be installed from one side, solving the challenge of bolting a hollow section to another member (Mourad et al. 1996, France et al. 1999, Lee et al. 2010, Wang et al. 2017, Jiao et al. 2020). Researchers have also attempted to increase the rotational stiffness of moment connections assembled with blind bolts by anchoring them within the concrete infill of the steel tube (Gardner and Goldsworthy 2005, Yao et al. 2008, Pitrakkos & Tizani 2013, Tizani et al. 2013, 2020, Agheshlui et al. 2016, Tao et al. 2017, Jeddi & Sulong 2018, Jiao et al. 2020).

Among the various blind bolting systems currently available, the Slip-Critical Blind Bolt (SCBB) is one of the very few that can achieve the same pre-tension as the conventional high strength bolts (Gao et al. 2022), which is important for rigid beam-to-column connections. However, researchers (Wang et al. 2017, Jiao et al. 2020) have found that endplate beam-to-column connections using SCBBs are classified as semi-rigid according to Section 5.2 in Eurocode 3 Part 1-8 (ECS 2005), especially for sway frames. Therefore, in order to satisfy the requirements for a rigid beam-to-column connection according to Section 5.2 in Eurocode 3 Part 1-8, the SCBBs are modified with an extension to allow anchorage to the concrete infill of the SHS member in this paper. The resulting system is called Concrete-Anchored SCBB (CASCBB).

This paper presents a series of seven pull-out tests of CASCBBs and SCBBs connected to SHS members.

It investigates the potential of the CASCBB connections at the component level, with varying parameters such as types of bolts, tube thickness and bolt edge distance. Discussions of test results are presented with respect to failure modes, strength and stiffness, plate separation, and contributions of different components to the total resistance.

2. TESTING PROGRAM

The CASCBB technology is an extension of the SCBB system, which consists of five components (Gao et al., 2022). The components of CASCBB are shown in Fig. 1. The only difference between the SCBB and the CASCBB systems is in the presence of an anchor stud with screw threads that is added to the head of the SCBB, as shown in Fig. 1(e). The installation procedure of a CASCBB connection is the same as that of an SCBB one (Gao et al., 2022).

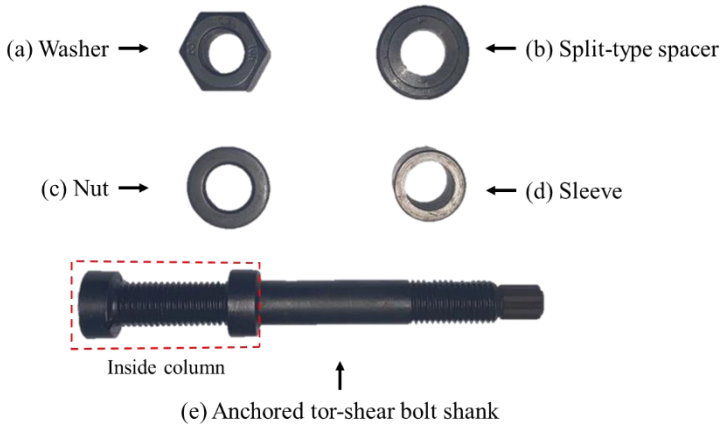

Figure 1. Components of CASCBB assembly

Seven blind bolted SHS connections were tested under tension (direct pull-out), as illustrated in Fig. 2. The dimensions of the SHS tube (all 250 mm) and the diameter of the bolts (all equal to 24 mm) were selected based on the research results obtained by Wang et al. (2017) involving eight cruciform extended endplate beam-to-column joints using SCBBs. The length of the anchor stud (the dimension *l* in Fig. 2) was set to 75 mm for the CASCBB in the present experiment. The infill concrete had a nominal unconfined compressive strength of 45 MPa.

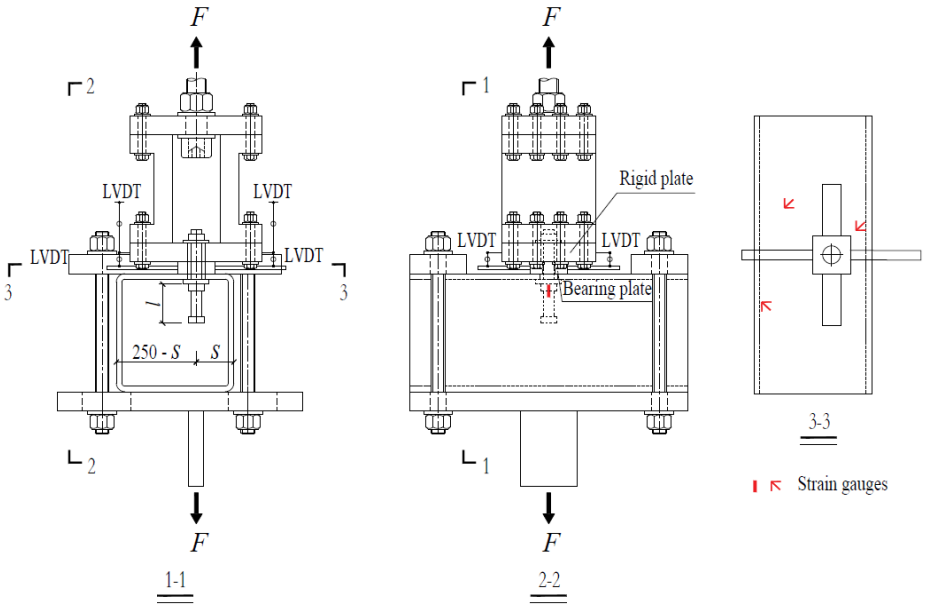

Figure 2. Pull-out test set-up

Each specimen is labelled *B*24-T*t*-*S*, where *B* is the type of the 24-mm bolt (S for SCBB, C for CASCBB), *t* is the thickness of SHS tube in millimetres, *S* is the distance in millimetres between the center of the bolt hole and the edge of the SHS flange (see Fig. 2). The average measured yield stresses f_y and tensile strengths f_u of the Grade 10.9 bolt and the Q345 tubes (rounded to the nearest 5 MPa) are given in Table 1, along with their elastic modulii and uniform elongations at fracture. The average compressive strength of the infill concrete was found to be 47.3 MPa after 28 days of curing.

Table 1. Material properties of bolt and SHS tubes

Component	f_y (MPa)	f_u (MPa)	E (GPa)	Uniform elongation at fracture
(CA)SCBB	1180	1440	239	12%
Thin steel tube (6 mm)	335	480	195	33%
Thick steel tube (12 mm)	370	505	171	31%

3. TEST RESULTS AND DISCUSSIONS

Figure 3 shows the load-deflection graphs of the tested specimens, plotted against the global displacement δ_g of the bolt. It can be seen from Fig. 3(b) that the SCBB specimen, S24-T6-80, quickly lost its initial stiffness at a load below 20 kN, while its CASCBB counterpart C24-T6-80 only lost the same above 50 kN. The CASCBB specimen had a maximum load of 204.5 kN (due to anchorage failure - denoted Mode I), as shown in Fig. 3(a), almost double that of its SCBB counterpart that was caused by bolt pull-out (denoted Mode III) at 105.1 kN. The SCBB specimen could not achieve any anchorage (concrete cone) failure as there was bonding failure between the bolt and the concrete at about 15 kN, as indicated in Fig. 3(b). Even the pull-out load of the CASCBB specimen (150.5 kN) was 43.2% higher than that of its SCBB counterpart. Therefore, the CASCBB studied in the present work proved to be superior to the original SCBB (Jiao et al. 2020, Gao et al. 2022) for anchorage to the concrete infill.

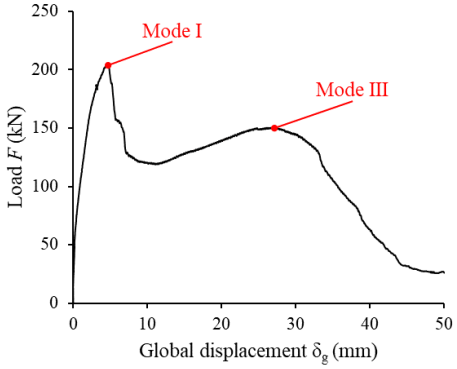

(a) C24-T6-80

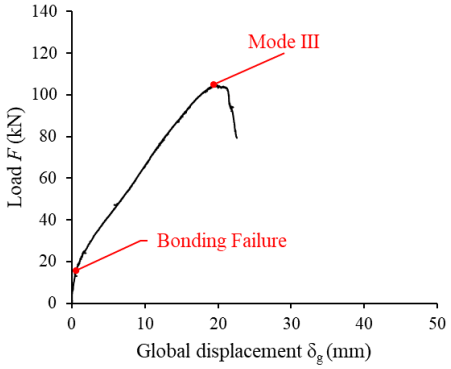

(b) S24-T6-80

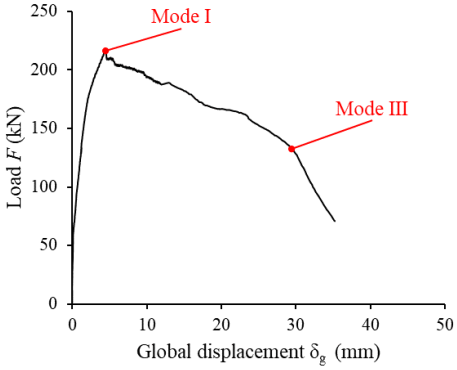

(c) C24-T6-50

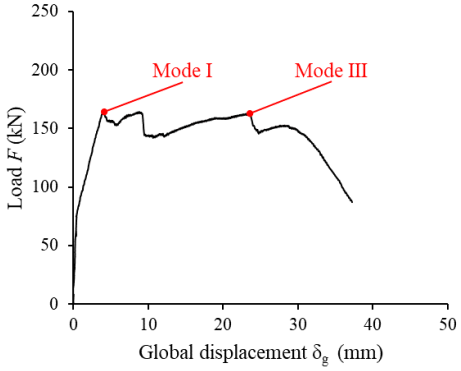

(d) C24-T6-125

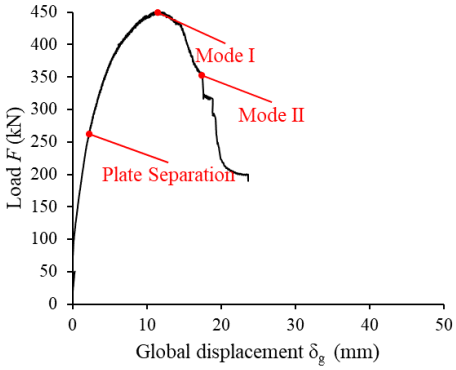

(e) C24-T12-50

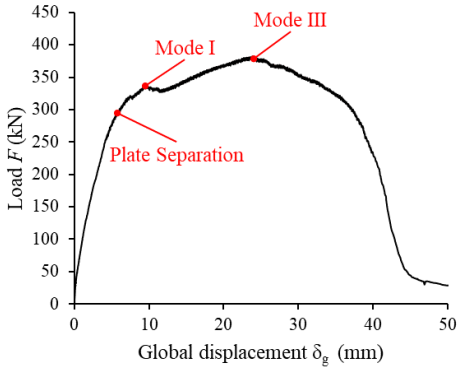

(f) C24-T12-80

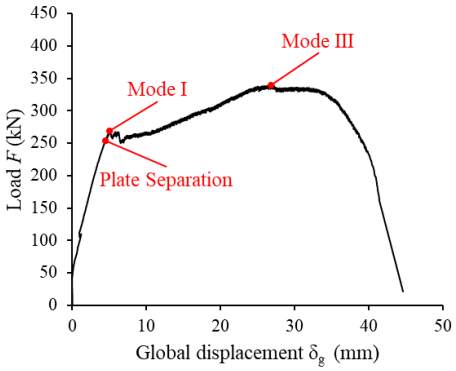

C24-T12-125

Figure 3. Load-global displacement (F-δ_g) graphs

As indicated in Figures 3(e)-(g), the thicker specimens (12 mm tube) experienced separation of the connected plates at loads slightly higher than the bolt pre-tension of almost 245 kN. The test results confirm that the CASCBB connection behaves in the same manner under tension as a normal high strength steel bolted connection.

The anchorage or concrete cone failure mode (Mode I), which is distinct from bonding failure, took place in all CASCBB specimens. When the anchorage failed, the applied load typically dropped but could pick up again depending on the strength of the SHS flange. The tube corner fracture (Mode II) only took place in Specimen C24-T12-50, as indicated in Fig. 3(e). The bolt was located close to the SHS web (only 50 mm away) and was attached to the (failed) concrete cone, so the corner fractured before any pull-out failure of the bolt through the 12-mm thick flange. This specimen was also the only one that did not undergo bolt pull-out failure (Mode III).

For the CASCBB specimens with thin (6 mm) steel tube, the ultimate loads F_u were invariably reached when the concrete cone failure (Mode I) occurred, as indicated in Fig. 3. Although the resistance might pick up again following a sharp decline from F_u, the second peak load, associated with the bolt pull-out (Mode III), was lower than the first peak. The load was mainly transferred to the column wall after the concrete cone failure until the bolt was pulled out at the second peak. In fact, for Specimen C24-T6-50, where the bolt was close to the tube corner, there was only one peak load (being the anchorage failure load). The design strength of such connections may be based on the concrete cone failure load.

On the other hand, for the thick (12 mm) steel tube specimens C24-12-80 and C24-12-125, the bolt pull-out loads were higher than the preceding concrete cone failure loads, as shown in Fig. 8(f) and (g). They were also much higher than the ultimate loads of the thin (6 mm) steel tube specimens because of the larger bearing capacity of the thick column wall. For Specimen C24-T12-50, the applied load nearly

reached the nominal tensile strength of the bolt shank before the anchorage failed near the closest web.

Figure 3 shows that, for a given tube thickness, the tensile capacity of the CASCBB specimens increased with decreasing edge distance *S*. Relative to a bolt in the middle of the flange, placing the bolt close to a web increased the tensile capacity by 30% or more. For the thin (6 mm) tube specimens, the initial stiffness doubled when the bolt was moved from the SHS flange's centre (Specimen C24-T6-125) to near the web (Specimen C24-T6-50). A similar observation can be made for the thick (12 mm) tube specimens between Specimens C24-T12-125 and C24-T12-50.

4. CONCLUSIONS

The behavior and strength of a newly proposed concrete-anchored slip-critical blind bolt (CASCBB) system have been studied experimentally through a series of bolt pull-out tests from concrete-filled steel SHS. Three failure modes were observed, being anchorage or concrete cone failure, tube corner fracture and bolt pull-out. A concrete cone failure may be followed by a bolt pull-out or tube corner fracture, depending on the edge distance and the tube thickness. However, neither mode is necessarily associated with the maximum load-carrying capacity, depending on the tube flange's ratio of thickness to width.

The CASCBB system has been shown to result in a much stiffer and stronger connection compared to the existing SCBB system, which could not achieve the concrete cone failure mode due to premature bonding failure with the infill concrete.

A blind-bolted tubular connection with a sufficiently thick flange benefits from the substantial contribution of the flange to the tensile resistance, which can be of the same order as that of the concrete anchorage. Plate separation only takes place in tubes of sufficient thickness as thinner tube connections will experience concrete cone failure prior to reaching the plate separation load, which is slightly higher than the bolt pre-tension. Based on the present test results and those published in the literature, it is apparent that the relative contribution of the tube flange to the connection's resistance is a function of the ratio of the tube's thickness to its flange width (and the concrete strength).

The anchored bolt close to the SHS web has increased stiffness and strength compared to that in the middle of the flange due to the greater contribution of the steel tube. For the tested specimens, the stiffness at least doubled, while the increase in strength could be more than 30%.

REFERENCES

Agheshlui, H., Goldsworthy, H., Gad, E., & Yao, H. (2016). Tensile behavior of groups of anchored blind bolts within concrete-filled steel square hollow sections. *Journal of Structural Engineering*, https://doi.org/10.1061/(ASCE)ST.1943-541X.0001388.

ECS (2005). Eurocode 3: Design of Steel Structures, Part 1.8: Design of Joints, EN 1993-1-8, European Committee for Standardisation, Brussels, Belgium.

France, J. E., Buick Davison J., & Kirby P. A. (1999). Strength and rotational stiffness of simple connections to tubular columns using flowdrill connectors. *Journal of Constructional Steel Research*, https://doi.org/10.1016/S0143-974X(98)00236-3.

Gao, X., Wang, W., & Teh, L. H. (2022) A novel slip-critical blind bolt: Experimental studies on shear, tensile and combined tensile-shear resistances. *Thin-Walled Structures*, https://doi.org/10.1016/j.tws.2021.108630.

Gardner, A. P., & Goldsworthy, H. M. (2005). Experimental investigation of the stiffness of critical components in a moment-resisting composite connection. *Journal of Constructional Steel Research*, https://doi.org/10.1016/j.jcsr.2004.11.004.

Jeddi, M.Z., & Sulong, N.H.R. (2018) Pull-out performance of a novel anchor blind bolt (TubeBolt) for beam to concrete-filled tubular (CFT) column bolted connections. *Thin-Walled Structures*, https://doi.org/10.1016/j.tws.2017.12.028.

Jiao, W., Wang, W., Chen, Y., & Teh, L. H. (2020). Seismic performance of concrete-filled SHS column-to-beam connections with slip-critical blind bolts. *Journal of Constructional Steel Research*, https://doi.org/10.1016/j.jcsr.2020.106075.

Knowles, R. B., & Park, R. (1969). Strength of concrete filled steel tubular columns. *Journal of the Structural Division ASCE*, https://ascelibrary-org.ezproxy.uow.edu.au/doi/10.1061/JSDEAG.0002425.

Lee, J., Goldsworthy, H.M., & Gad EF. (2010). Blind bolted T-stub connections to unfilled hollow section columns in low rise structures. *Journal of Constructional Steel Research*, https://doi.org/10.1016/j.jcsr.2010.03.016.

Mourad, S., Korol, R. M., & Ghobarah, A. (1996). Design of extended endplate connections for hollow section columns. *Canadian Journal of Civil Engineering*, https://doi.org/10.1139/l96-029.

Pitrakkos, T., & Tizani, W. (2013) Experimental behaviour of a novel anchored blind-bolt in tension. *Engineering Structures*, https://doi.org/10.1016/j.engstruct.2012.12.023.

Tao, Z., Hassan, M. K., Song, T. Y., & Han, L. H. (2017). Experimental study on blind bolted connections to concrete-filled stainless steel columns. *Journal of Constructional Steel Research*, https://doi.org/10.1016/j.jcsr.2016.10.016.

Tizani, W., Al-Mughairi, A., Owen, J. S., & Pitrakkos, T. (2013). Rotational stiffness of a blind-bolted connection to concrete-filled tubes using modified Hollo-bolt. *Journal of Constructional Steel Research*, https://doi.org/10.1016/j.jcsr.2012.09.024.

Tizani, W., Mahmood, M., & Bournas D. (2020). Effect of concrete infill and slenderness on column-face component in anchored blind-bolt connections. *Journal of Structural Engineering*, https://doi.org/10.1061/(ASCE)ST.1943-541X.0002557.

Wang, W., Chen, Y., & Jian, X. (2017). Cyclic behavior of endplate connections to tubular columns with novel slip-critical blind bolts. *Engineering Structures*, https://doi.org/10.1016/j.engstruct.2017.07.015.

Yao, H., Goldsworthy, H., & Gad, E. (2008). Experimental and numerical investigation of the tensile behavior of blind-bolted T-stub connections to concrete-filled circular columns. *Journal of Structural Engineering*, *134*, 198-208.

Proc. 3rd International Conference on Structural Engineering Research (iCSER 2022)
27-30 Nov 2022, Sydney, Australia
ISBN: 978-0-6456692-1-3

Axial Load Capacity of Circular Concrete Filled Double Tube Stiffened Columns

Mohamed Ghannam [1],*, Ibrahim M. Metwally [2], Md Kamrul Hassan[3]

[1] Associate Professor, Structural Engineering Department, Faculty of Engineering, Mansoura University, Mansoura, Dakahlia 35516, Egypt
[2] Professor of Structural Engineering (Concrete Structures)Housing & Building National Research Center, Concrete Structures Research Institute
[3]Associate Lecturer, School of Engineering, Design and Built Environment, Western Sydney University, Penrith, NSW 2751, Australia,

* Corresponding author's E-mail: m.ghannam@mans.edu.eg

Abstract

The aim of this paper is to study the behaviour of stiffened concrete-filled double tube (CFDT) columns through numerical analysis. In this study, the inner and outer steel tubes are circular. Two types of stiffeners are studied (T, bar and rectangular stiffeners). The stiffeners are welded with inner and outer steel tubes. Finite element (FE) model that was verified with previous test results is used to study the behaviour of CFDT columns with the proposed stiffening method. FE model was used to study the effect of different parameters on the behaviour of stiffened CFDT columns. From the obtained result it can be noticed that using stiffeners with CFDT columns can increase its axial load capacity by about 15%. A simplified equation is developed to predict the axial design strength of stiffened CFDT columns.

Keywords: CFDT columns, *design axial strength*, Stiffeners, FE model, simplified equation.

1. INTRODUCTION

Now days more researches (Elchalakani et al. 2018; Han et al. 2006; Hassanein et al. 2018; Mohan and S 2016; Tao and Han 2006; Tao et al. 2004; Zhao and Han 2006) have been increasingly performed on concrete-filled double-skin steel tubular (CFDST) columns, and concrete filled double tube (CFDT) columns which has better performance and advantages compared to concrete-filled steel (CFST) tube columns, enhanced ductility, lighter structure, more strength better fire and dynamic behavior (Ghannam and Metwally 2020). CFDST column consists of double but where concrete fills the ring gap between these outer and the inner tubes, with no filling in the core (inside the inner tube). However, in the CFDT column, concrete also fills the core. The main disadvantage that may affect the behaviour of the CFDST column is the contact between steel tubes and concrete, where contact is only formed at the end of the loading stage when the lateral expansion of concrete increases as a result of concrete cracking (Tao et al. 2004 and Huang et al. 2010).

This disadvantage can be overcome by using stiffeners which can significantly improve the contact interaction between steel tubes and concrete. Circular tubes give better confinement to concrete than square columns due to tension circumference stress formed in the circular tube as a result of lateral concrete expansion occurring from axial loading. However, contact interaction can be improved using different types of stiffeners (Alatshan et al. 2020; Benzaid and Mesbah 2013; Campione et al. 2004; Song et al. 2013; Tabsh 2007).

Previously many research were performed on the effect of stiffeners on the behaviour of CFST columns using different types of stiffeners as Using binding bars, welding bar stiffeners (ties), rib stiffeners, T stiffeners, Saw shaped ribs, PBL rib, curling ribs, horizontal rings (Cai and He 2006; Lai and Ho 2013; Younes et al. 2016) Huang et al. (2002) (Tao et al. 2007; Tao et al. 2008; Tao et al. 2005) Tao et al. (2008). Most of these types positively affect the performance and capacity of the CFST columns with different degrees. However, limited research has been done on circular stiffened CFDST or CFDT columns (Hasan and Ekmekyapar 2019; Wang et al. 2017; Zakir et al. 2021). The aim of this paper is to

cover the gap in this area.

In this paper, the performance of circular stiffened CFDT columns was investigated by using a verified finite element (FE) model using ABAQUS software (ABAQUS 2012). The FE model was verified against test results reported by Romero et al. (2015). A parametric study was performed using a verified FE model and considered different parameters such as steel tube strength, concrete cylinder strength steel tube type (stainless steel or carbon steel), and slenderness steel tube width to thickness ratio between outer and inner steel tube diameter. Based on the parametric results, a simplified design equation was developed for predicting the axial load capacity of Circular stiffened CFDT columns.

2. FE MODEL DESCRIPTION AND VERIFICATION

2.1. FE model Description

FE model has been done using the ABAQUS program (ABAQUS 2012). Circular steel tubes were modelled using S4R shell element with elastic-plastic stress-strain curve for material properties as proposed by Tao et al. (2013). Concrete material is simulated using concrete-damaged plasticity, and the value of plasticity parameters is calculated as adopted by Tao et al. (2013) and the compressive stress-strain curve as adopted by Pagoulatou et al. (2014). Concrete was modelled using (C3D8R) solid element. T3D2 truss elements were used to simulate bar stiffeners. T and rectangular stiffeners were modelled using S4R shell element.

Surface-to-surface contact was used to model the interaction between the concrete of steel tubes with 0.25 as the coulomb friction coefficient. Imperfection was introduced to the model through buckling analysis with an amplitude of column length /200 as proposed by (Eurocode-4_1.1 2004). FE model is presented in Figure 1. A quarter model (half section and half length) was used to simulate the full column behavior, and this is to save computational time. The top boundary condition was simulated through a reference point coupled with the top of column two symmetric boundary condition was used as indicated in Figure 1. The load was applied to the reference point. The column width was divided into 16 mesh elements, while the element size in the longitudinal direction was double the size through the cross-section.

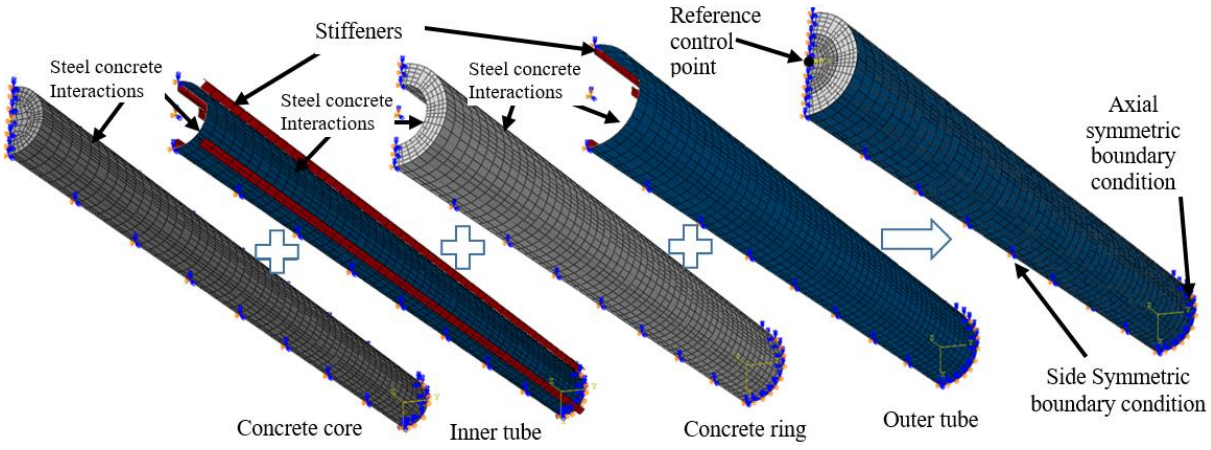

Figure 1. Finite element model

2.2. FE model verification

The FE model was verified against three experimental results ((Huang et al. 2002; Tao et al. 2007) (Romero et al. 2015)) as shown in figure 2. Huang et al. (2002) studied the effect of using ties at corners in strengthening square concrete-filled steel tube columns stiffened, while Tao et al. (2007) used rectangular stiffener with the four sides of square concrete-filled steel tube. Romero et al. (2015) studied the experimental behaviour of CFDT columns under fire and room temperature under axial load. Six specimens were tested in fire, and another six were tested at room

temperature. The model in this paper was verified against the experimental test at room temperature. Details of specimens are presented in Figure 1. It can be seen from Figure 2 that there is a good agreement with previous test results.

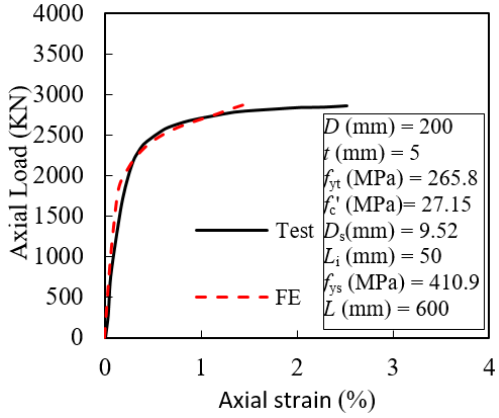

(a) SS-040-50(3)Huang et al. (2002)

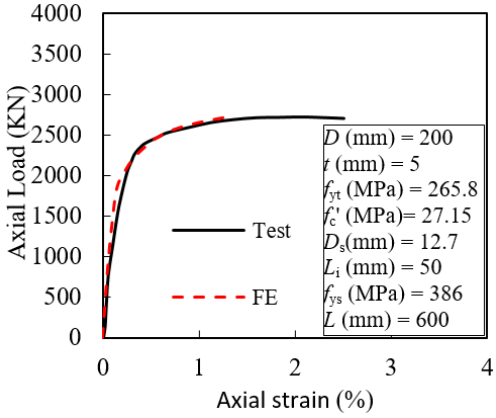

(b) SS-040-50 (4)Huang et al. (2002)

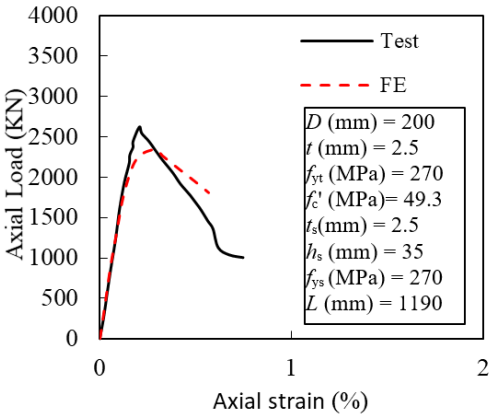

(c) SCFT1-1Tao et al. (2007)

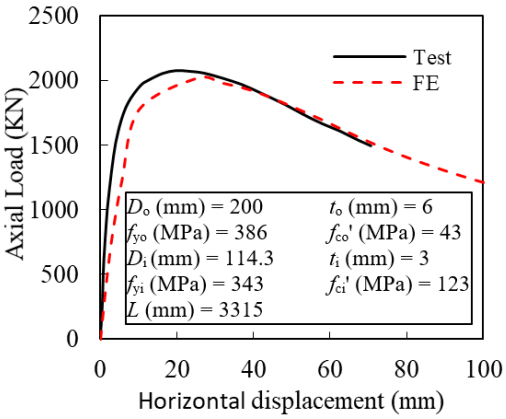

(e) C200-6-30-C114-3-150Romero et al. (2015)

Figure 2. FE model verification

3. PARAMETRIC STUDIES

This study investigated three stiffeners: T stiffeners, rectangular (R) plate stiffeners, and bar stiffeners, as shown in the next Figure 3. The comparison between different types is indicated in Figure 4. As can be seen that R and T stiffeners give the most improvement for the column's axial capacity. This improvement can reach up to 15 %. It is also observed that there is no significant difference between the behaviour of CFDT columns with no stiffener and when using bar stiffeners. This is due to the spacing (100 mm) between bars and the impeded length 15 mm was not adequate to form full bond between steel tube and concrete core.

Many parameters have been studied; however, due to the word limit, only conclusion will be presented for the most important parameters. The parameters included: concrete strength (fc') (30, 60 and 120 MPa), yield strength of steel tube (fy) (360, 500 and 800 MPa), outer steel tube type (carbon steel or stainless steel), column length (L/Do) (6, 16 and 26), inner tube size to thickness ratio (Di/ti) (14, 28 and 70), outer tube size to thickness ratio (Do/to) (31.25, 62.5 and 100), column size (Do) (250, 500 and 1000 mm) and outer to inner tube size ratio (Di/Do) (0.3, 0.56 and 0.7).

The axial strength of CFDT columns is directly proportional to the inner-to-outer tube diameter ratio and inversely proportional to the diameter-to-thickness ratio. Based on the parametric study, the maximum ratio between the inner and outer tube diameter is 0.7, and the minimum is 0.55 for the ratio of 11 % or higher between the stiffener area and tube area.

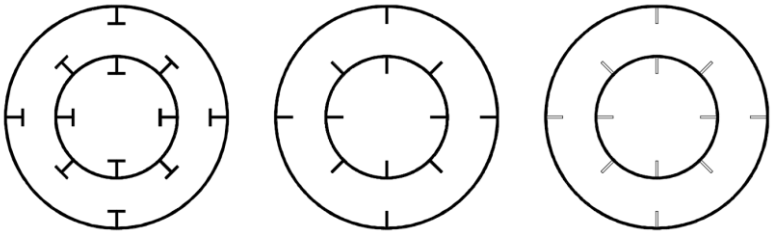

(a) T stiffeners (b) R stiffeners (c) Bar stiffener

Figure 3. Stiffeners used in this paper

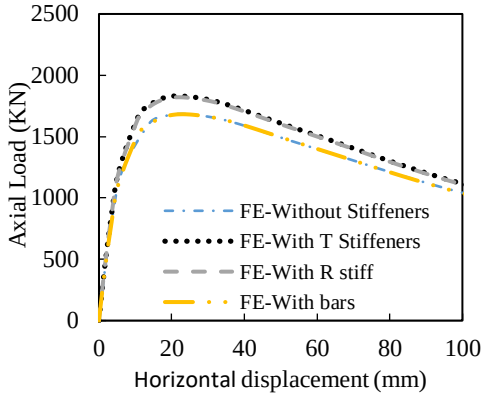

Figure 4. Different types of stiffeners comparison

4. PROPOSED MODEL

From the literature review done by the authors, it was found that no design model is available for predicting the axial strength of circular stiffened CFDT columns. A simplified design model based on Eurocode 4 is presented in this section. The Eurocode model was chosen due to its popularity among design engineers, and it is easy to be applied. Equations (1,2 and 3) present the model provided by Eurocode 4:

$$\boldsymbol{N_{pl,Rd} = A_s \times f_{s,y} + A_c \times f_c'} \quad (1)$$

where $N_{pl,Rd}$ is the load carrying capacity; A_c is the total cross-sectinal area of concrete; f_c' is the cylinder compressive strength of the concrete core and concrete ring; A_s is the outer and inner steel tube cross section area; and $f_{s,y}$ outer and inner steel tube cross yield strength.

$$N_{U,Euro} = \chi . N_{pl,Rd}, \quad (2)$$

Where $N_{U,Euro}$ is axial load capacity for long columns

$$\chi = \frac{1}{\phi + \sqrt{\phi^2 - \lambda^{\ 2}}} \quad (3)$$

$\phi = 0.5\,(1 + \alpha\,(\lambda - 0.2) + \lambda^{2.4})$, $\alpha = 0.21$ or 3% based on reinforcement <3% or >3% respectively. In this case, the inner tube is the replacement of reinforcement.

where

$$\lambda = \sqrt{N_{pl,Rd}\,/N_{cr}}$$

$N_{cr} = \pi^2 . (E I)_{eff} / l_T^2$ $E I_{eff} = E_s . I_s + 0.6 E_c . I_c$

E_s and E_c are the modulus of steel and concrete, respectively, and Ic and Is are the second moments of the concrete and steel area, respectively.

The verified FE model was used to assess the Eurocode model in predicting axial capacity for circular stiffened double tube columns. As shown in Table 1, Eurocode gives an unsafe prediction for the axial load capacity. This is compatible with the conclusion drawn by Romero et al. (2015), which shows the need to propose a new simplified model.

A new model was proposed in this study which is described in equation (4).

$$\boldsymbol{N_{pl,PM} = A_{so} \times f_{so,y} + A_{si} \times f_{si,y} + \mu_{stiff}(A_{cr} \times f'_{cr} + A_{cc} \times f'_{cc})} \quad (4)$$

where $N_{pl,PM}$ is axial load carrying capacity; A_{si} and A_{so} are the area for the inner and outer steel tube respectively; $f_{so,y}$ and $f_{si,y}$ are the steel yield strength for the outer and inner steel tube, respectively; A_{cc} and A_{cr} are the cross-sectional area of the concrete core and ring, respectively ; f'_{cc} and $f_{cr}{}'$ are the cylinder strength of the concrete core and ring, respectively; and μ_{stiff} is a factor that takes into account the increase in the confinement of concrete due to stiffener, which increases the interaction between steel tube and concrete.

$\mu_{stiff} = 1+A_{stiff} / A_{steel}$, where A_{stiff} / A_{steel} is the ratio between the area of stiffener and the cross-sectional area of steel tubes (inner and outer).

The load capacity for the long column can be calculated from equation (5).

$N_{U,PM} = \chi . N_{pl,PM}$, (5)

χ is as stated before. However, regression analysis was performed to obtain the value of α, which is taken as 0.5.

From the next Table 1, it can be concluded that the new proposed simplified model gives closer results to the FE model result compared to Eurocode 4 model.

Table 1. Compression between proposed model and Eurocode prediction.

	$N_{U, Euro} / N_{FE}$	$N_{U, PM} / N_{FE}$
Average	1.09	0.998
COV	0.064	0.04

5. CONCLUSIONS

The following conclusion can be drawn from this paper:

1. It is concluded that bar stiffeners have no significant effect on CFDT column performance. However, the axial capacity can be increased by 15% when using T or R stiffeners. It is recommended to use R-stiffener as it is easier to use in the practical instalment of columns.
2. Better and safer prediction for axial load capacity is obtained using the new simplified design model compared to the existing Eurocode 4 model.
3. More test experiments should be performed on these types of columns to better understand CFDT column behavior using different types of stiffeners.
4. The effect of stiffeners on Square columns should be investigated as it is predicted to have more positive impact on the column behavior compared to circular columns

REFERENCES

ABAQUS (2012). "ABAQUS standard user's manual, Version 6.12." Dassault Systèmes Corp., Providence, RI, USA.

Alatshan, F., Osman, S. A., Hamid, R., and Mashiri, F. (2020). "Stiffened concrete-filled steel tubes: A systematic review." *Thin-Walled Structures*, 148, 106590.

Benzaid, R., and Mesbah, H. A. (2013). "Circular and Square Concrete Columns Externally Confined by CFRP Composite: Experimental Investigation and Effective Strength Models." *Fiber Reinforced Polymers - The Technology Applied for Concrete Repair*, Intech, ed., INTECH, 167-201.

Cai, J., and He, Z.-Q. (2006). "Axial load behavior of square CFT stub column with binding bars." *Journal of Constructional Steel Research*, 62(5), 472-483.

Campione, G., Miraglia, N., and Papia, M. (2004). "Strength and strain enhancements of concrete columns confined with FRP sheets." *Structural Engineering and Mechanics*, 18.

Elchalakani, M., Hassanein, M. F., Karrech, A., and Yang, B. (2018). "Experimental investigation of rubberised concrete-filled double skin square tubular columns under axial compression." *Engineering Structures*, 171, 730-746.

Eurocode-4_1.1 (2004). "Design of composite steel and concrete structures, part 1.1 General rules and rules for buildings.", BS EN 1994-1-1:2004. British Standards Institution, London.

Ghannam, M., and Metwally, I. M. (2020). "Numerical investigation for the behaviour of stiffened circular concrete filled double tube columns." *Structures*, 25, 901-919.

Han, L.-H., Huang, H., Tao, Z., and Zhao, X.-L. (2006). "Concrete-filled double skin steel tubular (CFDST) beam–columns subjected to cyclic bending." *Engineering Structures*, 28(12), 1698-1714.

Hasan, H. G., and Ekmekyapar, T. (2019). "Mechanical Performance of Stiffened Concrete Filled Double Skin Steel Tubular Stub Columns under Axial Compression." *KSCE Journal of Civil Engineering*, 23(5), 2281-2292.

Hassanein, M. F., Elchalakani, M., Karrech, A., Patel, V. I., and Daher, E. (2018). "Finite element modelling of concrete-filled double-skin short compression members with CHS outer and SHS inner tubes." *Marine Structures*, 61, 85-99.

Huang, C. S., Yeh, Y.-K., Liu, G.-Y., Hu, H.-T., Tsai, K. C., Weng, Y. T., Wang, S. H., and Wu, M.-H. (2002). "Axial Load Behavior of Stiffened Concrete-Filled Steel Columns." *Journal of Structural Engineering*, 128(9), 1222-1230.

Huang, H., Han, L.-H., Tao, Z., and Zhao, X.-L. (2010). "Analytical behaviour of concrete-filled double skin steel tubular (CFDST) stub columns." *Journal of Constructional Steel Research*, 66(4), 542-555.

Lai, M. H., and Ho, J. C. M. (2013). "Uni-axial Compression Test of Concrete-filled-steel-tube Columns Confined by Tie Bars." *Procedia Engineering*, 57, 662-669.

Mohan, A. P., and S, A. (2016). "Non-Linear Analysis of Concrete Filled Double Skin Circular Steel Column." *International Journal of Engineering Research & Technology (IJERT)*, 5(7), 204-206.

Pagoulatou, M., Sheehan, T., Dai, X. H., and Lam, D. (2014). "Finite element analysis on the capacity of circular concrete-filled double-skin steel tubular (CFDST) stub columns." *Engineering Structures*, 72, 102-112.

Romero, M. L., Espinos, A., Portolés, J. M., Hospitaler, A., and Ibañez, C. (2015). "Slender double-tube ultra-high strength concrete-filled tubular columns under ambient temperature and fire." *Engineering Structures*, 99, 536-545.

Song, X., Gu, X., Li, Y., Chen, T., and Zhang, W. (2013). "Mechanical Behavior of FRP-Strengthened Concrete Columns Subjected to Concentric and Eccentric Compression Loading." *Journal of Composites for Construction*, 17(3), 336-346.

Tabsh, S. W. (2007). "Stress-Strain Model for High-Strength Concrete Confined by Welded Wire Fabric." *Journal of Materials in Civil Engineering*, 19(4), 286-294.

Tao, Z., and Han, L.-H. (2006). "Behaviour of concrete-filled double skin rectangular steel tubular beam–columns." *Journal of Constructional Steel Research*, 62(7), 631-646.

Tao, Z., Han, L.-H., and Wang, D.-Y. (2007). "Experimental behaviour of concrete-filled stiffened thin-walled steel tubular columns." *Thin-Walled Structures*, 45(5), 517-527.

Tao, Z., Han, L.-H., and Wang, D.-Y. (2008). "Strength and ductility of stiffened thin-walled hollow steel structural stub columns filled with concrete." *Thin-Walled Structures*, 46(10), 1113-1128.

Tao, Z., Han, L.-H., and Wang, Z.-B. (2005). "Experimental behaviour of stiffened concrete-filled thin-walled hollow steel structural (HSS) stub columns." *Journal of Constructional Steel Research*, 61(7), 962-983.

Tao, Z., Han, L.-H., and Zhao, X.-L. (2004). "Behaviour of concrete-filled double skin (CHS inner and CHS outer) steel tubular stub columns and beam-columns." *Journal of Constructional Steel Research*, 60(8), 1129-1158.

Tao, Z., Wang, Z.-B., and Yu, Q. (2013). "Finite element modelling of concrete-filled steel stub columns under axial compression." *Journal of Constructional Steel Research*, 89, 121-131.

Wang, Z.-B., Tao, Z., and Yu, Q. (2017). "Axial compressive behaviour of concrete-filled double-tube stub columns with stiffeners." *Thin-Walled Structures*, 120, 91-104.

Younes, S. M., Ramadan, H. M., and Mourad, S. A. (2016). "Stiffening of short small-size circular composite steel–concrete columns with shear connectors." *Journal of Advanced Research*, 7(3), 525-538.

Zakir, M., Sofi, F. A., and Naqash, J. A. (2021). "Experimentally verified behavior and confinement model for concrete in circular stiffened FRP-concrete-steel double-skin tubular columns." *Structures*, 33, 1144-1157.

Zhao, X.-L., and Han, L.-H. (2006). "Double skin composite construction." *Progress in Structural Engineering and Materials*, 8(3), 93-102.

Proc. 3rd International Conference on Structural Engineering Research (iCSER 2022)
27-30 Nov 2022, Sydney, Australia
ISBN: 978-0-6456692-1-3

Experimental Investigation on The Flexural Stiffness of A Composite Steel Decking With Web Voids

K. Duot[1], D. Kahagala Hewage[1], O. Mirza[1], Andrew[2], D. Allen[3]

[1]Western Sydney University, Locked Bag 1797, Penrith, New South Wales, Australia
[2]ABES Australia, PO Box 467 Emu Plains NSW 2750, Australia
[3]Premier Steel Technologies, 229 Newton Road, Wetherill Park, NSW, 2164, Australia, Australia

Corresponding author's E-mail: d.kahagalahewage@westernsydney.edu.au

Abstract

In Australia, steel-concrete composite (SCC) construction is favoured due to its enhanced concrete strength and reduced construction time. In addition, the recyclability of the steel without losing its original material characteristics makes the SCC a sustainable alternative. According to literature study, the majority of steel decks are lacking the necessary qualities to be utilised in their cold-formed state. Unlike the other steel decking, the TrueDek (TD) deck system has top and bottom plates connected with webs. The truss shape profile has resulted in higher stiffness compared to contemporary steel decking systems. But the presence of the web prevents efficient utility layering. Therefore, the web holes have been introduced to allow utility lines to pass through the slab making it convenient for construction. These voids, however, have an impact on the deck's capacity and influence its failure mechanism. Thus, this experimental study aims to investigate the influence of web voids on the flexural stiffness and failure mechanisms of the deck. TD profiles of different depths and spans were tested under a uniformly distributed load in a simply supported beam configuration. The structural behaviour of the deck was assessed in terms of displacement, ultimate capacity, strain behaviour and failure modes. The experimental results concluded that buckling failure near the web voids reduces the deck's capacity while affecting flexural stiffness. In addition, it was observed that the effect of the voids further depends on the deck span and depth.

Keywords: Composite construction, Cold-formed steel deck, Web voids, Web buckling

1. INTRODUCTION

Steel-concrete composite construction refers to the encasement of steel sections in concrete for columns and slabs or using shear connectors to link profiled deck slabs to steel beams (Tedia & Maru 2014). This composite construction aims to maximise both steel and concrete benefits while minimising their drawbacks. Uy (2002) indicated that steel-concrete composite construction is widely used in the construction of both buildings and bridges. Steel is also utilised in steel-concrete composite construction in the form of profiled steel sheeting. According to Wright et al. (1987) the advantages of the profiled steel sheet are: the steel deck serves as a permanent formwork during concrete slab casting stopping the need for false formwork, the steel deck serves as an immediate basis for supporting construction loads, and the steel deck eliminates the need for reinforcement bars for the slab as it acts as a tensile reinforcement.

Lim et al. (2021) tested the flexural strength of two profiled composite slabs of different thicknesses. In comparison to a conventional slab, the authors found that adding a steel sheet profile increased the ultimate load capacity and ductility by 537.4% and 100.9%, respectively, while decreasing deflection. This indicates that composite structures can also be used to reduce the use of concrete and steel reinforcement. Arrayago et al. (2019) and John et al. (2020) identified the failures of the steel deck as web buckling, web crippling, crushing and shear deformation. These failures are influenced by the type of deck profile, varied span configurations, loading, and web thicknesses.

In Australian construction, the use of structural steel decking as a dual formwork/reinforcement system has significantly increased recently due to the advantages and availability of various profile types (Tse & Chung 2008). Out of the available steel decking, TrueDek (TD) system shown in Figure 1 may offer higher structural performance due to its deeper cross section. TD was designed to span more than 8m without propping and to prevent vertical deflections in the formwork stage, which are caused mostly by the weight of wet concrete. There are two distinct variations of TD: voided, in which case the web has holes, and solid, in which case the web is solid. The web holes are provided to ease the service lines distributions.

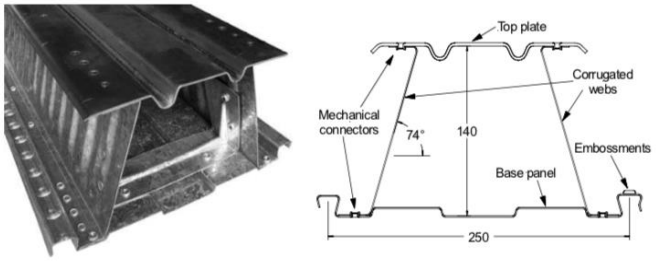

Figure 1: TD panel of 140mm height

Gibson (2020) and Birkandan (2021) performed four-point loading tests of various TD profiles under composite conditions subjected to static stress to evaluate the structural behaviour of both solid and voided decking systems. Both authors identified similar failure modes, such as flexural cracking, end slippage, deflection, and tearing beneath the TD profile. The authors identified parameters such as slab types, TD steel arrangement in slabs, profile types, and types of reinforcements that influenced the failures. Singh (2019) conducted an experimental study to investigate the vertical shear capacity of the voided TD at the formwork stage. The experiment was carried out on 2m spans under monotonic and cyclic load. The failures observed were web buckling and bending failure, which were influenced by shear stress and the profile depths. Yet, the effect of web holes on the flexural behaviour of TD systems has not been studied under uniformly distributed loading, which is the loading type that the steel deck is subjected to in practise. Therefore, this study aims to investigate the structural behaviour of a voided TD under uniformly distributed load at the formwork stage.

2. EXPERIMENTAL STUDY

The experiment focused on the structural behaviour of a TD with web openings. Twelve specimens with differing depths and spans were tested under uniformly distributed loading conditions.

2.1. Experimental specimen

The specimens were made of cold-formed steel and consisted of different depths, top and bottom plate widths and spans, as shown in Table 1. The web (t_w), top pate (t_t)and base plate (t_b) thicknesses were 0.7, 1.9 and 0.75 mm, respectively, as shown in Figure 2. The voids in the web are 50 × 90 mm, placed 200 mm apart at the mid-height of the web. The specimen designation is given in Table 1. A separate concurrent study was conducted to investigate the structural behaviour of respective solid sections, the results of which were used as a comparison.

2.2. Experimental setup

A loading frame was configured to test the specimens as single spans under uniformly distributed loading conditions. Figure 3 illustrates the simply supported setup condition of the specimens. The east end indicated by A allowed horizontal movement, while the west end indicated by B was pinned. LVDTs were placed in the midspan and at quarter spans to measure displacement. The strain was measured by gauges between the web voids (340mm from the East end) and the midspan.

Table 2: Experimental specimens

Profile	Height,h (mm)	Top plate width, w_t (mm)	Bottom plate width, w_b (mm)	Span(m)	Specimen Name
TD90	90	200	250	*3*	3TD90V
				4.4	4TD90V
				6	6TD90V
TD110	110	200	250	*3*	3TD110V
				4.4	4TD110V
				6	6TD110V
TD140	140	180	250	*3*	3TD140V
				4.4	4TD140V
				6	6TD140V
TD160	160	180	250	*3*	3TD160V
				4.4	4TD160V
				6	6TD160V

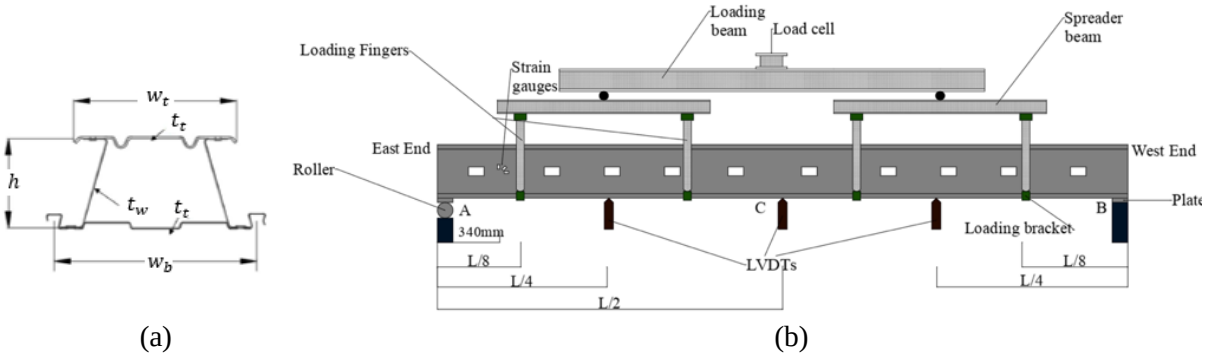

(a) (b)

Figure 2: Experimental information; (a) Profile cross section, (b) Setup

3. RESULTS AND DISCUSSION

Since the specimens were simply supported, the midpoint was deemed the critical region. The load versus midspan displacement relationship was used to analyse the effect of span and truss height on the specimens' stiffness, maximum capacity load and ductility. The results obtained for the voided TD specimens are discussed and compared with those obtained for solid TD specimens under the same test setup.

3.1. Effect of span and depth on structural behaviour

Figure 3(a) shows the load versus mid-span displacement for all profiles for 3 m span. Points B-E represent the failure loads identified as the capacity of each specimen. In comparison to other specimens, 3TD90V demonstrated ductile behaviour with significant plastic deformation. The ductility of the specimen decreases as the depth increases. According to the findings, the capacity of the TD profile increased by 54% as the height increased. Regardless of the higher depth, the capacity of TD160 was reduced when compared to TD140 due to the influence of web buckling.

Figures 4(a) and 5(b) show load versus midspan deflection for spans of 4.1 and 6 m, respectively. As with the 3m span results, the most ductile specimen was TD90, and ductility decreased with depth. Under all spans, the capacity increases with web height. Compared to the TD90, the TD160 capacity increased by 77.7% and 125% for 4.1 and 6 m spans, respectively. Therefore it can be concluded that,

as the span increases, so does the effect of depth on capacity. As a result, deeper profiles in longer spans are more effective than that in short spans.

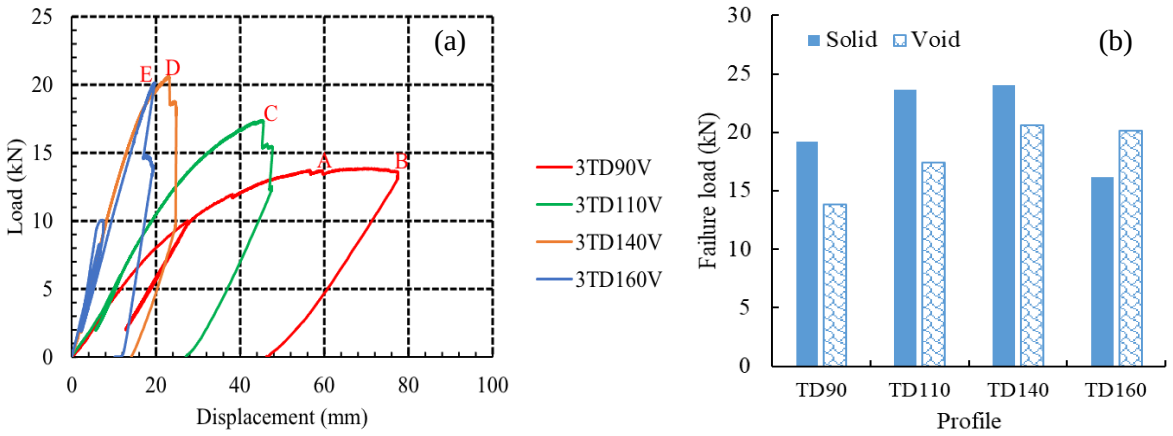

Figure 3: Experimental results for 3m span; (a) Load-displacement behaviour, (b) Failure load

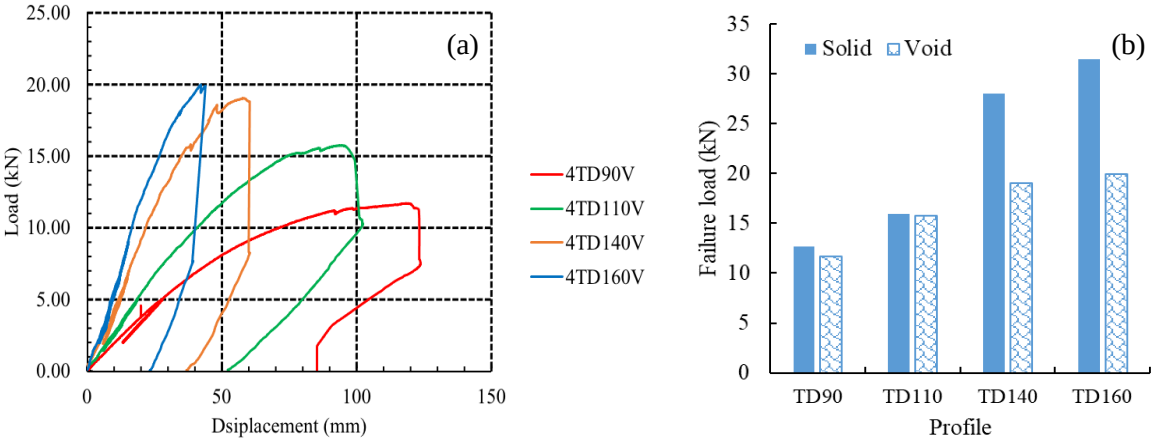

Figure 4: Experimental results for 4.1m span; (a) Load-displacement behaviour, (b) Failure load

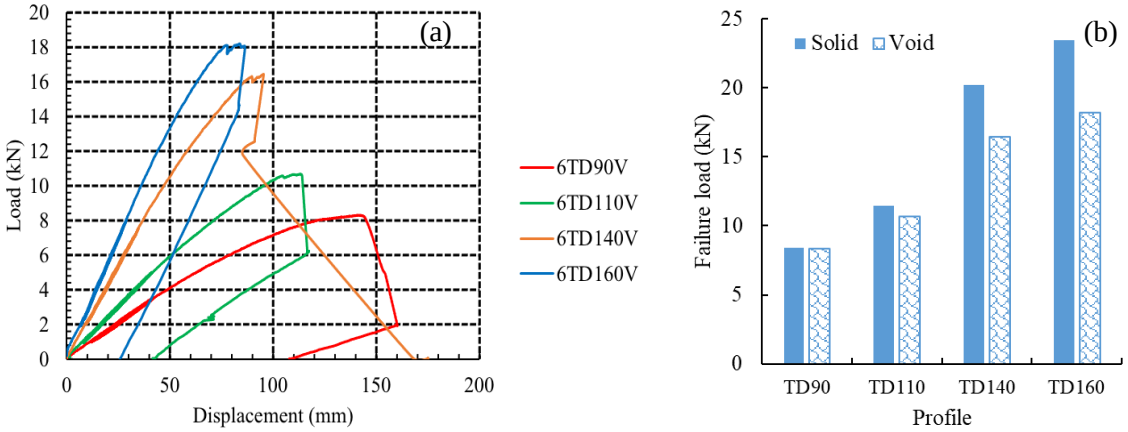

Figure 5: Experimental results for 6m span; (a) Load-displacement behaviour, (b) Failure load

3.2. Effect of span and depth on the failure mode

All 3 m specimens failed due to either end bracket distortion at the support or web buckling. The specimens originally displayed buckling near the corner void of the web. Later, 3TD90V and 3TD110V experienced a gradual web failure (Figure 6(a)), whereas other samples experienced a sudden end bracket failure (Figure (b)). Therefore, it can be concluded that shorter-span failures are governed by shear action.

As the span increases, the smaller depths (TD90 and TD110) exhibited a midspan top plate buckling, highlighting the flexural action as shown in Figure 6(c). However, as the depths increased, the web buckled and deformed, causing the end brackets to buckle similar to 3 m span. Accordingly, for larger spans, the flexural action governs the TD behaviour for lower profile depth, whereas shear-induced failure occurs in deeper profiles.

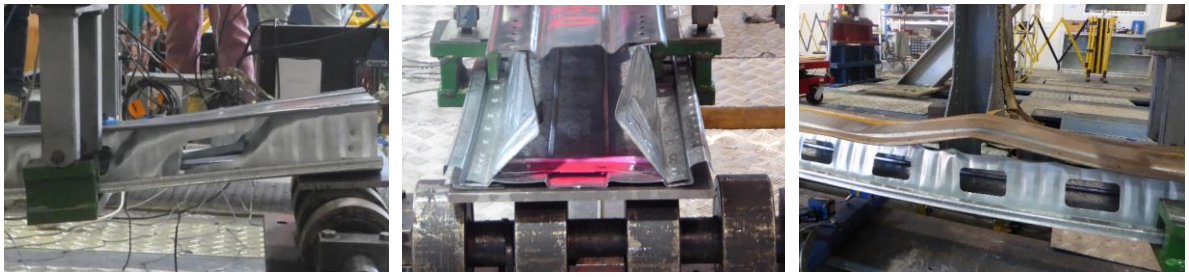

(a) (b) (c)

Figure 6: Failure modes; (a) Web buckling, (b) End bracket distortion, (c) Top late buckling

3.3. Effect of web voids on structural behavior

The failure load of all the voided specimens under each span was compared with that of solid specimens in Figures 4(b), 5(b) and 6(b). It indicated that the presence of web voids had reduced the capacity of the voided sample. Except for 3m span, the capacity reduction of voided samples compared to solid samples increased as the profile depth increased. For 3m span, the capacity of the solid samples with deeper profiles was reduced due to web buckling. The presence of the voids has aggravated the buckling, thus reducing the capacity further. As the web height increases, the void ratio in deeper profiles reduces because the voids are of constant dimensions. Therefore the effect of voids on web buckling has reduced, resulting a lower capacity difference.

In larger spans (4 and 6 m), flexural action governs the failure of profiles with lower web depths, so the presence of web voids has little or no influence. However, as the depth increases, the buckling resistance of the web influences the capacity, which is reduced when web voids are present. As a result, the presence of voids has the greatest impact on long span TD members with deeper profiles.

4. CONCLUSION

This research investigated the structural behaviour of TD steel decking under a uniformly distributed load. The effect of span and truss height on the stiffness, capacity and ductility were evaluated. From the experimental investigation, it can be concluded in key points that;

- The specimens' capacity increased with depth. However, due to web buckling, the capacity increase is ineffective for shorter spans. Deeper cross sections become more effective as the span increases.
- Regardless of span, ductility decreases as depth increases, with the TD90 being the most ductile profile.
- Shear action reduces the short span member capacity, resulting in web buckling at the end, and the presence of web voids reduces the buckling resistance of lower depth profiles even

further. However, as the void ratio decreases, the effect of voids decreases as the profile depth increases in short span members.

- Because flexural action governs the failure of long span TD members with shallower profiles, the presence of voids had little or no effect on capacity. On the other hand, web buckling influences the failure of long span members with deeper cross sections, resulting in a significant capacity reduction due to voids.

5. REFERENCES

Arrayago, I., Real, E., Mirambell, E., Marimon, F., & Ferrer, M. (2019). Experimental study on ferritic stainless steel trapezoidal decks for composite slabs in construction stage. *Thin-Walled Structures*, *134*(2019), 255–267.

Birkandan, MS. (2021). Behaviour of Truedek Decking System Under Composite Conditions Subjected to Static Loading. Penrith NSW, Western Sydney University.

Gibson, S. (2020). Behaviour of The Innovative Composite Slab Decking Design Truedek Decking Systems. Penrith NSW, Western Sydney University.

John, K., Ashraf, M., Weiss, M., & Al-Ameri, R. (2020). Experimental Investigation of Novel Corrugated Steel Deck under Construction Load for Composite Slim-Flooring. *Buildings*, *10*(11), 208. https://doi.org/10.3390/buildings10110208

Lim, S.-S., Wong, J.-Y., Yip, C.-C., & Pang, J.-W. (2021). Flexural strength test on new profiled composite slab system. *Case Studies in Construction Materials*, *15*(2021), e00638.

Singh, N. (2019). Vertical Shear Capacity of the Truedek Steel Decking System in the Formwork Stage. Penrith NSW, Western Sydney University.

Tedia, A., & Maru, S. (2014). "Cost, Analysis and Design of Steel-Concrete Composite Structure Rcc Structure." *IOSR Journal of Mechanical and Civil Engineering*, *11*(1), 54–59.

Tse, W. T., & Chung, K. F. (2008). Web crippling behaviour of laterally restrained cold-formed steel re-entrant profiled deckings. *Journal of Constructional Steel Research*, *64*(7-8), 785–801.

Uy, B.(2002). "Composite Steel-Concrete Structures" in WF Chen WF Chen & JYR Liew (eds), *The Civil Engineering Handbook*, CRC Press, Routledge, Research Direct library, Western Sydney University. http://handle.uws.edu.au:8081/1959.7/10966

Wright, H. D., Evans, H. R., & Harding, P. W. (1987). The use of profiled steel sheeting in floor construction. *Journal of Constructional Steel Research*, *7*(4), 279–295.

Proc. 3rd International Conference on Structural Engineering Research (iCSER 2022)
27-30 Nov 2022, Sydney, Australia
ISBN: 978-0-6456692-1-3

Effects of Elastically Restrained Edge on The Natural Frequencies of Functionally Graded Beam

Saman Karimi[1], Mohammad Molla-Alipour[2], Olivia Mirza[1]

[1]Western Sydney University, Locked Bag 1797, Penrith NSW, 2751 Australia

[2] University of Mazandaran, Babolsar, Iran

Corresponding author's E-mail: S.karimi@westernsydney.edu.au

Abstract

In recent years, the use of functionally graded beams has increased due to its smooth variety of material properties along a certain direction. Functionally graded (FG) beams are used in various industries and machine elements such as aerospace, mechanical, and civil engineering, so it is necessary to understand their dynamic behaviour. In this paper, free vibration analysis of a functionally graded beam with elastically restrained edge is carried out. Governing equations are obtained based on the first-order shear deformation theory (FSDT). The extracted governing differential equations are analytically solved for free vibration analysis of the beam. This analytical method can be used for various non-classical boundary conditions. In this paper, the elastically restrained edge is modelled with a horizontal linear spring, rotational spring, and transverse linear spring. Different stiffnesses have been given to these springs, and the natural frequencies of the beam have been investigated and compared with the natural frequencies of clamped-clamped and clamped-free, and clamped-simply beams, and also the natural frequencies of the beam when one of the springs was constant *been measured. Accuracy and efficiency of the proposed method are demonstrated by comparing the obtained results of the FG beam with the classical edge conditions with the results of TBT and CBT methods.*

Keywords: Beam; Functionally graded materials, Free vibration, First-order shear deformation theory, Elastically restrained edge

1. INTRODUCTION

Beam is one of the main parts of the structure which is capable of bearing loads, especially by resisting bending. Functionally graded materials (FGM) are two-component composites and have a material composition that changes gradually with volume. One of the most common methods in analysing the beam is the use of modal data and free vibration analysis, which have been studied in recent years. Simsek (2010) investigated FG simply-supported beam based on Euler–Bernoulli, Timoshenko and the third-order shear deformation beam theories. Manoach et al. (2012) investigated the free vibration of composite beams. The damaged beams were under dynamic loads and temperature variations. Filippi et al. (2015) investigated static analysis of FG beams based on FEM and 1D Carrera unified formulation (CUF). Thom and Kien (2018) investigated the free vibration of two-directional FG beams based on higher-order Timoshenko beam element and finite element method. Uzun et al. (2020) developed a finite element formulation for analysing the free vibration of FG nanobeams. Azandariani et al. (2022) investigated the free vibration of axially-loaded FG beams based on FSDT. As can be seen, few works have been carried out on free vibration analysis of FG beams with an elastically restrained edge. Therefore, this paper provides an analytical method to investigate the effect of elastically restrained edges on the natural frequencies of the FG beam.

2. GOVERNING EQUATIONS

This section presents the governing equations of the beam based on FSDT. For this purpose, the following displacement function is used as suggested by Mindlin (1951).

$$u = u_0 + z\psi_x \qquad -\frac{h}{2} \le z \le \frac{h}{2} \tag{1}$$

Where u_0 is the in-plane displacement of the middle layer of the beam, u is the in-plane displacement, and ψ_x is the rotation of the transverse surface. For extracting the governing equations of the beam, the following equation is used:

$$\delta(W + K) = 0 \tag{2}$$

Where W and K are the internal and kinetic energy, respectively. These components are defined as follows:

$$\delta W = \int_{-\frac{h}{2}}^{\frac{h}{2}} (\sigma_x \delta\varepsilon_x + \tau_{xz}\delta\gamma_{xz}) dA \ , \ \delta K = -\int_{-\frac{h}{2}}^{\frac{h}{2}} (\rho\ddot{u}\delta u + \rho\ddot{y}\delta y) dz dx \tag{3}$$

In the above equation, $\ddot{P}$ is the second derivative of time of the function P, ρ mass density, τ shear stress, γ shear modulus, ε strain component, y displacement of the beam, k_φ and k_s are rotational and longitudinal stiffness, respectively. Now we introduce the following equations:

$$\begin{aligned} &A = \int_{-\frac{h}{2}}^{\frac{h}{2}} \frac{E}{1-\nu^2} dz \ , \ B = \int_{-\frac{h}{2}}^{\frac{h}{2}} \frac{E}{1-\nu^2} z dz \ , \ C = \int_{-\frac{h}{2}}^{\frac{h}{2}} \frac{E}{1-\nu^2} z^2 dz \\ &\bar{A} = \int_{-\frac{h}{2}}^{\frac{h}{2}} \frac{E^{(s)}}{2(1+\nu^{(s)})} dz \ , \ I_0 = \int_{-\frac{h}{2}}^{\frac{h}{2}} \rho dz \ , \ I_1 = \int_{-\frac{h}{2}}^{\frac{h}{2}} \rho z dz \ , \ I_2 = \int_{-\frac{h}{2}}^{\frac{h}{2}} \rho z^2 dz \end{aligned} \tag{4}$$

By substituting Equation 1 into Equation 3 and using Equation 4, the governing equations of the beam are extracted as follows:

$$\begin{aligned} &Equation\ 1: \ Au_{0,xx} + B\psi_{x,xx} = I_0\ddot{u}_0 + I_1\ddot{\psi}_x \\ &Equation\ 2: \ Bu_{0,xx} + D\psi_{x,xx} - \bar{A}(\psi_x + y_{,x}) = I_1\ddot{u}_0 + I_2\ddot{\psi}_x \\ &Equation\ 3: \ \bar{A}(\psi_{x,x} + y_{,xx}) = I_0\ddot{y} \end{aligned} \tag{5}$$

3. SOLUTION OF THE GOVERNING EQUATIONS

The governing equations of the beam should be solved for extracting the displacement components. For this purpose, power series are used as follows:

$$u_0 = \sum_{j=0}^{R} U_j (x-n)^j \ , \ \psi_x = \sum_{j=0}^{R} \varphi_j (x-n)^j \ , \ y = \sum_{j=0}^{R} Y_j (x-n)^j \tag{6}$$

To solve the governing equations of the beam, the power series of Equation 6 should be substituted into Equation 5. For this purpose, the power series expands around $n = 0$. After this step, the following three equations of the beam are resulted:

$$\begin{aligned} &Equation\ 1: \ \sum_{j=0}^{R} [A(j+2)(j+1)U_{j+2} + B(j+2)(j+1)\varphi_{j+2} + I_0\omega^2 U_j + I_1\omega^2\varphi_j] x^j = 0 \\ &Equation\ 2: \ \sum_{j=0}^{R} [B(j+2)(j+1)U_{j+2} + D(j+2)(j+1)\varphi_{j+2} - \bar{A}(\varphi_j + (j+1)Y_{j+1}) + I_1\omega^2 U_j + I_2\omega^2\varphi_j] x^j = 0 \\ &Equation\ 3: \ \sum_{j=0}^{R} [\bar{A}(j+1)\varphi_{j+1} + \bar{A}(j+2)(j+1)Y_{j+2} + I_0\omega^2 Y_j] x^j = 0 \end{aligned} \tag{7}$$

4. BOUNDARY CONDITIONS

4.1 Boundary conditions of the beam

The following boundary conditions are expressed in terms of various support conditions:

Free edge:

$$Free\ edge: \begin{cases} M_x = 0 \\ N_x = 0 \\ Q_x = 0 \end{cases}, \ Simply-supported\ edge: \begin{cases} u_0 = 0 \\ M_x = 0 \\ y = 0 \end{cases}, \ Clamped\ edge: \begin{cases} u_0 = 0 \\ \psi_x = 0 \\ y = 0 \end{cases} \tag{8}$$

Where M_x, N_x and Q_x are bending torque, in-plane force, and transverse shear force per unit length, which are defined as follows:

$$N_x = Au_{0,x} + B\psi_{x,x} \ , \ M_x = Bu_{0,x} + D\psi_{x,x} \ , \ Q_x = \overline{A}(\psi_x + y_{,x}) \tag{9}$$

4.2 Substitution of power series into the boundary conditions

In this section, the power series are substituted into the boundary conditions of the beam as follows:

$$Free\ edge: \begin{cases} BU_1 + D\varphi_1 = 0 \\ AU_1 + B\varphi_1 = 0 \\ \overline{A}(\varphi_0 + Y_1) = 0 \end{cases}, \ Simply-supported\ edge: \begin{cases} U_0 = 0 \\ BU_1 + D\varphi_1 = 0 \\ Y_0 = 0 \end{cases}, \ Clamped\ edge: \begin{cases} U_0 = 0 \\ \varphi_0 = 0 \\ Y_0 = 0 \end{cases} \tag{10}$$

After solving the governing using the power series and also substituting the power series into the boundary conditions of the beam, Equation 11 is formed as follows:

$$\begin{bmatrix} X_{11}(\omega) & X_{12}(\omega) & X_{13}(\omega) \\ X_{21}(\omega) & X_{22}(\omega) & X_{23}(\omega) \\ X_{31}(\omega) & X_{32}(\omega) & X_{33}(\omega) \end{bmatrix} \times \begin{Bmatrix} U \\ \varphi \\ Y \end{Bmatrix} = \begin{Bmatrix} 0 \\ 0 \\ 0 \end{Bmatrix} \tag{11}$$

After this step, the determinant of the above matrix is calculated and then, based on the Newton-Raphson method, the natural frequencies of the beam are extracted.

5. VALIDATION OF THE PROPOSED METHOD

In this section, validation of the proposed method is presented. The proposed method is compared with Pradhan and Chakraverty (2013). In Table 1, the results of the natural frequencies of the beam are presented. The functionally graded materials in this section are mixtures of Alumina and Aluminium; therefore, it is necessary to mention their properties. Also, the non-dimensional frequency parameter and the power-law variation are expressed as follows:

$$Alumina: E = 380\,Gpa,\ \nu = 0.3,\ \rho = 3800\frac{kg}{m^3}\ ,\ Aluminium: E = 70\,Gpa,\ \nu = 0.3,\ \rho = 2700\frac{kg}{m^3}$$
$$\omega = \frac{\lambda L^2}{h}\sqrt{\frac{\rho_m}{E_m}}\ ,\ F(z) = (F_c - F_m)\left(\frac{z}{h} + \frac{1}{2}\right)^k + F_m \tag{12}$$

Where λ is the extracted frequency from Maple, L length of the beam, h thickness of the beam, ρ_m and E_m are mass density and Young's modulus of Aluminium respectively, c and m denote to the properties of the Alumina and Aluminium, respectively. As can be seen, the results of the proposed method are close to the results of the TBT method, which indicates the accuracy of the proposed method.

Table 1. Natural frequencies of FG beam with L/h = 5

Natural frequency	K=0.5			K=5			K=10		
	CBT	TBT	This Study	CBT	TBT	This Study	CBT	TBT	This Study
ω_1	12.4508	10.4432	9.3470	8.8444	7.2733	7.0954	8.4517	6.7977	6.7405
ω_2	32.0690	22.5745	21.7403	21.4108	15.4037	16.2161	19.5030	14.2226	15.2798
ω_3	33.4736	32.9460	29.0048	23.3156	21.6583	20.9120	22.1017	19.5473	19.1003

6. ELASTICALLY RESTRAINED EDGE

In this section, the elastically restrained support is introduced (Figure 1). An elastically restrained edge is modelled with three springs which are called horizontal linear spring, rotational spring, and transverse linear spring with stiffnesses k_u, k_φ, and k_w respectively.

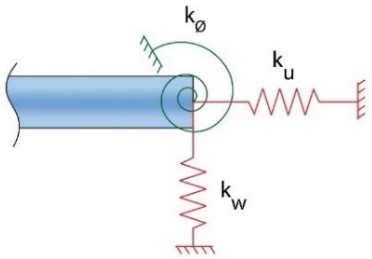

Figure 1. Beam with an elastic support

The stiffness of the springs introduced in this section should be added to the boundary conditions which for free condition is as follows:

$$\begin{cases} M_x + k_\varphi \psi_x = 0 \\ N_x + k_u u_0 = 0 \\ Q_x + k_w y = 0 \end{cases} \tag{15}$$

7. RESULTS AND DISCUSSION

In this section, by inserting different values to the stiffnesses of the horizontal linear spring, rotational spring, and transverse linear spring, the effect of the support's rigidity on the natural frequencies of the beam has been investigated. The properties of the beam in this section are as follows:

$$\rho = (\rho_m - \rho_n)(\frac{z}{h} + \frac{1}{2})^P + \rho_n \ , \ E = (E_m - E_n)(\frac{z}{h} + \frac{1}{2})^P + E_n \ , \ E_m = 380Gpa \ , \ E_n = 70Gpa$$
$$\rho_m = 3800 \, {kg}/{m^3} \ , \ \rho_n = 2700 \, {kg}/{m^3} \ , \ \nu = 0.3 \ , L = 1 \ , \ h = 0.2 \tag{16}$$

Where P is the power-law indices. The proposed method is compared with previous studies, and the obtained natural frequencies are close to the TBT method which indicates the superiority and precision of the proposed method. In Table 2 and Table 3, the natural frequencies of the beam with different boundary conditions are presented. By inserting different values for the stiffnesses of the horizontal linear spring, rotational spring, and transverse linear spring, the effect of support's rigidity on the natural frequencies of the beam is investigated. In this section, the stiffnesses of the horizontal linear spring, rotational spring, and transverse linear spring is generally represented by K. As can be seen, by increasing the value of K which in fact increases the rigidity of the support, the natural frequencies of the beam are increased, which causes the beam to be changed from clamped-free condition or clamped-simply condition to clamped-clamped condition. In table 4, a large value for k_w is assumed, and the effect of the two other stiffnesses are measured; In fact, the effect of K which here referred to

the values of k_u and k_φ on the natural frequencies of the beam is investigated. As can be seen, by increasing the value of K, the natural frequencies of the beam have increased, but since k_w is assumed to be constant, the beam has not reached the clamped-clamped condition. In conclusion, support's rigidity has little effect on natural frequencies of the beam for K less than 1E8 and more than 1E11.

Table 2. Effect of support's rigidity on the natural frequencies of the beam

p	Natural frequency	C-F	K=1E8	K=1E9	K=5E9	K=1E10	K=5E10	K=1E11	K=1E12	C-C
2	ω_1	1.412	1.8232	2.8785	4.5311	5.5223	7.1548	7.4237	7.6672	7.6940
	ω_2	7.7049	8.2731	9.7858	10.871	11.6623	15.1307	16.4369	17.7389	17.8762
	ω_3	12.2074	12.2217	12.3433	12.8432	13.4155	16.5529	18.6104	23.3326	24.2027
5	ω_1	1.3334	1.7681	2.8278	4.4758	5.3823	6.6945	6.8948	7.0754	7.0954
	ω_2	7.148	7.7441	9.1389	10.1755	10.9964	14.1628	15.1790	16.1172	16.2161
	ω_3	10.5644	10.5843	10.7448	11.3637	12.049	15.279	17.0494	20.3807	20.9120
10	ω_1	1.2889	1.7338	2.7928	4.4216	5.2661	6.4047	6.5725	6.7238	6.7405
	ω_2	6.8490	7.4573	8.7763	9.7942	10.6238	13.6008	14.4451	15.1995	15.2798
	ω_3	9.6166	9.6392	9.8237	10.5197	11.2733	14.4475	16.0366	18.7043	19.1003

Table 3. Effect of support's rigidity on the natural frequencies of the beam

P	Natural frequency	C-S (K=0)	K=1E8	K=5E8	K=1E9	K=5E9	K=1E10	K=1E11	K=1E12	C-C
2	ω_1	5.6633	5.9509	6.5833	6.9312	7.4769	7.5793	7.6819	7.6928	7.6940
	ω_2	12.136	12.1488	12.1998	12.2629	12.7445	13.295	17.72	17.8708	17.8762
	ω_3	15.8009	16.0058	16.5477	16.9110	17.6003	17.7506	18.6892	23.3328	24.2027
5	ω_1	5.2744	5.5783	6.1875	6.4918	6.9316	7.0095	7.08637	7.0945	7.0954
	ω_2	10.4838	10.4995	10.5620	10.6391	11.2165	11.8539	16.0712	16.2106	16.2161
	ω_3	14.4912	14.6996	15.2081	15.5177	16.0486	16.1576	17.1186	20.3812	20.9120
10	ω_1	5.0477	5.3576	5.9439	6.2207	6.6031	6.6689	6.7331	6.7398	6.7405
	ω_2	9.5634	9.5812	9.6519	9.7388	10.3807	11.0715	15.1777	15.2758	15.2798
	ω_3	13.7454	13.9513	14.4275	14.7006	15.1425	15.2294	16.0866	18.7048	19.1003

Table 4. Effect of support's rigidity on the natural frequencies of the beam with h=0.2 and $k_w = 1E10$

P	Natural frequency	K=1E6	K=1E7	K=1E8	K=1E9	K=1E10	K=1E11	K=1E12
2	ω_1	4.999	5.0105	5.1041	5.3848	5.5223	5.5417	5.5437
	ω_2	11.0048	11.0158	11.1070	11.4108	11.6623	11.7464	11.7572
	ω_3	12.3419	12.3434	12.3580	12.4713	13.4155	18.5608	22.4265
5	ω_1	4.7681	4.7834	4.9038	5.2347	5.3823	5.4024	5.4045
	ω_2	10.202	10.2067	10.2463	10.4309	10.9964	11.138	11.1483
	ω_3	11.1508	11.1547	11.1877	11.3126	12.049	16.9837	20.2698
10	ω_1	4.6155	4.6328	4.7672	5.1178	5.2661	5.2859	5.2879
	ω_2	9.4779	9.4805	9.5036	9.6733	10.6238	10.7908	10.7973
	ω_3	10.7064	10.7105	10.7426	10.8382	11.2733	15.9867	18.662

8. CONCLUSION

This paper has developed an analytical method for obtaining the natural frequencies of the beam with different boundary conditions and the effect of the support's rigidity on the natural frequencies of the beam. The proposed method is based on the first-order shear deformation theory (FSDT) and can be used to find the natural frequencies of the beam with a low computational cost. The results have

shown that the proposed method is in good agreement with previous studies and can accurately analyse the beam with elastically restrained edge.

REFERENCES

Azandariani, M. G., Gholami, M., & Zare, E. (2022). Development of spectral element method for free vibration of axially-loaded functionally-graded beams using the first-order shear deformation theory. *European Journal of Mechanics-A/Solids*, 104759.

Filippi, M., Carrera, E., & Zenkour, A. M. (2015). Static analyses of FGM beams by various theories and finite elements. *Composites Part B: Engineering*, *72*, 1-9.

Manoach, E., Samborski, S., Mitura, A., & Warminski, J. (2012). Vibration based damage detection in composite beams under temperature variations using Poincaré maps. *International Journal of Mechanical Sciences*, *62*(1), 120-132.

Mindlin, R. (1951). Influence of rotatory inertia and shear on flexural motions of isotropic, elastic plates.

Pradhan, K. K., & Chakraverty, S. (2013). Free vibration of Euler and Timoshenko functionally graded beams by Rayleigh–Ritz method. *Composites Part B: Engineering*, *51*, 175-184.

Şimşek, M. (2010). Vibration analysis of a functionally graded beam under a moving mass by using different beam theories. *Composite structures*, *92*(4), 904-917.

Thom, T. T., & Kien, N. D. (2018). Free vibration of two-directional FGM beams using a higher-order Timoshenko beam element. *Vietnam Journal of Science and Technology*, *56*(3), 380-396.

Uzun, B., Yaylı, M. Ö., & Deliktaş, B. (2020). Free vibration of FG nanobeam using a finite-element method. *Micro & Nano Letters*, *15*(1), 35-40.

Proc. 3rd International Conference on Structural Engineering Research (iCSER 2022)
27-30 Nov 2022, Sydney, Australia
ISBN: 978-0-6456692-1-3

Modelling Methods for Robustness Analysis of Composite Steel-Concrete Modular Buildings

Gaurav Swami[1] and Huu-Tai Thai[2]

[1]PhD student, The University of Melbourne, Parkville, VIC, Australia

[2]Associate Professor, The University of Melbourne, Parkville, VIC, Australia

Corresponding author's E-mail: gaurav.swami@student.unimelb.edu.au

Abstract

This paper investigates the modelling methods for composite steel-concrete modular buildings subject to progressive collapse using the alternate load path (ALP) method. A finite element (FE) model for a 10-storey steel-concrete composite tall modular building with concrete-filled steel tube (CFST) columns and proposed inter-module connection based on the beam-shell approach was developed in the commercial software package ABAQUS. Non-linear dynamic analysis was conducted based on the ALP method. The outcomes demonstrated the excellent capability of the suggested composite modular system with CFST columns to avoid gravity-induced progressive collapse following the sudden module removal. The removal of module from the corner location was observed to be the most critical scenario for progressive failure. It was observed that the inter-module connections transfer forces primarily in shear and are critical to shear failure. The 10-storey composite modular building was determined to be adequately resistant against progressive collapse caused by critical corner module removal scenarios.

Keywords: Modular building, CFST column, semi-rigid connection, progressive failure

1. INTRODUCTION

Modular building construction is a method of construction that is becoming more popular around the world as it provides efficient and sustainable structures. The construction process includes the production of modular units in a factory-controlled environment, transfer to the construction site, and fast assembly to construct the whole building. The main on-site task is to assemble modules with appropriate inter-module connections, which constitute the primary load path for force transfer between modules. Dangerous occurrences such as fire, blast, explosion, and impact can cause catastrophic damage to multi-storey structures, especially if the primary load-bearing elements are disturbed. In the event of an initial local failure with no ALP available, a break in the primary load path can result in progressive collapse. However, such research into the performance of multi-storey modular buildings under exceptional loading conditions and progressive collapse can only be carried out using numerical simulation with the FE approach. Inter-module connections are typically examined using experimental programs, and the results are validated using analytical and numerical research. Whereas numerical simulation using the FE method is the primary means that can be used to explore how multi-storey modular structures operate under scenarios of wind, earthquake, abnormal loads, and progressive collapse. The FE approach has emerged as the principal analysis tool for estimating the behaviour of steel-concrete composite multi-storey buildings during severe events, owing to an appropriate material model and effective modelling technique. The various modelling techniques are categorized as "shell-solid" models and "beam-shell" models (Wang et al., 2013). In the shell-solid concept, the concrete slab is represented by solid components, and the steel beam is represented by shell parts. The beam-shell model, on the other hand, uses multilayer shell elements for the concrete slab and beam elements for steel beams. Both methods offer good precision for estimating the structural response of steel-concrete composite multi-storey structures. However, the beam-shell model has a higher computing efficiency and a faster modelling speed (Wang et al., 2013).

The progressive collapse of a modular building has primarily been observed due to the buckling of neighbouring columns or due to the failure of horizontal inter-module connections to transmit loads in the event of module or column removal scenarios (Chua et al., 2022; Thai et al., 2021). To overcome the drawbacks of conventional steel structures with rigid or pinned connections, comprehensive research on the progressive collapse and structural robustness of steel-concrete composite modular buildings was conducted in this work. Nonlinear time-history analysis was conducted for a typical 10-storey modular structure under a sudden module removal scenario in ABAQUS software using ALP method. CFST columns were used to replace conventional steel columns to provide resistance against progressive collapse by buckling of columns. A semi-rigid inter-module connection modelling approach was proposed with force-displacement and moment-rotation relationships to accurately model and predict the response of connections. The modelling methods for CFST columns and semi-rigid connections were verified with experimental results from the literature.

2. MODELLING METHODS

2.1. CFST columns

To investigate the accuracy of the CFST column numerically, a FE model using beam elements (B31) was developed based on the modelling approach presented by Tao et al. (2021). The material model for the CFST columns was adopted by Tran et al. (2021). The beam element type B31 is a two-node, 3D Timoshenko element. The keyword *REBAR was used to assign the steel section as a material integration point. The geometric properties of the rebar were defined as the area and the coordinates of the rebar with respect to the cross-section. The longitudinal strain at the material integration locations in the section was assumed to follow the linear strain assumption over the section depth, and the relation between shear stress and shear strain was assumed to be linear elastic. A perfect bond was assumed between the steel box section and the concrete infill. The beam element was modelled as the concrete material and the steel box section was specified as rebar layer on the edges of the beam element, as shown in Fig. 1.

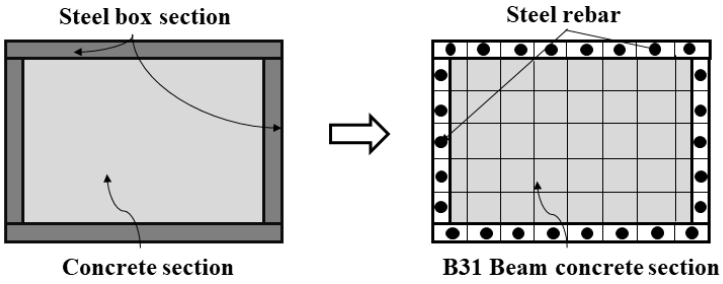

Fig. 1. Modelling approach for CFST column with B31 beam element

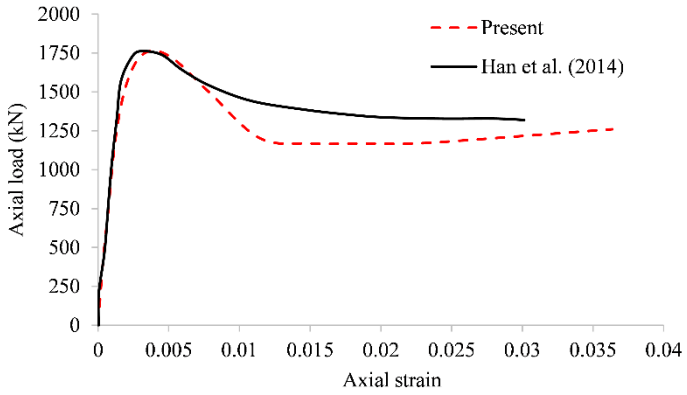

Fig. 2. Comparison of axial load-strain curves

Experiments on CFST columns conducted by Han et al. (2014) were used to validate the modelling technique for CFST columns. Han et al. (2014) considered CFST column with steel box section of (140x140x5.86) mm with 36 MPa infill concrete of length 420 mm. A FE model with similar properties was investigated, and good agreement between the FE model and experimental results was observed, as shown in Fig. 2. The slight discrepancy in the result is obtained due to the material modelling of confined concrete as compared to the experimental values.

2.2. Semi-rigid connection modelling

Inter-module and intra-module connections are critical because they maintain structural robustness and general stability of the modular building. In numerical modelling, fully rigid connections or pin connections are usually considered. However, these can either overestimate or underestimate the rotational stiffness of joints. The connectors are modelled as elements with 12 available degrees of freedom (DoF) (6 translations and 6 rotations), which can be specified based on the available connection type and design, as shown in Fig. 3(a). Several techniques, including the Kishi-Chen three-parameter model, can be employed to predict the joint behaviour in a semi-rigid connection (Kishi & Chen, 1990).

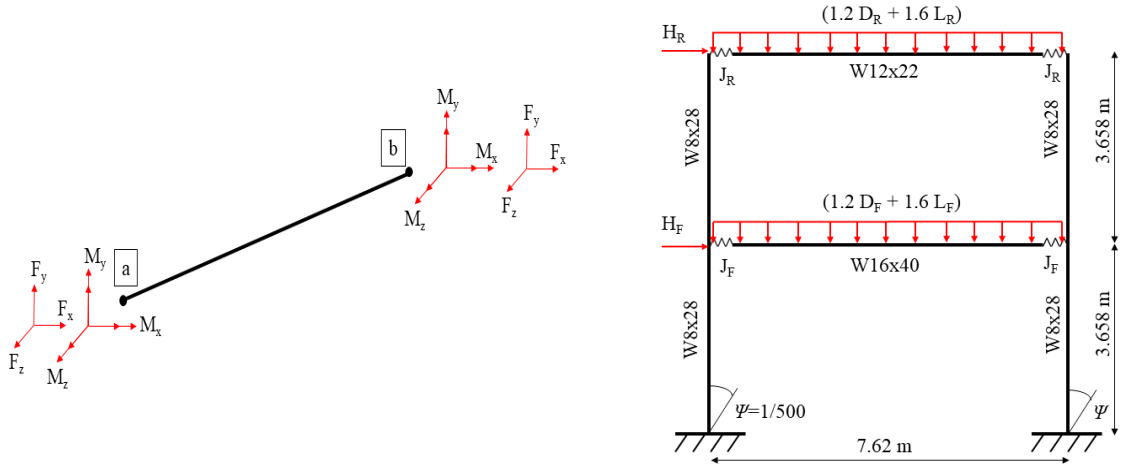

(a) Connector element (b) Two-storey single bay frame

Fig. 3. Semi-rigid connection modelling approach and verification study

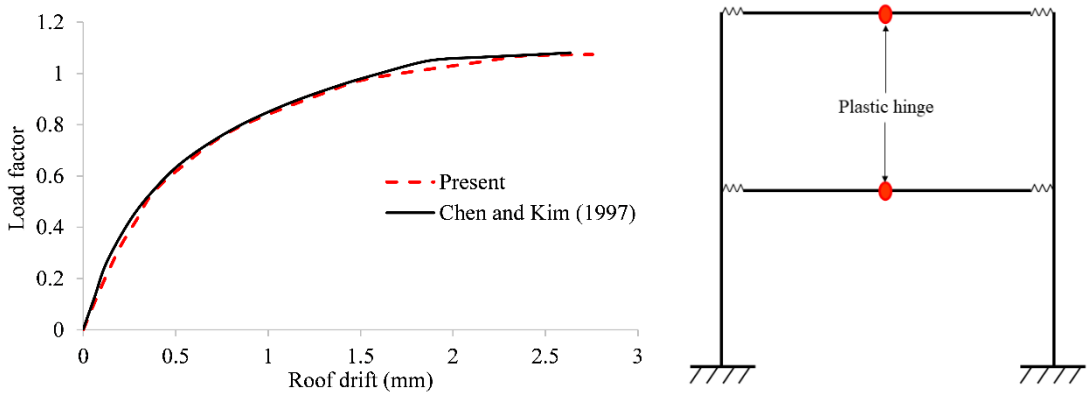

(a) Load factor v/s roof drift comparison (b) Plastic hinge location

Fig. 4. Comparison of results for frame with semi-rigid connections

A steel frame with a modified moment-rotation relationship for joints investigated by Chen and Kim (1997) as shown in Fig. 3(b) was selected to verify the ability of the connection type to predict the semi-rigid behavior of the beam-column connection in frames. The three parameters of the Kishi–Chen power

model were calculated by curve fitting analysis for the experimental moment-rotation curve as: R_{ki} = 68630 kNm/rad, M_u = 153.78 kNm and n = 0.927 for floor connections and R_{ki} = 10270 kNm/rad, M_u = 50.42 kNm and n = 1.403 for roof connections. The translational DoF and torsional rotation were modelled as rigid elements and the bending rotational DoF were modelled using the Kishi-Chen model. The initial out of plumb straightness of ψ = 1/500 was accounted for using the horizontal notional loads and stiffness reduction for columns (Alvarenga & Silveira, 2009). It was observed that the frame collapsed as soon as the beam mechanism was developed in both beams even before the development of plastic hinges in columns. A good agreement between the experimental and simulation results of load factor value and generation of plastic hinges in the beams was obtained as shown in Fig. 4.

2.3. Progressive collapse modelling

To study the gravity induced progressive collapse behavior of structures, the beam-shell modelling approach was adopted. The structural elements were modelled as two-node beam elements (B31) and the cross-section was defined using the relevant cross-section. The floor slab was modelled by a four-node shell element (S4R) with bending and membrane stiffness. Reinforcement in the shell element was provided using the rebar option by specifying the area of steel and the distance from the mid-surface of the slab. A 10-storey office steel-concrete composite modular building with CFST columns was modelled in the FE software ABAQUS, as shown in **Error! Reference source not found.**(a).

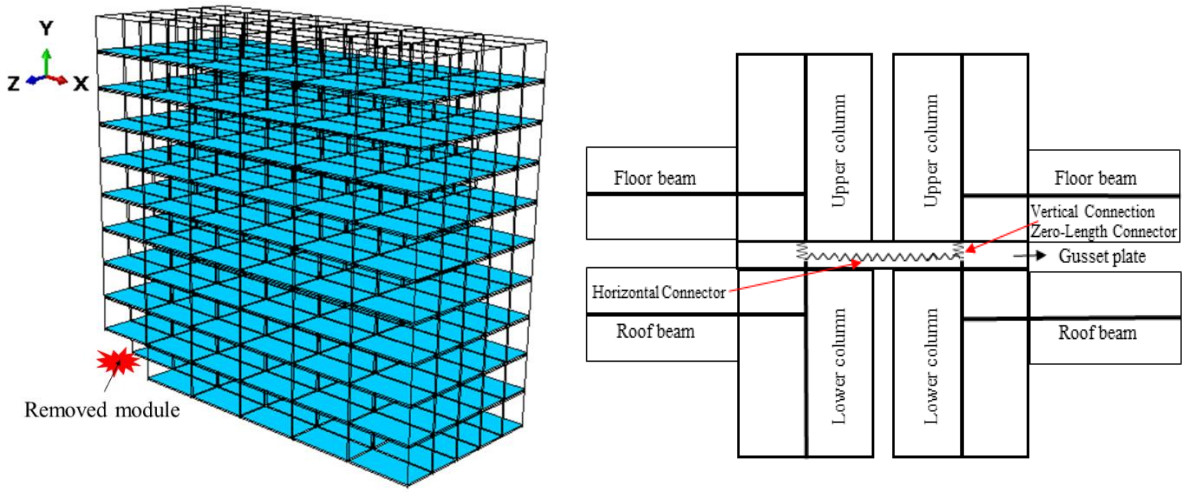

(a) 12-storey modular building (b) Inter-module connection design

Fig. 5. Design of modular building and inter-module connections

The dimensions of the modular unit were chosen as 6 x 3 x 3.3 m based on the commercially available module sizes (Thai et al., 2020). Corner supported modules were used to design the modular building that are connected at the corner joints. The structure was designed as per the Australian design standard AS/NZS 2327 (Standards Australia, 2017). The size of structural elements was determined for the load case of 1.5 (D.L + L.L) (American Society of Civil Engineers, 2002; General Services Administration, 2013). The dead loads and live loads were taken as per the ASCE-7:2002 (American Society of Civil Engineers, 2002) guidelines for office buildings. FE modelling of the structure was conducted based on the proposed modelling methods. The main reinforcement provided in the slab was A252 mesh acting at 30 mm from the top of the slab and a 0.9 mm thick metal deck at the bottom of the slab. This reinforcement was specified in both slab directions and acted as a smeared layer. The rebar mesh and sheeting for the slab were modelled as steel sections. It was concluded in the existing research that the ceiling slab lacks sufficient in-plane stiffness to operate as a floor diaphragm for lateral load transmission (Chua et al., 2022). As a result, its contribution was not accounted for in the frame modelling. The floor slabs, although discontinuous, contribute to stiffness in the lateral direction (Chua et al., 2022). The slab's concrete material was modelled as un-confined concrete using the concrete damaged plasticity model. The stress-strain curve was considered linear till 0.5f_{ck} and a parabolic curve

was adopted as specified in EC2 (C.E.N.-European Committee for Standardization, 2004). The material model for structural steel and confined concrete was modelled as per the equations considered by Tran et al. (2021).

A traditional spring connector model that illustrates the load transfer mechanism of a standard module connection was proposed here. As shown in **Error! Reference source not found.**(b), the connection involves zero-length connector elements for modelling the vertical connectivity of modules and a horizontal connector element joining the columns of the lower modules. The proposed connection approach was designed in accordance with a bolted gusset plate between the modules. The length of the horizontal connector was selected as the center-to-center spacing of columns, including the gap between modules. The proposed inter-module connection was used in this study for a 25 mm gusset plate. The rotational DoFs were defined using the moment-rotation relationships depending upon the connection type. The translational DoFs for the vertical connections were considered as rigid. The axial and shear stiffness of the gusset plate were calculated mathematically. The progressive collapse analysis was conducted in 3 steps: (1) Static load application, (2) Dynamic removal of column, and (3) Dynamic step for response stabilization. The structure was subjected to load combinations as per the GSA (General Services Administration, 2013). To simulate the removed module, *MODEL CHANGE command was selected from the ABAQUS library (Smith, 2009). The module removal was conducted in a short duration of 0.02 seconds to meet the requirement from GSA (General Services Administration, 2013), which specifies that the duration should be less than 10% of the fundamental period of the remaining structure.

3. RESULTS AND CONCLUSIONS

The structural response of the 10-storey composite modular structure was examined under various module loss scenarios at: (a) corner, (b) internal, and (c) middle of the shorter span, as illustrated in Fig. 6(a). The following locations were selected based on the suggestions provided in GSA for column loss scenarios. The time-displacement curve for nonlinear dynamic analysis under various module removal cases is shown in Fig. 6(b). It was observed from the results that the corner module removal shows the highest vertical deflection of 31.34 mm, thereby making it the most critical location of module removal. The maximum displacement observed for mid-span module removal was 8.39 mm and for the internal module was 8.35 mm, which was significantly lower compared to corner module loss due to a greater number of available load paths compared to corner module.

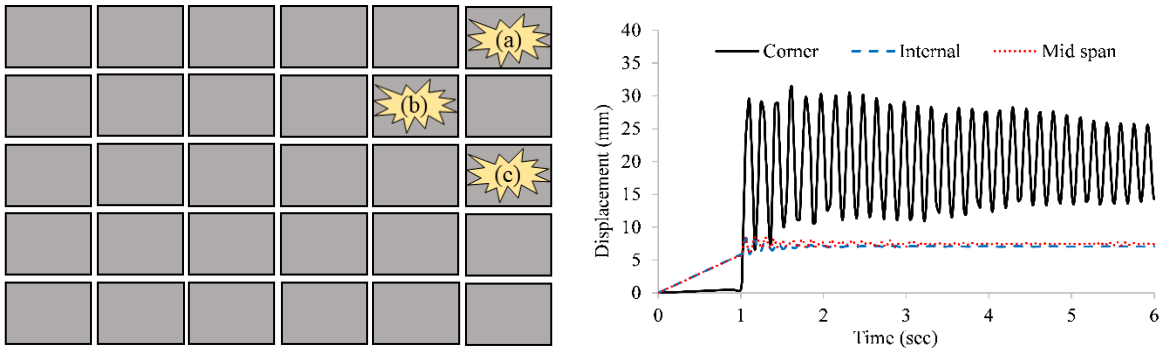

(a) Location of module removal from a) corner; b) internal; and c) mid span)

(b) Displacement time history for various locations of module removal

Fig. 6. Response of modular building to various module loss scenarios

Fig. 7(a) shows the results for the axial forces observed in the adjacent columns for modular building with pin inter-module connections subjected to corner module removal. Higher forces were observed in the adjacent column on the shorter edge of the removed module. This can be attributed to the floor slab aspect ratio of the upper module and the transfer of moments to the nearest column in the vicinity of the formed cantilever structure. Since the module is removed from the ground floor, the forces from the

upper modules cannot be directly transferred to the foundation. Therefore, the forces are transferred via the gusset plates into the adjacent columns and thereafter, the adjacent beams. This leads to the deflection of the gusset plate with the development of axial and shear forces. It was observed that the horizontal shear forces were negligible and did not contribute enough to the connection capacity. As observed from Fig. 7(b), the magnitude of vertical shear forces is significantly higher than the axial forces. The structure was deemed safe against progressive collapse as the buckling of columns was not observed, and the maximum value of shear force developed in the gusset plate was within the shear strength limit of a 25 mm steel plate.

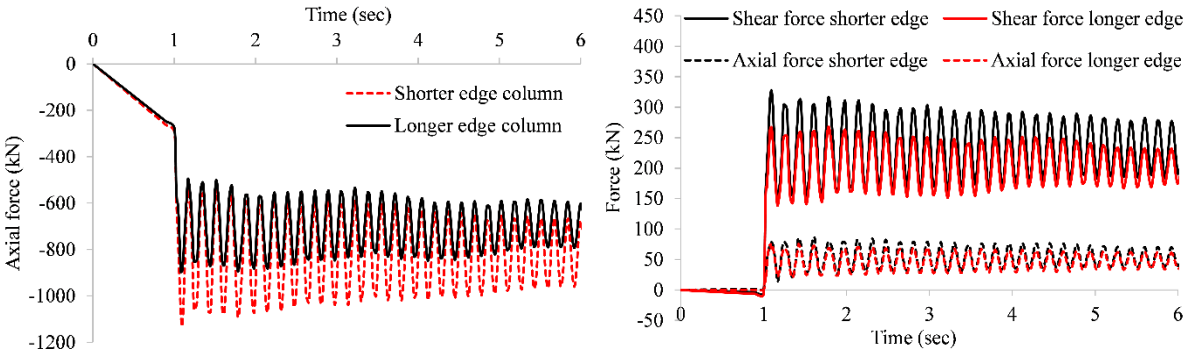

(a) Axial force time history of adjacent columns

(b) Variation of forces generated in the adjacent horizontal inter-module connection

Fig. 7. Response of modular building subjected to corner module removal

ACKNOWLEDGMENTS

This research was funded by the Australian Research Council (ARC) under its Future Fellowship Scheme (Project No: FT200100024). The financial assistance is gratefully acknowledged.

REFERENCES

Alvarenga, A., & Silveira, R. (2009). Second-order plastic-zone analysis of steel frames - Part II: Effects of initial geometric imperfection and residual stress. *Latin American Journal of Solids and Structures, 6*, 323-342.

American Society of Civil Engineers, A. S. C. E. (2002). ASCE 7- Minimum design loads for buildings and other structures. In. Virginia: American Society of Civil Engineers.

C.E.N.-European Committee for Standardization. (2004). Eurocode 2: Design of concrete structures - Part 1-1: General rules and rules for buildings. In. Brussels.

Chen, W. F., & Kim, S. E. (1997). *LRFD steel design using advanced analysis* (Vol. 13): CRC press.

Chua, Y. S., Pang, S. D., Liew, J. Y. R., & Dai, Z. (2022). Robustness of inter-module connections and steel modular buildings under column loss scenarios. *Journal of Building Engineering, 47*, 103888.

General Services Administration, G. S. A. (2013). Alternate path analysis & design guidelines for progressive collapse resistance. In. Washington, DC.

Han, L.-H., Li, W., & Bjorhovde, R. (2014). Developments and advanced applications of concrete-filled steel tubular (CFST) structures: Members. *Journal of Constructional Steel Research, 100*, 211-228.

Kishi, N., & Chen, W. F. (1990). Moment Rotation Relations of Semirigid Connections with Angles. *Journal of Structural Engineering, 116*(7), 1813-1834.

Smith, M. (2009). *ABAQUS/Standard User's Manual, Version 6.9*. Providence, RI: Dassault Systèmes Simulia Corp.

Standards Australia. (2017). AS/NZS-2327 Composite structures. In *Composite steel-concrete construction in buildings*. Australia.

Tao, Z., Katwal, U., Uy, B., & Wang, W.-D. (2021). Simplified Nonlinear Simulation of Rectangular Concrete-Filled Steel Tubular Columns. *Journal of Structural Engineering, 147*(6), 04021061.

Thai, H.-T., Ho, Q. V., Li, W., & Ngo, T. (2021). Progressive collapse and robustness of modular high-rise buildings. *Structure and Infrastructure Engineering*, 1-13.

Thai, H.-T., Ngo, T., & Uy, B. (2020). A review on modular construction for high-rise buildings. *Structures, 28*, 1265-1290.

Tran, H., Thai, H. T., Ngo, T., Uy, B., Li, D., & Mo, J. (2021). Nonlinear inelastic simulation of high-rise buildings with innovative composite coupling shear walls and CFST columns. *The Structural Design of Tall and Special Buildings, 30*(13).

Wang, Y.-h., Nie, J.-g., & Cai, C. S. (2013). Numerical modeling on concrete structures and steel–concrete composite frame structures. *Composites Part B: Engineering, 51*, 58-67.

Proc. 3rd International Conference on Structural Engineering Research (iCSER 2022)
27-30 Nov 2022, Sydney, Australia
ISBN: 978-0-6456692-1-3

Structural Performance of Truss Steel Decking Formwork Under Construction Loads

Y. Deshe[1], D. Kahagala Hewage[1], O. Mirza[1], Andrew[2], D. Allen[3]

[1]Western Sydney University, Locked Bag 1797, Penrith, New South Wales, Australia
[2]ABES Australia, PO Box 467 Emu Plains NSW 2750, Australia
[3]Premier Steel Technologies, 229 Newton Road, Wetherill Park, NSW, 2164, Australia, Australia

Corresponding author's E-mail: d.kahagalahewage@westernsydney.edu.au

Abstract

Steel-concrete composite structures have seeped their way into the construction industry within the last few decades. This is due to major benefits such as high stiffness and strength, reduced weight, and increased load-carrying capacity. The truss steel decking (TSD), which is composed of top and bottom plates connected with angled webs, offers significant benefits over conventional sheet-like steel decking, including the ability to pre-camber and reduce slab depth, flexural cracking and deflection because of its higher flexural stiffness. Most of the TSD are of height more than half of its respective composite slab. Despite of the straightforward section flexural capacity calculation, the presence of shear and web buckling results in unexpected member capacity reduction, particularly during the construction stage. Therefore, this paper presents an experimental study on the TSD with different spans and depth ratios under a uniformly distributed load. The structural behaviour of TSD was assessed through load-deflection response and failure modes. The results concluded that the web shear and buckling influence the structural performance of the TSD and are affected by the span and depth. Furthermore, rather than the yielding of the cross-section, the predominant failures observed were the top plate buckling associated with flexural stresses and the web buckling.

Keywords: *Composite construction, Truss steel decking, Web Buckling, Construction stage, Uniformly distributed loading*

1 INTRODUCTION

Steel concrete composite (SCC) construction has proven to be one of the simplest, quickest, lightest, and most cost-effective steel-framed building systems (Hedaoo et al., 2012). Because of its load-bearing capacity and increased structural stiffness, it is also commonly used in multi-story buildings. Some advantages of SCC structures include good fire and corrosion resistance because the steel beams are concrete encased, as well as maintaining the building's structural integrity by delaying cracking and flaking (Kathir, 2019). Furthermore, SCC can be prefabricated offsite, which reduces construction time and accelerates the process (Piloto et al., 2020). Finally, steel confinement improves the compressive strength and ductility of concrete (Mahbuba et al., 2013). One common application of SCC is composite floor construction, which uses steel decking as permanent formwork and construction platform, providing greater capacity without adding weight. Steel decking systems come in a variety of types, gauges, and lengths. Re-entrant, trapezoidal, rectangular, and truss steel decking (TSD), which was recently introduced, are popular types of commercial steel decking.

Re-entrant steel decking is known for its shear-bond capacities and high fire resistance (Tse & Chung, 2008). Web crippling failure in steel restricts the spanning capacities of currently available steel decking. Tse and Chung (2008) demonstrated localised web deformation, web crippling, and web buckling in re-entrant steel decking with 52 mm web height and 600 mm span. Trapezoidal and rectangular steel decking, as opposed to re-entrant profiles, can provide a greater depth, increasing load carrying capacity. Siva et al. (2021) compared trapezoidal decking to re-entrant and rectangular decking. The results show that the trapezoidal decking exhibited the highest deflection for the lowest load-carrying capacity, early

buckling, and significant strain energy caused by the large deflection value. Trapezoidal steel decking had weaker results than the others, hence showing a need for improvement, focusing on producing a better profile and web strengthening(Siva et al., 2021).

During the construction stage, the composite behaviour is ignored because no bond between the concrete and steel deck is formed until the concrete hardens. As a result, the steel deck should be able to withstand the weight of the concrete, reinforcement, construction equipment, and construction workers on its own. Most steel deckings, in general, cannot provide strength under construction load and thus require propping. Truss type steel decking (TSD) was recently introduced, which eliminates the need for propping in construction. TSD systems achieve higher load carrying capacity by increasing deck height by approximately 90 - 160 mm, as opposed to a maximum of 60 mm in other steel decking types. However, as no confinement is provided by the concrete, the increase in height is associated with plate buckling, reducing the cross-sectional capacity during the construction stage. As a result, steel deck only behaviour during the construction stage is critical. Despite the fact that the composite behaviour of TSD has been studied, the structural behaviour of TSD alone under construction loading has not been studied yet. Accordingly, the paper presented herein discusses the behaviour of the steel decking only under uniformly distributed load.

2 EXPERIMENTAL STUDY

The experiment focused on TSD profiles in the formwork conditions and its behaviour under a UDL. The TSD used for the investigation had a full web.

2.1 Experimental Specimen

The TSD profile consists of top and bottom plates connected to two aligned webs with 'Tox' as seen in Figure 1(a). TSD profiles with the height (h) 90, 110, 140 and 160 mm were tested under three spans 3, 4.1 and 6m and designated as shown in Table 1. For all the specimens, the web (t_w), top pate (t_t)and base plate (t_b) thicknesses were 0.7, 1.9 and 0.75 mm, respectively. The width of the base plate (w_b) was 250mm. The width of the top plate was 200 mm for TD90 and TD110, whereas TD140 and TD160 comprised of the top plate of 180 mm wide.

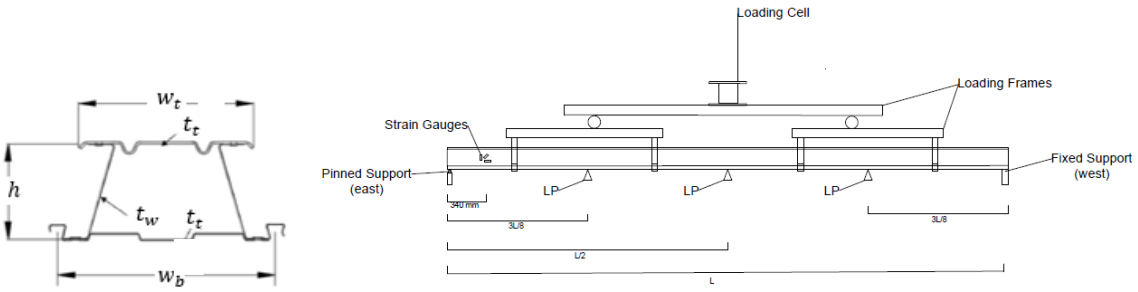

(a) (b)

Figure 1: TSD Specimen Profile; (a) Cross section, (b) Test setup

2.2 Experimental Setup

TSD specimens were tested in a simple supported configuration. Figure 1(b) depicts the specimens' experimental setup, where the letter 'L' denotes the span length of the steel decking. The vertical deflection of the TSD was measured using four linear potentiometers (LPs). Two LPs were placed in the middle of the span (L/2) and two others were placed L/4 from either end. Three strain gauges were placed 340 mm away from the edge on the east side, and one was placed at the midspan (L/2) on the bottom of the specimen. Strain gauges were used to measure shear and flexural strains on the steel decking.

The load was applied via the load cell, which recorded the load applied. Prior to the collapse, the load was increased to about 40% of its capacity and unloaded twice. As a result, the specification underwent two loading cycles ranging from 0 to 40% of capacity and one load cycle until failure.

Table 1: TSD test specimen details

Specimen designation	Web Depth 'h' (mm)	Span 'L' (mm)
TD(h) – (L)	h	L
Example (Deck profile height of 140 mm)		
TD140 - 3000 TD140 - 4400 TD140 - 6000	140	3000 4100 6000

3 RESULTS AND DISCUSSION

The results primarily discuss the effect of span and depth on load-displacement behaviour. Furthermore, this section investigates the effect of depth on load-deflection behaviour, capacity, and ductility under different spans.

3.1 Effect of span and depth on structural behaviour

Figures 3, 4 and 5 display the load versus mid-displacement relationship and different failures observed for the 3, 4.2 and 6m span specimens for various depths. All the specimens initially behaved linearly, owing to the elastic behaviour of cold-formed steel. Subsequently, the specimens depicted non-linear behaviour before the collapse due to local yielding and buckling. Irrespective of the span, the lowest depth resulted in the highest deflection at the maximum capacity. For a 3m span, the maximum deflection for TD90 is about 2.4 times that of TD160, highlighting the higher ductility of TD90. The TD160 showed a sudden collapse as opposed to the gradual collapse of the TD90. However, as the span increases, the difference in ductility decreases, with the TD90 deflection being only 1.4 times that of the TD160 deflection. When the span increased, the deeper profiles also demonstrated ductile failure, as opposed to the sudden collapse observed at lower spans.

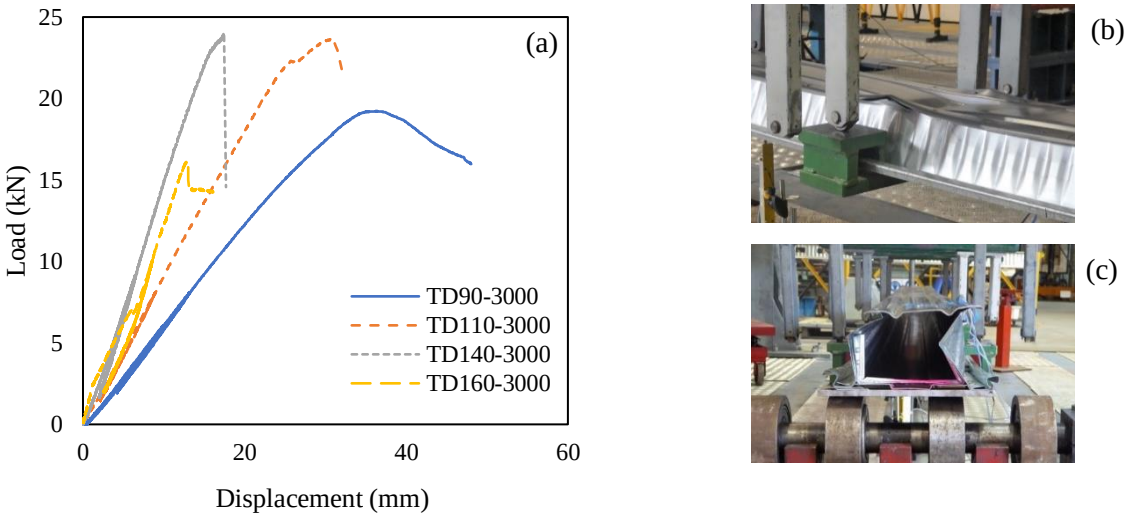

Figure 3: Experimental results for 3 m span; (a) Load-displacement behaviour, (b) Top plate buckling, (c) Web distortion at the edge

As the height increased, the specimens experienced different failure modes. Under 3m span, the specimens with lower depths (TD90 and TD110) experienced buckling on the top plate closer to mid-span, as shown in Figure 3(b). The specimens with higher depth (TD140 and TD160) experienced web buckling at the support and end bracket distortion, as seen in Figure 3(c). Similar to 3m, under 4m span,

the two lower heights of 90 mm and 110 mm buckled on the top plate and 140 mm and 160 mm, buckled on end brackets at the edge, as seen in Figure 4(b) and 4(c), respectively. Therefore it can be concluded that for 3 and 4m spans, the flexural action at the mid-span is prominent, and as the depth increases, the failure of the deck is governed by end shear. As a result, the shear resistance of the deeper sections should be improved to utilise the full section when it is used for short spans.

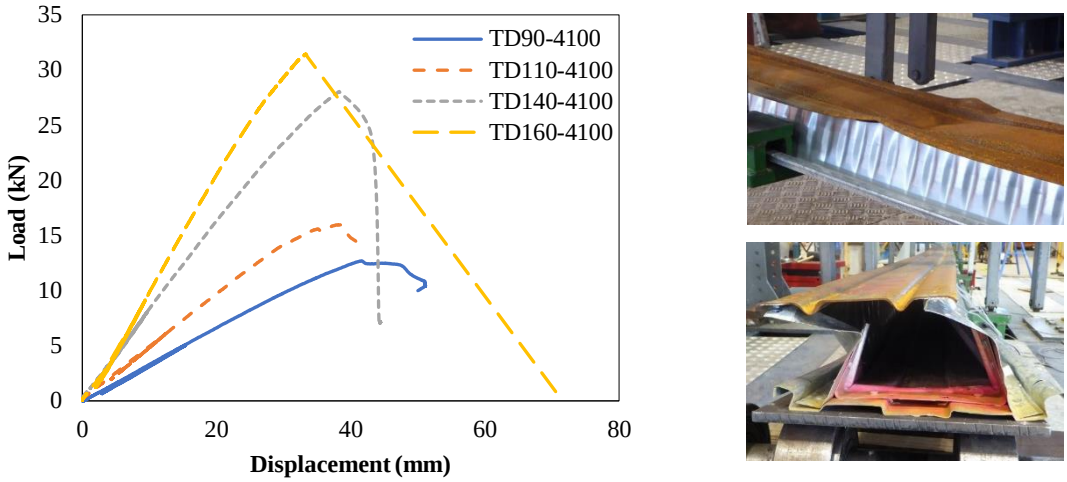

Figure 4: Experimental results for 4.1 m span; (a) Load-displacement behaviour, (b) Top plate buckling, (c) Web distortion at the edge

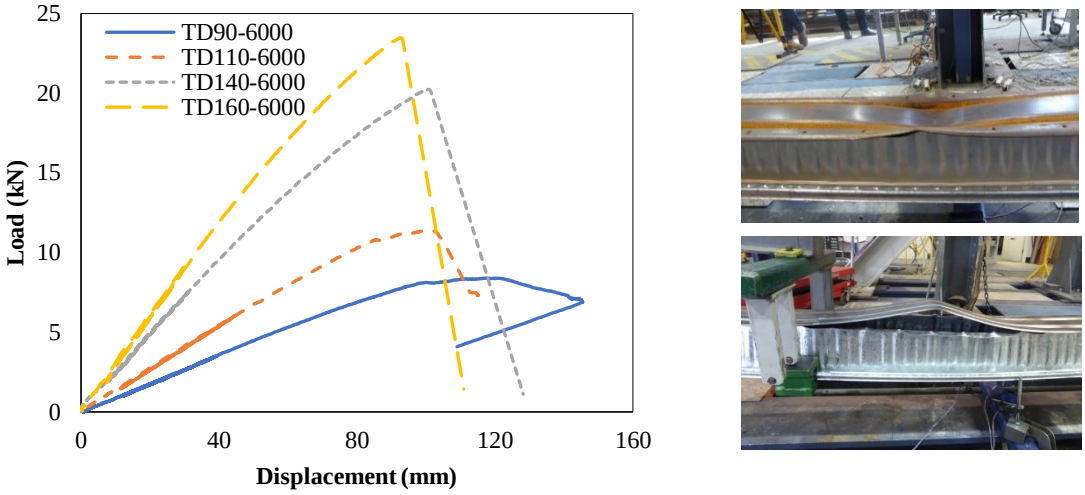

Figure 5: Experimental results for 6 m span; (a) Load-displacement behaviour, (b) Top plate buckling, (c) Tox failure

For a 6 m span, TD90 and TD110 failed due to top plate buckling (Figure 6(b)), whereas TD140 and TD160 failed due to tox failure (Figure 6(c)) in the midspan. Because both failures occur in the mid-span and are associated with flexural action, it can be concluded that, regardless of height, the sectional moment resistance governs the failure for a 6 m span.

3.2 Effect of span and depth on the capacity

Figure 6 shows the experimental flexural capacity determined under each span plotted against the height of the steel deck. The theoretical sectional moment capacity, denoted by 'yield,' is also plotted in the same figure. Except for the 3 m span, the flexural moment capacity increases as the web height of the specimens increases. For 3 m span, the TD160 recorded a lower capacity than the TD90, and the TD140

achieved only about 63% of the theoretical capacity due to web buckling at the support. As a result, the flexural capacity of the member is reduced, and having a deeper profile for a small span may be ineffective. On the other hand, the deck members with larger spans (i.e. 4 and 6m) achieve the full sectional capacity. It is evident that irrespective of the span, TD90 and TD110 only achieve 75% of the capacity, which failed due to top plate buckling. This can be attributed to the wider top plate in TD90 and TD110, which is 20 mm higher than the other profiles. Therefore, deeper profiles are compelling in larger spans.

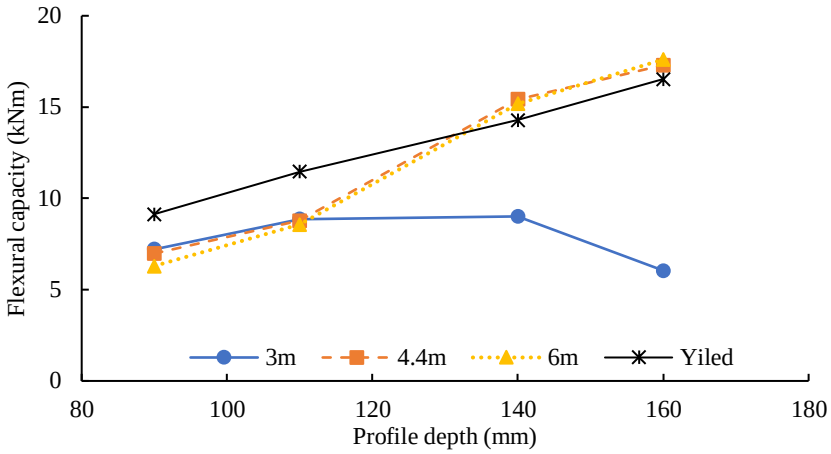

Figure 6: Load vs Displacement (midspan) 6m Span

3.3 Effect of span and depth on the flexural stiffness

Figure 7 depicts the experimental and theoretical flexural stiffness calculated using the load-displacement slope. The experimental stiffness was calculated using the second loading cycle. Except for TD160 at 3 m span, the experimental stiffness is similar or slightly higher than the theoretical stiffness. As a result, it can be concluded that analysis and design calculations using the fundamental equations for all profiles are valid until approximately 40% of the capacity is reached. The lower stiffness of TD160-3000 can be attributed to early web buckling during the loading process.

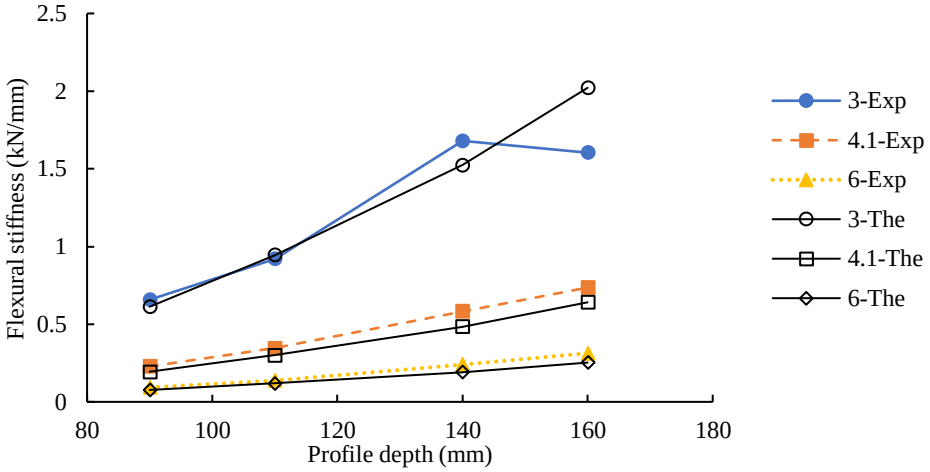

Figure 7: Load vs Displacement (midspan) 6m Span

4 CONCLUSION

This study investigated the behaviour of TSD under a uniformly distributed load. The results analysed the influence of span and web depth on the specimens' stiffness, capacity, and ductility. It was concluded that;

- TSD structural behaviour is heavily influenced by profile depth and member span. For smaller depths, the top plate was buckled at the midspan regardless of span, concluding the flexural action governing for smaller depths.
- Shear action governs the behaviour as the depth increases, with web buckling for shorter spans. However, for longer spans, the flexural action and web and top plate connection govern the failure as the connection failed in the middle of the span.
- The flexural capacity of short-span members decreases as profile depth increases due to web buckling, implying that using a deeper profile for a short span is ineffective. Contrary to short spans, members with deeper profiles reach sectional yield capacity when used in spans greater than 4 m.
- The elastic behaviour of all the profiles across all the spans is not affected by the shear or buckling. Therefore flexural stiffness can be estimated using the current elastic theories.

5 REFERENCES

Hedaoo, N. A., Gupta, L. M., & Ronghe, G. N. (2012). Design of composite slabs with profiled steel decking: a comparison between experimental and analytical studies. *4*(1).

Kathir. (2019). Advantages of composite beams. https://civilsnapshot.com/advantages-of-composite-beams/

Mahbuba, B., M.D., S. S., N.M, T. B. K., & W, A. (2013). Cost Analysis Of Steel Concrete Composite Structures In Bangladesh. *14*(6). https://www.sid.ir/en/Journal/ViewPaper.aspx?ID=356300

Piloto, P. A., Balsa, C., Santos, L. M., & Kimura, É. F. (2020). Effect of the load level on the resistance of composite slabs with steel decking under fire conditions. https://journals-sagepub-com.ezproxy.uws.edu.au/doi/full/10.1177/0734904119892210

Siva, A., Erick, I. S. F., Gerardo, A.-L., Walter Jonathan, T., Sudharshan, N. R., Gunasekaran, M., Mugahed, A., Maria, K., Roman, F., & Nikolai, V. (2021). Experimental Investigation on Composite Deck Slab Made of Cold-Formed Profiled Steel Sheeting. *Metals (Basel)*, *11*(2), 229. https://doi.org/10.3390/met11020229

Tse, W. T., & Chung, K. F. (2008). Web crippling behaviour of laterally restrained cold-formed steel re-entrant profiled deckings. *Journal of constructional steel research*, *64*(7), 785-801. https://doi.org/10.1016/j.jcsr.2008.01.033

Proc. 3rd International Conference on Structural Engineering Research (iCSER 2022)
27-30 Nov 2022, Sydney, Australia
ISBN: 978-0-6456692-1-3

Analysis of Normal Stress Distribution And Mechanism of Girders With Corrugated Webs Under Uniform Bending

Guoji Zuo[1], Lewei Tong[1,2], Zhenbei Zhao[1], Hailin Wang[3], Yan Li[2], Chunyu Pan[4] and Xiaojing Wang[3]

[1]College of Civil Engineering, Tongji University, Shanghai, China
[2]Jiaxing Key Laboratory of High-performance and Functional Materials in Civil and Environmental Engineering, Tongji Zhejiang College, Zhejiang, China
[3]Qianshan Steel Structure of Xingtai Road and Bridge Construction Co., Ltd., Hebei, China
[4]China Construction Industrial & Energy Engineering Group Co., Ltd, Jiangsu, China

Corresponding author's E-mail: gjzuo@tongji.edu.cn

Abstract

A steel I-girder with corrugated webs (IGCWs) is a new type of structure, which has been increasingly used in the field of civil engineering due to its excellent structural performance. It is necessary to understand stress distribution in the cross-section to conduct flexural strength design and assess the fatigue strength of this girder. Due to the web corrugation, the normal stress distribution in the flange of IGCWs is quite complicated in comparison with that of the conventional I-girders under in-plane loads. The normal stress distribution in the cross-section of I-girder with trapezoidal corrugated webs (IGTCWs) subjected to uniform bending is investigated in this paper. Finite element (FE) modelling is developed using the software ABAQUS and is verified by the existing test results in the literature. Both FE analysis and the existing test data indicated that the feature of normal stress distribution in the cross-section with a parallel web fold was quite different from that with a flat web. Its mechanism is explored using a new concept of secondary transverse bending moment, which is distinct from the conventional theory of transverse bending moment in the flange. It is found that the normal stress distribution in the flange predicted by the concept of the secondary transverse bending moment was consistent with the FE and existing test results.

Keywords: Steel girders with corrugated webs, Normal stress distribution, Finite element analysis, Secondary transverse bending moment

1. INTRODUCTION

Traditionally, I-girders with flat webs are generally designed with high cross-sections to maximize their bending moment of inertia. This may, however, result in local buckling of flat webs. Stiffeners, including longitudinal and transverse stiffeners, are utilized to prevent local buckling of flat webs, but they increase steel usage, and welding decreases fatigue strength. Corrugated webs (CWs) have much higher out-of-plane stiffness and shear buckling strength compared with flat webs, as well as eliminating the use of stiffeners. Therefore, I-girders with corrugated webs (IGCWs) are commonly utilized to replace conventional I-girders with flat webs in bridge construction (shown in Figure 1(a)). Additionally, due to their better fatigue strength, IGCWs are suitably used as crane girders (Figure 1(b)) in industrial plants. It is necessary to identify the stress distribution in the cross-section of this girder in its elastic phase before assessing its fatigue strength.

The elastic flexural behavior, as the fundamental properties, of IGCWs under in-plane loads was first investigated experimentally and analytically by Lindner (1992) and Aschinger and Lindner (1997). It was found that under primary moment and shear, the shear flow at the web-to-flange junction can induce transverse bending of the flange due to the eccentricity of the web concerning the flange centerline. However, the analysis procedure of Aschinger and Lindner (1997) was limited to I-girders with trapezoidal corrugated webs (IGTCWs) in the case of constant shear. An in-depth study was

conducted by Abbas (2006, 2007a, b) with an emphasis on the flange transverse bending behavior of IGCWs under in-plane loads. They directly solved the controlling differential equation to obtain accurate closed-form solutions for the flange transverse bending problem of I-girders with sinusoidal corrugated webs under in-plane uniform loads (Abbas et al. 2006). Afterwards, Abbas et al. (2007a) suggested using the so-called fictitious load method to determine the flange transverse bending moments of I-girders with piecewise linear folds web (such as trapezoidal or rectangular web profiles). They also investigated the relationship between the flange transverse bending moment solutions for various corrugated web profiles. Then the C-factor method was presented as a simplified way of examining the flange transverse bending (Abbas et al. 2007b). Kövesdi et al. (2012) researched the determination of the maximum transverse bending moment in the flanges of IGTCWs. The tendency of the additional normal stresses caused by the transverse bending moment under different boundary and loading conditions was also analyzed by Kövesdi et al. (2016).

According to Aschinger and Lindner (1997), there is no transverse bending moment in the flange and the normal stresses in the flange should be uniformly distributed (ignoring the shear lag effect) under uniform bending. However, the experiments and finite element (FE) analyses in Abbas et al. (2007a) and Kövesdi et al. (2012) showed that the normal stress of the flange in the constant bending region leads to a transverse stress gradient across the flange width. A study by Abbas et al. (2007a) on this phenomenon proposed a secondary transverse bending moment, which differed from the conventional theory of transverse bending moments in flanges, but did not study it in depth. In consideration of this research gap, based on the verified FE model, the normal stress distribution in the cross-section of IGTCWs under uniform bending was examined. Different normal stress distribution phenomena were found in the different cross-sections, and the mechanism of the aforementioned events was evaluated by the secondary transverse bending moment.

(a) Dole bridge girders with CWs, France

(b) Crane girder with CW, China

Figure 1. Examples of CWs in bridge and construction projects

2. FE MODEL DEVELOPMENT AND VALIDATION

In this section, IGTCWs were modeled by the FE software ABAQUS (version 6.16). All FE models were simply-supported and loaded under a constant moment. Since the study focused on normal stresses of the flange in the linear elastic stage, the "Static, General" analysis method was applied to the FE models without considering geometric initial imperfections. This is attributed to the fact that the introduction of geometric initial imperfections can seriously affect the distribution of flange normal stresses and that the theory of second transverse bending moment targets the ideal models.

2.1. FE model development

To save computational time and cost, four-node shell elements with reduced integrations (S4R) were used to mesh IGTCWs in this work. The S4R element is effective for thin and thick shell problems, and each node of S4R has six degrees of freedom, including three displacement degrees of freedom (U_x, U_y, U_z) and three rotation degrees of freedom (UR_x, UR_y, UR_z). Regarding the mesh size, it was found that using an overall element size of 40 mm provides accurate results. The elastic-perfect plastic stress-strain curve (as shown in Figure 2) has been used in the FE models and Young's modulus E, yield strength f_y, yield strain ε_y and Poisson's ratio are 200,000 MPa, 345 MPa, 0.17 % and 0.3 respectively.

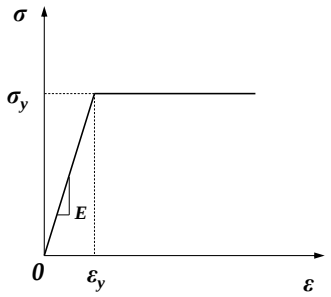

Figure 2. Elastic-perfect plastic stress-strain curve used in FE model

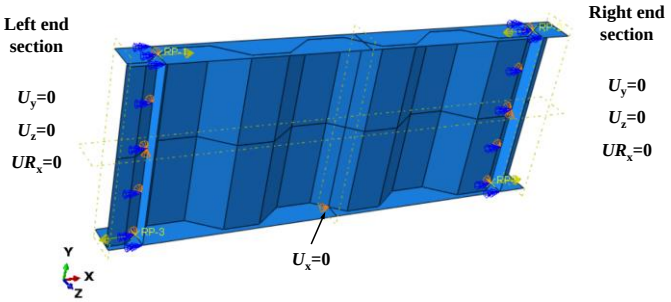

Figure 3. The loading and boundary conditions of a typical FE model

There are two ways to apply constant bending moment (BM) over the girder's length; one is to impose concentrated BMs at the centroid of both end sections; the other is to equate the BM as a pair of force couples acting on the top and bottom flanges. As the first way was prone to local buckling, the second method was chosen to apply the BM, whose accuracy has been confirmed by Shao et al. (2020).

Figure 3 presents the simply-supported boundary conditions set at both end sections of the FE model. At each end section, the vertical displacement (U_y) of the node at the centroid of the web, the lateral displacement (U_z) of all web nodes, and the twist rotation about the *x*-axis (UR_x) of all nodes were restrained. To maintain the stability of the girder, a point at the centreline of the girder on the bottom flange was restrained in the longitudinal direction (U_x).

2.2. Validation of the current FE model

In the absence of the tests of IGTCWs under uniform bending, Driver's shear test and Abbas' four-point bending test were used to verify the FE model. The specimen GA7 was one of two shear test specimens of Driver (2006) under single concentrated loads. Table 1 gives the comparison of the test and FE calculation results of shear strength, and Figure 4 (a) presents the comparison of shear stress-displacement curves. It can be found that the error of ultimate shear stress of FE and test is only 4%, the trend of the curve is the same, and the residual strength is also relatively close.

An elastic phase loading of 489 kN was performed on specimen G2A in a four-point bending test by Abbas et al. (2007a), but the specimen did not reach its ultimate load-carrying capacity at this load level. From Figure 4 (b) and Table 1, it can be seen that the FE agrees reasonably with the test result, and the error of the initial stiffness is only 7%.

The verification of the above tests can determine that the boundary conditions of the FE model are reasonable. In addition, the correctness of the loading method has been validated by Shao et al. (2020).

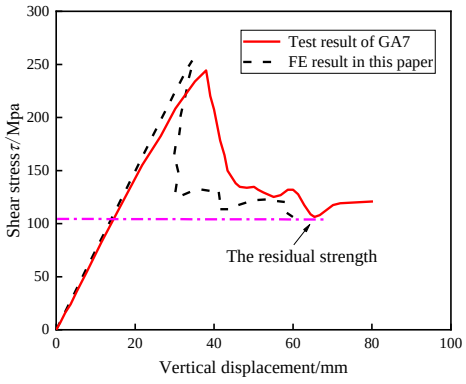

(a) Shear stress versus vertical displacement of specimen GA7

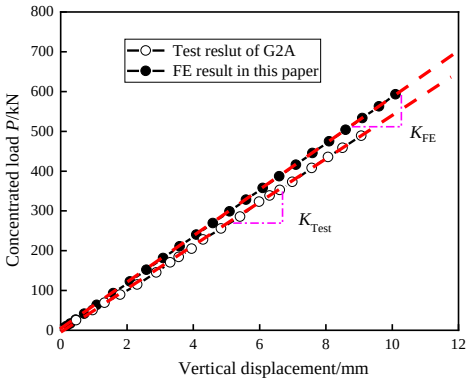

(b) Load versus vertical displacement of specimen G2A

Figure 4. Comparison between experimental and FE results

Table 1. Comparison of the FE and existing test results

Specimen	FE results (a) $\tau_{u,FE}$ (MPa)	FE results (b) K_{FE} (kN·mm)	Test results (c) $\tau_{u,Test}$ (MPa)	Test results (d) K_{Test} (kN·mm)	(a)/(c)	(b)/(d)
GA7	254.1	-	244.3	-	1.04	-
G2A	-	58.2	-	54.3	-	1.07

3. NORMAL STRESS DISTRIBUTION IN THE FLANGE AND MECHANISM ANALYSIS

Based on the validated FE model, static analysis is carried out on the IGTCWs. The characteristics and mechanisms of the normal stress distribution in the middle of each web fold along the whole girder length will be carefully investigated in this section. Figure 5 presents the cross-sections of the studied normal stress.

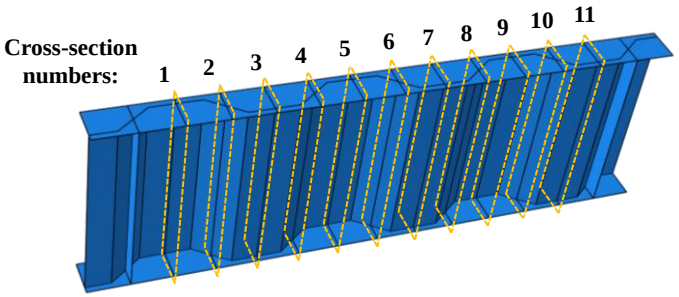

Figure 5. The cross-sections of the studied normal stress

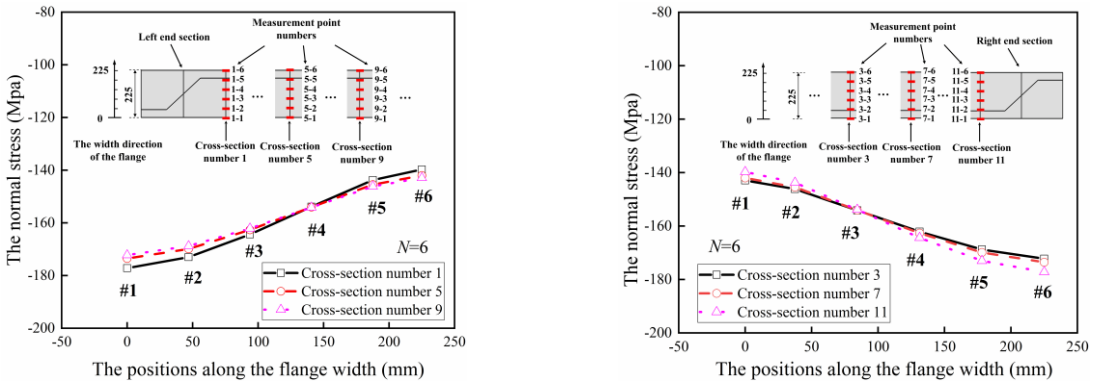

(a) Cross-sections 1, 5 and 9 **(b) Cross-sections 3, 7 and 11**

Figure 6. The normal stress distribution in cross-sections with parallel web folds of the top flange along the flange width direction

3.1. Normal stress distribution in the flange

Six of the eleven cross-sections in Figure 5 are with parallel web folds. It is possible to divide these six cross-sections into two categories based on the position of the parallel web folds: one for cross-sections 1, 5, and 9 and another for cross-sections 3, 7, and 11. For each cross-section, six stress measurement points were located at 45 mm intervals along the flange width (225 mm) and were designated "the cross-section numbers - the measurement point numbers". For example, 1-1 represents the first stress measurement point of cross-section 1.

From Figure 6, the stresses in the flange are approximately linearly distributed along the width direction for the cross-section with parallel web folds. Additionally, the flange stresses at positions away from the web side of the cross-section (#1 in Figure 6 (a) and # 6 in Figure 6 (b)) are greater than

those at positions close to the web side (#6 in Figure 6 (a) and # in Figure 6 (b)). It was also confirmed in the experimental study by Kövesdi et al. (2012).

In Figure 5, five of the eleven cross-sections have inclined web folds: cross-sections 2, 4, 6, 8, and 10. On each cross-section, five stress measurement points were set along the flange width direction. Figure 7 depicts the normal stress distribution in cross-sections with inclined web folds of the top flange along the flange width direction. It is still possible to consider that normal stresses are approximately uniformly distributed over the cross-section flange, despite the slightly smaller stresses at the middle measurement point (#3).

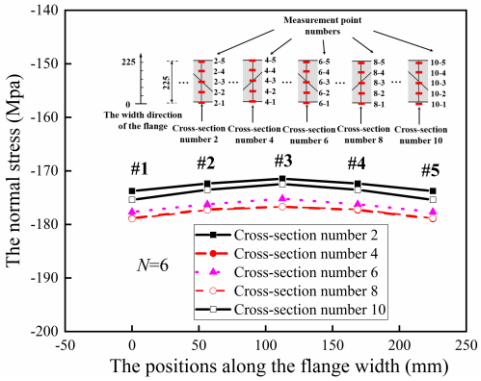

Figure 7. The normal stress distribution in cross-sections with inclined web folds of the top flange along the flange width direction

3.2. Mechanism analysis

According to the results of Abbas et al. (2007a), the normal stresses near the web-to-flange junction were significantly higher in the cross-section with a parallel web fold than in the cross-section with an inclined web fold. It means that the parallel web folds contribute more to the bending resistance of the cross-section than the inclined web folds.

The non-uniform contribution of the web to the bending resistance of the cross-section results in the non-uniform distribution of normal stresses in the flange in the case of uniform bending. As shown in Figure 8 (a), the resultant force of normal flange stress in the cross-section with a parallel web (F_{parallel}) is less than the resultant force of normal flange stress in the cross-section with an inclined web (F_{inclined}). Therefore, a shear flow (q) is created between the flange of cross-sections 4 and 5 to balance this force gap. Due to the eccentricity of the shear flow concerning the centreline of the flange (e), secondary transverse bending moment (M_t^{II}) and secondary transverse shear force (V_t^{II}) are generated in the flange. Moreover, this secondary transverse bending moment induces additional normal stresses (σ_t^{II}) in the flange, the distribution of which is shown in Figure 8 (b). It should be noted that the secondary transverse bending moment differs fundamentally from the transverse moment proposed by Aschinger and Lindner (1997).

From Figure 8, it can be seen that normal stresses in the flange of the cross-sections with parallel web folds are the superposition of the normal stress from the secondary transverse bending moment and the in-plane moment. This results in a linear distribution of normal stresses in the flange along the width direction and the flange stresses at positions away from the web side of the cross-section are greater than those at positions close to the web side, as shown in Figure 6.

Due to the approximatively uniform distribution of normal stresses in the flange of cross-sections with inclined web folds (Figure 7), it can be assumed that there are no secondary transverse bending moments. Consequently, only in-plane moments generate normal stresses in the flange of cross-sections with inclined web folds.

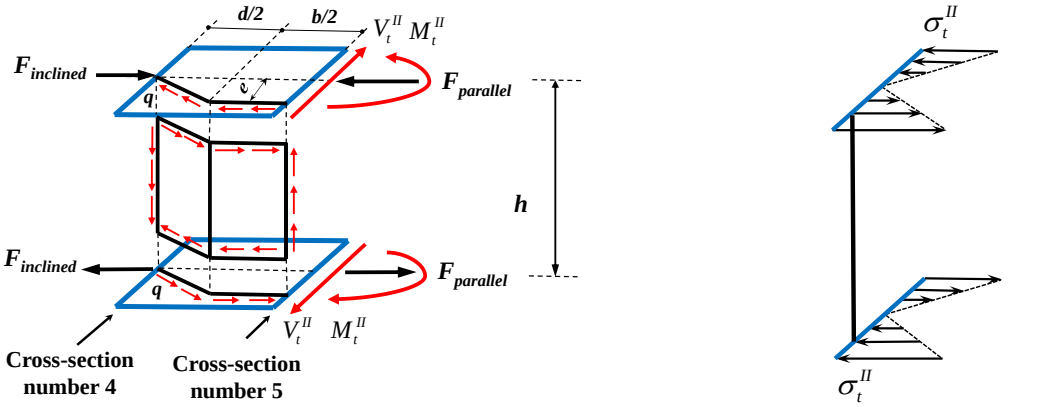

(a) The generation of M_t^{II} and V_t^{II} **(b) The distribution of σ_t^{II}**

Figure 8. The secondary transverse bending moment theory

4. CONCLUSIONS

Based on the validated finite element (FE) models, the current study presented a detailed investigation of the analysis of stress distribution and mechanism of I-girders with trapezoidal corrugated webs (IGTCWs) subjected to uniform bending. The following main conclusions could be drawn:

(1) The stresses in the flange are approximately linearly distributed along the width direction for the cross-sections with parallel web folds. Also, the flange stresses at positions away from the web side of the cross-section are greater than those at positions close to the web side.

(2) The normal stresses are nearly uniformly distributed over the flange in cross-sections with inclined web folds.

(3) The uniform bending of the cross-sections of IGTCWs does produce a secondary transverse bending moment, leading to a transverse stress gradient across the flange width.

(4) Only cross-sections with parallel web folds present secondary transverse bending moments, but not cross-sections with inclined web folds.

ACKNOWLEDGMENTS

The author gratefully acknowledges the financial support provided by the National Natural Science Foundation of China (NO. 52178154).

REFERENCES

Abbas, H. H., Sause, R., & Driver, R. G. (2006). Behavior of corrugated webs I-girders under in-plane loading. *Journal of Engineering Mechanics*, 132(8), 806-814.

Abbas, H. H., Sause, R., & Driver, R. G. (2007a). Analysis of flange transverse bending of corrugated web I-girders under in-plane loads. *Journal of Structural Engineering*, 133(3), 347-355.

Abbas, H. H., Sause, R., & Driver, R. G. (2007b). Simplified analysis of flange transverse bending of corrugated web I-girders under in-plane moment and shear. *Engineering Structures*, 29(11), 2816-2824.

Aschinger, R., & Lindner, J. (1997). Zu Besonderheiten bei Trapezstegtr¨agern. *Stahlbau* 66(3),136–42 (in German).

Driver, R. G. & Abbas, H. H. (2006). Shear Behavior of Corrugated Web Bridge Girders. *Journal of Structural Engineering*, 132(2), 195-203.

Kövesdi, B., Jáger, B., & Dunai, L. (2012). Stress distribution in the flanges of girders with corrugated webs. *Journal of Constructional Steel Research*, 79, 204-215.

Kövesdi, B., Jáger, B., & Dunai, L. (2016). Bending and shear interaction behavior of girders with

trapezoidal corrugated webs. *Journal of Constructional Steel Research*, 121, 383-397.
Lindner, J. (1992). Zur Bemessung von Trapezstegtr¨agern. *Stahlbau*. 61(10), 311-318 (in German).
Shao, Y. B., Zhang, Y. M., & Hassanein, M. F. (2020). Strength and behavior of laterally-unrestrained S690 high-strength steel hybrid girders with corrugated webs. *Thin-Walled Structures*, 150, 106688.

Proc. 3rd International Conference on Structural Engineering Research (iCSER 2022)
27-30 Nov 2022, Sydney, Australia
ISBN: 978-0-6456692-1-3

Metaconcrete Structure to Resist Impulsive Loads

Hong Hao[1], Cheng Xu[2], Wensu Chen[3], Thong M. Pham[4] and Kaiming Bi[5]

[1] John Curtin Distinguished Professor, Center for Infrastructural Monitoring and Protection, School of Civil and Mechanical Engineering, Curtin University, Australia. Email: hong.hao@curtin.edu.au
[2] Research Fellow, Center for Infrastructural Monitoring and Protection, School of Civil and Mechanical Engineering, Curtin University, Australia. Email: cheng.xu@curtin.edu.au
[3] Associate Professor, Center for Infrastructural Monitoring and Protection, School of Civil and Mechanical Engineering, Curtin University, Australia. Email: wensu.chen@curtin.edu.au
[4] Senior Lecturer, Center for Infrastructural Monitoring and Protection, School of Civil and Mechanical Engineering, Curtin University, Australia. Email: thong.pham@curtin.edu.au
[5] Associate Professor, Center for Infrastructural Monitoring and Protection, School of Civil and Mechanical Engineering, Curtin University, Australia. Email: kaiming.bi@curtin.edu.au

Keywords: Metaconcrete, impulsive loads, bandgap, stress wave attenuation

ABSTRACT

With the increasing risk and prevalence of extreme events (e.g., vehicle collisions, accidental explosions or terrorist attacks), concrete structures during their service life may experience extreme impulsive loadings, leading to severe damage or failure and significant casualties and economic loss. For safety requirements, concrete structures need to be protected against those extreme loads. This study explores the novel concept of converting the impulsive loading energy to local resonance and energy trapping mechanism for structural protection. The state-of-the-art metamaterial based on the local resonance mechanism is employed to make metaconcrete consisting of engineered aggregates (EAs). A series of laboratory tests are carried out to investigate the performance of metaconcrete structures by conducting non-destructive and destructive tests with an instrumented impulse hammer and a Split-Hopkinson pressure bar (SHPB). The effectiveness of embedding EAs into metaconcrete on the equivalent damping properties and the mitigation performance of wave propagation induced by longitudinal and transverse impulsive loading are experimentally investigated. Experimental results confirm the bandgaps in which wave propagation is inhibited. To address the strength reduction problem owing to the soft layer of conventional EAs in metaconcrete material, EAs with enhanced coating outside the soft layer are proposed, fabricated, and tested under static and dynamic loading conditions. The results from this study demonstrate that the properly fabricated EAs mixed in metaconcrete can mitigate stress wave propagations while not compromising the strength of metaconcrete material, which can therefore be used in the design of metaconcrete structures to resist impulsive loads.

1. INTRODUCTION

Concrete structures in their service life may experience different types of dynamic loads induced by accidental or natural hazards such as earthquakes and accidental explosions with relatively low probability but disastrous consequences. For instance, the recent devastating Beirut explosion in Lebanon has caused tremendous economic losses and casualties (BBC News, 2020). Besides, most concrete structures designed to be seismic resistant may not be able to resist blast and impact loads due to different structural response modes and damage mechanisms under intrinsically different loading characteristics regarding amplitudes and frequency contents. The susceptibility of structures to the threads of multi-hazardous loading has become a widespread issue (Ngo et al., 2007), which has stimulated substantial interest in the research and engineering community to find a more effective mitigation strategy to protect essential civil engineering structures.

Metaconcrete consisting of engineered aggregates (EAs) is a state-of-the-art manmade construction material, which may provide a novel paradigm to protect civil engineering structures from hazardous

loadings by utilising its unique wave-filtering capacity (Jin et al., 2021; Jin et al., 2020; Xu et al., 2020; Xu et al., 2021a). This attractive feature of metaconcrete is owing to the local resonance of EAs activated at the prescribed frequency range. The conventional EA consisted of a solid core coated with a relatively soft layer enables the core to be able to vibrate at specific frequencies. This vibration behaviour triggers the tunable negative effective properties whilst impulsive loading energy can be trapped by the embedded EAs, resulting in stress wave attenuation (Mitchell et al., 2014, 2015; Mitchell et al., 2016). Despite its attractive properties, it was found that metaconcrete composed of conventional EAs (i.e., metallic core with soft coating) could suffer a significant reduction of compressive and spalling strengths as compared to normal concrete due to the mismatched modulus of elasticity and deformation capacity between mortar and soft coating as observed by both numerical (Jin et al., 2021) and experimental investigations (Xu et al., 2022b). This adverse effect may limit the applications of metaconcrete in construction. To overcome the shortcoming of using conventional EAs, a relatively stiff layer attached to the outside of conventional EAs has been proposed to enhance the strength of metaconcrete while keeping its wave-filtering capability.

In the present study, the plain mortar (PM) specimen without inclusion is prepared as a reference specimen. In addition, two types of EAs named RCSBs and ERCSBs, as shown in Figure 1, are used to fabricate metaconcrete specimens (Xu et al., 2022a). More specifically, the 20 mm-diameter silicone rubber-coated steel balls (RCSBs) made of 15.4 mm-diameter steel ball and coated with a 2.3 mm thick rubber layer are added into the mortar to fabricate the M-RCSB specimen. Besides, the 20 mm-diameter ERCSBs made of 18 mm-diameter rubber-coated steel balls and an additional 1mm thick steel layer are mixed with mortar to cast M-ERCSB specimen. Mechanical properties of PM, M-RCSB and M-ERCSB material are firstly evaluated through quasi-static compressive tests. Then, the wave filtering capacity of the specimens is examined by non-destructive impulsive loading tests, followed by destructive impulsive loading tests to investigate the impact mitigation properties. The failure process of specimens with different configurations is compared and discussed. The effectiveness of adding a steel shell outside RCSBs on the performance of metaconcrete material is demonstrated.

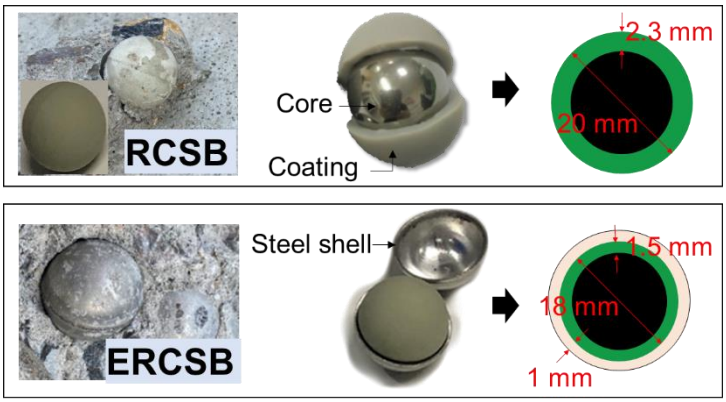

Figure 1. Illustration of EAs' configurations (Xu et al., 2022b).

2. SPECIMEN PREPARATION AND TEST SET-UP

A series of laboratory tests, including quasi-static material tests, non-destructive and destructive impulsive loading tests, are carried out and reported in the present study. All specimens are casted by using the moulding technique. High-strength mortar is used as the matrix of all specimens. Dry-mix Davco Lanko 701 duragrout produced by Sika Australia Pty Ltd is adopted to make the mortar matrix (Davco Australia, 2020). The mix ratio of cement/sand/water/additives for the mortar is 1/2/0.5/0.33. Besides, PM, M-RCSB and M-ERCSB cylindrical specimens with a dimension of $\emptyset 100 \times 200$ are casted, as shown in Figure 2(a). Moreover, the rod specimens with the geometrical size of 30×30×270 mm are prepared for the non-destructive impulsive loading tests, as shown in Figure 2(b). All the specimens are placed and cured in the ambient environment for 28 days by following ASTM C192/C192M-19 (2019). More detailed information on the specimens and casting method for the specimens can refer to Xu et al. (2022a, 2022b).

The quasi-static test on material compressive strength is firstly carried out by using a MATEST testing machine, as shown in Figure 3(a), in which three cylinders per configuration are tested following the standard (ASTM C39/C39M-21, 2021). To evaluate the longitudinal response of specimens under non-destructive impulsive loading, the rod specimen is placed between two bars (Bar I and Bar II) and hanged by two nylon threads as shown in Figure 3(b), where the purpose of using nylon thread is to align the specimen to the apparatus and minimise the unwanted wave dispersion. All the tests are conducted as consistently as possible by using the Split-Hopkinson pressure bar (SHPB) as a loading apparatus, in which the non-destructive impulsive load is generated by manually sliding the striker bar to impact bar I. It should be noted that the specific SHPB technique via analysing wave signals recorded on the incident and transmitter bars is not used in this study. Instead, two strain gauges (i.e., SG1 and SG2) are respectively attached at 30 mm and 230 mm from the incident surface of the rod specimen to measure stress waves. Furthermore, the hammer impact test by using Dytran® 5800B3 impulse hammer equipped with a soft tip (6250PS) is conducted to investigate the damping ratio and out-of-plane transverse response of the rods under non-destructive impulsive loading, as shown in Figure 3(b) (Xu et al., 2021b). One accelerometer (i.e., accelerometer #1 (a_1)) is adhered to underneath the impact location to record the input acceleration. Another accelerometer (i.e., accelerometer #2 (a_2)) is installed near the support to measure the output acceleration, and the data is recorded by using a universal data acquisition system with a sampling rate of 19.2 kHz.

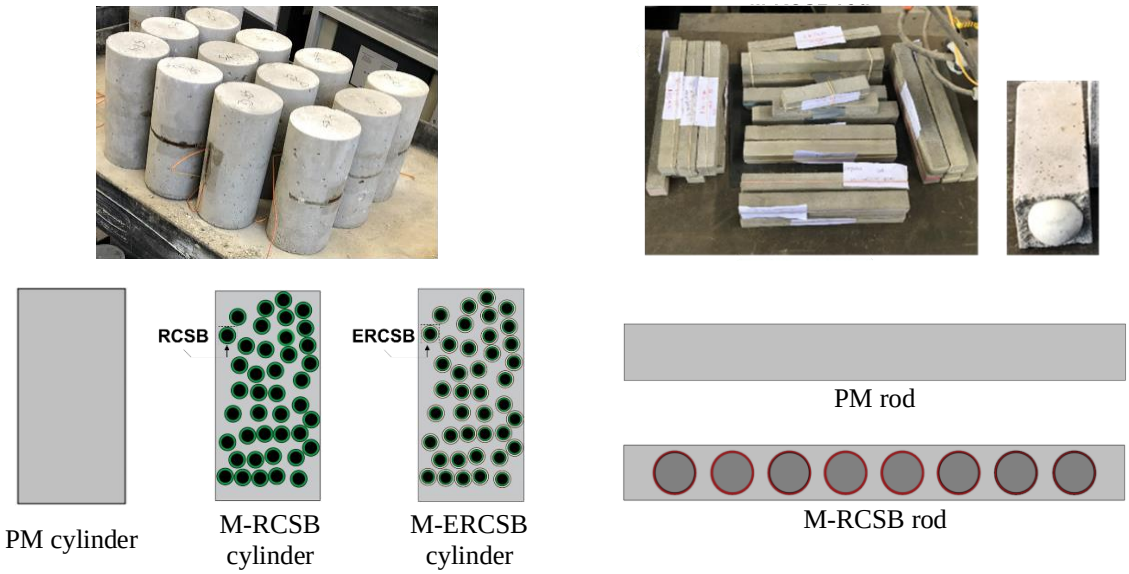

(a) Cylindrical specimens **(b) Rod specimens**

Figure 2. Illustration of specimens (Xu et al., 2022a).

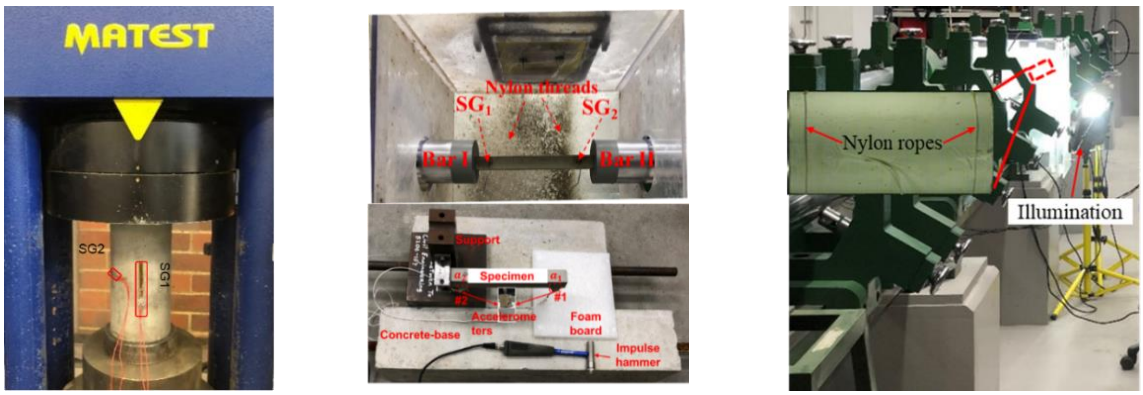

(a) Quasi-static material test **(b) Non-destructive test in the longitudinal (top) and transverse direction(bottom)** **(c) Destructive test**

Figure 3. Illustration of test set-up (Xu et al., 2021b).

The set-up for destructive impulsive tests is shown in Figure 3(c). SHPB is adopted as a loading apparatus. All cylindrical specimens are placed between two steel bars with a diameter of 100 mm to examine the effectiveness in mitigating stress wave propagation subjected to destructive impulsive loading. The striker bar is launched by a pressure vessel to generate destructive impulsive loads. Signals recorded by two strain gauges on the specimens (SG1 and SG2) are used to evaluate the effectiveness of mitigating stress wave propagation. A high-speed camera with a frame rate of 12500 frames per second (FPS) is employed to capture the failure process of all specimens under destructive tests. More detailed information on the test set-up can refer to Xu et al. (2022b).

3. QUASI-STATIC TEST RESULTS AND DISCUSSIONS

The static compressive properties of plain and metaconcrete material can be evaluated by conducting quasi-static compressive tests, which have been reported by Xu et al. (2022b). As reported, the average compressive strength of PM cylinder is 67.49 MPa. However, when using 10.6% volume percentage of RCSBs for M-RCSB cylinder, the compressive strength is greatly reduced to 29.98 MPa. Namely, the compressive strength of M-RCSB cylinder is 55.6% lower than PM specimen due to the following reasons: 1) the surrounding mortar is brittle while a soft coating with low stiffness of RCSBs is prone to deform, resulting in the damage of the mortar matrix; 2) the surrounding matrix is vulnerable to be damaged owing to the mismatch of the elastic modulus and deformation capacity between mortar and silicone rubber (Xu et al., 2021b). To improve the compressive strength of M-RCSB cylinder, a hard steel shell is added outside the RCSBs to form M-ERCSB cylinder, which reaches 54.97 MPa of compressive strength with an increase of 80.3% as compared to M-RCSB cylinder. The compressive strength of M-ERCSB cylinder is still lower than the PM cylinder, which is due to the insufficient bonding strength between the surrounding matrix and smooth steel shell surface, as observed in Xu et al. (2022b). Nevertheless, adding the steel shell to the conventional EAs significantly improves the compressive strength of metaconcrete specimens as compared to the one with conventional EAs. It is worth noting that further improvement on the bonding strength between the EAs and cementitious matrix through mechanical or chemical treatment, such as roughing EAs' surface or adding bonding additives outside the EAs can be made to further enhance bonding between EAs and matrix.

4. NON-DESTRUCTIVE TEST RESULTS AND DISCUSSIONS

4.1. Longitudinal impulsive loading test results

Figure 4(a) and (b) compare the strain time histories for PM and M-RCSB rods. To evaluate the effectiveness of metaconcrete rod in mitigating stress wave propagation along the longitudinal direction, the peak reduction ratio of the maximum longitudinal strain, i.e., the ratio of the maximum strain recorded by SG2 to the peak value of the strain measured by SG1, is used as the performance index (Xu et al., 2022a). As computed, the peak reduction ratio for PM rod is 0.09, and the peak reduction ratio for M-RCSB rod is 0.56, which indicates a peak reduction of 56% in the longitudinal strain for M-RCSB rod. Therefore, M-RCSB rod with embedded RCSBs is effective in mitigating stress waves as compared with PM rod within the elastic range.

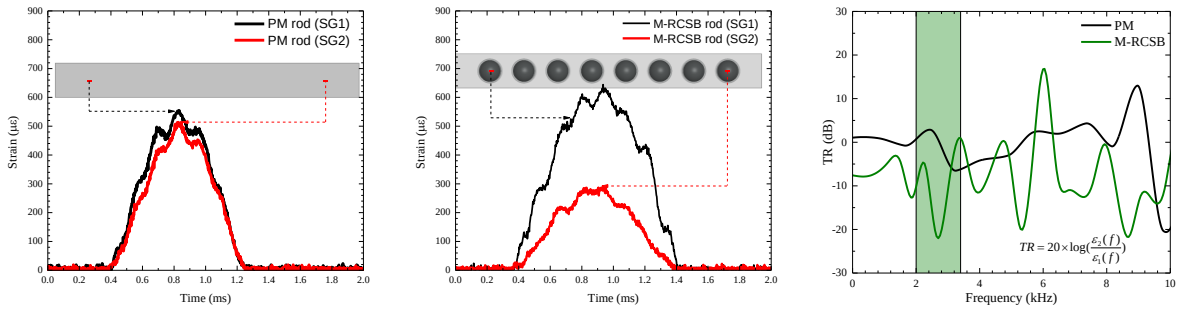

(a) Strain time histories of PM rod (b) Strain time histories of M-RCSB rod (c) TR spectra

Figure 4. Longitudinal dynamic responses of specimens (Xu et al., 2022a).

The stress wave attenuation phenomenon can be further explained by using the transmission ratio (TR) spectrum, which has been used in previous studies (Matlack et al., 2016; Xu et al., 2022a). TR spectrum can be computed as the ratio of output ($\varepsilon_2(f)$) to input ($\varepsilon_1(f)$) amplitudes in the frequency domain. The negative value of the shaded frequency band in the TR spectrum suggests the region of the bandgap or wave filtering zone. As plotted in Figure 4(c), it shows an obvious frequency dip with the minimum TR around -23 dB at the frequency band from 2 kHz to 3.4 kHz, i.e., shaded in green, indicating that the stress wave induced by impulsive loading within this bandgap is noticeably suppressed. Therefore, it can be concluded that adding RCSBs is effective in stress wave attenuation and filtering along the longitudinal direction owing to the local resonance mechanism.

4.2. Damping ratio and transverse impulsive loading test results

The equivalent damping ratio is evaluated by conducting a forced vibration test on the cantilevered rods with an instrumented impact hammer. The free vibration phase of the specimens under hammer impact is used to evaluate the equivalent damping ratio of the specimen, and the results have been reported in Xu et al. (2021b). As reported, the equivalent damping ratio for the M-RCSB rod is 2.683%, which is 98% higher than PM rod of 1.355%. Thus, the M-RCSB rod with conventional EA can dissipate vibrational energy more effectively than PM rod.

To demonstrate the effectiveness of M-RCSB rod in mitigating transverse loading induced stress wave propagation, the attenuation ratio R_a, which is the amplitude ratio of peak acceleration recorded by two accelerometers at locations #1 and #2 of the test specimens, is used. Figure 5(a) and (b) respectively show the acceleration time histories of PM and M-RCSB rods subjected to transverse impulsive loading. As shown, R_a of M-RCSB rod is calculated as 57% which is higher than 39% of PM rod. Thus, adding RCSBs inside M-RCSB rod can effectively mitigate the stress wave propagation induced by impulsive loading along the transverse direction (Xu et al., 2021b). The attenuation mechanism can be further explained by frequency domain analysis. In this work, the attenuation ratio (AR) spectrum, i.e., the ratio between the output ($a_2(f)$) and input ($a_1(f)$) acceleration amplitudes in the frequency domain, is adopted to show the effectiveness. As shown in Figure 5(c), an apparent dip of the AR curve only occurs in M-RCSB rod at the prescribed frequency range (i.e., shaded in green), indicating that the attenuation mechanism is attributed to the local resonance effect (Xu et al., 2021b).

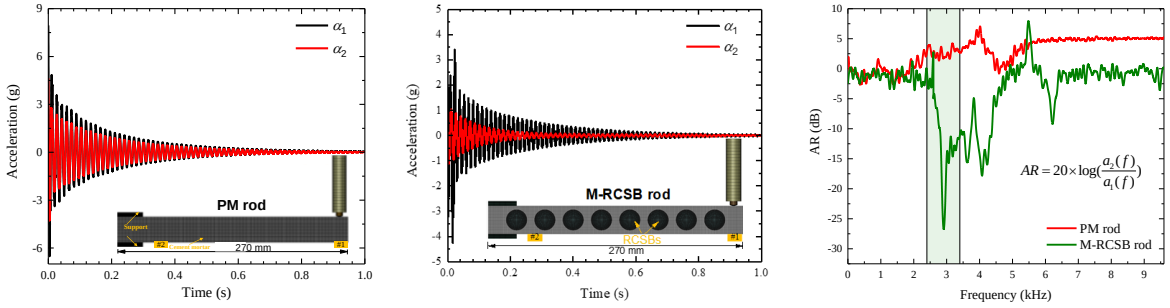

(a) Acceleration time histories of PM

(b) Acceleration time histories of M-RCSB

(c) AR spectra

Figure 5. Transverse dynamic responses of specimens (Xu et al., 2021b).

5. DESTRUCTIVE TEST RESULTS AND DISCUSSIONS

To examine the effectiveness of specimens in mitigating destructive impulsive loading, two types of impulses, i.e., impulse I and II, are generated with increasing intensity through changing air pressure in the pressure vessel, in which the loading profiles of two impulses are shown in Figure 6. Besides, the failure processes of the PM, M-RCSB and M-ERCSB cylinders under impulses I and II are presented in Figure 7. It is worth noting that the comparison between the impulsive behaviour of normal concrete with natural coarse aggregate and metaconcrete is not presented here as this study is aimed at examining the proposed design to overcome the shortcoming of using conventional EAs. More details on the comparison of normal and metaconcrete can be referred to Xu et al. (2022b). As observed in Figure 7(a1), PM cylinder experiences severe dynamic fracture (i.e., spalling) at the time instant of 16 ms and

it is broken into two parts under impulse I as a result of insufficient tensile strength. These failure modes of PM cylinder are consistent with the experimental results reported in the literature (Brara et al., 2001). Moreover, M-RCSB cylinder experiences columnar cracking (16 ms) through both ends (Figure 7(a2)), and severe localised damage is found (60 ms) due to stress concentration around the interfacial area around RCSBs. At 120 ms, the specimen remains intact without breaking into two parts as specimen PM owing to the stress wave attenuation caused by the activation of local resonance of RCSBs. However, it still experiences damage due to the low compressive strength and modulus of elasticity (Xu et al., 2022b), and the damage mode is consistent with the results reported in the literature (Jin et al., 2021; Kettenbeil and Ravichandran, 2018). In addition, M-ERCSB cylinder experiences localised damage and only several cracks appear near the loading end under impulse I, as illustrated in Figure 7(a3). Thus, M-ERCSB cylinder demonstrates better impulsive loading resistance as compared to M-RCSB as well as PM cylinders under impulse I.

When subjected to impulse II, PM cylinder initially experiences significant spalling damage (16 ms) as shown in Figure 7(b1) and then it is broken into smaller pieces (60 ms-120 ms). As shown in Figure 7(b2), M-RCSB cylinder exhibits unsatisfactory loading resistance, in which the specimen is crushed into numerous pieces at an earlier stage owing to its lower compressive strength. For M-ERCSB cylinder under impulse II, it experiences damage in the front (16 ms), propagating towards the end (60 ms). The obvious columnar cracks are observed but the overall specimen is still intact until 120 ms (Figure 7(b3)). Thus, M-ERCSB cylinder has higher loading resistance and better performance as compared to PM and M-RCSB cylinders under both impulse I and II. Nevertheless, M-ERCSB cylinder still experiences significant peel-off damage under impulse II because of the insufficient bonding as well as the wave impedance mismatch between the steel shell and cementitious matrix (Xu et al., 2022b). Hence, the enhanced coating material should be properly selected and treated to reduce interfacial failure for better performance.

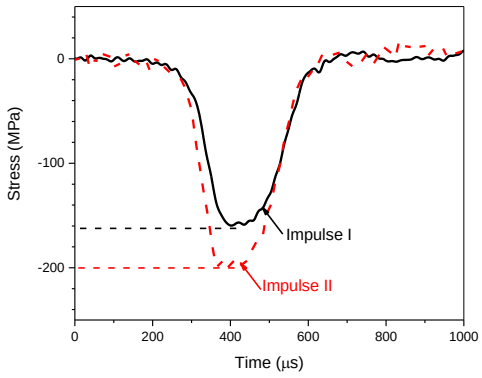

Figure 6. Loading profile of impulse I and II (Xu et al., 2022b).

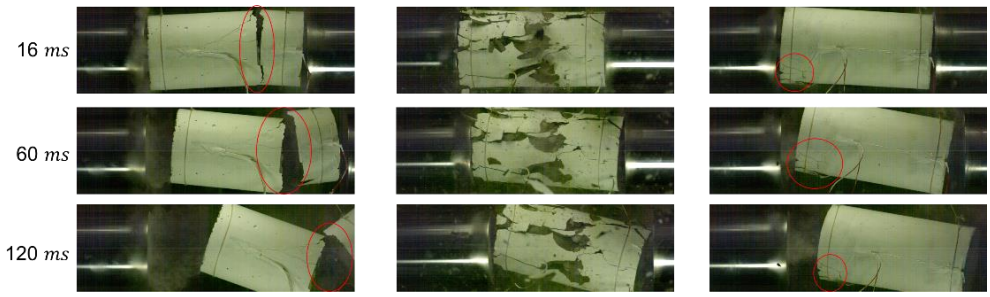

a1 **a2** **a3**

(a) Impulse I

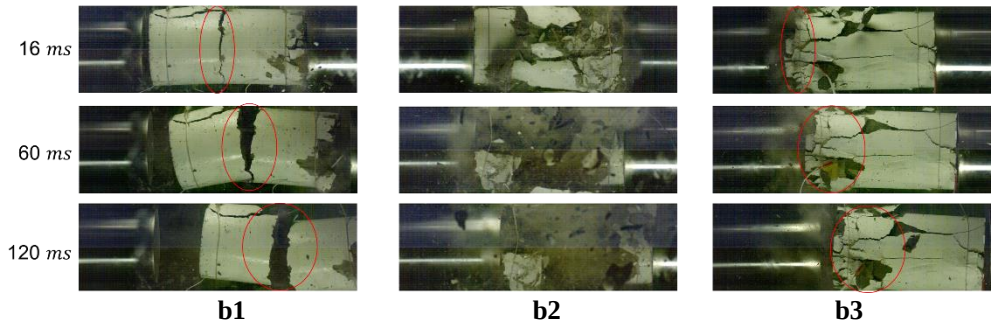

(b) Impulse II

Figure 7. Failure process of specimens subjected to impulse I and II (Xu et al., 2022b).

To further evaluate their effectiveness in mitigating stress wave propagation, the strain-time histories for cylindrical specimens under two loading scenarios are compared in Figure 8. It is worth mentioning that if a substantial reduction in the transmitted peak strain (i.e., SG2) is obtained, the stress wave propagating along the specimen is inhibited. No significant peak strain reduction signifies that there is no noticeable stress wave attenuation effect. As shown in Figure 8(a), PM cylinder exhibits no significant wave attenuation effect. On the contrary, Figure 8 (b) shows the noticeable peak strain reduction in M-RCSB cylinder, implying that the stress wave is attenuated after passing through the conventional RCSBs owing to the local resonance effect. Meanwhile, M-RCSB cylinder has the highest value of peak strain recorded by SG2 owing to its lowest modulus of elasticity or stiffness of the material, which has been discussed in Xu et al. (2022b). Meanwhile, because of the severe damage to the M-RCSB cylinder (see Figure 7(a)), the strain gauge near the loading end (i.e., SG1) fails at an early stage. Moreover, Figure 8(c) demonstrates a more pronounced reduction of peak strain in M-ERCSB cylinder, indicating that adding the steel shell outside RCSBs could provide a comparable or even better wave mitigation effect than the one with conventional RCSBs. Furthermore, M-ERCSB cylinder has smaller values of SG2 as compared to PM cylinder owing to its higher modulus of elasticity. In conclusion, using properly designed EAs (i.e., ERCSBs) for metaconcrete specimens can improve their compressive strength whilst maintaining their stress wave attenuation capacity.

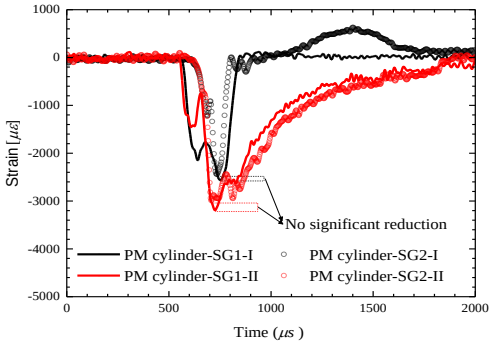

(a) PM cylinder

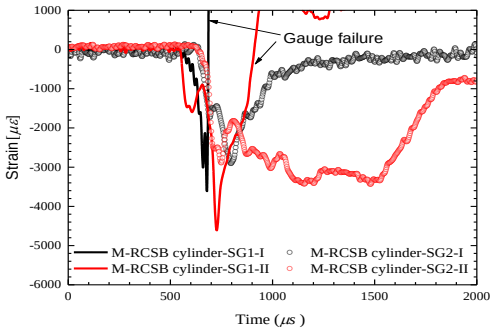

(b) M-RCSB cylinder

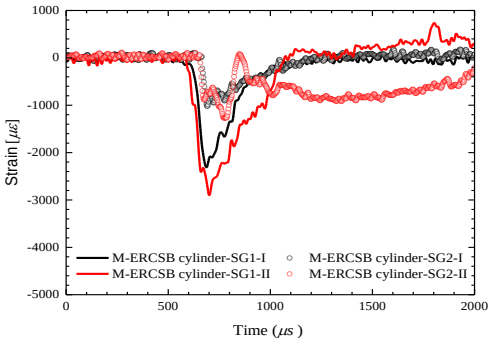

(c) M-ERCSB cylinder

Figure 8. Comparison of strain-time histories of specimens subjected to impulses I and II (Xu et al., 2022b).

6. CONCLUSIONS

In this paper, the static compressive strength of metaconcrete specimens with conventional (i.e., RCSBs) and enhanced (i.e., ERCSBs) EAs are reported. Their dynamic performances and effectiveness in stress wave mitigation are revealed, which can be used for the design of metaconcrete material and structures. The main findings are summarised as follows.

(1) The tests demonstrate that adding RCSBs into mortar could improve the stress wave mitigation performance in comparison with PM rod subjected to both non-destructive longitudinal and transverse impulsive loading.

(2) The equivalent damping ratio of metaconcrete rod with RCSBs can substantially increase up to 98% as compared with the PM rod in this study.

(3) Using RCSBs could cause a reduction in the compressive strength of metaconcrete material. This issue can be solved by adding a hard shell outside RCSBs to form ERCSBs, which shows the enhancement of the compressive strength of metaconcrete by 80.3%.

(4) The specimen with ERCSBs is more effective in mitigating stress wave propagation induced by destructive loading as compared to others. However, bonding properties between the matrix and ERCSBs should be further improved to enhance the properties of metaconcrete material.

REFERENCES

ASTM C39/C39M-21, (2021). Standard test method for compressive strength of cylindrical concrete specimens. ASTM International, West Conshohocken, PA.

ASTM C192/C192M-19, (2019). Standard practice for making and curing concrete test specimens in the laboratory. ASTM International, West Conshohocken, PA.

BBC News, (2020). What We Know About The Beirut Explosion, BBC News.

Brara, A., Camborde, F., Klepaczko, J.R., Mariotti, C., (2001). Experimental and numerical study of concrete at high strain rates in tension. Mechanics of Materials 33, 33-45.

Davco Australia, (2020). Davco lanko 701 duragrout data sheet.

Jin, H., Hao, H., Chen, W., Xu, C., (2021). Spall behaviors of metaconcrete: 3d meso-scale modelling. International Journal of Structural Stability and Dynamics, 2150121.

Jin, H., Hao, H., Hao, Y., Chen, W., (2020). Predicting the response of locally resonant concrete structure under blast load. Construction and Building Materials 252, 118920.

Kettenbeil, C., Ravichandran, G., (2018). Experimental investigation of the dynamic behavior of metaconcrete. International Journal of Impact Engineering 111, 199-207.

Matlack, K.H., Bauhofer, A., Krödel, S., Palermo, A., Daraio, C., (2016). Composite 3D-printed metastructures for low-frequency and broadband vibration absorption. Proceedings of the National Academy of Sciences 113, 8386-8390.

Mitchell, S.J., Pandolfi, A., Ortiz, M., (2014). Metaconcrete: designed aggregates to enhance dynamic performance. Journal of the Mechanics and Physics of Solids 65, 69-81.

Mitchell, S.J., Pandolfi, A., Ortiz, M., (2015). Investigation of elastic wave transmission in a metaconcrete slab. Mechanics of Materials 91, 295-303.

Mitchell, S.J., Pandolfi, A., Ortiz, M., (2016). Effect of brittle fracture in a metaconcrete slab under shock loading. Journal of Engineering Mechanics 142, 04016010.

Ngo, T., Mendis, P., Gupta, A., Ramsay, J., (2007). Blast loading and blast effects on structures - An overview.

Xu, C., Chen, W., Hao, H., (2020). The influence of design parameters of engineered aggregate in metaconcrete on bandgap region. Journal of the Mechanics and Physics of Solids, 103929.

Xu, C., Chen, W., Hao, H., Bi, K., Pham, T.M., (2022a). Experimental and numerical assessment of stress wave attenuation of metaconcrete rods subjected to impulsive loads. International Journal of Impact Engineering 159, 104052.

Xu, C., Chen, W., Hao, H., Jin, H., (2021a). Effect of engineered aggregate configuration and design on stress wave attenuation of metaconcrete rod structure. International Journal of Solids and Structures 232, 111182.

Xu, C., Chen, W., Hao, H., Pham, T.M., Bi, K., (2021b). Damping properties and dynamic responses of metaconcrete beam structures subjected to transverse loading. Construction and Building Materials 311, 125273.

Xu, C., Chen, W., Hao, H., Pham, T.M., Bi, K., (2022b). Static mechanical properties and stress wave attenuation of metaconcrete subjected to impulsive loading. Engineering Structures 263, 114382.

Proc. 3rd International Conference on Structural Engineering Research (iCSER 2022)
20-22 Nov 2022, Sydney, Australia
ISBN: 978-0-6456692-1-3

Seismic Performance of RC Shear Wall with New Replaceable Corner Components

Haozuo Wang[1, 2] and Huanjun Jiang[1, 2]

[1]State Key Laboratory of Disaster Reduction in Civil Engineering, Tongji University, Shanghai 200092, China
[2]Department of Disaster Mitigation for Structures, Tongji University, Shanghai 200092, China

Corresponding author's E-mail: jhj73@tongji.edu.cn

Abstract

When subjected to strong earthquakes, conventional reinforced concrete (RC) shear walls may suffer severe damage, which is generally difficult to recover or even impossible to repair. In this study, a new type of replaceable corner component with self-centering capability installed at the base of RC shear walls is proposed. The new replaceable corner component not only protects the main structure from damage but also provides the restoring force for the wall to return initial position after yielding of the component. The new replaceable corner component consists of the self-centering part and energy-dissipation part. The details and the loading mechanism of the new component are introduced. To verify the seismic performance of RC shear walls with the new replaceable corner components, the numerical model of the new shear wall is developed and validated by previous experimental results. The effect of stiffness and preload of disc spring group in the new components of the shear wall are analyzed. The results show that the shear wall with the new replaceable corner components has good seismic performance and the characteristics of low residual deformation and low damage. The function of the shear wall structure can be quickly restored by replacing the replaceable components after the earthquake.

Keywords: RC wall, replaceable corner component, seismic performance, self-centering

1. INTRODUCTION

Conventional RC shear walls have been widely used as main lateral force-resistance members in tall buildings because of their high lateral stiffness and strength. However, it has been found that RC walls suffered from severe damage in plastic hinge regions of the wall base when subjected to moderate or strong earthquakes. The structural damage is generally difficult to recover or even impossible to repair, resulting in poor seismic performance, interruption of building function, and adverse socioeconomic influence.

To improve the seismic performance of building structures and fulfill quick recovery of building function after earthquakes, replaceable shear walls have been proposed in earthquake engineering (Fortney et al. 2007; Jiang et al. 2022). Lu et al. (2013) first proposed the installation of replaceable components at the two bottom corners of the RC wall to prevent the bottom corners of the wall from damage, and the replaceable combined rubber bearing was adopted as replaceable corner components. Liu et al. (2017) developed a new kind of replaceable corner component whose stiffness and energy-dissipation capacity were improved. Wang et al. (2019) arranged replaceable tension-and-compression damper at the bottom of structural walls. For most of the replaceable corner components, the construction details, such as the shim and connector with slotted hole, were designed to accommodate a certain amount of residual deformation of shear walls. Despite the misalignment can be tolerated within a certain rage, the lager residual deformation occurs in the shear wall due to the plastic deformation of replaceable corner components under strong earthquakes, resulting in difficulties in

replacing the components and restoring the structural function.

In this study, a new type of replaceable corner component with self-centering capability is proposed. The new replaceable corner component combines the two mechanisms of replaceable and self-centering capability, which not only protect the main structure from damage but also provide the restoring force for structural wall to return initial position after yielding of the components. The numerical model of RC shear wall with the new replaceable corner components is established, the seismic performance of the new shear walls is analyzed. The effect of stiffness and preload of disc springs in components on the shear walls is studied.

2. THE NEW TYPE OF REPLACEABLE CORNER COMPONENT

The configuration of the proposed replaceable corner component is shown in Fig. 1(a), which consists of the self-centering part and energy-dissipation part. The self-centering part is of piston-type damper structure hinged with connection plates. The disc spring group, combined by disc springs in parallel and in series, is arranged in the external tube along the internal rod. The nuts set at the end of the internal rod are used to apply preload into the disc spring group for improving the self-centering ability. For the energy-dissipation part, it is comprised of the dog-bone-shape mild steel bar and the steel tube filled with high-performance grouting material. The infill grouting material prevents the mild steel bar from buckling, and the polytetrafluoroethylene layer is added between them to relieve the bonding. The bottom of stopper plate, welded with the mild bar, is in contact with the top of the upper grouting material and there is no connection between them, allowing for free separation. The work mechanism of the replaceable corner component is illustrated in Fig. 1(b) and (c). When the component is subjected to the tension, the disc spring group of the self-centering part is compressed and the mild bar of the energy-dissipation part is stretched, while the grouting material does not come into play. Correspondingly, all of the disc spring group, the mild steel bar and the grouting material are compressed together when the component is subjected to compression. Fig. 1(d) shows the theoretical hysteretic response of the proposed replaceable corner component.

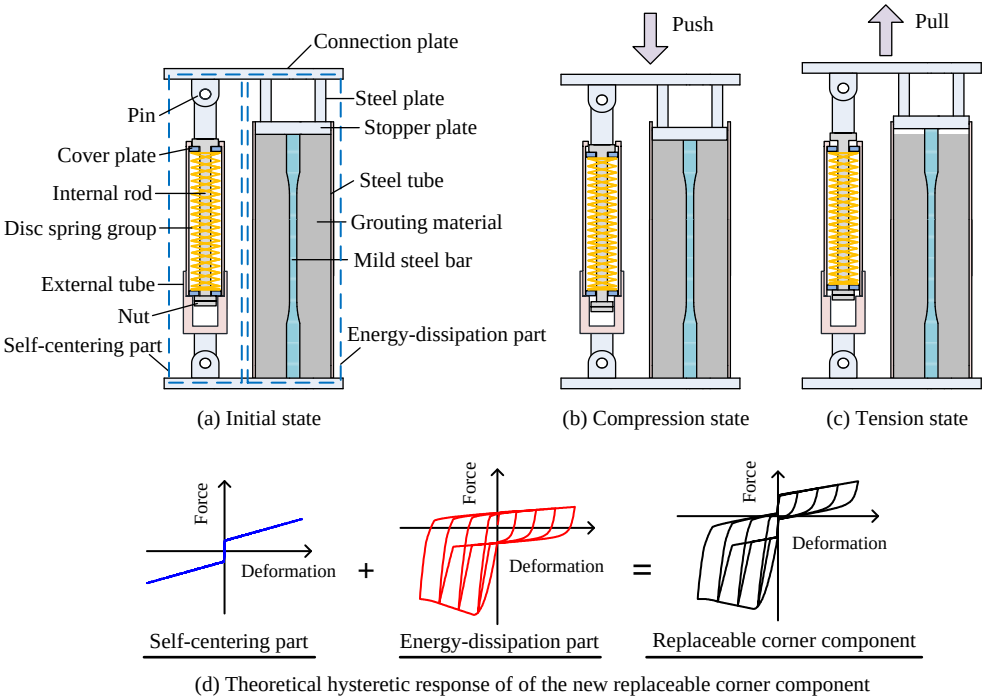

Figure 1. Details and mechanical behavior of the new replaceable corner component

3. NUMERICAL MODELLING

The modeling and nonlinear analyses in this study are conducted using the finite element program

OpenSees. Fig. 2(a) illustrates the numerical model of RC wall with new replaceable corner components. The ShellNLDKGQ element, which is a quadrilateral multi-layer shell element, is used to model RC wall panel. The longitudinal reinforcements of the boundary zones are modeled by the truss elements that are incorporated into the shell element by sharing the same nodes, while the vertical steel reinforcements within the wall web and all the stirrups are smeared into one or more layers into the shell element. For the new replaceable component, the self-centering part and energy-dissipation part are simulated by the truss element and the displacement-based beam-column fiber element, respectively, and the end nodes of the two elements are connected via the command RigidLink. The elastic beam-column elements are used to model the rigid loading beam.

The PlateFromPlaneStress material constitutive model developed by Lu et al. (2015) is used to simulate concrete materials. The steel materials are simulated by the Steel02 material. The Concrete02 material are used to model the hysteretic behavior of grouting material. The force-displacement relationship of disc spring group is simulated by the ElasticMultiLinear material.

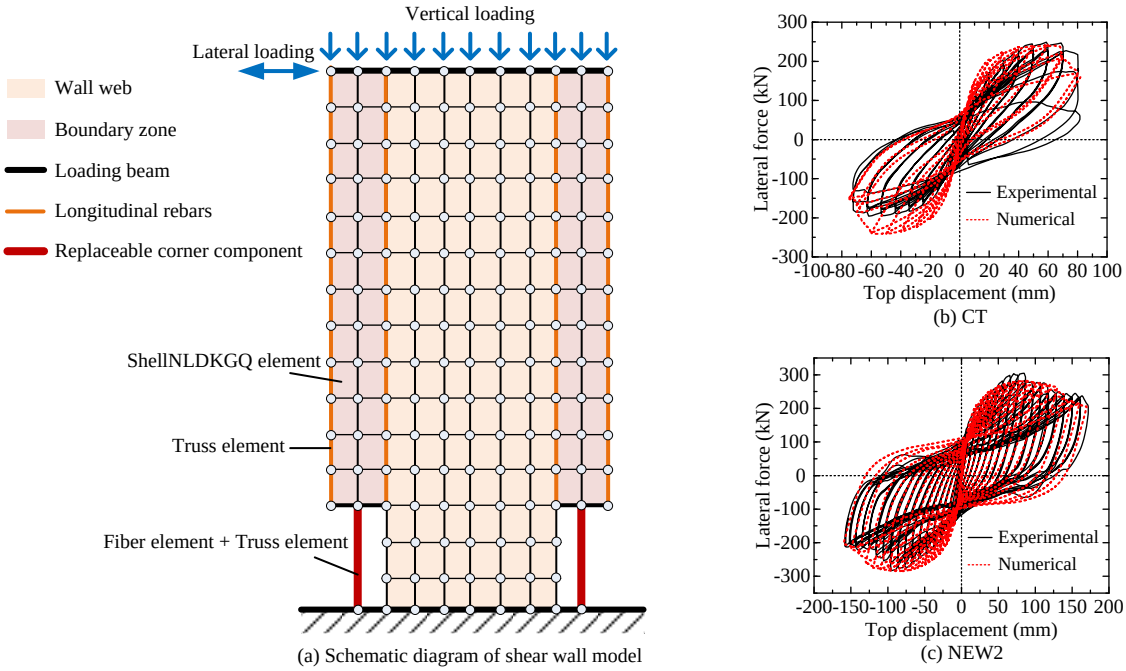

(a) Schematic diagram of shear wall model

Figure 2. Numerical model and verification

The effectiveness of the numerical model is validated by comparing it with the experiment results of specimens CT and NEW2 described by Liu et al. (2017). The specimen CT was a representative conventional RC wall, whose height was 3600mm and cross-section was 1200 mm × 140 mm. The reinforcement details and material properties can be found in the literature. The specimen NEW2, which was designed as the RC wall with replaceable components, had similar construction and building material to specimen CT. The replaceable corner components of NEW2 were without self-centering part, so the fiber elements are used to simulate them. In addition, the ShellNLDKGQ element with J2 plasticity material is used to simulate the embedded steel plate at the bottom of NEW2. Fig. 2(b) and (c) compares the hysteretic curves of CT and NEW2 generated from the numerical model results and the experimental results, which are generally consistent. The mean absolute errors of peak load between the simulated and test result (the absolute difference divided by the test result) are 7.45% and 0.53% for CT and NEW2, respectively; the mean absolute errors of initial elastic stiffness are 2.25% and 0.40% for CT and NEW2, respectively. The validated numerical model is used to evaluate the seismic performance of the new shear walls.

4. NUMERICAL SIMULATION RESULTS AND DISCUSSIONS

A total of eight numerical models are designed, including one control model RCC, represented RC

wall with previous replaceable components, and seven new shear wall models with the new replaceable components. The model RCC has geometric, material properties and reinforcement details similar to those of the specimen NEW2 except that there is no steel plate. The stiffness, K_{ds}, and preload, P_{ds}, of disc spring group are varied among different new shear walls, and Table 1 shows the details of the design parameters. It should be noted that the design bearing capacity, under compression and tension, of all replaceable corner components is consistent. Therefore, the area of mild steel bar, A_{ms}, varies with the stiffness and preload in the new replaceable component, while the area of grouting material remains unchanged.

Table 1. Design parameters and analysis results of shear wall models

Specimen	A_{ms} (mm^2)	K_{ds} (kN/mm)	P_{ds} (kN)	F_y (kN)	Δ_y (mm)	F_m (kN)	Δ_u (mm)	DI	E_{total} (kN·m)
RCC	1017.36	—	—	201.05 (-191.92)	31.0 (-27.3)	227.85 (-215.12)	141.1 (-140.0)	4.55 (5.13)	287.7
DISC1	863.50	2	0	195.89 (-187.65)	32.7 (-29.1)	224.02 (-215.20)	134.3 (-138.8)	4.10 (4.77)	256.5
DISC2	637.42	5	0	184.93 (-175.12)	34.7 (-30.6)	212.12 (-210.20)	145.8 (-140.1)	4.20 (4.59)	209.4
DISC3	357.18	8	0	191.92 (-186.28)	43.4 (-41.3)	215.30 (-214.94)	136.2 (-130.2)	3.14 (3.15)	163.2
DISC4	486.70	5	20	194.58 (-183.31)	38.4 (-33.7)	221.19 (-212.89)	136.5 (-140.1)	3.55 (4.15)	185.1
DISC5	401.92	5	40	194.06 (-184.35)	39.0 (-34.8)	220.16 (-208.31)	135.2 (-139.8)	3.46 (4.01)	167.5
DISC6	502.90	2	70	200.29 (-190.76)	36.6 (-33.0)	226.99 (-215.05)	134.5 (-136.3)	3.67 (4.14)	185.9
DISC7	310.86	8	10	190.29 (-196.86)	42.6 (-40.1)	213.58 (-217.48)	146.3 (-137.8)	3.43 (3.44)	149.9

Note: the values in brackets represent the data of the models under negative loading.

The hysteretic responses of all shear walls are shown in Fig. 3. It is observed that the hysteretic behaviors of the new shear walls are similar to that of RCC, exhibiting stable energy dissipation and the lateral bearing capacity do not suddenly decrease. With the increase of the stiffness and preload of disc spring group in the new components, the curves have a significant pinch phenomenon, indicating the new replaceable components can effectively reduce the residual deformation of the shear walls. Compared with RCC, the hysteresis loop area of all new shear walls is smaller, which is due to the smaller area of the mild steel bar in component. The total energy consumption, E_{total}, defined as the total area of hysteresis curve loop, is used to characterize the energy-dissipation capacity of shear wall, as shown in Table 1. The energy-dissipation capacity of the RC wall with replaceable components is related to the area of the mild steel bar in components.

The initial elastic stiffness of all shear walls is basically the same, meaning that the new replaceable corner components will not significantly change the lateral stiffness of shear walls. However, the bearing capacity of each shear wall is different. Taking the maximum bearing capacity as an example, the peak load, F_m, of specimen decreases with the increase of stiffness of the disc spring group while decreases slightly with increasing preload.

The deformation capacity of shear wall is expressed by displacement ductility index, DI, the figure of dividing ultimate displacement, Δ_u, by yield displacement, Δ_y. The yield displacement based on the equivalent elastoplastic method is suggested by Park (1989), and the ultimate displacement is defined as the displacement corresponding to 15% of degradation with respect to the peak load. In general, the values of DI of shear walls decrease with increasing stiffness and preload, as listed in Table 1. Although the installation of new replaceable components will weaken the deformation capacity of RC wall to a certain extent, the DI values of each wall are greater than 3, indicating that the RC walls with new replaceable components still have good deformation capacity.

Fig. 4 compares the residual deformations of CT, RCC, and the new shear walls. It shows that after loading step of 45 mm, all the RC walls with new replaceable corner components performed as expected with much less residual deformation on unloading when compared to CT. As shown in Fig. 4(a) and (b), the residual deformation of the new shear walls shows a decreasing trend with the increase of the stiffness and preload of disc spring group. It is due to the restoring force provided by disc spring group and reduction of the area of mild steel bar. Compared with three different combinations of stiffness and preload in Fig. 4(c), the maximum residual drifts of all new shear walls before loading step of 135 mm are less than 0.5%, which means the replacement of replaceable corner components can be implemented conveniently after earthquakes. In addition, the new component with low stiffness and high preload can provide higher energy-dissipation capacity for the shear wall than that with high stiffness and low preload. Therefore, it is recommended to adopt the new replaceable corner component with low stiffness and high preload in practical engineering.

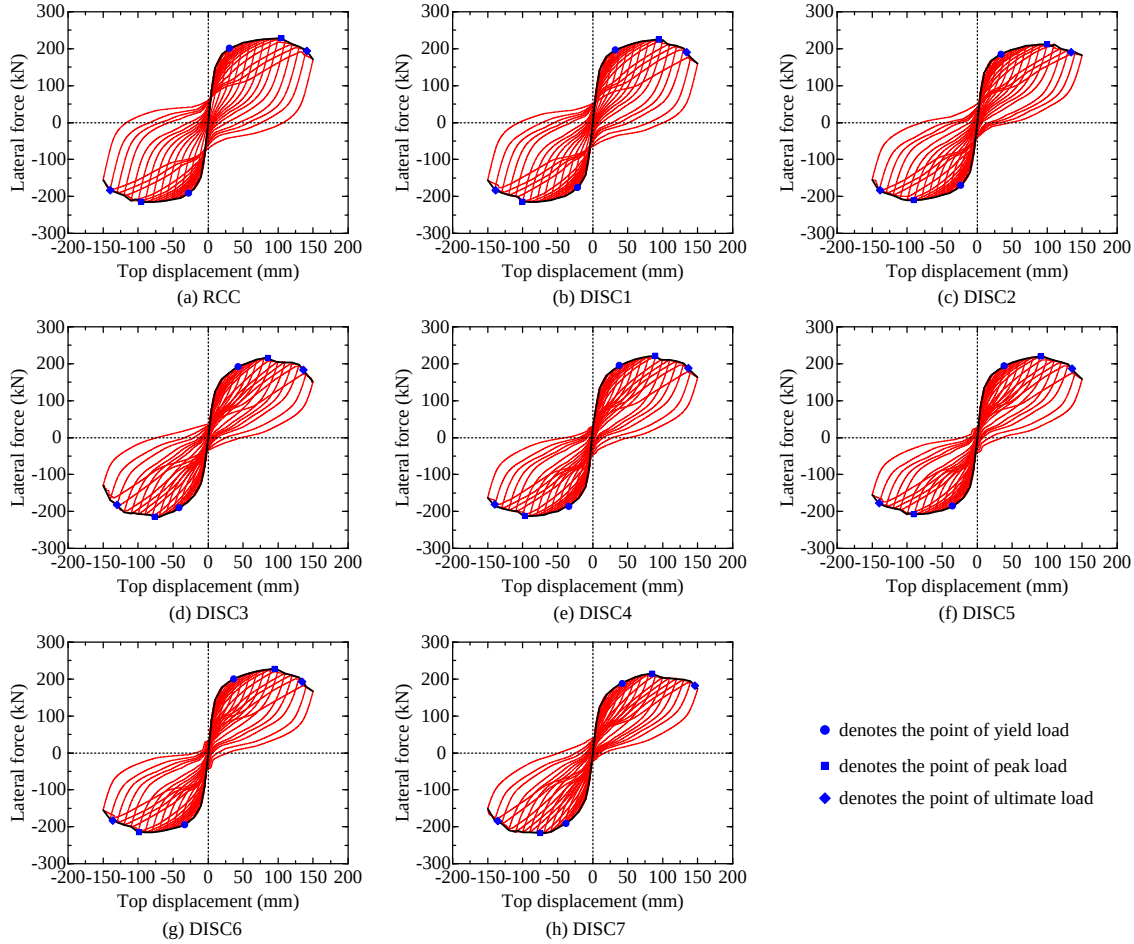

Figure 3. Hysteretic responses of the shear walls with replaceable corner components

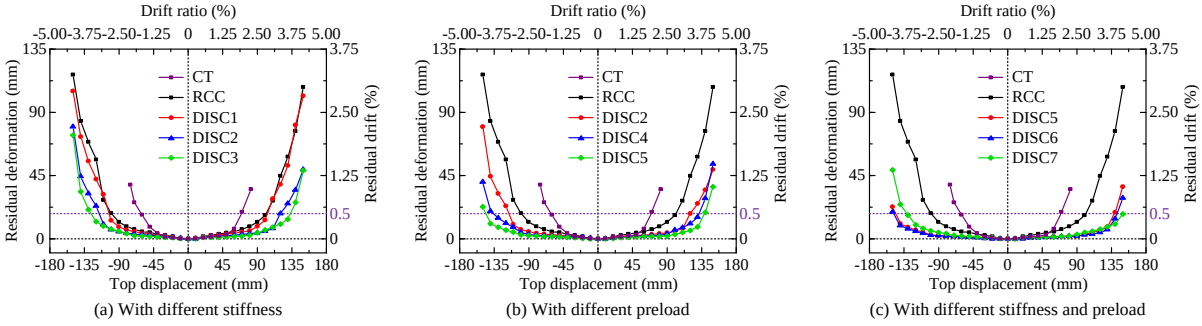

Figure 4. Residual deformation of the shear walls

The longitudinal reinforcements and concrete wall panel of DISC5 in where are vulnerable to damage under earthquakes are selected to represent the structural damage of the non-replaceable parts of the new shear walls, as shown in Fig. 5. Compared with conventional RC wall (CT), the strain of longitudinal reinforcements in DISC5 is lower than yield strain during the loading process, while the stress of concrete at the bottom of wall panel reached the maximum compressive stress at loading step of 135 mm. It means the damage mainly concentrates on the new replaceable corner components and the rest part is well protected, the new shear wall has the characteristics of low damage.

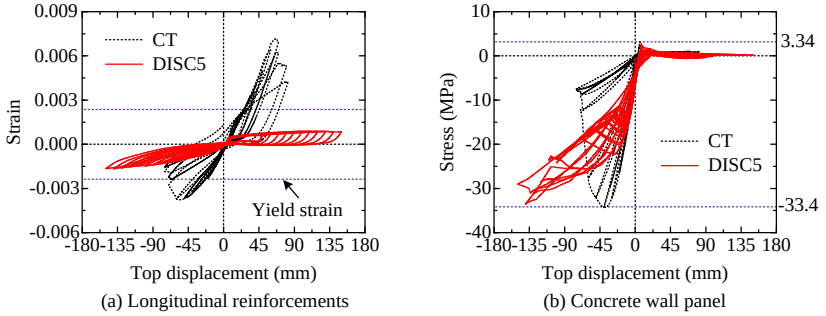

Figure 5. Structural damage of the shear walls

5. CONCLUSIONS

A new type of replaceable corner component is proposed in this study. Numerical analysis on the seismic performance of RC walls with new components is carried out. Based on the numerical simulation results, the following conclusions can be drawn:

(1) The RC walls with new replaceable corner components have sufficient bearing capacity, lateral stiffness, and good ductility and energy-dissipation capacity.

(2) Increasing the stiffness and preload of the disc spring group results in acceptable reduction in the bearing capacity, ductility and energy-dissipation capacity of the shear walls, but can effectively reduce the residual deformation of the walls.

(3) The non-replaceable parts of the new shear walls are well protected. The function of structural walls after the earthquake can be restored through convenient replacement of replaceable corner components.

ACKNOWLEDGMENTS

The authors gratefully acknowledge the support from National Natural Science Foundation of China under Grant No. U2239253.

REFERENCES

Fortney, P. J., Shahrooz, B. M., & Rassati, G. A. (2007). Large-scale testing of a replaceable “fuse” steel coupling beam. *Journal of Structural Engineering*, *133*(12), 1801-1807.

Jiang, H., Li, S., Bolander, J. E., & Kunnath, S. K. (2022). Seismic Performance of a New Type of Coupled Shear Wall with Replaceable Components: Experimental Validation. *Journal of Earthquake Engineering*, 1-23.

Lu, X., Mao, Y., Chen, Y., Liu, J., & Zhou, Y. (2013). New structural system for earthquake resilient design. *Journal of Earthquake and Tsunami*, *7*(03), 1350013.

Liu, Q., & Jiang, H. (2017). Experimental study on a new type of earthquake resilient shear wall. *Earthquake Engineering & Structural Dynamics*, *46*(14), 2479-2497.

Wang, W., Song, J., Hou, M., Liu, G., & Wang, W. (2019). Experimental study and numerical simulation of replaceable corrugated steel plate-concrete composite shear walls. *Soil Dynamics and Earthquake Engineering*, *127*, 105827.

Lu, X., Xie, L., Guan, H., Huang, Y., & Lu, X. (2015). A shear wall element for nonlinear seismic analysis of super-tall buildings using OpenSees. *Finite Elements in Analysis and Design*, *98*, 14-25.

Park, R. (1989). Evaluation of ductility of structures and structural assemblages from laboratory testing. *Bulletin of the New Zealand Society for Earthquake Engineering*, *22*(3), 155-166.

Proc. 3rd International Conference on Structural Engineering Research (iCSER 2022)
20-27 Nov 2022, Sydney, Australia
ISBN: 978-0-6456692-1-3

Numerical Modelling Of 3D Dry-Stack Tyre Wall By Combined Finite And Discrete Element Method (FDEM)

Yachong Xu[1], Yan Zhuge[2, *], Md. Rajibul Karim[3], Reza Hassanli[4], Martin Freney[5], Md. Mizanur Rahman[6]

[1] *PhD candidate, University of South Australia, UniSA STEM, Mawson Lakes, Australia*
[2] *Professor, University of South Australia, UniSA STEM, Mawson Lakes, Australia*
[3] *Senior lecturer, University of South Australia, UniSA STEM, Mawson Lakes, Australia*
[4] *Lecturer, University of South Australia, UniSA STEM, Mawson Lakes, Australia*
[5] *Lecturer, University of South Australia, UniSA Creative, Adelaide, Australia*
[6] *Professor, University of South Australia, UniSA STEM, Mawson Lakes, Australia*

**Corresponding author's email:* yan.zhuge@unisa.edu.au.

Abstract

This study aims to develop a numerical approach to investigate the structural performance of tyre walls by using commercial software Abaqus. Tyre walls are similar to dry-stack masonry walls but are constructed of tyre-encased compacted soil units. Previous investigations and empirical evidence showed that tyre walls have excellent architectural performance and can provide numerous environmental and economic benefits, including but not limited to effectively recycling waste tyres. Published experimental work showed tyre walls performed well under combined compressive and out-of-plane loads. This paper presents the detailed procedures for generating a numerical model of the tyre wall using the combined finite and discrete element method (FDEM). The numerical model was verified by comparing the results with those obtained from the laboratory testing, i.e., the failure mode and force-displacement relationships. The structural responses of the tyre wall subjected to quasi-static loading were accurately captured. The methodology discussed in this paper can be referred by researchers and built environment professionals to design and analyse the structural performance of tyre walls and similar masonry structures.

Keywords: Earthship, tyre wall, masonry structure, finite element analysis, discrete element model

1 INTRODUCTION

More than 50 million end-of-life (EOL) equivalent passenger car tyre units are generated yearly in Australia (Gilson, 2017). More than half of these tyres are stockpiled or illegally dumped. The number of EOL tyres is estimated at 1.5 billion on a global scale (Bianco, Panepinto, & Zanetti, 2021). Tyres are non-biodegradable and resistant to compaction. Applying EOL tyres as construction materials in civil engineering has great potential to address the associated problems with tyre disposal and storage.

Tyres encased with compacted soil can form segmental tyre-encased-soil elements (TESEs) with considerable load-bearing capacity. The TESEs can be laid in a staggered manner to build masonry-like load-bearing tyre walls (Reynolds, 1990). The tyre walls proved successful in architectural performance (Freney, Soebarto, & Williamson, 2013; Grindley & Hutchinson, 1996; Kruis & Heun, 2007; Reynolds, 2000). However, insufficient understanding of the structural performance restricts the further application of tyre walls. The experimental work (Xu et al., 2022) carried out by the authors examined the structural response of a full-scale tyre wall subject to combined compressive and out-of-plane loads. The results revealed the tyre wall had a linear axial compressive force-displacement response and a nonlinear out-of-plane flexural force-displacement behaviour. The flexural failure of the tyre wall was governed by a shear sliding and rotational gap opening at the wall's mid-height. It was concluded that tyre walls could function well as load-bearing walls of low-rise buildings.

This paper attempted to develop a 3-dimensional numerical model using a combined finite-discrete element method (FDEM) to replicate the tyre wall structural responses observed in the laboratory experiments. After verification, the numerical model can be used as a base model for future computational investigations on the structural performance of tyre walls.

2 MODELLING STRATEGY

A 3-dimensional numerical tyre wall model was generated using commercial software Abaqus/Explicit. A combined finite-discrete element method (FDEM), initially developed for studying fracturing problems considering deformable blocks that may split and separate during the analysis (A Munjiza & John, 2002; Ante Munjiza et al., 2020; Smoljanović, Živaljić, Nikolić, & Munjiza, 2018), has been adopted to simulate the arbitrary displacement and rotation of TESEs. The detailed modelling methodology is discussed as follows.

2.1 Tyre wall geometry and element discretisation

The numerical tyre wall model was constructed of two forms of TESEs (i.e., TESE1 and TESE2, as shown in Figure 1) to replicate the real construction patterns and the dimensions of the laboratory-tested tyre wall (i.e., a length of 2855 mm, a height of 1858 mm and a thickness of 570.7 mm). The TESEs were discretised with 3D solid elements with reduced integration, i.e., C3D8R & C3D6R. The C3D8R elements are eight-node linear brick elements with three translational degrees of freedom per node and reduced integration. The C3D6R elements are six-node linear triangular prisms with three translational degrees of freedom per node and reduced integration. These elements are capable of linear analysis and complex nonlinear analyses involving contact, plasticity, and large deformations. Hourglass control with enhanced algorism and distortion control was used for both types of elements to overcome the excessive distortion of the elements during analysis.

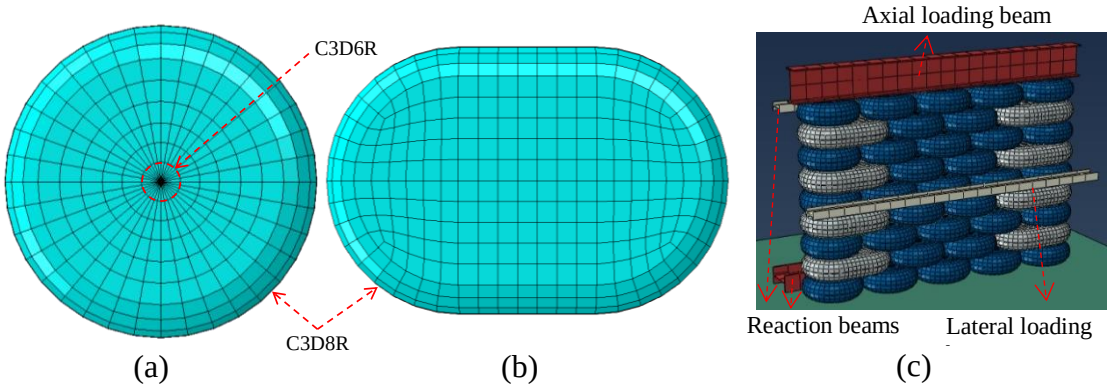

Figure 1 Tyre wall's numerical model: (a) TESE1; (b) TESE2; (c) Tyre wall.

2.2 Boundary condition and contact properties

The loading beams, reaction beams and the strong floor interact with the tested tyre wall, establishing complicated boundary conditions. The numerical model also generated these test setup components to best replicate the tyre wall's boundary condition. The interaction among the TESEs and the test setup components was prescribed with "hard" behaviour in the normal direction and isotropic Coulomb frictional behaviour (frictional coefficient of 0.75) in the tangential direction. The "hard" contact behaviour allows minimal penetration between the geometry surfaces and edges to generate contact pressure to be transmitted between the geometry surfaces when they are in contact. The contact pressure reduces to zero when the contact surfaces are separate.

2.3 Material properties and load definition

The TESEs are modelled with homogenised elastic material properties (i.e., the elastic modulus of 12 MPa and Poisson's ratio of 0.15). The density of the TESEs was defined as 1750 kg/ m^3. The strong floor and loading beams were modelled as rigid bodies whose constituent elements do not deform during analysis. The loading beams were modelled with a density of 7792 kg/m^3.

A gravity acceleration was assigned to the entire model and increased linearly from 0 to 9.81 m/s^2 in 5 seconds, then kept at 9.81 m/s^2 till the end of the analysis. As soon as the gravity load reached 9.81 m/s^2, an axial load was linearly increased from 0 to 10 kN in 10 seconds at the centre of the axial loading beam and was kept at 10 kN till the end of the analysis. The lateral load was applied at the lateral loading beam as a linearly increasing displacement from 0 to 128 mm in 49 seconds.

3 NUMERICAL MODEL VERIFICATION

The model verification was done by comparing the modelling results with the experimental results in terms of failure mode, gravity load and force-displacement relationships.

3.1 Failure mode

Figure 2 compares the tyre wall's failure mode obtained from the laboratory test and numerical model. The numerical model simulated the bending behaviour of the tyre wall subject to out-of-plane flexural load, and the rotational gap opening failure at the wall's mid-height was replicated. The tyre wall performance from the numerical modelling agreed well with the visual observations in the laboratory experiment.

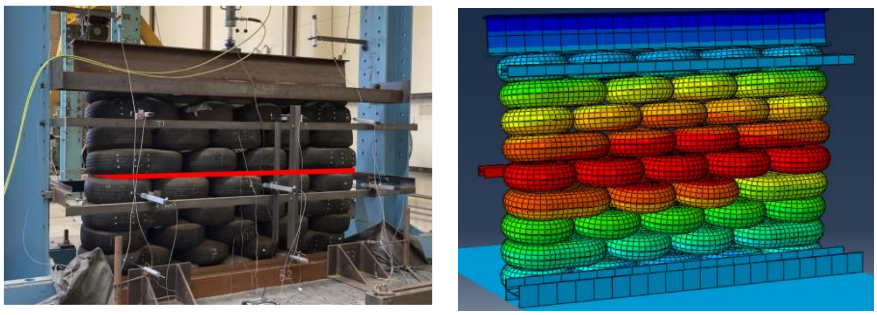

(a) (b)

Figure 2 Comparison of the tyre wall failure: (a) experiment; (b) numerical model (out-of-plane deformation).

3.2 Gravity load

The weight of the tyre wall and the axial loading beam in the numerical model was around 37.18 kN, close to the laboratory measurements (37.2 kN).

3.3 Axial force-displacement relationship

Figure 3 compares the axial force-displacement results from the laboratory test and the numerical modelling. The overall trend agreed well, and the discrepancy of the axial force was less than 10%, which should be acceptable due to the simplification of the TESE material properties.

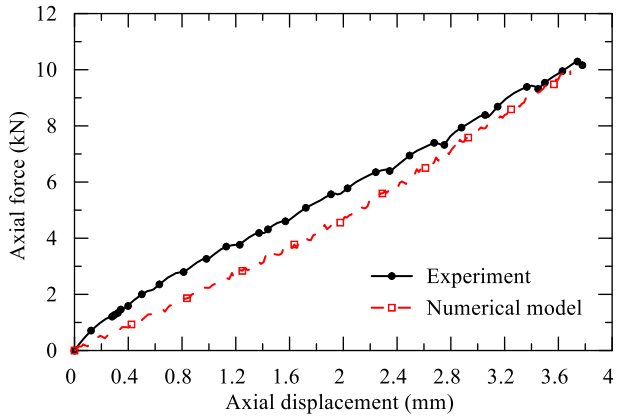

Figure 3 Axial force-displacement results from laboratory test and the numerical modelling

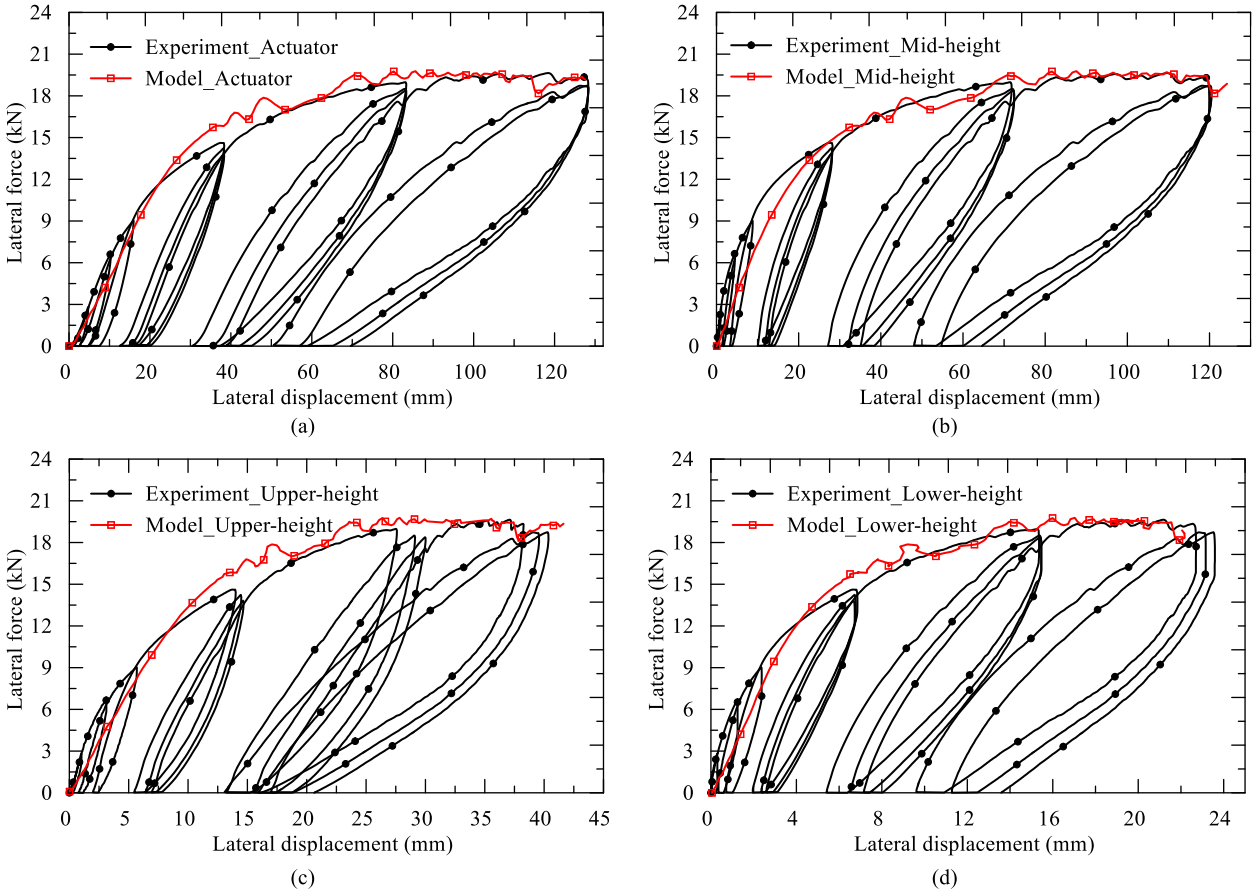

Figure 4 Comparison of the lateral force-displacement results from the numerical model and the experiment: (a) movement of the loading actuator; (b) wall mid-height (opposite side of the wall to the loading actuator); (c) upper-height (the course below the top reaction beam support); (d) lower-height (the course above the bottom reaction beam support).

3.3.1 Lateral force-displacement curves

The lateral force-displacement results of the numerical model were compared with the experimental results captured at three different heights (Figure 4), i.e., mid-height (loading actuator movement); mid-height (wall movement captured at the opposite side of the loading actuator); upper-height (the course below the top reaction beam); and the lower-height (the course above the bottom reaction beam).

The results indicated that the lateral force-displacement of the numerical model fitted the experimental envelope curves very well in terms of both the initial stiffness and the maximum lateral resistance. The fluctuation shown on the numerical lateral force-displacement curve was due to the rotational movement and the shear sliding that occurred at the intercourse interfaces.

Based on the comparison between numerical and experimental results, it can be concluded that the numerical model can reproduce the experimental performance of tyre walls subjected to combined compressive and OOP loads. The numerical model can be used as the base model for future research when performing a parametric study.

4 CONCLUSION

This project attempted to generate a numerical model for simulating the structural performance of tyre walls. A combined finite-discrete element modelling method (FDEM) was adopted. The composite structure of TESEs was simulated as a homogenised body with a linear elastic material model. The model verification was done by comparing the results with those obtained from the laboratory test. The force-displacement curves and failure performance agreed well. It was concluded that the numerical model could reproduce the structural performance of the laboratory tested tyre wall. The methodology discussed in this paper can be referred by researchers and built environment professionals to design and analyse the structural performance of tyre walls and similar masonry structures.

ACKNOWLEDGEMENT

The authors would like to acknowledge UniSA STEM and the industry partner Tyre Stewardship Australia for the research scholarship funding. Thanks to Tyrecycle Pty. Ltd for donating tyre materials and Dassault System for providing the Solidworks and Abaqus software licenses. The authors thank Mr. R. Brown and Mr. S. Gage for the IT support with high-performance computers running the simulation. The authors also thank Mr. T. Golding, Mr. I. Whitehead, Dr. H. Senko, Mr. G. ONeil, Mr. R. Muscher and Mr. C. Sweetman, for technical assistance when preparing and testing the tyre wall. The authors also acknowledge the contribution of the following master's final year students who assisted in the experimental work reported in this paper: Mr. J. K. Piprotar, Mr. A. Kansari, Mr. J. L. Changani and Mr. B. S. Viradiya. The authors also thank Mr. T. Ha and Mr. S. Plummer of MLEI Consulting Engineers for their support as the industry experts.

REFERENCES

Bianco, I., Panepinto, D., & Zanetti, M. (2021). End-of-life tyres: comparative life cycle assessment of treatment scenarios. *Applied Sciences, 11*(8), 3599.

Freney, M., Soebarto, V., & Williamson, T. (2013). *Thermal comfort of global model earthship in various European climates*. Paper presented at the Building Simulation 2013: 13th International Conference of the International Building Performance Simulation Association.

Gilson. (2017). *Tyre Stewardship Australia annual report*: Tyre Stewardship Australia.

Grindley, P. C., & Hutchinson, M. (1996). The thermal behaviours of an earthship. *Renewable Energy, 8*(1-4), 154-159.

Kruis, N. J., & Heun, M. K. (2007). *Analysis of the performance of Earthship housing in various global climates*. Paper presented at the ASME 2007 Energy Sustainability Conference. Retrieved from http://dx.doi.org/10.1115/ES2007-36030

Munjiza, A., & John, N. (2002). Mesh size sensitivity of the combined FEM/DEM fracture and fragmentation algorithms. *Engineering Fracture Mechanics, 69*(2), 281-295.

Munjiza, A., Smoljanovic, H., Zivaljic, N., Mihanovic, A., Divic, V., Uzelac, I., et al. (2020). Structural applications of the combined finite-discrete element method. [Article]. *Computational Particle Mechanics, 7*(5), 1029-1046.

Reynolds, M. (1990). *Earthship Volume 1: How to build your own*: Solar Survival Pr.

Reynolds, M. (2000). *Comfort in any climate*: Solar Survival Press.

Smoljanović, H., Živaljić, N., Nikolić, Ž., & Munjiza, A. (2018). Numerical analysis of 3D dry-stone masonry structures by combined finite-discrete element method. *International Journal of Solids and Structures, 136-137*, 150-167.

Xu, Y., Freney, M., Hassanli, R., Zhuge, Y., Rahman, M. M., & Karim, M. R. (2022). Experimental study on the structural performance of full-scale tyre wall for residential housing applications. *Engineering Structures, 259*, 114181.

Proc. 3rd International Conference on Structural Engineering Research (iCSER 2022)
27-30 Nov 2022, Sydney, Australia
ISBN: 978-0-6456692-1-3

Study on RC Shear Wall With and Without Opening And Its Effect On The Stability Of High-Rise Building

A. B. M. Golam Rabbany Palash[1] and Bulbul Ahmed[2]

[1]Structural Engineer, Advance Design and Consultancy, Dhaka, Bangladesh,
[2]PhD Candidate, School of Engineering, Design and Built Environment, Western Sydney University, Sydney, Australia

Corresponding author's E-mail: palashruet@gmail.com

Abstract

A well-designed shear wall provides sufficient stiffness and ductility to a high-rise building structure that decreases the overall displacement and drift of that structure. Architectural engineers may provide some openings in the shear wall for an aesthetic view. Reinforcement rebar is discontinued in the provided opening area. These opening areas can change the structural performance of high-rise buildings compared to the solid shear wall. The presence of an opening in the shear wall can affect the overall stability of a high-rise building. To minimise the stability issues, coupling beam or bracing or simple beam connection and modified reinforcement can be the efficient solution. In this research, the effects of the openings in the shear wall have been conducted numerically to observe how the performance of the shear wall changed. From the observation, it was worth noting that the presence of openings in the shear wall can increase the stress intensity adjacent to the opening before the deflection of the structure. Finally, a coupling beam was used to minimise the stability risk, and it was found that the presence of a coupling beam decreases the deflection of the building by around seven times. The stress concentration and distribution around the hole are a matter of study for the reinforcement details of that type of shear wall having holes or openings.

Keywords: Shear wall, opening, stability, coupling beam

1. INTRODUCTION

Recently, the number of high-rise buildings has rapidly increased with the development of engineering advancement to minimise land use in densely populated cities and advancements in engineering (Xu et al., 2011). However, high-rise buildings are prone to dynamic actions such as seismic, wind, and impact loading (Sharma et al., 2018; Jin et al., 2022), and there are no probabilistic assessment procedures to evaluate the seismic risk (Elnashai and Kuchma, 2007). For this reason, a shear wall is a viable solution for reinforced concrete (RC) buildings, as demonstrated in Figure 1. A shear wall is a vertical plate like RC load-bearing wall which normally starts at the foundation level and continuous throughout the total height of the building (Singhal et al., 2019). Shear wall resists horizontal loading caused by seismic action and wind load and transfers to the foundations (Aydin and Bayrak, 2021; Rainer and Karacabeyli, 2000; Qiang et al., 2022; Zhou et al., 2022). The lateral stability and/or sway of the building has been reduced significantly and increased the strength and stiffness of the buildings (Lago et al., 2018).

To increase lateral resistance of a high-rise building, a well-designed RC shear wall is required (Tawil et al., 2010; Zhou et al., 2021; Hu et al., 2021). The application of lateral force on the RC shear wall partly increases its internal stress, bending moment, tension, and compression on different sides (Chou et al., 2022). Further increment of forces leads to deflection and finally exceeds the elastic limit that initiates cracking by releasing some energy. The presence of an opening in the RC shear wall, the stress concentration occurs around the opening or along the weak points. A major portion of forces concentrates here accelerates the cracking consequently. The behaviour of the shear wall drastically changes due to the presence of the opening, opening size (Rai and Prasad, 2006) and coupling or link beam that would be illustrated in the subsequent sections.

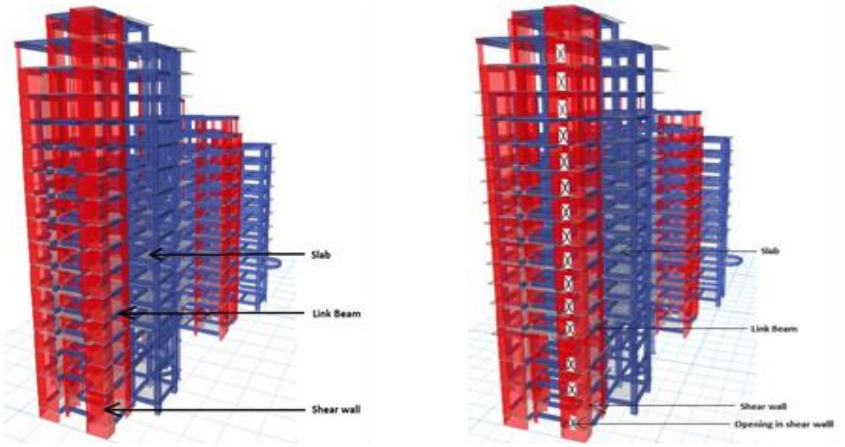

a) RC shear wall without opening **b) RC shear wall with opening**

Figure 1. Shear wall and other structural building components

2. BEHAVIOR OF RC SHEAR WALL

The main target of the structural mechanism is that the load on the slab transfer to the beam, beam to column, and finally, column to the foundation. The components should be designed so that the foundation is stiffer than the column, the column is stiffer than the beam and the beam is stiffer than the slab. The displacement control is not the ultimate target for the shear wall. The main target is that the displacement should affect the shear wall with the opening. Balkaya and Kalkan (2004) investigated the load capacity and stress distribution around the opening and the result showed that stress flow and the crack pattern are different from than solid wall (Taranath, 1988). If the displacement occurs surrounding the opening of the shear wall, then there is a possibility of crack around the opening, which is defined as local failure. Displacement needs to transfer to the pier by transferring the shear by any means for less possibility of cracking adjacent to the opening or any weakest point. The component of the shear walls is connected more efficiently in the structural system (Anwar, 2012). The coupling beam is one of the most effective solutions in connecting systems to improve the efficiency of the structural system. RC shear walls can obviously resist higher lateral load compared to columns. However, advanced analysis is required for the shear wall with coupling beam system. The connecting system is a matter of concern how the system has connected to each other. The elements are connected to the slab, but the thickness of the slab is smaller, and it can be assumed that this connection is not good enough to increase the stiffness. So, some other ways to shear transfer mechanisms need to be adopted. The main concern of the shear wall with the opening is that there is no concrete or rebar to transfer the shear. But the shear must be transferred by and to a good carrier. Thus, providing diagonal rebar around the opening can be a better solution to transfer the forces diagonally to the nearest main vertical bar. That means the diagonal bar act as a strut and tie action (Rabbany et al., 2018) and transfers the increased shear to the nearest concrete or steel.

3. NUMERICAL ANALYSIS

3.1. Model building (deflection approach)

In this study, a multi-storey high-rise building is considered having total height 59.4 m for the analysis. The height of ground floor and second floor is 6.0 m, and all other floor is 3.0 m height. In general, soft story mechanism can be happened for floor with for 6.0 m height. In the present study, the soft story mechanism is not discussed. The yield strength of steel rebar is 420 MPa and concrete compressive strength is 30 MPa. The numerical analysis has been performed by commercial numerical tools ETABS.

From the mesh sensitivity analysis and to increase the computational capacity of numerical simulation proper mesh size for floor and shear wall was considered. The mesh size was considered as 600 × 600 mm and 450 × 450 mm for floor and shear wall, respectively. From the Linear Dynamic analysis, the deflection of the building was measured as 58 mm for a critical load combination 0.9 DL-EXY, where DL denotes dead load and EXY is seismic load in X direction. In the analysis, a total of 12 models with the combination of four different cases such as Case 01, 02, 03 & 04 and three patterns (Pattern 01, Pattern 02, Pattern 03) were used. Case 01, 02, 03 & 04 indicates rigid shear wall, shear wall with 273 × 300 mm opening, shear wall with 1000 × 2200 mm opening and shear wall with 1650 × 4500 mm opening, respectively. Pattern 01, Pattern 02, and Pattern 03 indicates straight shear wall, shear wall with leg in two directions and core type shear wall connected coupling beam & adjacent shear wall, respectively. It is worth mentioning that the analysis was conducted for selected macro part not for whole building to reduce the computational cost. Different combinations of analysis are presented in Figure 2.

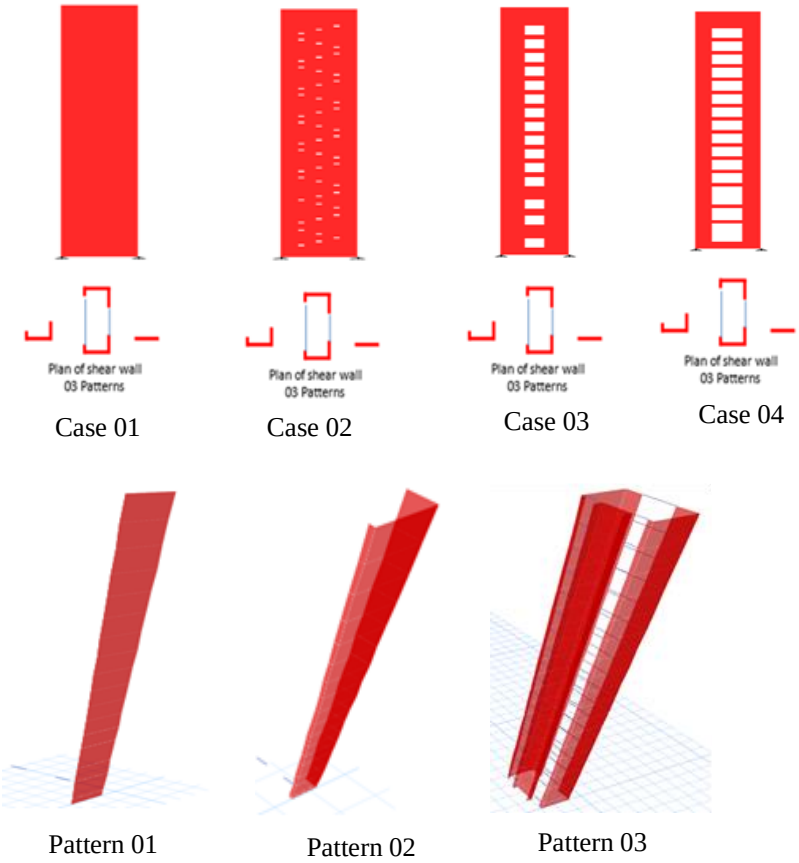

Figure 2. Numerical model building with different combinations

3.2. Model building (stress approach)

The numerical analysis based on the stress concentration approach was conducted for all four cases and pattern 01, as depicted in Figure 3. Materials and other geometric parameters are kept similar as the analysis based on the deflection approach. In this approach, stress concentration analysis has been performed for the first floor, as shown in Figure 3.

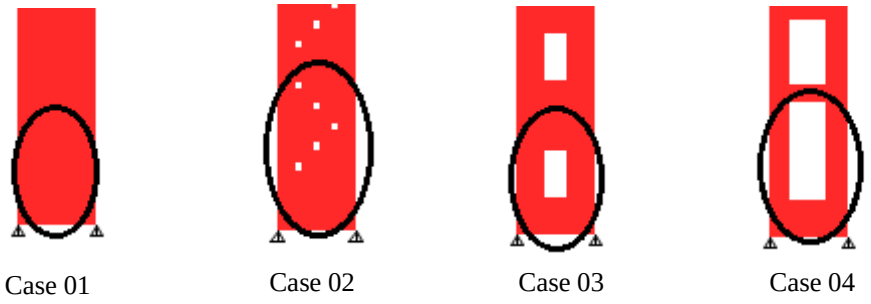

Figure 3. Numerical model building based on stress concentration approach

4. RESULT AND DISCUSSIONS

In the analysis, 150 kN lateral load was applied to understand the behaviour of shear walls without and with different opening sizes. The numerical results are presented in bar char, as depicted in Figure 4, for four different cases and three patterns. From the analysis based on the deflection approach, it is observed that the lateral deflection increases from 295.75 mm to 324.30 mm for four cases with pattern 01. For pattern 02, this value varies from 150.7 mm to 160.10 mm, while is quite similar for pattern 03. The lateral deflection is higher due to the presence of an opening in the shear wall. But the lateral deflection is similar for the shear wall without and with opening. This is due to the sudden local shear failure before reaching the maximum lateral deflection (Nilson et al., 2006) and the application of coupling beam.

It is also found that small opening doesn't affect the shear wall performance overall unless it hampers the reinforcement placement and locates near the edge of the shear wall. The link beam and leg type shear wall help to reduce lateral deflection significantly, which increases the efficiency of the system, whether it contains an opening or not. The presence of a coupling beam improves the system efficiency drastically, which is illustrated here. Shear failure can be occurred instead of bending failure when smaller link beam is used. It indicates that analysis based on deflection only cannot be able to represent the actual behaviour of the shear wall. For this reason, stress analysis is required for a clear understanding of the structural behaviour of all four cases of the shear wall, which is discussed in sub-section 3.2. In the comparison of case 01 and case 04, the lateral deflection decreases by seven times with a similar fashion for all four cases.

From the analysis based on the stress concentration approach, it was found that the stress intensity is highly dense in the compression zone compared to the tension zone. The stress intensity around the opening of the shear wall increases more adjacent to the opening. The stress intensity in the rigid shear wall is less compared to the shear wall with an opening. It is also observed that the stress intensity around the opening of the shear wall increases with the increase of opening, as shown in Figure 5.

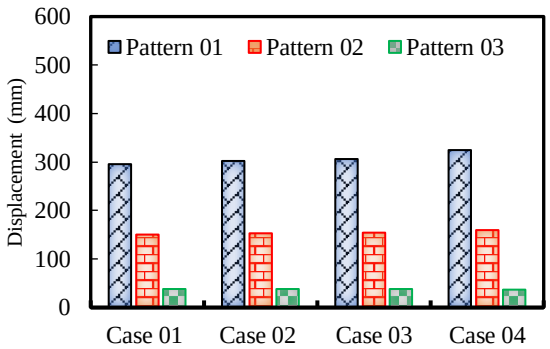

Figure 4. Shear wall displacement

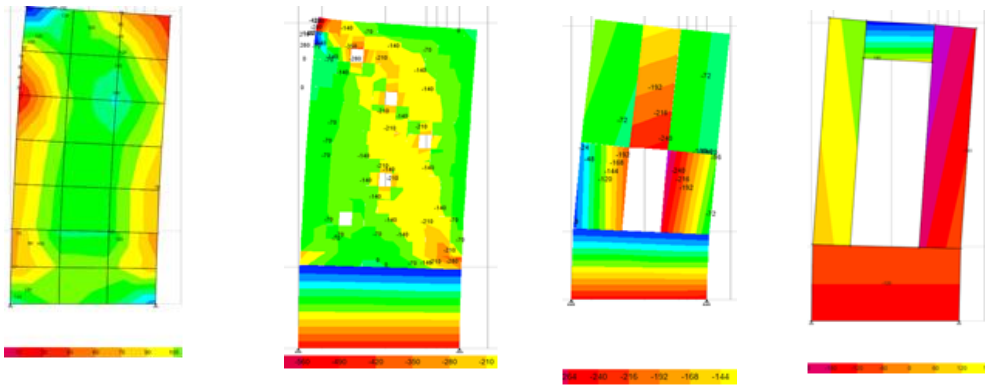

Figure 5. Building displacement for 4 cases with pattern 01

Shear wall with opening, shear generates compression or tension in the component and the shear transfer mechanism is changed due to the absence of concrete in the opening area. Stress concentration is more at the wall adjacent to the opening in shear wall as the effective concrete area is small compared to the shear wall without opening. But if the opening size is less than 150 mm, reinforcement bars may be displaced, and there is no need of additional reinforcement. Stress concentration is more at the wall adjacent to the opening in shear wall as the effective concrete area is small compared to the shear wall without opening. To resist this extra force on additional concrete reinforcement is provided around the openings. Generally diagonal bars are used in the opening for shear. This reinforcement can also be placed horizontally or vertically. Sometimes U bar can also be used to around the opening to hold the concrete for better confinement. For walls with openings more than 150 mm and less 450 mm, at least one half the quantity of main steel reinforcement (using factor of safety 1.5) intersected by the opening is provided parallel to the main reinforcement bars on each side of the opening extending a length of development length (L_d) beyond edges of the opening as per stress concentration result. This reinforcement is provided in both the inner and outer faces of the wall, as shown in Figure 6.

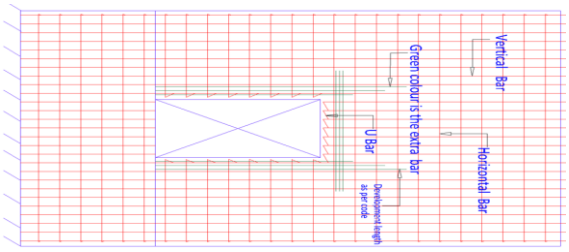

Figure 6. Reinforcement detailed around the opening of shear wall.

CONCLUSIONS

This paper presents the effect of opening in the shear wall to investigate the performance of shear wall. Numerical analysis has been conducted for different sizes of openings based on deflection and stress concentration approaches. From the deflection approach analysis, it was exhibited that the lateral deflection increases with the opening size in the shear wall. Furthermore, the core type shear wall connected the coupling beam & adjacent shear wall significantly increased the lateral stiffness and reduced later deflection by seven times compared to a straight shear wall. The stress concentration approach analysis indicates that stress concentration is highly densed around the larger opening size of the shear wall. Finally, diagonal steel rebars are used to resist the extra shear around the opening.

REFERENCES

Anwar, N. (2012). Behaviour, modelling, and design of shear wall-frame systems. Asian *Center for Engineering Computations and Software, ACECOMS, AIT*.

Aydin, A.C., Bayrak B. (2021). Design and performance parameters of shear walls: a review. *Archit. Civ. Eng. Environ*, 14(4), 69-93.

Balkaya, C., Kalkan, E. (2004). Three-dimensional effects on openings of laterally loaded pierced shear walls. *Journal of Structural Engineering*, 130(10), 1506-1514.

Chou, J. S., Liu, C. Y., Prayogo, H., Khasani, R. R., Gho, D., Lalitan, G. G. (2022). Predicting nominal shear capacity of reinforced concrete wall in building by metaheuristics optimised machine learning. *Journal of Building Engineering*, 135, 105046.

Elnashai, A., Kuchma A. D. (2007). Mid-America Earthquake Center-Headquarter: University of Illinois at Urbana-Champaign. *Report 07-14 September*.

Hu, H. F., Liu, J. P., Cheng, G. Z., Li, J., Chen, Y. F. (2021). Seismic behaviour of hybrid coupled wall system with replaceable endplate-steel coupling beam. *J. Constr. Steel Res*, 187, 106997.

Jin, L., Zhang, B., Chen, F., Yu, W., Lei, Y., Miao, L., Du, X. (2022). Numerical investigations on the strain-rate-dependent mechanical behavior and size effect of RC shear walls. *International Journal of Impact Engineering*,167, 104279.

Lago, A., Wood, A. (2018). Damping considerations in tall buildings Damping Technologies for Tall Buildings, 39-106.

Nilson, A. H. (1997). Design of concrete structures, McGraw-Hill, New York.

Qiang, R., Zhou, L., Ni, C., Huang, D. (2022). Seismic performance of high-capacity light wood frame shear walls with three rows of nails. *Engineering Structures*. 268, 114767.

Rabbany, A. B. M. G., Islam, S., Zaman, M. H. U. (2018). Pile cap performances in different consequences. *Architecture Research*, 8(2), 51-61.

Rai, S. K., Prasad, J., Ahuja, A. K. (2006). Importance of shear wall in tall buildings. *In the Proceedings of the national Conference on High-Rise Buildings: Materials and Practices, New Delhi, India,* 411-422.

Rainer, J. H., Karacabeyli, E. (2000). performance of wood-frame construction in earthquakes. *In Proceedings of the 12th World Conf Earthq Eng, 4*, 2454-2461.

Sharma, A., Mittal, H., Gairola, Ajay. (2018). Mitigation of wind load on tall buildings through aerodynamic modifications: Review. *Journal of Building Engineering*, 18, 180-194.

Singhal, S., Chourasia, A., Chellappa, S., Parashar, J. (2019). Precast reinforced concrete shear walls: state of the art review. *Structural Concrete*, 20, 886-898.

Taranath, B. S. (1998). Structural analysis & design of tall buildings, McGraw Hill, New York.

Tawil, S. E., Harries, K. A., Fortney, P. J. Shahrooz, B.M., Kurama, Y. (2010). Seismic design of hybrid coupled wall systems: state of the art. *J. Struct. Eng*, 136(7), 755-769.

Xu, N., Xu, B., Zeng, X., Chen, J. M. (2011). Dynamic load-displacement behavior of RC shear walls under different loading rates: tests and simulations. *Adv Mat Res*, 163-167, 1780-5.

Zhou, X. H., Liu, J. P., Cheng, G. Z., Li, D. S., Chen, Y. F. (2022). Automated structural design of shear wall structures based on modified genetic algorithm and prior knowledge. *Autom. Constr.* 139, 104318.

Zhou, X. H., Liu, J. P., Cheng, G. Z., Li, D. S., Chen, Y. F. (2021). Automated locating of replaceable coupling steel beam using terrestrial laser scanning. *Autom. Constr.* 122, 103468.

Proc. 3rd International Conference on Structural Engineering Research (iCSER 2022)
27-30 Nov 2022, Sydney, Australia
ISBN: 978-0-6456692-1-3

Influence of CFRP Strip Tie Configurations on the Behavior of GFRP Bar-Reinforced Normal Strength Concrete Columns under Axial Compression

Muhammad Ayoub[1,2]; M. Neaz Sheikh[3]; and Muhammad N. S. Hadi[4.]
[1]Ph.D. Candidate, School of Civil, Mining and Environmental Engineering, University of Wollongong, NSW 2522, Australia (email: ma723@uowmail.edu.au) (https://orcid.org/0000-0002-3899-6996)
[2]Department of Civil Engineering, Faculty of Engineering, Balochistan University of Information Technology, Engineering, and Management Sciences, Quetta, Pakistan
[3]Associate Professor, School of Civil, Mining and Environmental Engineering, University of Wollongong, NSW 2522, Australia (email: msheikh@uow.edu.au) (https://orcid: 0000-0003-0110-5034)
[4]Professor, School of Civil, Mining and Environmental Engineering, University of Wollongong, NSW 2522, Australia (email: mhadi@uow.edu.au) (https://orcid: 0000-0002-6490-889X)

Abstract

This study investigates the influence of Carbon Fiber-Reinforced Polymer strip tie (CST) configurations on the behavior of Glass Fiber-Reinforced Polymer (GFRP) bar-reinforced normal strength concrete columns under axial compression. A total of four specimens with a square cross-section of 200×200 mm and a height of 800 mm were tested. The first specimen was tested as a reference specimen, which was longitudinally reinforced with steel bars and transversely reinforced with the square configuration of steel bar ties. The remaining three specimens were longitudinally reinforced with the GFRP bars and transversely reinforced with the square, square square, and square circular (S, SS, and SC) configurations of CST. The experimental results showed that the axial load carrying capacity and deformability of GFRP bar-reinforced (G-RC) specimen with the SC configuration of the CST was greater than the axial load carrying capacity and deformability of the other steel and G-RC specimens. Moreover, the G-RC specimen with the SC configuration of the CST exhibited higher confinement efficiency than the G-RC specimens with the S and SS configurations of the CST.

Keywords

CST configurations, Axial load behavior, Deformability, Square columns, GFRP bars, Confinement Efficiency.

1. INTRODUCTION

The corrosion of steel reinforcement is one of the major concerns for steel bar-reinforced (S-RC) concrete structures in harsh and corrosive environments, which reduces the service life of the structures. Fiber-Reinforced Polymers (FRP) bars and FRP bar ties have been increasingly gaining acceptance as alternatives to steel bars and steel ties, respectively. The behavior of Glass FRP (GFRP) reinforced concrete columns in comparison to steel reinforced concrete columns was evaluated in a few research studies (Tobbi et al. 2012, Karim et al. 2015, Hadi et al. 2016, and Pham et al. 2021). These studies reported that GFRP bar-reinforced (G-RC) columns showed adequate performance in terms of maximum axial load and deformability under axial compression.

The influence of C and closed types GFRP bar tie configurations on the behavior of G-RC columns under axial compressive load was investigated by Tobbi et al. (2012) and Tobbi et al. (2014b). Test results showed that the load-carrying capacity and ductility of G-RC columns with the closed-type GFRP bar ties were similar to that of the corresponding columns with the C-type GFRP bar ties. However, the lower tensile strength of FRP bar tie at the bent section is a significant concern because of the kinking of fibers at the bent section during the fabrication process (Lee et al. 2013, Spadea et al. 2017, Zhang

and Deng 2018, and Ayoub et al. 2022). Also, the slippage failure of FRP bar tie at the overlapping region is another significant concern, which occurs due to the opening of FRP bar tie legs in the FRP bar-reinforced concrete columns (Tobbi et al. 2014a, Elchalakani and Ma 2017, and Elchalakani et al. 2020).

The influence of the closed-type FRP strip ties in S-RC normal strength concrete columns was investigated in a few research studies (Dong et al. 2018 and Tahir et al. 2019). They reported that S-RC normal strength concrete columns with the FRP strip ties achieved higher maximum axial load and ductility than the corresponding columns reinforced with the FRP bar ties. These research studies only investigated the behavior of S-RC normal strength concrete columns with FRP strip ties under axial compressive load. However, the influence of Carbon Fiber-Reinforced Polymer Strip Tie (CST) configurations on the behavior of G-RC normal strength square concrete columns has not been investigated yet.

The influence of CST on the axial compressive behavior of G-RC normal strength square concrete columns was investigated in this study. The influence of using different configurations of the CST as transverse reinforcement on the failure modes, axial load-carrying capacity, deformability, and confinement efficiency of the G-RC columns under axial compressive load was investigated in this study.

2. EXPERIMENTAL PROGRAM

2.1. Description of Specimens

In this study, a total of four Glass Fiber-Reinforced Polymer (GFRP) bar-reinforced concrete specimens with a cross-section of 200 mm×200 mm were tested under axial compression. The specimens had a height of 800 mm and were tested under axial compressive load. The specimens had square, square square, and square circular (S, SS, and SC) configurations of CFRP strip ties (CST), as shown in Figure 1. For further details about the fabrication, casting, and testing of specimens, please refer to Ayoub et al. (2022).The test matrix of all the specimens is shown in Table 1.

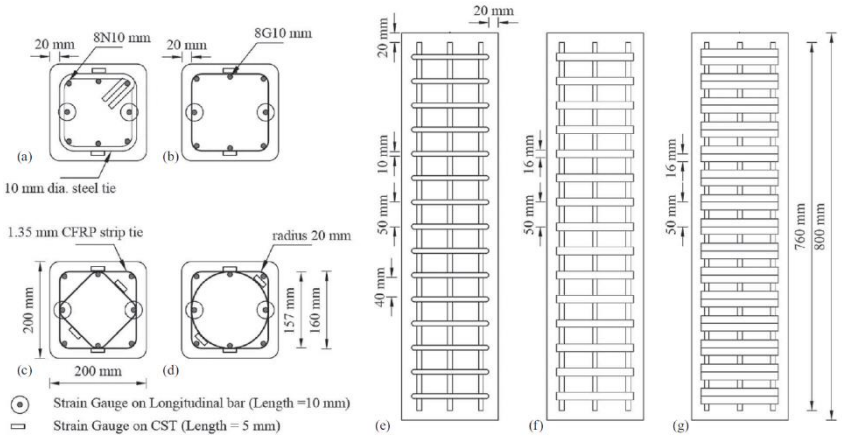

Figure 1. Configuration and reinforcement details: (a) square steel bar tie; (b) square CST; (c) square square CST; (d) square circular CST; (e) S-RC specimen with square steel bar tie; (f) G-RC specimen with square CST; and (g) G-RC specimen with square square or square circular CST.

Table 1. Test Matrix

Specimen	Longitudinal Reinforcement		Transverse Reinforcement		
	Number of bars	ρ_l[a] (%)	Center-to-center spacing (mm)	ρ_t[b] (%)	Configuration
S-SS50-0	8N10	1.57	R10@50	4.2	S
S-GC50-0	8G9.5	1.42	CST@50	1.1	S
SS-GC50-0	8G9.5	1.42	CST@50	2.0	SS
SC-GC50-0	8G9.5	1.42	CST@50	2.0	SC

[a] Ratio of longitudinal reinforcement.

[b] Ratio of transverse reinforcement.

2.2. Fabrication of CFRP Strip Ties

In this study, Carbon Fiber-Reinforced Polymer (CFRP) tubes were fabricated using the hand layup technique. The CFRP sheets were saturated with a mix of epoxy resin and hardener at a ratio of 5:1. Then, the saturated CFRP sheets were wrapped around the styrofoam molds in three layers to form CFRP tubes, as shown in Figure 2(a) and (b). An overlap length of 150 mm was provided between the last two layers of the CFRP sheets to prevent premature debonding failure. Afterward, the CFRP tubes were cured at room temperature for 21 days. After the curing period, the fabricated CFRP tubes were cut to form CFRP strip ties (CST) having a width of 16 mm using an advanced metal cutting machine available at the University of Wollongong, Australia. As a result of CFRP tubes cutting, a total of three different configurations of the CST were fabricated: (i) square (S), (ii) square square (SS), and (iii) square circular (SC). In the S configuration, the square CST had external dimensions of 160 mm×160 mm. In the SS configuration, the small square CST was placed on the square CST making a square square configuration of the CST. The small square and square CST had external dimensions of 130 mm×130 mm and 160 mm×160 mm, respectively, as shown in Figure 2(c). In the SC configuration, the circular CST was placed on the square CST making a square circular configuration of the CST. The square CST had external dimensions of 160 mm×160 mm, whereas the circular CST had an external diameter of 160 mm, as shown in Figure 2(c).

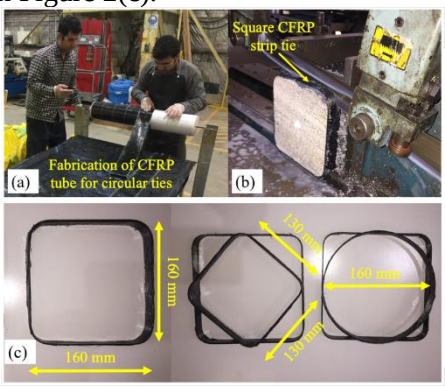

Figure 2. Fabrication and cutting process of CFRP tubes for CST: (a) CFRP tube formation; (b) cutting of CFRP tubes; and (c) S, SS, and SC configurations of CST.

2.3. Material Properties

Normal strength ready-mix concrete was used for casting the concrete specimens. Three concrete cylinders of 100 mm in diameter and 200 mm in height were tested in compression at 28 days in accordance with AS 1012.9 (2014). The average 28-day compressive strength of the concrete cylinders was 28.3 MP.

The longitudinal reinforcement for S-RC specimen consisted of eight N10 (diameter = 10 mm) deformed steel bars with 500 MPa nominal tensile strength. The transverse reinforcement consisted of R10 (diameter = 10 mm) round steel bars with 250 MPa nominal tensile strength. Five samples of N10 and R10 were cut and tested in accordance with AS 1391-17 (2017). The average yield tensile strengths of the deformed and round steel bars (N10 and R10) were 528 and 345 MPa, respectively. The average of five test results is reported in Table 1.

The GFRP bars used in this study were G9.5 bars (9.5 mm diameter). The mechanical properties of the G9.5 bars were found by tensile test, as recommended in ASTM D7205-16 (2016). Five samples of the G9.5 bars were tested. The G9.5 bars had an average ultimate tensile strength of 1240 MPa with the corresponding strain of 2.01%. The average tensile modulus of elasticity of the G9.5 bars was 57 GPa.

The mechanical properties of the CFRP sheets were found by coupon test, as recommended in ASTM D3039-14 (2017). Five samples of the CFRP sheets were tested. Each sample consisted of three layers of the CFRP sheets with an average width of 25 mm and a length of 250 mm. The CFRP sheets

had an average ultimate tensile strength of 1338 MPa with the corresponding strain of 1.69%. The average tensile modulus of elasticity of the CFRP sheets was 93 GPa.

Table 2. Material Properties

Material properties of bar/sheet	Diameter (mm)	Nominal area (mm^2)	Elastic tensile modulus (GPa)	Tensile strength (MPa)	Tensile strain corresponding to tensile strength (%)
N10	10	78.5	202	528[a]	0.26
R10	10	78.5	210	345[a]	0.16
G9.5	9.5	71.0	57	1240[b]	2.01
CFRP	25	26.3	93	1338[b]	1.69

[a] Yield strength.
[b] Ultimate strength.

2.4. Fabrication and Casting of Specimens

Plywood molds were fabricated to cast the specimens tested under axial compressive loads, which had internal cross-sectional dimensions of 200 mm×200 mm and a height of 800 mm. In addition, wooden formworks were manufactured to hold the plywood molds during the casting of concrete, as shown in Figure 3. Afterward, the reinforcement cages were fabricated according to the design configuration of the specimens, as shown in Figure 3(a). Firstly, the longitudinal steel or GFRP bars were placed horizontally using two plywood templates. The steel ties or CFRP strip ties (CST) were placed at 50 mm center-to-center spacing using the plywood spacer jig and was fixed with steel or GFRP longitudinal bars using nylon cable ties. Then, the fabricated FRP reinforcement cages were placed inside the plywood molds. All the specimens were cast in three layers using ready-mix normal strength concrete, as shown in Figure 3(b). Each layer of the concrete was vibrated to remove any air voids present in the concrete.

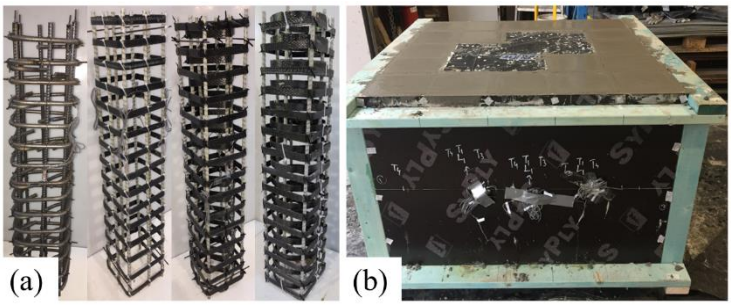

Figure 3. Preparation of specimens: (a) assembling of steel and FRP reinforcement cages and (b) casting of specimens.

2.5. Instrumentation and Testing Procedure

The specimens were tested under axial compressive load using a compression testing machine, with a loading capacity of 5,000 kN. The axial deformations of the specimens were measured with two linear variable differential transducers (LVDTs). The LVDTs were connected to a data logger and the readings were saved in a control computer. The test started with a force-controlled loading of the specimens at a loading rate of 1.5 kN/s to about 100 kN and then unloading the specimens to 10 kN. Afterward, the test was resumed with a displacement-controlled loading having a loading rate of 0.005 mm/s until the failure of specimens. Further details about the fabrication, casting, and testing of specimens can be found in Ayoub et al. (2022).

3. TEST RESULTS AND DISCUSSION

3.1. Failure Modes of Steel and G-RC Specimens

All the specimens were tested under axial compressive load up to failure. For the S-RC specimen, the vertical and inclined hairline cracks started appearing on the sides of the specimen at approximately 80-

90% of the first peak axial load (P_1). At P_1, the spalling of the concrete cover started at the mid-height of the specimen. After the spalling of the concrete cover, the S-RC concrete specimen started to carry additional loads. As a result, the failure of the S-RC concrete occurred due to the buckling of the steel longitudinal bars, followed by the crushing of the concrete core (Figure 4). For the G-RC specimens, small noticeable cracks began to appear at 90-95% of the P_1. At P_1, spalling of the cover occurred. With further increase of the axial load, cracks expended on the surface of specimens, causing the spalling of large chunks of the concrete cover. After the spalling of the concrete cover, the passive confinement pressure of the CFRP strip ties (CST) significantly increased. As a result, the CST provided enough stiffness to the concrete core to carry loads without failure. With further increase of the axial loads, the transverse strain in the CST increased until fracture of the CST occurred, as shown in Figure 4. The fracture of the CST led to the rupture of the GFRP longitudinal bars, crushing of concrete core, and complete failure of the G-RC specimens.

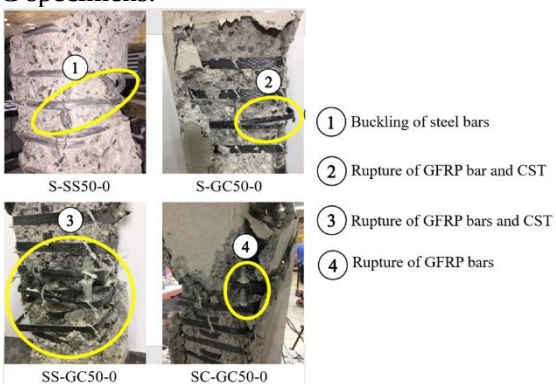

Figure 4. Failure modes of the specimens tested under axial compression loads.

3.2. Behavior of Steel and G-RC Specimens

All specimens generally displayed a linear ascending axial load-axial deformation behavior up to the first peak axial load (P_1). The P_1 in the axial load-axial deformation curve represents the maximum axial load sustained by the cross-section of the specimen. After the P_1, a drop in the axial load with an increase in the axial deformation was observed as a result of the spalling of the concrete cover. After the spalling of the concrete cover, the lateral concrete strain increased significantly and, as a result, the passive confinement became activated. Therefore, the axial load-axial deformation curves for the S-RC specimen with the square (S) configuration of the steel bar ties and G-RC specimens with the square square and square circular (SS and SC) configurations of the CFRP strip ties (CST) showed a gain in the strength and reached the second peak axial loads (P_2) greater than the P_1, as shown in Figure 5. The P_2 shows the maximum axial load sustained by the concrete core (without the concrete cover). However, the P_2 of G-RC specimen with the S configuration of CST was smaller than its P_1 due to the insignificant confinement provided by the CST.

3.2.1. Specimens with S Configuration of CST

The behavior of specimens with the square (S) configuration of steel ties and CFRP strip ties (CST) under axial compression is shown in Figure 5. The reference Specimen S-SS50-0 obtained the first peak load (P_1) of 1212 kN, whereas Specimen S-GC50-0 obtained 9.2% lower P_1 than Specimen S-SS50-0 because of the lower elastic modulus of the GFRP longitudinal bars. The direct replacement of the steel bars and steel ties with the GFRP bars and CST resulted in a decrease of the P_1 in the G-RC concrete specimen. The steel longitudinal bars of Specimen S-SS50-0 sustained an average axial strain of 1503 με at the P_1, which is 57.8% of the yield strain of the steel bars. The axial strain of Specimen S-SS50-0 indicates that the steel longitudinal bars did not yield and contributed to the specimen strength after the P_1. However, the GFRP longitudinal bars of Specimen S-GC50-0 sustained an average strain of 3525 με at the P_1, which is about 17.5% of the ultimate tensile strain of the GFRP bar. The recorded strains of the steel and GFRP longitudinal bars are reported in Table 3.

After the spalling of the concrete cover, Specimen S-SS50-0 experienced a drop in the axial load of 2.5% of the P_1. However, Specimen S-GC50-0 experienced a significant drop in the axial load of about 19.1% of the P_1 due to the crushing of specimen.

Table 3. Confinement Efficiency and Deformability of Specimens

Specimen ID	P_1 kN	P_2 kN	Δ_1 mm	Δ_u mm	ε_{b1} με	ε_{b2} με	$C.E$ -	μ -
S-SS50-0	1212	1279	4.8	21.6	1503	4305[b]	-	4.5
S-GC50-0	1100	891[a]	3.1	6.7	3525	7148	1.3	2.2
SS-GC50-0	1075	1324	3.7	16.3	4624	13098	1.6	4.4
SC-GC50-0	1109	1464	3.7	17.6	5106	12428	1.8	4.8

Note: P_1 = first peak load; P_2 = second peak load; Δ_1 = axial deformation at P_1; Δ_u = axial deformation at 85% of maximum peak axial load; ε_{b1} = strain in longitudinal steel or GFRP bars at P_1; ε_{b2} = strain in longitudinal steel or GFRP bars at P_2; $C.E$ = confinement efficiency of specimens; μ =deformability of specimens; [a]Axial load at the rupture of first GFRP bar; and [b]Yielded strain of steel longitudinal bar at P_2.

3.2.2. Specimen with SS Configuration of CST

The behavior of the specimen with the square square (SS) configuration of the CFRP strip ties (CST) under axial compression is shown in Figure 5. Specimen SS-GC50-0 obtained the P_1 of 1075 kN, which is about 11.3 and 2.3% lower than the P_1 of Specimens S-SS50-0 and S-GC50-0, respectively. This was because the spalling of the concrete cover in Specimen SS-GC50-0 occurred at earlier stages due to the SS configuration of the CST, which resulted in a separation plane between the concrete core and the concrete cover of the specimen. At the P_1, the average axial strain in the GFRP longitudinal bars of Specimen SS-GC50-0 was about 23% of the ultimate tensile strain of the GFRP bars. The measured strain value showed that the GFRP longitudinal bars of the specimen carried load after the spalling of the concrete cover. After the P_1, Specimen SS-GC50-0 experienced a drop in the axial load of 4.4% due to the spalling of the concrete.

After the spalling of the concrete, Specimen SS-GC50-0 obtained the P_2 of 1324 kN, which is about 3.5% greater than the P_2 of Specimen S-SS50-0. Also, the P_2 of Specimen SS-GC50-0 was about 48.6% greater than the P_2 of Specimen S-GC50-0. This was because SS configuration of the CST continued to provide support to the middle GFRP longitudinal bars. After the P_2, failure of Specimen SS-GC50-0 occurred due to the rupture of the remaining GFRP longitudinal bars and CST, followed by the crushing of the concrete core, as shown in Figure 5.

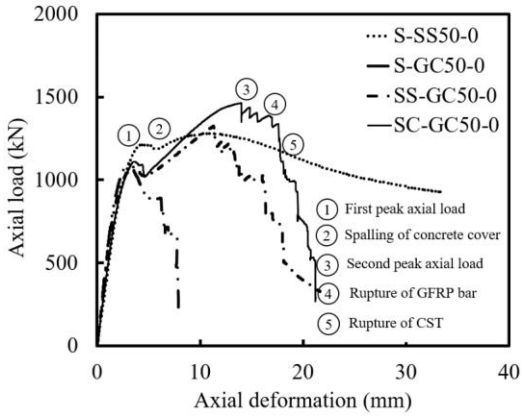

Figure 5. Effects of steel and CFRP strip tie configurations on axial load-axial deformation behavior of steel and G-RC specimens.

3.2.3. Specimen with SC Configuration of CST

The behavior of specimen with the square circular (SC) configuration of the CFRP strip ties (CST) under axial compression is shown in Figure 5. Specimen SC-GC50-0 achieved the first peak load (P_1) of 1109

kN, which is about 8.5% lower than the P_1 of Specimen S-SS50-0. The lower P_1 of Specimen SC-GC50-0 occurred at earlier stages due to the SC configuration of the CST, which resulted a separation plane between the concrete core and concrete cover of the specimen. The average axial strain in the GFRP longitudinal bars of Specimen SC-GC50-0 at the P_1 was 5106 με, which is about 25.4% of the ultimate tensile strain of the GFRP bars. Specimen SC-GC50-0 experienced a sudden drop of the axial load of about 7.9% due to the spalling of the concrete cover.

After the spalling of the concrete cover, Specimen SC-GC50-0 achieved the second peak load (P_2) of 1464 kN, which is about 14.5% greater than the P_2 of Specimen S-SS50-0. This was because the SC configuration of the CST effectively delayed the buckling of GFRP longitudinal bars. The P_2 of Specimen SC-GC50-0 was about 32.0% higher than its P_1. In addition, the P_2 of Specimen SC-GC50-0 was about 64.3 and 10.6% higher than the P_2 of Specimens S-GC50-0 and SS-GC50-0, respectively. The highest P_2 was achieved by Specimen SC-GC50-0, which was due to the better confinement provided by the SC of CST.

3.3. Effect of CST Configurations

The behavior of the G-RC specimens with the square, square square, and square circular (S, SS, and SC) configurations of the CST under axial compression is shown in Figure 6. The effect of CST configurations on the improvement of the first peak axial load (P_1) of specimens was not highly significant. Specimen SC-GC50-0 achieved 0.8 and 3.1% higher P_1 than the corresponding Specimens S-GC50-0 and SS-GC50-0, respectively.

The effect of the CST configurations on the second peak axial load (P_2) of specimens can be seen in Figure 6. Specimen SC-GC50-0, with the SC configuration of the CST achieved the P_2 of 1464 kN, which is about 66.1 and 10.6% greater than the P_2 of Specimens S-GC50-0 and SS-GC50-0, respectively. The above observations indicated that the SC configuration of the CST confined the concrete core more effectively than the S and SS configurations of the CST.

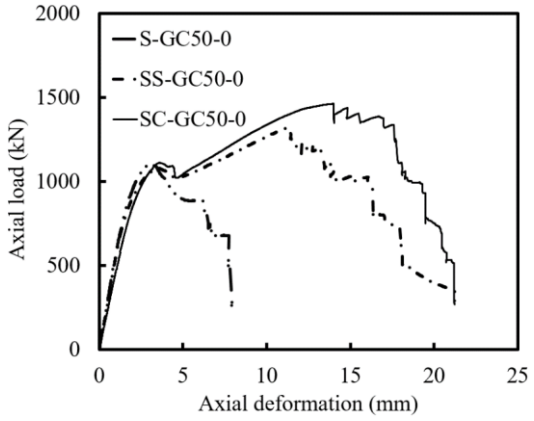

Figure 6. Behavior of steel and G-RC specimens with S, SS and SC configurations of steel and CST.

3.4. Confinement Efficiency and Deformability of Specimens

The details about the confinement efficiency ($C.E$) and deformability (μ) of the specimens under axial compression have been reported by Ayoub et al. (2022). Table 3 reports the $C.E$ of specimens tested under axial concentric loads. The SC configuration of the CST significantly influenced the $C.E$ of specimen compared to the specimens with the S or SS configuration of the CST. The $C.E$ of Specimen SC-GC50-0 was 1.8, which is about 38.5 and 12.5% greater than the $C.E$ of Specimens S-GC50-0 and SS-GC50-0, respectively. The observation indicated that the specimen with the SC configuration of the CST effectively restrained the concrete core compared to the specimens with S and SS configurations of the CST.

Table 3 reports the μ of specimens tested under axial compression. Specimen SC-GC50-0 with the SC configuration of the CST achieved deformability of 4.8, which is about 120.0 and 7.9% higher than the deformability of Specimens S-GC50-0 and SS-GC50-0, respectively. This indicated that the SC configuration of the CST had significant effects on the μ of specimens as compared to specimens with

either S or SS configuration of the CST. In addition, the μ of Specimen SC-GC50-0 was about 6.7% higher than Specimen S-SS50-0 due to the overlapping circular CST continued to provide support to the middle GFRP longitudinal bars, which led to effectively confined the concrete core of Specimen SC-GC50-0.

4. CONCLUSIONS

Based on the observations recorded through the experimental results, the following conclusions are drawn.

1. The G-RC specimen with the S configuration of the CST achieved 9.2% lower peak axial load than the corresponding S-RC specimen. However, the G-RC specimens with the SS and SC configurations of the CST achieved 48.6 and 64.3%, respectively, higher peak load than the G-RC specimen with the S configuration of the CST.
2. The configuration of CST significantly influenced the confinement efficiency of the G-RC specimens. The specimen with the SC configuration of the CST achieved about 38.5 and 12.5% higher confinement efficiency than the corresponding specimens confined by the S and SS configurations of the CST.
3. The deformability of the specimen with the SC configuration of the CST was 100 and 118% greater than the corresponding specimens with the S and SS configuration of the CST, respectively.

Based on the experimental results, the SC configuration of the CST can be used as effective transverse reinforcement for the G-RC square columns for sustaining higher peak axial load with enhanced deformability and confinement efficiency.

REFERENCES

AS 1012.9 (2014). Methods of testing concrete Compressive strength tests - Concrete, mortar and grout specimens. Standards Australia.

ASTM D7205/7205M (ASTM 2016). Standard Test Method for Tensile Properties of Fiber Reinforced Polymer Matrix Composite Bars. West Conshohocken, PA, American Society for Testing and Materials .

ASTM D7565/7565M (ASTM 2017). "Standard test method for determining tensile properties of fiber reinforced polymer matrix composites used for strengthening of civil structures."

Ayoub, M., M. N. Sheikh, and M. N. S. Hadi (2022). "Investigation on the effectiveness of CFRP strip ties as transverse reinforcement for GFRP bar-reinforced concrete columns." *Journal of Composites for Construction* https://doi.org/10.1061/(ASCE)CC.1943-5614.0001249.

Dong, H. L., D. Wang, Z. Wang, and Y. Sun (2018). "Axial compressive behavior of square concrete columns reinforced with innovative closed-type winding GFRP stirrups." *Composite Structures*, 192, 115-125 https://doi.org/10.1016/j.compstruct.2018.02.092.

Elchalakani, M., M. Dong, A. Karrech, M. S. Mohamed Ali, and J.-S. Huo (2020). "Circular concrete columns and beams reinforced with GFRP bars and spirals under axial, eccentric, and flexural loading." *Journal of Composites for Construction*, 24(3), 04020008 https://doi.org/10.1061/(ASCE)CC.1943-5614.0001008.

Elchalakani, M., and G. Ma (2017). "Tests of glass fibre reinforced polymer rectangular concrete columns subjected to concentric and eccentric axial loading." *Engineering Structures*, 151, 93-104 https://doi.org/10.1016/j.engstruct.2017.08.023.

Hadi, M. N. S., H. Karim, and M. N. Sheikh (2016). "Experimental investigations on circular concrete columns reinforced with GFRP bars and helices under different loading conditions." *Journal of Composites for Construction*, 20(4), 04016009 https://doi.org/10.1061/(ASCE)CC.1943-5614.0000670.

Lee, C., M. Ko, and Y. Lee (2013). "Bend strength of complete closed-type carbon fiber-reinforced polymer stirrups with rectangular section." *Journal of Composites for Construction*, 18(1), 04013022 https://doi.org/10.1061/(ASCE)CC.1943-5614.0000428.

Pham, T. M., W. Chen, M. Elchalakani, T. V. Do, and H. Hao (2021). "Sensitivity of lateral impact response of RC columns reinforced with GFRP bars and stirrups to concrete strength and

reinforcement ratio." *Engineering Structures*, 242, 112512 https://doi.org/10.1016/j.engstruct.2021.112512.

Spadea, S., J. Orr, and K. Ivanova (2017). "Bend-strength of novel filament wound shear reinforcement." *Composite Structures*, 176, 244-253 https://doi.org/10.1016/j.compstruct.2017.05.032.

Tahir, M., Z. Wang, and K. M. Ali (2019). "Axial compressive behavior of square concrete columns confined with CFRP strip ties using wet lay-up technique." *Construction and Building Materials*, 200, 282-292 https://doi.org/10.1016/j.conbuildmat.2018.12.127.

Tobbi, H., A. S. Farghaly, and B. Benmokrane (2012). "Concrete Columns Reinforced Longitudinally and Transversally with Glass Fiber-Reinforced Polymer Bars." *ACI Struct J*, 109(4)(4), 1-8.

Tobbi, H., A. S. Farghaly, and B. Benmokrane (2014a). "Behavior of Concentrically Loaded Fiber-Reinforced Polymer Reinforced Concrete Columns with Varying Reinforcement Types and Ratios." *ACI Struct J*, 111(2)(2) https://doi:10.14359/51686528.

Tobbi, H., A. S. Farghaly, and B. Benmokrane (2014b). "Strength model for concrete columns reinforced with fiber-reinforced polymer bars and ties." *ACI Struct J*, 111(4), 789-798.

Zhang, X., and Z. Deng (2018). "Experimental study and theoretical analysis on axial compressive behavior of concrete columns reinforced with GFRP bars and PVA fibers." *Construction and Building Materials*, 172, 519-532 https://doi.org/10.1016/j.conbuildmat.2018.03.237.

Proc. 3rd International Conference on Structural Engineering Research (iCSER 2022)
27-30 Nov 2022, Sydney, Australia
ISBN: 978-0-6456692-1-3

Rehabilitation of Concrete Bridge Deck Cracking using High-Performance Fibre Reinforced Concrete (HPFRC)

Ella Shibram, Saman Karimi, Olivia Mirza

Western Sydney University, Locked Bag 1797, Penrith NSW, 2751 Australia

Corresponding author's E-mail: S.karimi@westernsydney.edu.au

Abstract

Concrete bridges of all types and sizes are important elements in transportations network due to their materials' performance and durability. As time progresses, the serviceability of these bridges will deteriorate due to several factors such as corrosion of reinforcement bars, environmental conditions, chemical damage, and fatigue. One of the biggest problems affecting concrete bridges is deck cracking which caused by temperature effects, drying, and shrinkage. It is important to monitor these bridges to keep them safe and functional. In the last decade, fibre-based rehabilitation methods such as Carbon Fibre-Reinforced Polymer (CFRP) and Glass *Fibre Reinforced Concrete (GFRC) have gained considerable attention which have several limitations, especially requiring a complex manufacturing procedure. In contrast, limited attentions have been devoted to High-Performance Fibre Reinforced Concrete (HPFRC) for the rehabilitation of deck cracking; therefore, HPFRC is utilised in this study as an alternative approach for the rehabilitation of concrete bridge deck cracking. A finite element model (FEM) will be compared with the theoretical calculations in order to validate the efficiency of the proposed method. The results showed an enhancement in stiffness and ductility after applying HPFRC. Furthermore, HPFRC declined the cracking failure and energy which indicated the cost-effectiveness of the proposed rehabilitation method.*

Keywords: High-performance Fibre Reinforced Concrete (HPFRC), Cracking, Concrete bridge, Concrete deck, Rehabilitation

1. INTRODUCTION

One of the most important parts of the transport networks is bridges. These structures are expected to withstand many factors during their life span. Concrete bridge failure is now a prevalent problem across the world; therefore, strengthening and rehabilitating of these bridges are crucial. To gain a good understanding of concrete bridge failures, different damaging factors have been investigated in the last few years. Pircher et al (2011) developed research to analyse the influence of transportation loads on the concrete bridge. ElSafty and Abdel-Mohti (2013) examined the efficiency of Carbon Fibre Reinforcement Concrete CFRP on concrete bridge cracking. Zhao et al (2017) evaluated the impacts of Glass Fibre Reinforced Concrete (GFRC) and Nylon Fibre Reinforced Concrete (NFRC) on fracture. Wang et al. (2019) examined the environmental impacts on concrete bridges. Based on the findings, sudden and massive thermal changes led to the cracking or other failure issues in the bridge structure. Reggia et al. (2020) studied the High-Performance Reinforced Concrete (HPFRC)'s impact on cracking. An improvement in concrete stiffness and cracking was achieved using fibre-based concrete materials. Treat and Dymond (2021) evaluated the effectiveness of crack epoxy injection. It was concluded that epoxy prevent the crack growth but did not prevent cracking due to its incapability in improving the concrete compressive strength. Few studies were carried out on the application of High-Performance Fibre Reinforced Concrete (HPFRC) on concrete bridges; therefore, this study aims to utilise the HPFRC as an alternative method for rehabilitating concrete bridge deck cracking to fulfil this gap.

2. PROJECT DESCIPTION

The case study in this research is a two-span bridge over New England Highway, which has deteriorated considerably due to heavy traffic load. The bridge is temporarily restricted for traffic operation. Figure 1 shows the severe cracking damage of the concrete bridge deck. The condition of the reinforcements is variable, with extreme pitting on the deck. The concrete deck is 26050 mm in length, 19300 mm in width and 320 mm in thickness. Figure 2 shows the bridge cross-section drawing.

Figure 1. Damaged deck

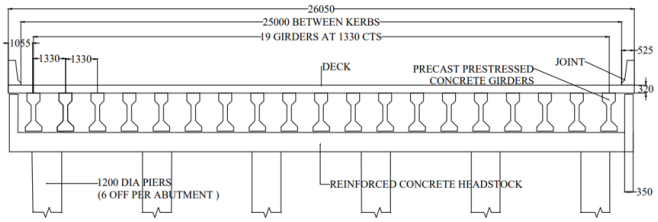

Figure 2. Bridge cross-section drawing

3. MATERIALS AND METHODS

3.1. Parts and Dimensions of Finite Element Modelling

Two three-dimensional (3D) finite element models (FEM) of the concrete decks have been simulated using ABAQUS software. The developed decks are modelled with the actual material and HPFRC layer respectively. The theoretical calculation is compared with the ABAQUS results in order to validate the accuracy of the simulated deck models. Table 1 shows the material properties that is used in ABAQUS to simulate the behaviour of the concrete deck.

Table 1. Deck models parameters

Property	symbol	PC Value	HPFRC value	Unit
Width	W	9.65	9.65	m
Height	H	0.32	0.01	m
Length	L	1	1	m
Ave. Density	ρ	2350	1400	kg/m^3
Ave. compressive strength of concrete	f_c'	65	120	MPa
Poisson's ratio	v	0.2	0.2	-

3.2. Material Property

3.2.1 Normal Concrete (NC)

Figure 3 shows the stress and strain curve of the concrete. To determine the first section of the stress/strain graph, ABAQUS needs Young's modulus of concrete (E_c) and Poisson's ratio (v), which are linear elastic with limit stress of $0.4f_c'$.

Using Equation 1 adapted from AS5100 Bridge Design (Standards Australia (2017)), Young's modulus of concrete is calculated as 39,493.62 MPa, and Poisson's ratio (v) is taken as 0.2.

$$Young's\ modulus, E_c\ (MPa) = 0.043 \times \rho^{1.5} \times \sqrt{f'_{ck}} \leq 40\ (MPa) \quad (1)$$

Equation 2 considers the compressive behaviour of the concrete while Equation 3 calculates the tension.

$$Strain\ , \varepsilon_{ys} = \frac{\sigma_c \times 40\%}{E} = 0.000658$$

$$Stress, \sigma_c(MPa) = \frac{f_c' \times \gamma \times (\frac{\varepsilon_c}{\varepsilon_c'})}{\gamma - 1 + (\frac{\varepsilon_c}{\varepsilon_c'})^{\times \gamma}} \quad (2)$$

$$Concrete\ Plasticity, \gamma = \left|\frac{f_c}{32.4}\right|^3 + 1.55 = 9.62$$

$$Concrete\ Tension, T(kN) = 0.6\sqrt{f_c} = 4.84\ kN \quad (3)$$

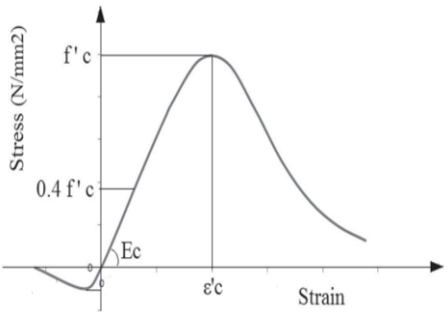

Figure 3. Concrete stress/strain curve

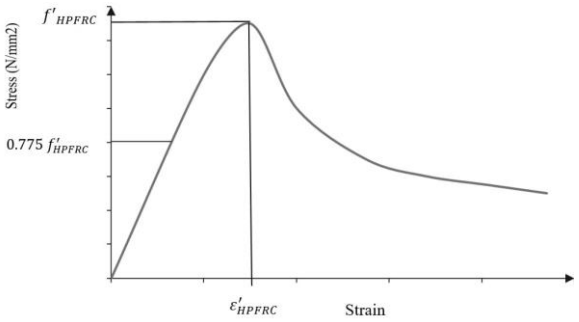

Figure 4. HPFRC stress/strain curve

3.2.2 High Performance Reinforced Concrete

High-Performance Fibre Reinforced Concrete (HPFRC) is a novel approach for enhancing concrete bridge cracking performance. HPFRC is a popular material due to its high strength, elasticity, durability, stiffness, and ability to withstand massive loading. Therefore, HPRFC is utilised as a strengthening method in this study. Figure 4 shows the stress-strain curve of the HPFRC. The first section of this graph is linear elastic with a limit stress of 0.775. The nonlinear behaviour of HPFRC is characterised by Young's modulus degradation caused by cracking. In this section, the HPFRC fails rapidly at the weakest point due to the maximum strain localisation in a single crack that is greater than the strain limit. In order to rehabilitate the cracking, a 10 mm layer of HPFRC is applied on top of the plain concrete bridge deck. The combination of fibre-based materials with high-performance concrete significantly enhances the characteristics of concrete, tensile strength, fracture resistance, and ductility effectiveness. In addition, HPFRC has significantly high compression strength. In this study, two concrete decks are simulated with ABAQUS. The first model is used to analyse the normal concrete bridge deck cracking capacity against the service load, and the second model is used for the comparison of the deck behaviour after applying the HPFRC layer. This method is developed to provide a better understanding of the efficiency of the HPFRC material.

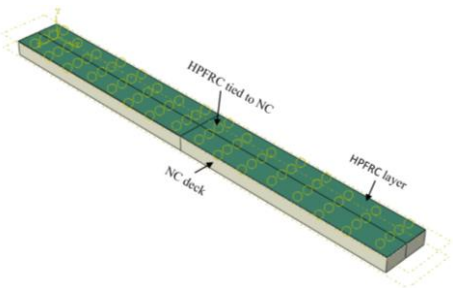

Figure 5. Tie constraint

3.3 Constraints

Because of the time constraints and computational costs, this research has used the "tie" type constraint in ABAQUS to adequately simulate the connections between the deck and the HPFRC layer. As shown in Figure 5, a tie constraint links two surfaces and restraints any displacement between them. This restriction is versatile since it can combine two surfaces as an interface even if the meshing nodal patterns differ.

3.4 Boundary Condition and Loading Application

Sufficient boundary conditions (BC) are crucial for any computational model since they simulate the real-life scenario behaviour of the element. The original dimension of the deck is 26050 mm in length, 19300 mm in width, and 230 mm in depth. In order to save computation time, the deck is symmetrical with uniform pressure; therefore, only half of the deck width and 1000 mm length are modelled. Accordingly, Figure 6 shows the BC, and as it is shown, section (1) is fixed in every direction, section (2) and section (3) are fixed on the z-axis, and section (4) is fixed on the x-axis. It should be noted that the purple downward arrows illustrate the 7.03 MPa pressure acting on top of the deck.

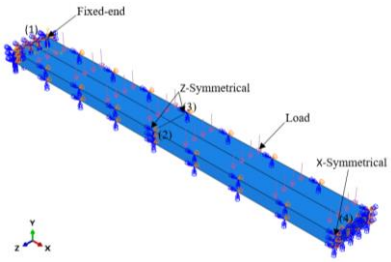

Figure 6. Boundary conditions and loading

Table 2. Sensitivity analysis according to mesh

Mesh size (mm)	Deflection (m)	Error (%)
200	0.063207	96.92
220	0.366781	82.13
225	**2.02194**	**1.53**
230	4.191	-104.14
250	4.191	-104.14
300	4.191	-104.14

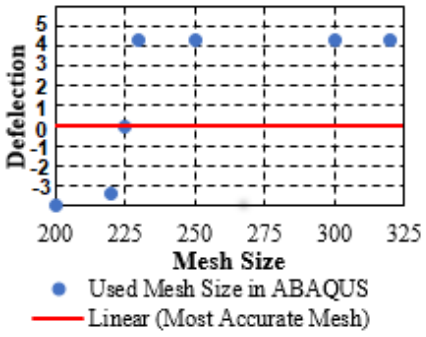

Figure 7. Sensitivity analysis

3.5 Sensitivity Analysis

A comprehensive insight into the sensitivity analysis is required to evaluate an appropriate mesh size for finite element modelling accuracy. The sensitivity analysis has been undertaken by applying various mesh to compare with the theoretical values shown in Equation 4.

$$Moment\ of\ Inertia, I = \frac{bh^3}{12} = 2.65 \times 10^{10} mm^4$$

$$Point\ Load\ Defelection, \delta_{max} = \frac{PL^3}{3EI} = 2053.3\ mm$$

$$Error\ Percentage = \frac{2053.3 - 2021.94}{2053.3} \times 100 = 1.53\% > 10\% \quad (4)$$

25-mesh size with 1.53% discrepancy will be applied to the model since its error percentage is under 10% and coincides with the used mesh size in ABAQUS. Table 2 shows the various mesh sizes used and Figure 7 represents the applied mesh size on the deck model and their calculated values.

4. RESULTS AND DISCUSSION

4.1 The rehabilitation of the concrete bridge deck

Figure 8 depicts the current deck's extreme cracking failure due to traffic load, and Figure 9 illustrates the performance of the plain concrete profile deck generated from initial finite element modelling and analysis. Cracking is the dominant failure mechanism in the whole bridge deck. Section (A) is almost the middle of the bridge deck and experiences the lowest stress level (88.8 MPa); therefore, cracking starts from section (A). According to the stress values, the whole deck is cracking under normal traffic loading with different severity. The stress value increases on the x-axis and reaches its highest point at section (B). Thus, the failure becomes severe at the fixed end since the stress level at the section (B) is 64.6 MPa. Figure 10 illustrates the addition of the 10 mm thick layer of HPFR concrete. As it can be seen, the stresses level on the deck significantly decreases, and only section (C) is prone to cracking. Moreover, the damaged area is considerably smaller than the plain concrete. The highest stress value at section (C) is 89.4 MPa; thus, the deck's load capacity is improved. The cracking failure occurs when the concrete stress exceeds 10% of its compressive strength. The stress distribution in Figure 9 shows that the deck is severely cracked at 64.6 MPa. It can be concluded that the 65 MPa concrete is inadequate for the traffic loading; thus, the HPFRC layer is needed. When the HPFRC layer is added, the deck cracking capacity is increased to 89.4 MPa. Figure 10 illustrates that the entire section improved in cracking and the deck is able to withhold 44.5 MPa stress. This stress value is 28% higher than plain concrete. HPFRC compressive strength is between 120-200 MPa on average. In this study, the lowest HPFRC strength has been considered. Therefore, increasing the strength and thickness of the HPFRC is expected to improve the cracking further.

Figure 8. Bridge Deck Cracking

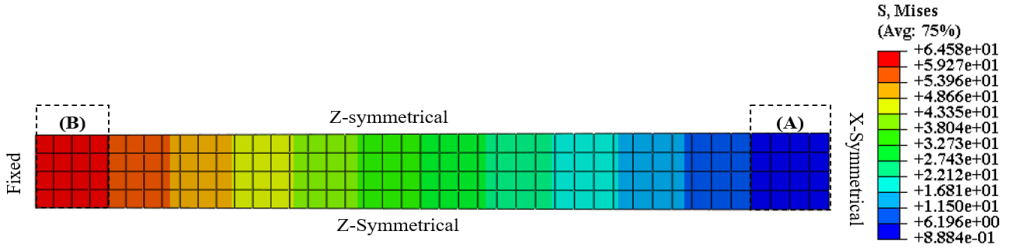

Figure 9. Top view of NC deck model before HPFRC application and its stress values

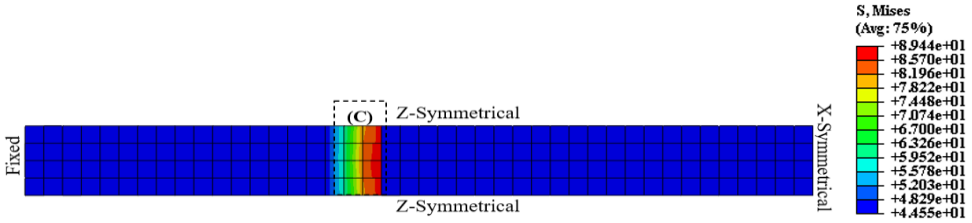

Figure 10. Top view of deck after HPFRC application and its stress values

5. CONCLUSION AND FIRTHUR STUDIES

This research investigated the impact of using HPFRC for the strengthening and rehabilitating of the bridge deck cracking. Based on the investigation, it was concluded that combining fibre-based materials with high-performance concrete enhances the capacity of the concrete's tensile strength, fracture resistance, and flexibility, HPFRC, in comparison with the plain concrete, has a greater load capacity and considerably reduces the cracking and crack depths, and cracking affects the load-bearing capacity of the deck causing the bridge to be more vulnerable to various failures. It was also concluded that HPFRC has superior material characteristics, which improves its structural performance, and HPFRC has high-stress capacity and reduces the cracking by 28%. Therefore, the deck can withstand a higher traffic load. For further investigation, it is recommended to use the HPFRC with higher strength compression and thickness in concrete bridge deck.

REFERENCES

ElSafty, A., & Abdel-Mohti, A. (2013). Investigation of likelihood of cracking in reinforced concrete bridge decks. *International Journal of Concrete Structures and Materials*, *7*(1), 79-93.

Pircher, M., Lechner, B., Mariani, O., & Kammersberger, A. (2011). Damage due to heavy traffic on three RC road bridges. *Engineering structures*, *33*(12), 3755-3761.

Reggia, A., Morbi, A., & Plizzari, G. A. (2020). Experimental study of a reinforced concrete bridge pier strengthened with HPFRC jacketing. *Engineering Structures*, *210*, 110355.

Treat, C., & Dymond, B. Z. (2021). Deterioration of concrete bridge decks containing epoxy-coated and uncoated reinforcement. *Journal of Bridge Engineering*, *26*(4), 06021001.

Wang, J. F., Zhang, J. T., Xu, R. Q., & Yang, Z. X. (2019). Evaluation of thermal effects on cable forces of a long-span prestressed concrete cable–stayed bridge. *Journal of Performance of Constructed Facilities*, *33*(6), 04019072.

Zhao, X., He, X. J., & Yang, Y. C. (2017). Numerical simulation of GFRP reinforced concrete beams. *Advances in Materials Science and Engineering*, *2017*.

Proc. 3rd International Conference on Structural Engineering Research (iCSER 2022)
20-22 Nov 2022, Sydney, Australia
ISBN: 978-0-6456692-1-3

Strengthening of Steel Beams with Thermoplastic CFRP Overwrapping Using Automated Fibre Placement

Feleb N Matti[1], Ebrahim Oromiehie[2], Fidelis R Mashiri[3] and B.Gangadhara Prusty[4]

[1]Doctor, Western Sydney University, Penrith, NSW, Australia
[2]Doctor, ARC Training Centre for Automated Manufacture of Advanced Composites (AMAC), UNSW Sydney, NSW 2052, Australia
[3]Associate Professor, Western Sydney University, Penrith, NSW, Australia
[4]Professor, University of New South Wales, Sydney, NSW, Australia

Corresponding author's E-mail: f.matti@westernsydney.edu.au

Abstract

An experimental investigation on thin-walled square hollow section (SHS) beams with and without thermoplastic carbon fibre reinforced polymer (CFRP), overwrapped using the automated fibre placement (AFP) technique, was carried out. Four thermoplastic CFRP overwrapped beams and a control beam were tested for the determination of the bending capacity. Hot gas torch-assisted automated fibre placement (AFP) based manufacture of thermoplastic composites was used to strengthen the SHS tubular beam members. Loads were applied at the midspan of each beam. The control beam behaviour was compared to the different methods of strengthening using thermoplastic CFRP overwraps. The beam specimens were pin connected at both ends of each beam. Two strain gauges were placed at the top and bottom faces of each beam, respectively, to measure the strains during bending tests. Two linear potentiometers (LPs) were used at the bottom face of the beams to measure the deflections. There is inward deformation (concave deformation) on the upper surface of each beam. Outward deformations (convex deformations) were observed on the two side walls of the SHS beams. For the control beam, there is a comparable agreement between the predicted ultimate load and the experimental ultimate load. It was found that the ultimate loads for the strengthened beams were higher than that of the control beam.

Keywords: Automated fibre placement, thermoplastic CFRP composites, SHS beams, experimental investigation, deflection, ultimate loads.

1. INTRODUCTION

Cold-formed SHSs are widely used in engineering structures such as bridges, cranes, and towers. The SHSs in engineering structures are generally subjected to cyclic loading from permanent loads or imposed loads such as vehicles and wind loads. When loads are applied to a structure, cracks initiate and propagate, and subsequent fatigue failure may occur. Improving the behaviour of tubular structures and strengthening the metallic engineering structures can be achieved by reinforcing tubular members using CFRP sheets.

An extensive review of research in steel structures strengthened with CFRP is reported by Zhao and Zhang (2007). Oromiehie et al. (2019) presented a review on defects, impacts and inspection techniques on AFP-based composite structures. Tafsirojjaman et al. (2021) carried out experimental investigations on the behaviour of CFRP strengthened SHS connections under both monotonic and cyclic loadings. It was found that CFRP technique enhances the structural performances effectively under loadings. Keykha (2017) conducted a numerical investigation on the behaviour of SHS steel framed strengthened using CFRP. The results of this investigation showed that the coverage length and the number of layers of CFRP composite have a significant effect on increasing the ultimate load of the SHS steel frames. Rabinovitch and Frostig (2003) carried out an experimental and analytical investigation of five RC beams strengthened and rehabilitated using externally bonded CFRP strips.

The experimental results showed an increase in the flexural strength and stiffness of the strengthened and rehabilitated beams. On the other hand, a significant reduction in the deformability of the strengthened member has been observed. There is limited research on thin-walled SHS beams with thermoplastic CFRP, overwrapped using the AFP technique. The current paper focuses on experimental study on SHS beams with and without thermoplastic CFRP, overwrapped using AFP technique to observe the failure modes and to determine the values of ultimate loads as well as the deflections and strains at the ultimate loads.

2. EXPERIMENTAL PROGRAM

2.1. Test Specimens

A control beam and four thermoplastic CFRP overwrapped beams shown in Table 1 were tested for the determination of the bending capacity. The steel beam specimens were in the form of square hollow sections (SHS) with dimensions of 89 mm x 89 mm x 3.5 mm. The length of each beam is approximately 750 mm.

As shown in Figure 1(a), the control beam (B-b) does not have thermoplastic carbon fibre reinforced polymer (CFRP). Specimen (3-b) had two layers of CFRP sheets laid longitudinally (parallel to length), see Figure 1(b). Specimen (5-b) had two layers of CFRP laid transversally (perpendicular to length), see Figure 1(c). Specimen (6-b) shown in Figure 1(d) was made with three layers of CFRP placed vertically and at an angle of 45°. In addition, specimen (9-b) shown in Figure 1(e) had two layers of CFRP laid longitudinally and transversally.

Carbon-PEEK prepreg (AS4/APC2; supplied by Solvay) was used to reinforce the fibres. The prepreg tapes are 0.15 mm thick and 6.35 mm wide. Some of the key material properties of the prepreg tape, such as density, module of elasticity, shear modulus, Poisson's ratio and fibre volume fraction are 1570 kg/m3, 138 GPa, 5 GPa, 0.28 GPa and 0.6, respectively. The layup sequences and the AFP processing parameters for all the reinforced profiles are summarised in Table 1.

The Automated Dynamics-built AFP machine at UNSW Sydney was utilised for reinforcing the SHS specimens. This AFP machine is a seven-axis robot platform, including a coordinated spindle, a thermoplastic placement head which comprises a consolidation system, prepreg tape dispensing system and HGT as a heat source, and a computer controller (Oromiehie et al., 2022). The AFP processing parameters, shown in Table 1, were selected based on the author's earlier investigation (Oromiehie et al., 2021).

With the commencement of the layup process, the placement head brings the prepreg tape surfaces together under heat and pressure, as shown in Figure 2. To ensure strong and durable bond between the prepreg and SHS, the surface of the metal was treated via grinding.

Table 1. Specimen Summary

Specimen		Direction (H/V)	Beam Length L_l (mm)	Measured Beam Length L_m (mm)	Lay-up	Qty	Material	Tape width (mm)	AFP processing parameters Lay-up speed (mm/s)	HGT Temp (°C)	Consolidation Force (N)
B	b	-	750	750	-	-	-	-	-	-	-
3	b	H	750	751	[0,0]	1	CF/PEEK	6.35	76	900	200
5	b	V	750	750	[90,90]	1	CF/PEEK	6.35	76	900	200
6	b	V,45°	750	752	[90,90,45]	1	CF/PEEK	6.35	76	900	200
9	b	HV	750	751	[0,90]	1	CF/PEEK	6.35	76	900	200

Note: H = Horizontal (Transverse); and V = Vertical (Longitudinal).

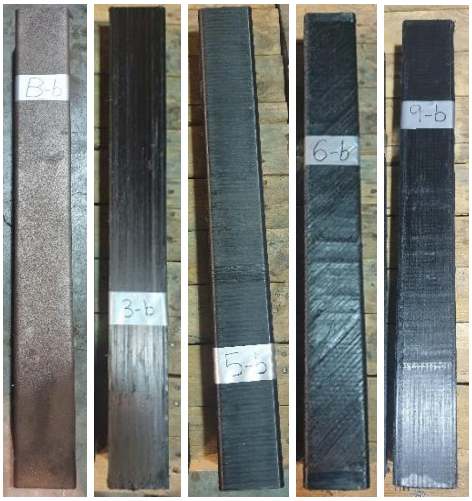

(a) (b) (c) (d) (e)

Figure 1. SHS beam: (a) Control beam; (b) Longitudinal reinforced specimen; (c) Transverse reinforced specimen; (d) Reinforced specimens with additional layer of 45° and (e) Transverse and longitudinal reinforced specimens

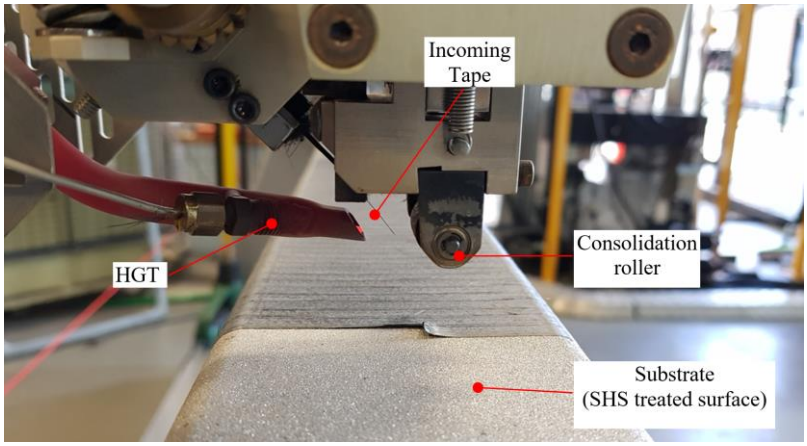

Figure 2. AFP machine with thermoplastic head; (Photo courtesy: Automated Composites Laboratory, UNSW Sydney).

2.2. Instrumentation and Testing of Beam Specimens

Two strain gauges were placed at the top and bottom faces of each beam to measure the strains during bending tests. These four strain gauges were installed at the middle of the beam's width. Two dial gauges were used at the bottom face of the beams to measure deflection. These are detailed in Figure 3(a). For the control beam, sanding paper (metal cloth) was used to remove the oxidised layer at the locations of the strain gauges. A conditioner was applied on the strain gauges' location to remove the oxidised layer and then a neutraliser was applied on the same locations to ensure that the acid of the conditioner was removed. Cyanoacrylate-based strain gauge adhesive was used to adhere the strain gauges to the surface of the beams. The single element strain gauges were covered with SB Adhesive Tape for protection. The gauge length of the single element strain gauges used for the control beams was 2 mm. The gauge length of the single element strain gauges used for the CFRP beams was 5 mm.

The bending capacity of the control beams and 4 CFRP strengthened beams were investigated using the test setup shown in Figure 3(a). Loads were applied at the midspan of the beams using a hydraulic jack, see Figure 3(b). The control beam behaviour will be compared to the different methods of strengthening using CFRP. The beam specimens were pin connected at both ends of each beam. The pinned supports are located 25 mm away from the end edges of the beam. Two linear potentiometers

(LPs) were used to measure the deflections. The load was applied to these test specimens at a rate of 0.016 mm/s until the specimens failed. The test continued at the same rate after obtaining the peak load until the load dropped to a value of 49 kN.

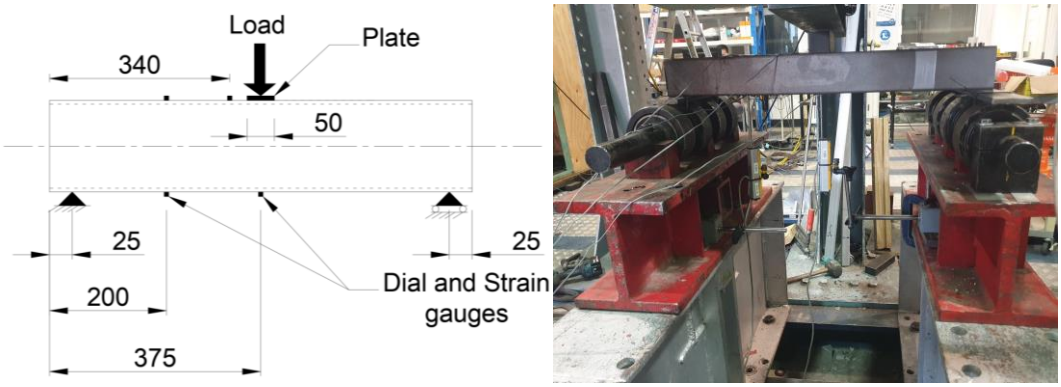

(a) **(b)**

Figure 3. Test setup: (a) Schematic diagram; and (b) Test rig

3. RESULTS

3.1. Deflection and Strains

The ultimate loads and the deflections at the ultimate load for the one SHS control beam and four CFRP beams are shown in Figure 4 and Table 2. The experimental ultimate load of specimens B-b, 3-b, 5-b, 6-b, and 9-b are 77.82 kN, 82.73 kN, 88.81 kN, 87.26 kN, and 83.57 kN, respectively. The ultimate load of CFRP beams are greater than the ultimate load of the control beam B-b.

B-b deflected 4.93 mm (LP1708 - bottom midspan of the beam) and 3.30 mm (LP1547 - bottom quarter point) at the peak load. Specimen 3-b deflected 5.12 mm (LP1708) and 3.69 mm (LP1547) at the peak load. Specimen 5-b deflected 4.93 mm (LP1708) and 3.75 mm (LP1547) at the peak load. Specimen 6-b deflected 4.86 mm (LP1708) and 3.31 mm (LP1547) at the peak load. Specimen 9-b deflected 4.51 mm (LP1708) and 3.32 mm (LP1547) at the peak load.

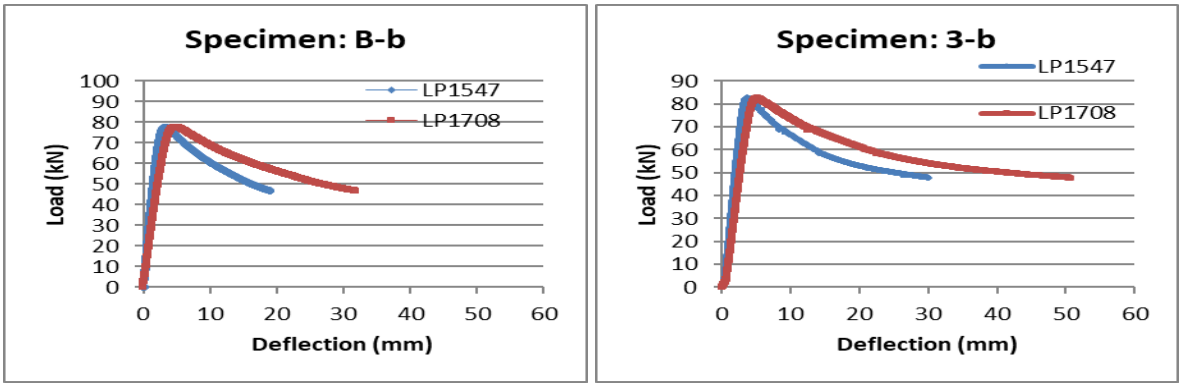

(a) **(b)**

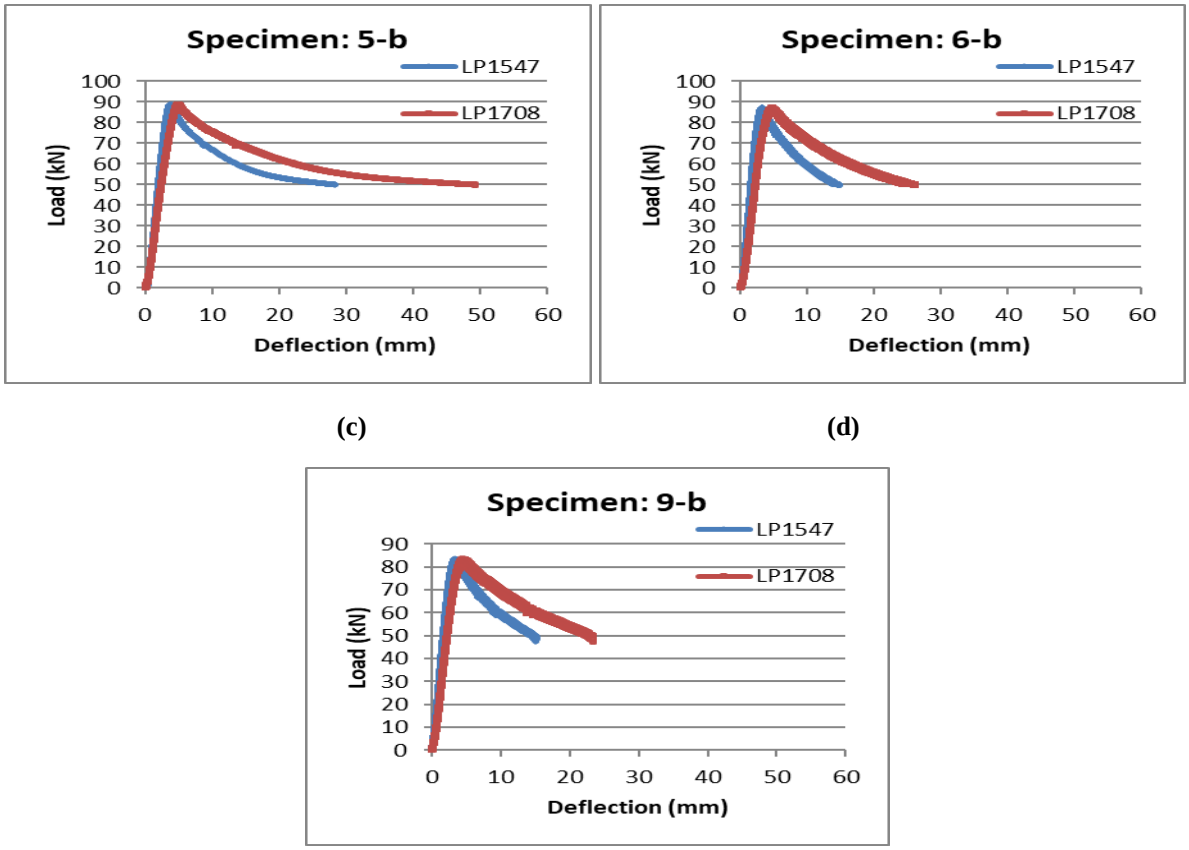

Figure 4. Load-Deflection curves of beams: (a) B-b; (b) 3-b; (c) 5-b; (d) 6-b; and (e) 9-b

Table 2. Ultimate loads and deflections for 89 × 89 × 3.5 SHS beams

Specimen		Direction (H/V)	Ultimate load (kN)	Deflection at peak load (mm)	
				LP1708	LP1547
B	b	-	77.82	4.93	3.30
3	b	H	82.73	5.12	3.69
5	b	V	88.81	4.93	3.75
6	b	V,45°	87.26	4.86	3.31
9	b	HV	83.57	4.51	3.32

Figure 5(a) shows the load-strain results of control beam B-b. As shown in Figure 5(a), elastic, plastic, peak, and post-peak behaviours are observed. The curves are linear at the initial phase, and non-linear in the second phase. Figure 5(b-e) show the load-strain curves of SHS beams with thermoplastic CFRP, overwrapped using AFP. The values of strains 1 and 2 (strain gauges 1 and 2 are located at the top of the beam) are generally negative as the top side of the beam is under compression. The values of strains 3 and 4 (strain gauges 3 and 2 are located at the bottom of the beam) are positive as the bottom side of the beam is under tension.

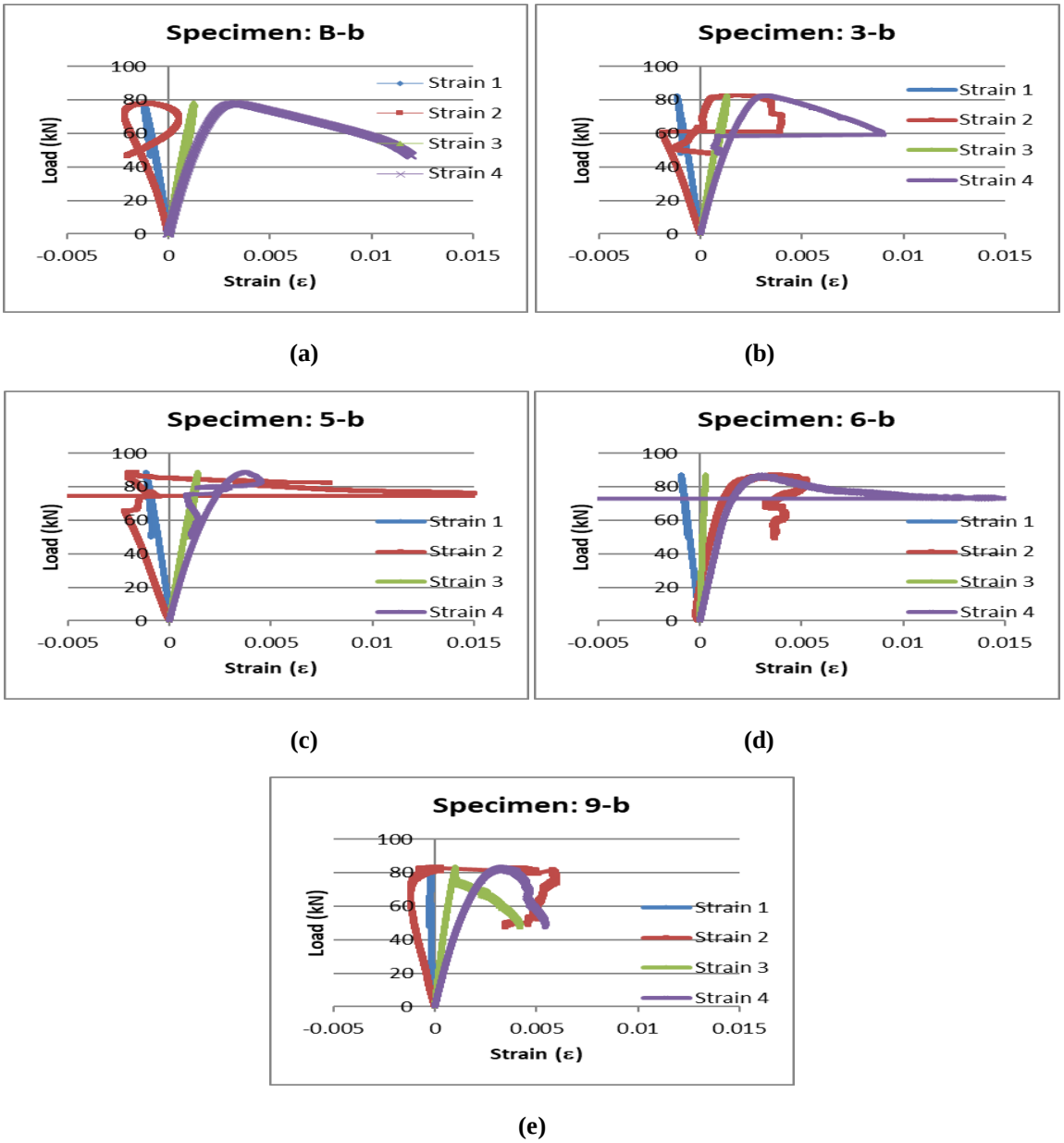

Figure 5. Load-Strain curves of beams: (a) B-b; (b) 3-b; (c) 5-b; (d) 6-b; and (e) 9-b

3.2. Failure Modes

For the SHS beams with and without thermoplastic carbon fibre reinforced polymer (CFRP), overwrapped using AFP, local deformations were observed under the load point at the control beams. As shown in Figure 6, there is inward deformation (concave deformation) on the upper surface of each beam. Outward deformations (convex deformations) were observed on the two side walls of the SHS beams. For beam specimen 3-b whose CFRP were laid longitudinally, the thermoplastic CFRP sheets separated from steel SHS, see Figure 6 (b). For beam specimens 5-b whose CFRP were laid transversally, the thermoplastic CFRP layers fractured as the load was applied on the specimens, see Figure 6(c). Figure 6(d) shows the failure mode of beam specimen 6-b whose CFRP were laid vertically and at an angle of 45°. Those 45° CFRP layers de-bonded from the thermoplastic transverse CFRP at the location of the load. For beam specimen 9-b whose CFRP were laid longitudinally and transversally, de-bonding of the thermoplastic CFRP from the steel tube was observed at the corners of the cross-section, see Figure 6(e).

(a)

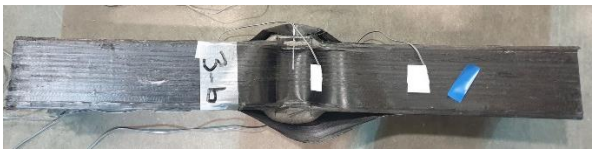

(b)

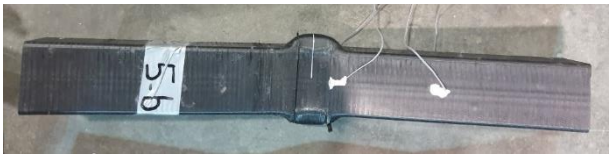

(c)

(d)

(e)

Figure 6. Failure modes of SHS beam: (a) B-b; (b) 3-b; (c) 5-b; (d) 6-b; and (e) 9-b

4. CONCLUSION

An experimental investigation on four thermoplastic CFRP overwrapped beams and a control beam was tested for the determination of the bending capacity. The steel beam specimens were made up of (SHS with dimensions of 89 mm x 89 mm x 3.5 mm. The length of each beam is approximately 750 mm. Hot gas torch-assisted AFP based manufacture of thermoplastic composites was used to strengthen the SHS tubular beam members. Loads were applied at the midspan of each beam. The beam specimens were pin connected at both ends of each beam. Two strain gauges were installed at the middle of the beam's width on the top and bottom faces of each beam to measure the strains during bending tests. Two linear potentiometers (LPs) were used at the bottom face of the beams to measure the deflections. There is inward deformation (concave deformation) on the upper surface of each beam. Outward deformations (convex deformations) were observed on the two side walls of the beams. Separation, snapping and debonding of thermoplastic CFRP layers were observed. It was found that the ultimate loads for the strengthened beams were higher than that of the control beam. To increase the ultimate load of the SHS beams reinforced with thermoplastic CFRP using AFP technique, the layers of the thermoplastic CFRP sheets should be increased. The GHT temperature in the AFP machine should be decreased as high temperatures could affect the strength of the steel.

5. ACKNOWLEDGMENTS

This project was funded by Western Sydney University (WSU) and University of New South Wales (UNSW). The authors would like to acknowledge the support received through following funding schemes of Australian Government:

ARC LIEF: An Australasian facility for the automated fabrication of high-performance bespoke components (LE140100082).

ARC ITTC: ARC Training Centre for Automated Manufacture of Advanced Composites (IC160100040).

REFERENCES

Keykha, A. H. (2017). Numerical investigation on the behavior of SHS steel frames strengthened using CFRP. *Steel and Composite Structures, An International Journal*, *24*(5), 561-568.

Oromiehie, E., Gain, A. K., & Prusty, B. G. (2021). Processing parameter optimisation for automated fibre placement (AFP) manufactured thermoplastic composites. *Composite Structures*, *272*, 114223.

Oromiehie, E., Gain, A. K., Donough, M. J., & Prusty, B. G. (2022). Fracture toughness assessment of CF-PEEK composites consolidated using hot gas torch assisted automated fibre placement. *Composite Structures*, *279*, 114762.

Oromiehie, E., Prusty, B. G., Compston, P., & Rajan, G. (2019). Automated fibre placement based composite structures: Review on the defects, impacts and inspections techniques. *Composite Structures*, *224*, 110987.

Rabinovitch, O., & Frostig, Y. (2003). Experiments and analytical comparison of RC beams strengthened with CFRP composites. *Composites part B: engineering*, *34*(8), 663-677.

Tafsirojjaman, T., Fawzia, S., Thambiratnam, D. P., & Zhao, X. L. (2021). FRP strengthened SHS beam-column connection under monotonic and large-deformation cyclic loading. *Thin-Walled Structures*, *161*, 107518.

Zhao, X. L., & Zhang, L. (2007). State-of-the-art review on FRP strengthened steel structures. *Engineering structures*, *29*(8), 1808-1823.

Proc. 3rd International Conference on Structural Engineering Research (iCSER 2022)
27-30 Nov 2022, Sydney, Australia
ISBN: 978-0-6456692-1-3

Stress-Strain Behaviours of Recycled Aggregate Concrete Under Triaxial Compression and Pore Water Pressure

Hanbing Zhao[a], Yong Hu[b,c], Mofang Yuan[d], Yunan Li[b], Wengui Li[a]*

[a] School of Civil and Environmental Engineering, University of Technology Sydney, NSW 2007, Australia
[b] Faculty of Engineering, China University of Geosciences, Wuhan, Hubei 430074, China
[c] Department of Civil Engineering, Wenhua College, Wuhan, Hubei 430074, China
[d] Faculty of Arts, Design and Architecture, The University of New South Wales, NSW 2052, Australia

Corresponding author's E-mail: wengui.Li@uts.edu.au

Abstract

Waste crushed concrete accounts for more than 70% of the construction and demolition waste, seriously occupying land space. If these waste materials can be made into recycled aggregate, it can realise sustainability in construction materials, and contribute to environmental protection. According to previous studies, recycled aggregate concrete (RAC) is not suitable for structural components of a building due to poor basic mechanical properties and durability compared with natural aggregate concrete (NAC). However, concrete is commonly under multiaxial stress states in real structures rather than simple uniaxial compressions, such as beam-column joints, bridge piers and underground structures. Moreover, most of these structures are also affected by pore water pressure when they are under triaxial compression. To explore the performance and mechanism of RAC under complicated stress states, the microstructure difference between old and new interfacial transition zones (ITZs) in RAC were analysed by electron microscope and image processing technology. The mechanical properties of RAC under triaxial compression and pore water pressure were also investigated. The results show that there were higher porosity and more microcracks in the new ITZs. Confining pressure converted the failure mode of RAC specimen from vertical splitting failure to shear failure and improved the compressive strength of RAC significantly. Pore water pressure reduced the triaxial compressive strength of concrete, but the elastic modulus of concrete was improved. According to axial-volumetric strain curves, lateral confinement increased the volumetric compression. Pore water pressure could reduce the volumetric compression when the specimen was damaged, but the value was still higher than uniaxial compression. The feasibility of using RAC in structural components gets a more comprehensive assessment.

Keywords: RAC, Image analysis, ITZ, Triaxial compression, Pore water pressure.

1. INTRODUCTION

Engineering construction contributes to the development of urbanization, whereas it has brought serious environmental problems. To achieve old urban transformation, many buildings and infrastructures near their service life were demolished, generating a large amount of construction and demolition (C&D) waste, among which abandoned crushed concrete accounts for the largest proportion (approximately 70%) (Y. Zaetang, 2016). Crushed waste concrete can be regarded as a substitute for natural coarse aggregate (NCA), named recycled coarse aggregate (RCA). However, the hardly removed old mortar on the surface of RCA weakened the bond strength between the RCA and new mortar (J. Thomas, 2018). In the case of uniaxial compressive strength, when NCA was completely replaced by RCA, the uniaxial compressive strength of concrete decreased by 10-15% (B. Wang, 2021). Therefore, many researchers concluded that RAC is incompetent for structural elements (D. Xuan, 2017; G. Dimitriou, 2018). It is worth noting that concrete is commonly under multiaxial stress states in real conditions rather than simple uniaxial compressions, such as beam-column joints, bridge piers and underground structures (Y. Chen, 2019). Studying the performance of RAC under triaxial compression states is vital for assessing its applicability to structural members.

The failure mechanism of RAC under triaxial compression is more complicated than NAC; because there are more interfaces, pores and microcracks within RAC (P. Folino, 2014). In general, the triaxial compressive strength of RAC was improved more obviously with confining pressure compared with NAC according to the testing results (J.J. Xu, 2021; P. Folino, 2014; Y. Chen, 2019). Folino and Xargay (2014) reported that when the confining pressure was 21 MPa, the triaxial compressive strength of NAC increased by 224.42% compared with uniaxial compression, while the strength of RAC increased by 252.13% under the same condition.

As we know, the pore network of concrete is intricate, so it is difficult for pore water to evaporate completely, and concrete tends to retain a quasi-saturated state for a long time (X.H. Vu, 2009; Y. Malecot, 2019). Moreover, bridge piers, dams and pile foundations etc. are inevitably exposed to underground water. The volume deformation of the structure due to high lateral restraint makes the influence of pore water pressure on the mechanical properties of concrete not negligible (X.H. Vu, 2009). Vu et al. (2015; 2009) investigated the performance of dried, wet and saturated concrete under high confinement. They found that the volumetric stiffness of saturated concrete subjected to triaxial compression was higher, but the compressive strength was limited in growth with confining pressure (X.H. Vu, 2009). Similarly, Malecot et al. (2019) examined the influence of free water and porosity on the triaxial compression behaviour of concrete. An empirical triaxial failure criterion considering uniaxial compressive strength, porosity and water content was proposed (Y. Malecot, 2019).

Although many researchers have realised that the study on pore water pressure has great significance for refining triaxial compressive behaviour and calibrating the constitutive model of concrete, few people successfully conducted triaxial compression experiments of concrete at constant pore water pressure (X. Vu, 2015; X.H. Vu, 2009; Y. Malecot, 2019). The porosity of RAC is generally higher than that of NAC (D. Pedro, 2017). The effect of pore water pressure on RAC deserves more consideration. Therefore, conventional triaxial compression tests were conducted on RAC in this study. The purpose of this paper is to investigate the stress-strain behaviour of RAC subjected to specified confining pressure and pore water pressure. The microscope observation on ITZs and failure patterns were compared. The effects of lateral confining pressure and pore water pressure on the peak stress, peak strain, elastic modulus etc. according to stress-strain curves were comprehensively analysed. This research contributes to improving the understanding of the triaxial compression behaviour of RAC affected by pore water pressure. The feasibility of using RAC in structural components gets a more accurate assessment.

2. EXPERIMENTAL PROGRAMME

2.1. Materials and specimen preparation

Cylindrical concrete specimens with a diameter of 50 mm and a height of 100 mm were fabricated for conventional triaxial compression tests. To satisfy the requirement about specimen size versus aggregate size in ASTM C192, the coarse aggregate size range used in this research was 5-16 mm. The apparent density, water absorption and crush index of the RCA used in the experiment was 2736.5 kg/m^3, 5.91 wt. % and 22 wt. % respectively. Natural river sand with a fineness modulus of 2.80, an apparent density of 2615 kg/m^3 and water absorption of 1.44% was adopted as natural fine aggregate (NFA). The particle size distribution of NFA is shown in Figure 1, which satisfies the requirements in ASTM C33. Ordinary Portland cement was mixed with water, naphthalene-based superplasticizer (SP), coarse and fine aggregate for concrete specimens. The 100% of NCA was substituted by RCA in the experiment. The mix proportion of RCA, NFA, cement, water and SP were 1055 kg/m^3, 675 kg/m^3, 498 kg/m^3, 174 kg/m^3 and 4.23 kg/m^3 respectively.

Considering the high water absorption of RCA, before the formal preparation of concrete mixtures, the RCA was soaked in water for 24 h and kept in a saturated surface dry (SSD) state. After all the raw materials were ready, coarse, and fine aggregate was poured into a drum mixer and dry-mixed for 1 min. Then, cement was poured into the drum mixer and dry-mixed with aggregate for another 1 min. Finally, the mixed solution with water and SP was poured into the mixer slowly and evenly. The mixer continued to work for 2-3 min until all constituents were mixed uniformly. When the mixing was

done, slump tests were conducted immediately. The slump of fresh RAC mixture was about 120 mm.

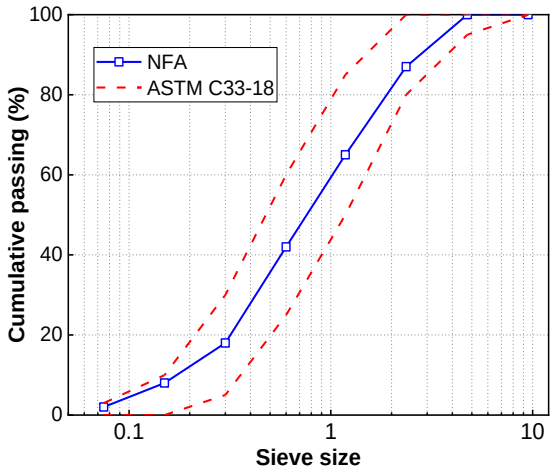

Figure 1. Particle size distribution of fine aggregate

The fully mixed fresh concrete mixtures were cast in Φ50 mm × 100 mm cylinder moulds and consolidated by a vibration table until no large bubbles emerged. The surface of concrete mixture exposed to the air was covered with a plastic film to prevent water evaporation. After curing in the moulds for one day, the solidified concrete specimens were transferred to a standard curing room (25 ± 5℃, 95% RH) for 28 days.

2.2. Microstructure test setup

Rectangular concrete blocks with the size of around 30 mm × 10 mm × 8 mm were cut out from the centre part of concrete specimens and used as samples for microscope analysis. The sample contained aggregate, ITZs and cement mortar matrix. The schematic diagram of RAC is shown in Figure 2. After that, the sample was embedded in epoxy resin in a Φ35 mm cylindrical mould, and the surface waiting for the observation was exposed to the air. Under the protection of epoxy resin, the sample was ground by grits abrasive papers and polished by 0.3 μm alumina and 0.05 μm cerium oxide slurry until a smooth surface was obtained. The ash and particles on the sample surface were cleaned by an ultrasonic bath. Finally, the prepared samples were placed in a vacuum drying oven at 40 ℃ for 48 h.

Old and new ITZs in RAC were observed by a scanning electron microscope (SEM, Zeiss EVO LS15). The accelerating voltage was set as 15 kV. To enhance the conductivity of the sample, the surface was sputter-coated with a layer of 10 nm carbon. At least 20 backscattered electron (BSE) images were obtained for each ITZ at a magnification of 500 ×.

Many researchers (Djerbi, 2018; P. Vargas, 2017; P.R. Rangaraju, 2010) have used image analysis techniques to calculate the proportion of pores, hydrated products and unhydrated products at ITZ. This research adopted a similar method. The BSE images were divided into 15 successively strips with 5 μm in width from aggregate surface to cement mortar. Image Pro was used to analyse the BSE image strips. According to the grey level, pores and cracks can be determined. The volume fraction of each constituent at different distances from the aggregate surface to the mortar matrix was obtained by dividing the object area by the total area of the strip.

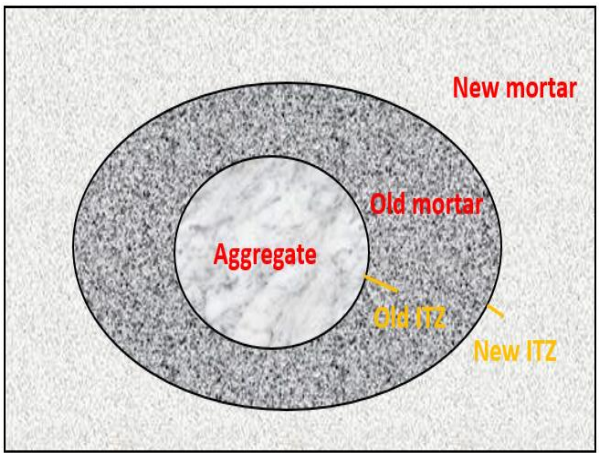

Figure 2. Schematic diagram of ITZs in RAC

2.3. Triaxial and pore pressure test setup

A triaxial multi-field coupled testing system (RTX-1000) was used to test the compression performance of concrete under different confining pressure and pore water pressure. The system has two axial Linear Variable Differential Transformers (LVDTs) and one circumferential LVDT (all with ± 2.5 mm range), for measuring axial and circumferential strains respectively. The system has an independent servo-controlled axial pressure actuator, confining pressure actuator and pore pressure actuator, which can apply 1000 kN of axial load and 70 MPa of confining and pore pressure respectively.

Table 1. Testing parameters

Specimens	**σ_c**	**σ_p**
RAC-0	0	0
RAC-14	14 MPa	0
RAC-14-9	14 MPa	9 MPa

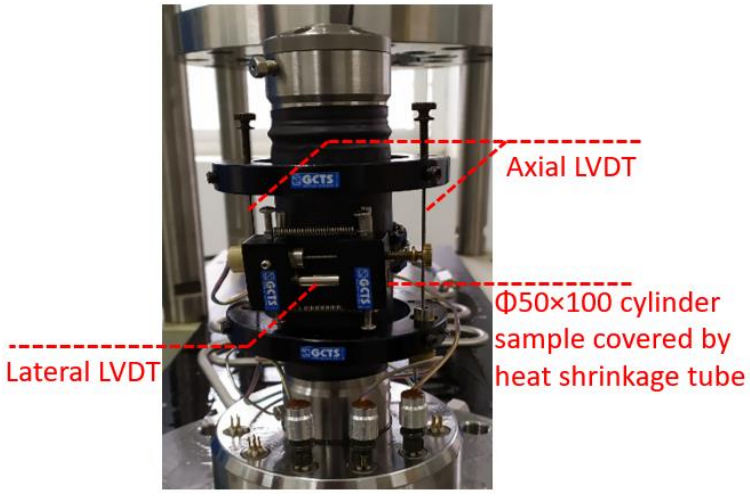

Figure 3. Concrete specimen awaiting test

Two different levels of confining pressure ($\sigma_c = \sigma_1 = \sigma_2$ = 0, 14 MPa) and two different levels of pore pressure (σ_p = 0, 9 MPa) were designed in this experiment. The specific pressure parameters are

shown in Table 1. Both ends of concrete specimens were ground flat with an error of less than 1 mm by a grinder. To prevent the hydraulic oil from being pressed into the concrete specimen, a heat shrink tube was wrapped and tightly attached to the surface of the specimen. The holes on the surface of the concrete specimen were sealed with the same water-cement ratio mortar. The sample covered with a heat shrink tube and installed LVDTs is shown in Figure 3.

The stress states of concrete specimens and the loading procedure in the experiment are shown in Figures 4 and 5 respectively. The uniaxial compression test ($\sigma_c = \sigma_p = 0$) was carried out at first. To ensure full contact between the loading panel and the compression surface of the specimen at the initial stage of the stress-strain curve, the specimen was loaded to 10% of the peak load and maintained for 20 s. The strain control method was adopted at the rate of 0.2%/min until 1.5% in the subsequent compression process. For triaxial compression tests ($\sigma_c \neq 0$, $\sigma_p = 0$), the test started with stress control at a rate of 0.2 MPa/s. Axial and confining pressure was improved to the targeted confinement value at the same time and maintained the concrete specimen under a hydrostatic pressure condition for 20 s. Then, the axial load was applied to the concrete specimen at a strain rate of 0.2%/min until 4%-5%. Regarding coupled test of confining pressure and pore water pressure, to make the internal pore pressure uniform, concrete specimens were vacuum-saturated for 24 h before the formal test. After that, pressure in three directions and pore pressure were raised to their respective designed values. The remaining steps were the same as in pure triaxial compression tests: the axial load continued rising at a rate of 0.2%/min and the corresponding stress-strain curves were obtained.

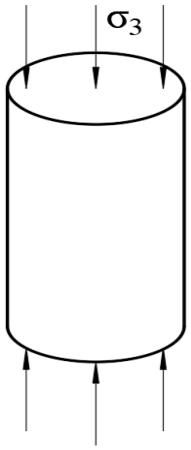

(a) Uniaxial compression

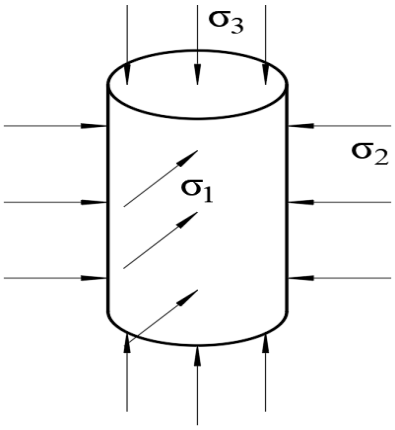

(b) Triaxial compression

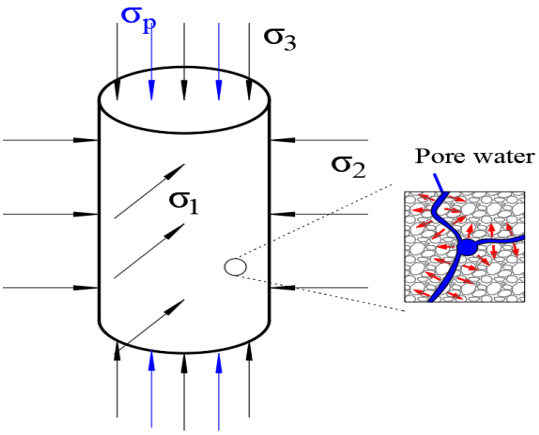

(c) Triaxial compression and pore water pressure

Figure 4. Stress states of concrete specimens

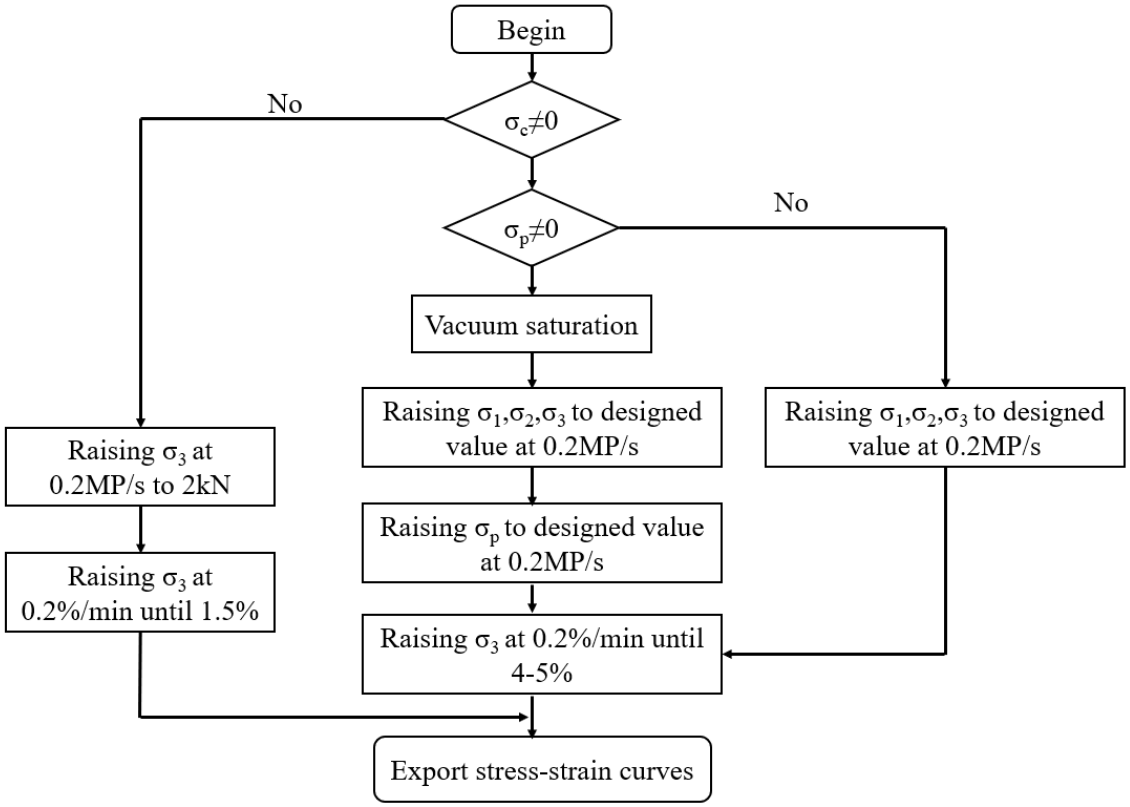

Figure 5. Flow chart of loading scheme

3. RESULTS AND DISCUSSIONS

3.1. Microstructure test results

Many researchers believe that the ITZ is the weakest part of the concrete structure in mechanical failure (Luo, 2021; W. Li, 2012; Z. Luo, 2022). To investigate the microstructure of the old and new ITZs within RAC, the volume fraction of each constituent (pores & cracks, reacted products and unreacted products) was collected and statistically analysed based on BSE images and image analysis technique. Figures 6 and 7 show the process flow of typical BSE images at new and old ITZs.

The grey value difference of constituents in BSE images was highlighted by adjusting the brightness and contrast. The interface of the aggregate to the ITZ can be manually determined and the aggregate part was removed. For the segmentation of constituents at ITZs and mortar matrix, grey value thresholds have to be determined. If the grey value threshold is too narrow, the entire area of the object cannot be completely selected. Correspondingly, if the grey value threshold is too wide, 'overflow' will occur, resulting in a higher calculated value than the actual value. According to Wong et al., (2006) the lower threshold level of pores in concrete was 0. The upper threshold level can be determined by the intersection between the two liner fittings at the inflection of the cumulative area curve with grey values, as shown in Figures 6 (b) and 7 (b). They declared, however, that this method may slightly overestimate the actual grey value threshold. In this study, Wong's method combined with manual selection was used to determine the grey value range of each constituent in RAC. Pores and cracks, reacted products and unreacted products were segmented by red, green and blue, respectively. The cement mortar with 75 μm from the aggregate boundary was equally divided into 15 strips of 5 μm in width. The volume fractions of constituents in the ITZ and a part of the mortar matrix adjoining the ITZ were calculated by the image analysis software. The statistical results are shown in Figure 8.

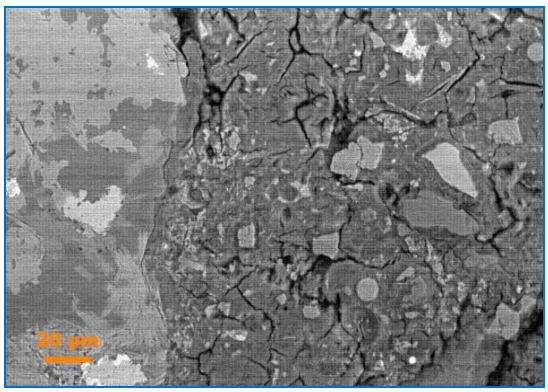

(a) BSE image at old ITZ

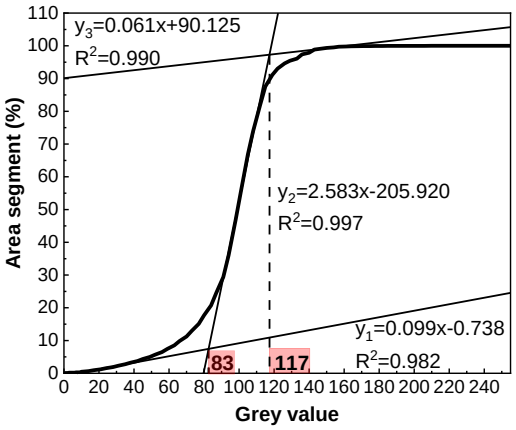

(b) Grey value threshold determination

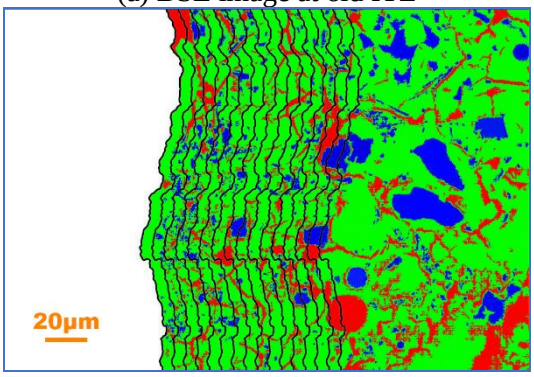

(c) Constituents' segmentation

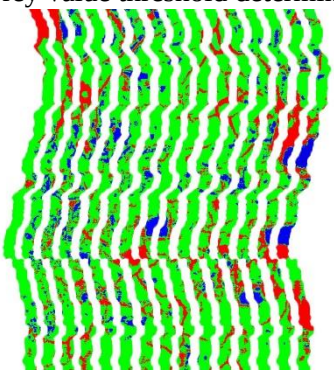

(d) Strips division

Figure 6. Image process of BSE photos at old ITZs

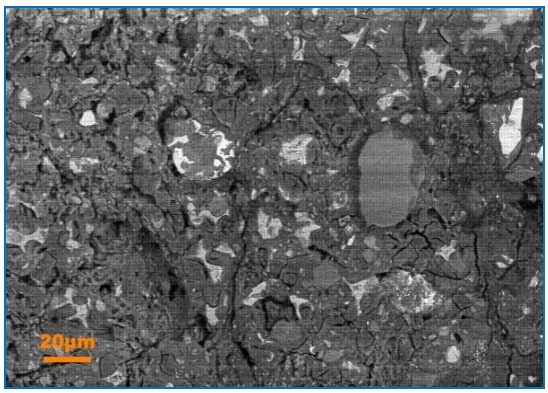

(a) BSE image at new ITZ

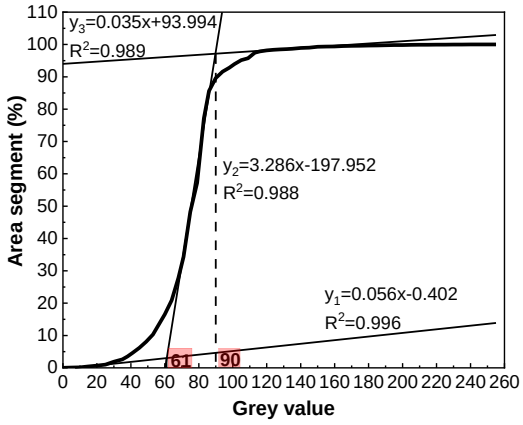

(b) Grey value threshold determination

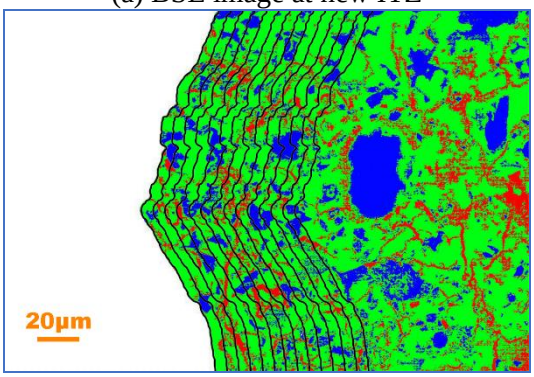

(c) Constituents' segmentation

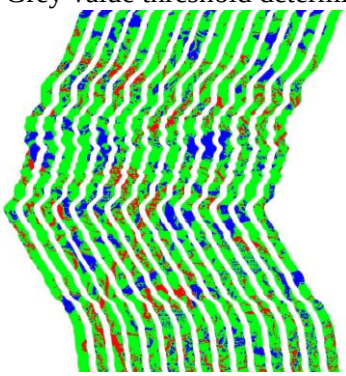

(d) Strips division

Figure 7. Image process of BSE photos at new ITZs

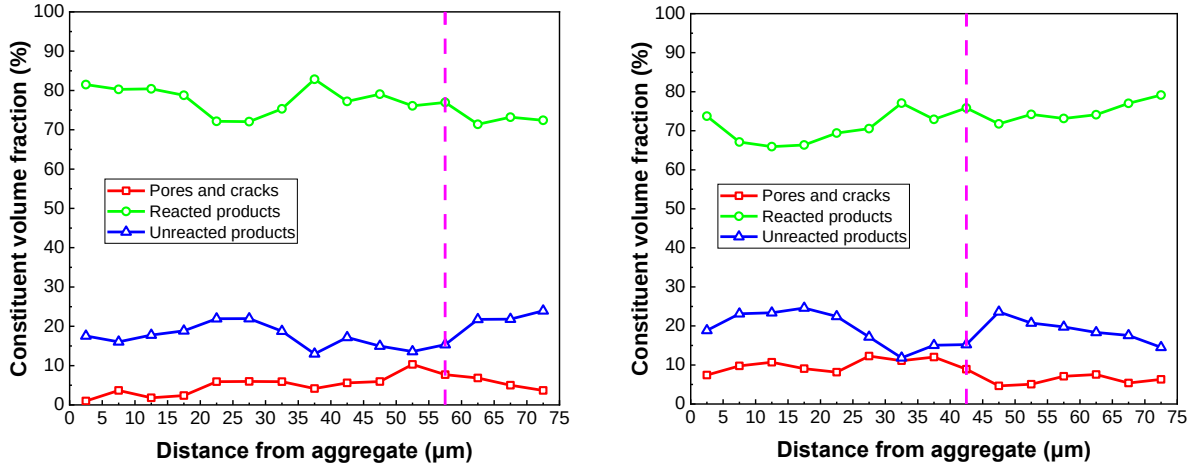

(a) Old ITZ (b) New ITZ

Figure 8. Statistical results of constituent proportions at ITZs

As shown in Figure 8 (a), the volume fraction of pores & cracks gradually decreased beyond 55-60 μm from the aggregate boundary. According to existing research results, the porosity in the ITZ region is higher and unreacted particles are comparatively less due to the 'wall effect' (G. Fang, 2020; I.F. Saez del Bosque, 2017; K. Lyu, 2019; M. Wang, 2019). Therefore, it can be confirmed that the width of the old ITZ in the RAC was about 55-60 μm. The volume fraction of pores & cracks in the old ITZ increased slightly with the distance from the aggregate boundary, and the value remained within 0-10%. The unreacted products include NFA and a small amount of unhydrated cement particles. NFA mainly plays the role of filling gaps in the mortar (D. Feng, 2016). In the area with less NFA, there were more micro-cracks caused by cement hydration shrinkage, so the volume fractions of pores & cracks and unreacted products showed roughly opposite trends. The volume fraction of reacted products, including CSH, CH and CAH in the old ITZ was between 75% to 85%.

In a similar way, the width of the new ITZ in the RAC can be determined to be approximately 40-45 μm. The volume fraction difference of unreacted products between old and new ITZs was not obvious, while the volume fraction of pores & cracks in new ITZ was higher. This is due to the lower content of reacted products (65%-75%) in the new ITZ, indicating that the bond strength of the new mortar to RCA may be weaker than that of the old mortar to NCA.

3.2. Triaxial test results

3.2.1. Failure patterns

Crack distributions of RAC under uniaxial compression (σ_3>0, σ_c=σ_p=0), pure triaxial compression (σ_3>0, σ_c=14 MPa, σ_p =0) and confining pressure coupled with pore water pressure (σ_3>0, σ_c=14 MPa, σ_p=9 MPa) are shown in Figure 9. It can be seen from Figure 9 (a) that when concrete was damaged by uniaxial compression, serval vertical branch cracks formed on the surface of the concrete. These cracks coalesced into the main crack showing vertical splitting failure mode. The pore water pressure would not pose a clear difference in the failure pattern of concrete under triaxial compression. It can be seen from Figures 9 (b) and (c) that there was only one oblique crack when the concrete was damaged by triaxial compression. Different from the failure mode under uniaxial compression, the concrete specimen exhibited a shear failure mode affected by confining pressure.

(a) Uniaxial compression (b) Triaxial compression (c) Triaxial compression with pore water pressure

Figure 9. Damage patterns of RAC samples at different loading conditions

3.2.2. Stress-strain curves analysis

Figure 10 shows the stress and strain development law of RAC under multiaxial stress and pore water pressure states. According to Figure 10 (a), confining pressure improved the compressive strength of concrete obviously. The peak deviatoric stress was improved by over three times compared with uniaxial compressive strength under 14 MPa of confining pressure. In addition to mechanical strength, confining pressure restricted the radial deformation of concrete and enhanced axial peak strain, which indicates that the ductility of concrete was improved under triaxial compression. The elastic modulus of concrete under triaxial compression was higher than that of concrete under uniaxial compression. This shows that confining pressure increases the early deformation resistance of concrete. However, the deformation of concrete increases significantly when it is near failure. The stress-strain behaviour of concrete under the coupled effect of confining pressure and pore water pressure was similar to that of concrete under pure triaxial compression. Pore pressure decreased the triaxial compressive strength of concrete and improved elastic modulus slightly because pore water promoted the propagation of microcracks caused by triaxial load and prevented the compressive deformation of concrete specimens.

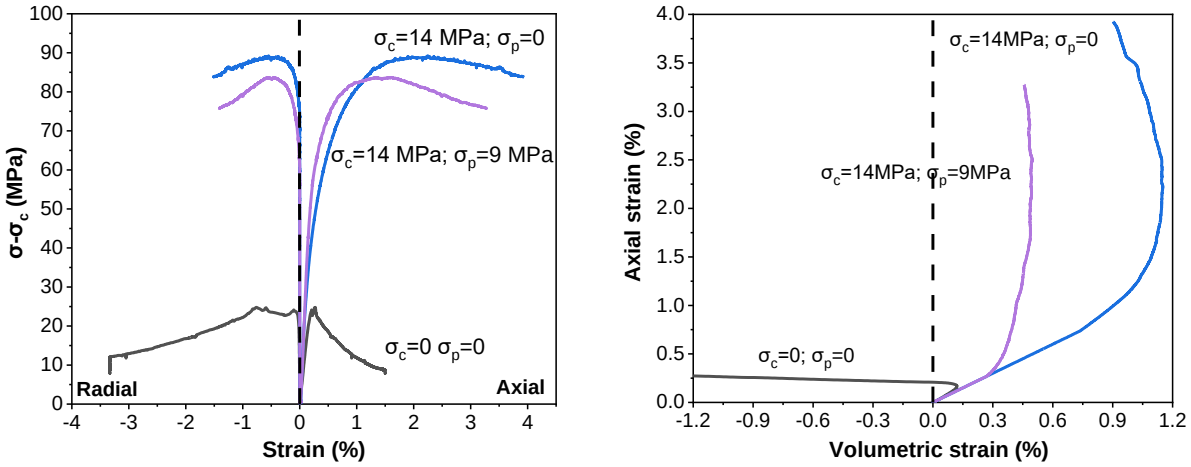

(a) Stress-strain curves (b) Axial-volumetric strain curves

Figure 10. Mechanical property curves of RAC under confining pressure and pore water pressure

Figure 10 (b) shows the relationship between axial and volumetric strain of RAC under different confinement and pore pressure levels. The volume of concrete decreased first and then increased with axial strain during the compression process, and the initial compression trends of concrete were similar regardless of whether it was affected by confining pressure and pore pressure. Volumetric

compression of concrete considerably increased under triaxial compression. In addition, pore water pressure can improve the volumetric deformation resistance of concrete, but the volumetric strain was still higher than that of concrete under uniaxial compression.

4. CONCLUSIONS

To explore the mechanical properties of RAC under the coupled action of confining pressure and pore water pressure, SEM, Zeiss EVO LS15 and triaxial multi-field coupled testing system (RTX-1000) were adopted to obtain BSE images at ITZs and stress-strain curves in the triaxial compression process respectively. According to the characteristics of RAC, the proportion of each constituent in the new and old ITZ was focused on, and the weakest area of RAC was deduced. In the subsequent mechanical property tests, the failure modes of specimens under different stress conditions were compared. Stress-strain curves and the propagation of volume strain-axial strain curves converted from testing data were analysed in detail. The main conclusion of this study are as follows:

(1) The width of old ITZ in RAC was around 55-60 μm. The volume fraction of pores & cracks within the old ITZ increased slightly with the distance from the aggregate boundary (between 0-10%), but gradually decreased beyond the range of the old ITZ. Unreacted products showed an opposite trend to pores & cracks, and the reacted products accounted for the largest proportion, between 75%-85%.

(2) The width of the new ITZ was slightly lower than the old ITZ. However, the porosity within the new ITZ was between 5% and 15%, which was higher than that of the old ITZ. Moreover, the content of hydration products in the new ITZ was lower than that in the old ITZ. This evidence indicated that RAC was more likely to be damaged from the new ITZ when it is subjected to mechanical loads.

(3) Many cracks along the load direction emerged on the surface of specimen when RAC was under uniaxial compression, showing vertical splitting failure mode. Confining pressure converted the failure mode of RAC into a shear failure mode. Only one oblique crack formed on the surface of specimen under triaxial stress states. In addition, the pore water pressure would not affect the failure pattern of the RAC specimen.

(4) The confining pressure limited the lateral deformation of the RAC, thus significantly increasing the compressive strength of the specimen. When the specimen was subjected to the combined action of confining pressure and pore water pressure, the compressive strength of RAC decreased slightly compared with the pure triaxial compression condition, but the elastic modulus was improved. This is because the pore water promoted the development of internal micro-cracks during the compression process, meanwhile providing an obstacle to vertical deformation.

(5) Due to the lateral restraint, the volumetric compression of the specimen under triaxial compression was significantly higher than that under uniaxial compression. Pore water pressure reduced the volumetric compression of the specimen but was still higher than the figure under uniaxial compression.

ACKNOWLEDGMENTS

The authors appreciate Australian Research Council (ARC), Australia (DE150101751, DP220100036, DP220101051, IH150100006; IH180100010) and University of Technology Sydney Research Academic Program at Tech Lab (UTS RAPT).

REFERENCES

B. Wang, L. Yan, Q. Fu, B. Kasal. (2021). A Comprehensive Review on Recycled Aggregate and Recycled Aggregate Concrete. *Resour. Conserv. Recycl., 171*, 105565.

D. Feng, X. Ren, J. Li (2016). Stochastic damage hysteretic model for concrete based on micromechanical approach. *Int. J. Non-Linear Mech., 83*, 15-25.

D. Pedro, J. de Brito, L. Evangelista (2017). Structural concrete with simultaneous incorporation of fine and coarse recycled concrete aggregates: Mechanical, durability and long-term properties. *Constr. Build. Mater., 154*, 294-309.

D. Xuan, B. Zhan, C.S. Poon. (2017). Durability of recycled aggregate concrete prepared with carbonated recycled concrete aggregates. *Cem. Concr. Compos., 84*, 214-221.

Djerbi, A. (2018). Effect of recycled coarse aggregate on the new interfacial transition zone concrete. *Constr. Build. Mater., 190*, 1023-1033.

G. Dimitriou, P. Savva, M.F. Petrou. (2018). Enhancing mechanical and durability properties of recycled aggregate concrete. *Constr. Build. Mater., 158*, 228-235.

G. Fang, M. Zhang. (2020). The evolution of interfacial transition zone in alkali-activated fly ash-slag concrete. *Cem. Concr. Res., 129*, 105963.

H.S. Wong, M.K. Head, N.R. Buenfeld. (2006). Pore segmentation of cement-based materials from backscattered electron images. *Cem. Concr. Res., 36*, 1083-1090.

I.F. Saez del Bosque, W. Zhu, T. Howind, A. Matías, M.I. Sanchez de Rojas, C. Medina. (2017). Properties of interfacial transition zones (ITZs) in concrete containing recycled mixed aggregate. *Cem. Concr. Compos., 81*, 25-34.

J. Thomas, N.N. Thaickavil, P.M. Wilson. (2018). Strength and durability of concrete containing recycled concrete aggregates. *J. Build. Eng., 19*, 349-365.

J.J. Xu, W.G. Chen, C. Demartino, T.Y. Xie, Y. Yu, C.F. Fang, M. Xu (2021). A Bayesian model updating approach applied to mechanical properties of recycled aggregate concrete under uniaxial or triaxial compression. *Constr. Build. Mater., 301*, 124274.

K. Lyu, E.J. Garboczi, W. She, C. Miao. (2019). The effect of rough vs. smooth aggregate surfaces on the characteristics of the interfacial transition zone. *Cem. Concr. Compos., 99*, 49-61.

Luo, Z. (2021). Comparison on the properties of ITZs in fly ash-based geopolymer and Portland cement concretes with equivalent flowability. *Cem. Concr. Res., 143*, 106392.

M. Wang, Y. Xie, G. Long, C. Ma, X. Zeng. (2019). Microhardness characteristics of high-strength cement paste and interfacial transition zone at different curing regimes. *Constr. Build. Mater., 221*, 151-162.

P. Folino, H. Xargay. (2014). Recycled aggregate concrete – Mechanical behavior under uniaxial and triaxial compression. *Constr. Build. Mater., 56*, 21-31.

P. Vargas, O. Restrepo-Baena, J.I. Tobón. (2017). Microstructural analysis of interfacial transition zone (ITZ) and its impact on the compressive strength of lightweight concretes. *Constr. Build. Mater., 137*, 381-389.

P.R. Rangaraju, J. Olek, S. Diamond. (2010). An investigation into the influence of inter-aggregate spacing and the extent of the ITZ on properties of Portland cement concretes. *Cem. Concr. Res., 40*, 1601-1608.

W. Li, J. Xiao, Z. Sun, S. Kawashima, S.P. Shah (2012). Interfacial transition zones in recycled aggregate concrete with different mixing approaches. *Constr. Build. Mater., 35*, 1045-1055.

X. Vu, M. Briffaut, Y. Malecot, L. Daudeville, B. Ciree. (2015). Influence of the Saturation Ratio on Concrete Behavior under Triaxial Compressive Loading. *Sci. Technol. Nucl. Ins.*, 976387.

X.H. Vu, Y. Malecot, L. Daudeville, E. Buzaud. (2009). Experimental analysis of concrete behavior under high confinement: Effect of the saturation ratio. *Int. J. Solids Struct., 46*, 1105-1120.

Y. Chen, Z. Chen, J. Xu, E.M. Lui, B. Wu. (2019). Performance evaluation of recycled aggregate concrete under multiaxial compression. *Constr. Build. Mater., 229*, 116935.

Y. Malecot, L. Zingg, M. Briffaut, J. Baroth. (2019). Influence of free water on concrete triaxial behavior: The effect of porosity. *Cem. Concr. Res., 120*, 207-216.

Y. Zaetang, V. Sata, A. Wongsa, P. Chindaprasirt (2016). Properties of pervious concrete containing recycled concrete block aggregate and recycled concrete aggregate. *Constr. Build. Mater., 111*, 15-21.

Z. Luo, W. Li, K. Wang, S.P. Shah, D. Sheng (2022). Nano/micromechanical characterisation and image analysis on the properties and heterogeneity of ITZs in geopolymer concrete. *Cem. Concr. Res., 152*, 106677.

Proc. 3rd International Conference on Structural Engineering Research (iCSER 2022)
27-30 Nov 2022, Sydney, Australia
ISBN: 978-0-6456692-1-3

Effect of Rice Straw Ash on mechanical properties of Fly Ash Based Geopolymer Concrete Cured at Elevated Temperature

Md. Ashraful Habib[1*], Md. Ahnaf Abid Basunia[1], Md. Rakibul Islam[1], Jani Ahammad[1], Md. Ibrahim Mostazid[1]

[1] *Department of Civil Engineering, Hajee Mohammad Danesh Science & Technology University, Dinajpur, Bangladesh*
**Corresponding author:nE-mail: ashrafulcivilhstu@gmail.com*

ABSTRACT

In this study, geopolymer concretes (GPC) are prepared from varying proportions of low-calcium fly ash (FA) and rice straw ash (RSA). The objective is to investigate the effect of RSA on FA based geopolymer concrete characterised by density, compressive, and tensile strength. Specimens were prepared by substituting 10 wt.%, 20 wt.%, 30 wt.%, and 40 wt.%, respectively of the FA by RSA, and 100 wt.% FA was considered as a control mix. As alkaline activator, sodium hydroxide (NaOH) and sodium silicate (Na_2SiO_3) solutions were used. The specimens were cured at 65 ℃ temperature for first 24 hours and then cured at room temperature (25 ± 2 ℃) until test date. The maximum and minimum compressive strength of the concrete mixes was found 45.1 and 17.07 MPa, respectively at 28 days curing, where the tensile strength ranged from 1.53 to 2.52 MPa. Density of the concrete mixes ranged from 2048 to 2196 kg/m^3. The experimental results show that 10% RSA incorporation gave the maximum compressive strength, while some of the other mixes also exceeded the M30 grade concrete strength.

***Keywords**: Geopolymer concrete; Fly ash; Rice straw ash; Thermal curing; Density; Compressive strength; Split tensile strength*

1. INTRODUCTION

In the present day, sustainable construction is a major concern. Since ordinary Portland cement (OPC) concrete is the primary building material for construction all over the world, it has a direct impact on the growth of the OPC industry. According to statistics, the production process of OPC alone is responsible for 8% of the world's current anthropogenic CO_2 emissions (Hardjito et al., 2004a). Therefore, researchers are working to develop stronger, more environmentally friendly concrete than conventional OPC concrete. As a result, alkali-activated binders referred to as "geopolymers" have come out with supreme focus in this field (Xie et al., 2020). The majority of industrial and agricultural waste materials such as low-calcium fly ash (FA), ground granulated blast furnace slag (GGBFS), rice husk ash (RHA), etc. have become used to produce geopolymer concrete (GPC) as experimented by Karthik et al. (2017), Wallah and Rangan (2006). By polycondensing -Si-O-Al-O oligomers, geopolymer binder is formed by three-dimensional amorphous formations (Panagiotopoulou et al., 2009). Alkali hydroxides, alkali silicates, alkali carbonates, or their combinations are the most common activating solutions used in GPC (Wijaya et al., 2017). Researchers found that FA based geopolymer concrete (GPC) has comparable physical and mechanical properties to conventional OPC concrete (Nikoloutsopoulos et al., 2021).

Hardjito et al. (2004b) investigated the influence of various parameters (like- molarity of NaOH, Na_2SiO_3 to NaOH ratio, curing temperature, curing time, age of curing) on the compressive strength of FA based GPC. They achieved the maximum compressive strength of 67.6 MPa for 14M NaOH solution when cured at 60 ℃ for first 24 h with Na_2SiO_3/NaOH ratio of 2.5. Ryu et al. (2013) investigated the effect of various alkaline activator with different molarity on FA based geopolymer concrete and observed that higher molarity of NaOH yielded higher strength. Wallah and Rangan (2006) studied the long-term performance of class F fly ash-based GPC where a combination of Na_2SiO_3 and NaOH

solution was used as the alkaline liquid. They found when the concentration of the NaOH solution was 8 M, the average compressive strength reached around 60 MPa.

Global production of rice straw is significant (731 million tons per year) as investigated by Michailos and Webb (2020). Managing rice straw is a concerning issue for many countries. Field burning of rice straw results in significant air pollution (Yuan et al., 2014). However, it has the potential to be used in geopolymer concrete production. According to Roselló et al. (2017), RSA is a potential pozzolana which can show cementing properties after a 7 – 28 days reaction process. In addition, its chemical composition is comparable with class F FA as investigated by El-Sayed and El-Samni (2006), Khan et al. (2013). Though several investigations took place on FA based GPC, there is hardly any study examined the combination of FA and RSA. Therefore, the authors of this study aimed to see the effect of RSA on FA based GPC to investigate its effect on density, compressive and tensile strength by maximising the incorporation of RSA (up to 40%).

2. MATERIALS AND METHODOLOGY

2.1. Fly Ash

Fly ash is a potential pozzolanic material, and when combined with activator forms cementitious composites. It is a very fine gray dust composed primarily of spherical and glassy particles produced by coal-based power plants. Class F fly ash was collected from Barapukuria Coal Mine Company Limited (BCMCL) located at Parbatipur Upazila in Dinajpur, Bangladesh. The chemical composition of BCMCL class F fly ash is presented in Table 1 as experimented by Khan et al. (2013). X-ray fluorescence (XRF) analysis was utilised to find out the chemical composition of the FA.

2.2. Rice Straw Ash

Rice straw has about 15% ash after burning; thus for every 1000 kg of rice straw burnt, 150 kg of ash and 82% silica content are produced. Rice straw was collected from a local village and sun-dried for about 8 h to eliminate extra moisture. Then it was kept into a chamber made of steel and burnt at a temperature of about 650-800 °C, and grounded carefully after collection and the particles were passed across 100 μm sieve.

Fig.1. Fly ash

Fig. 2. Rice straw ash

2.3. Aggregates

Fine sand (river sand) was used as fine aggregate, which was collected from Dhepa river, Dinajpur, Bangladesh. Crushed stone (maximum size 20 mm) was used as coarse aggregate in this experiment. Various tests were carried out on the aggregates to find their physical properties that are presented in Table 2.

2.4. Distilled Water

Distilled water with pH of 7 was used to prepare 10 M NaOH solution and as extra water in the concrete mixes. It was collected from the Chemistry laboratory of Hajee Mohammad Danesh Science and Technology University, Dinajpur, Bangladesh.

2.5. Alkaline Solution

The mechanism of geo-polymerisation enormously depends on the alkaline activator solution. As an alkaline solution, NaOH and Na_2SiO_3 were employed. The local producer supplied commercial Na_2SiO_3 in liquid state and NaOH in pellet form which was in 99% purity. To produce a 10 M NaOH solution, the pellets of NaOH were dissolved in distilled water. The NaOH solution and liquid Na_2SiO_3 solution were blended together to form the activation solution.

Fig. 3. NaOH (10 M) solution

Fig. 4. Na_2SiO_3 solution

Table 1. Chemical composition of FA sample determined by **XRF analysis (Khan et al., 2013)**

Composition	Percent (%)	Composition	Percent (%)
SiO_2	50.20	P_2O_5	0.66
Al_2O_3	40.10	SO_3	0.45
Fe_2O_3	3.32	MnO	0.05
TiO_2	2.38	NiO	0.01
CaO	1.29	CuO	0.0158
MgO	0.20	ZnO	0.0068
Na_2O	0.06	PbO	0.0073
K_2O	0.93	Loss on ignition	2.00

Table 2. Physical properties of aggregates

Materials	Specific gravity	Water absorption (%)	Bulk density (kg/m^3)	Fineness modulus (FM)
Fine aggregate	2.65	1.6	1620	2.54
Coarse aggregate	2.76	0.33	1734	6.85

2.6. Preparation of Geopolymer Concrete

The mix proportions of RSA incorporated GPC have been represented in Table 3. The binder-to-fine aggregate-to-coarse aggregate ratio was fixed as 1:1:1.5. For mixes R10, R20, R30 and R40, RSA incorporation was 0 wt.%, 10 wt.%, 20 wt.%, 30 wt.% and 40 wt.%, respectively of the total binder. 100% FA incorporated GPC mix (F100) was considered as a control mix. The GPC mixes included solution (Na_2SiO_3 and NaOH) to binder ratio of 0.6, where Na_2SiO_3 to NaOH ratio was 2.5. At first, the solid ingredients were well-mixed by using a mechanical pan mixer and mixed uniformly for about 4 min. Then the liquid solution and water were poured into the mixture successively and blending was conducted for another 5–6 minutes until the desired consistency was achieved. The freshly mixed concrete was put into the cylindrical molds (100 mm x 200 mm) in 3 layers, and each layer was tamped by a tamping rod 25 times. After that, the molds were vibrated for 30 to 40s. Finally, the specimens were kept in the oven at a steady temperature of 65 ℃ for 24 h, and the concrete specimens were demolded after 24 h of curing and rested in an open air (25 ± 2 ℃) until the testing ages.

Table 3. Mix combinations for GPC (kg/m^3)

Mix ID	FA	RSA	SH	SS	Sand	CA	H_2O	Water/Ash
F100	579	0	98	245	579	869	12	0.02
R10	521	58	98	245	579	869	12	0.02
R20	463	116	98	245	579	869	12	0.02
R30	405	174	98	245	579	869	12	0.02
R40	347	232	98	245	579	869	12	0.02

[RSA = Rice Straw Ash, SH=NaOH, SS=Na_2SiO_3, FA = Fly ash, CA=Coarse Aggregate]

Fig. 5. Oven curing

Fig. 6. Compressive strength test

3. RESULTS AND DISCUSSION

3.1. Density

Dry density of Geopolymer concrete was measured at 28 days for all five mixtures, as shown in Fig. 7. The mix R10 possessed a maximum density of 2005 kg/m^3 than all other RSA incorporated mixes. On the contrary, the incorporation of 40 % RSA content of FA yielded a lower density than other mixes. The mix F100 (100% FA) possessed the highest density of 2073 kg/m^3, whereas for incorporating 50% GGBFS in FA based GPC, Rao and Venu (2020) attained a higher density of 2480 kg/m^3 (which is higher than this study) with alkaline liquid to binder ratio as 0.6.

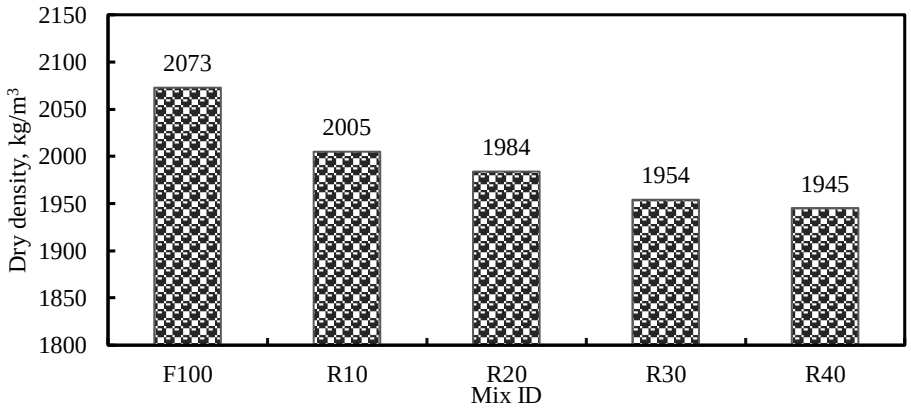

Fig. 7. Dry density of GPC after 28 days of curing

3.2. Compressive Strength

The compressive strength of GPC made with five different percentage replacements of RSA (0 wt.%, 10 wt.%, 20 wt.%, 30 wt.%, 40 wt.%) of total binder was conducted at 7 and 28 days are shown in Table 4. 10% RSA impregnation of total binder yielded the maximum compressive strength of 45.1 MPa, after increasing the incorporation of RSA possessed negative results and reached a lower value of 17.07 MPa

at 40% RSA incorporation. Besides, the control mix F100 attained 44.47 MPa, whereas Vignesh and Vivek (2015) achieved 16.3 MPa at 28 days for 100% FA incorporated GPC, which is much lower compared to other outcomes, and obtained a maximum of 45.55 MPa while 40% GGBFS incorporated of the total binder (FA).

Table 4. Compressive strength of GPC

Days	Compressive strength in MPa obtained after adding RSA				
	0%	10%	20%	30%	40%
7	22.87	29.97	16.77	8.76	7.1
28	44.47	45.1	30.73	22.2	17.07

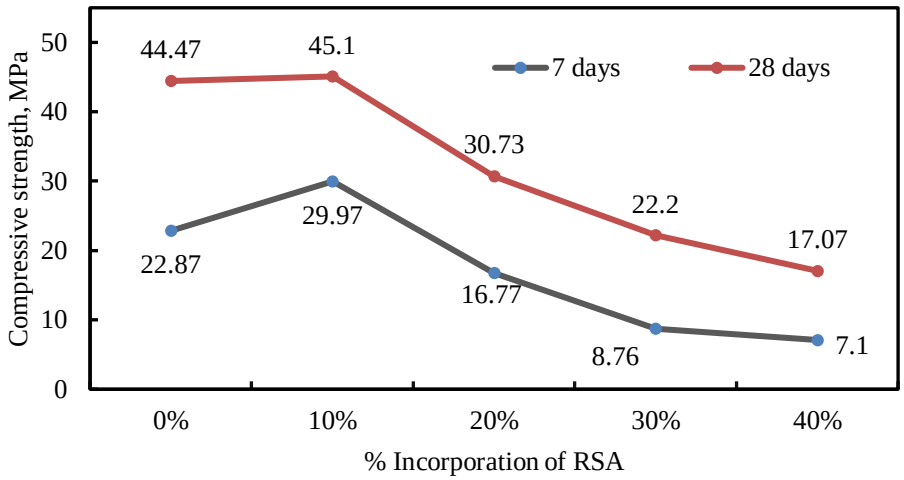

Fig. 8. Compressive strength test results of GPC specimens

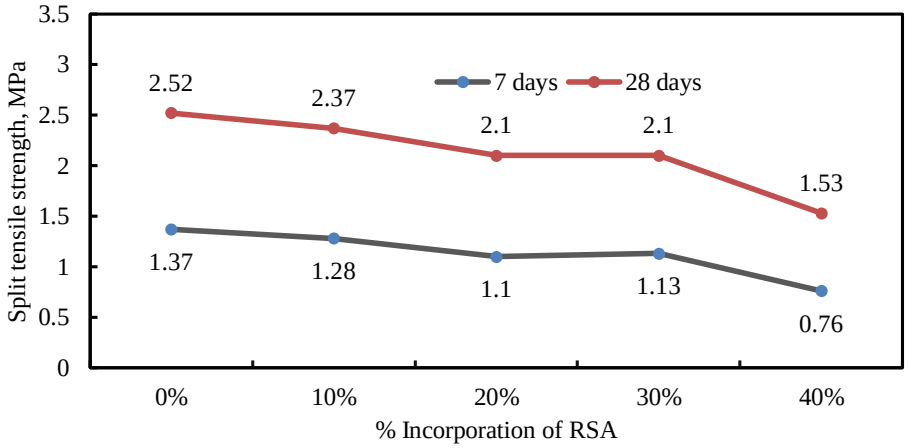

Fig 9. Split tensile strength test results of GPC specimens

3.3. Tensile Strength

The influence of substituting FA by RSA was also studied on split tensile strength at 7 and 28 days. The tensile strength values are shown in Table 5. Experimental results showed a minimum strength of 1.53 MPa (40% RSA) to a maximum of 2.52 MPa (100% FA) at 28 days. According to the study of Verma

and Kumar (2018), a higher value of split tensile strength of 3.54 MPa was achieved for 10% RHA incorporation in FA based GPC, which is higher comparing with our research.

Table 5. Split tensile strength of GPC

Days	Split tensile strength in MPa obtained after adding RSA				
	0%	10%	20%	30%	40%
7	1.37	1.28	1.1	1.13	0.76
28	2.52	2.37	2.1	2.1	1.53

4. CONCLUSION

Based on the test results, the following conclusions are drawn:

- RSA impregnated FA-based geopolymer concrete cured in the oven gains strength properties with age.
- The highest value of compressive strength of 45.1 MPa was found in 10% RSA impregnation.
- At 28 days, the compressive strength of RSA impregnated mixes R20, R30, and R40 fell by 31.9%, 50.8%, and 61.2%, respectively, as compared to the mix R10 (10% RSA).
- The maximum density was found 2005 kg/m^3 for 10% RSA impregnated GPC, whereas 40% RSA incorporation yielded a lower value of 1945 kg/m^3.

ACKNOWLEDGMENTS

The authors warmly acknowledge the Department of Civil Engineering, Hajee Mohammad Danesh Science and Technology University, Dinajpur, Bangladesh for providing support to perform laboratory works.

REFERENCES

El-Sayed, M. A., & El-Samni, T. M. (2006). Physical and chemical properties of rice straw ash and its effect on the cement paste produced from different cement types. *Journal of King Saud University-Engineering Sciences*, *19*(1), 21-29.

Hardjito, D., Wallah, S. E., Sumajouw, D. M., & Rangan, B. V. (2004a). Factors influencing the compressive strength of fly ash-based geopolymer concrete. *Civil engineering dimension*, *6*(2), 88-93.

Hardjito, D., Wallah, S. E., Sumajouw, D. M., & Rangan, B. V. (2004b). On the development of fly ash-based geopolymer concrete. *Materials Journal*, *101*(6), 467-472.

Karthik, A., Sudalaimani, K., & Kumar, C. V. (2017). Investigation on mechanical properties of fly ash-ground granulated blast furnace slag based self curing bio-geopolymer concrete. *Construction and Building Materials*, *149*, 338-349.

Khan, M. A. A., Saha, M. S., Sultana, S., Ahmed, A. N., & Das, R. C. (2013). Coal Fly ash of Barapukuria thermal power plant, Bangladesh: Physico chemical properties assessment and utilisation. *International Journal of scientific & engineering research*, *4*(11), 1456-1460.

Michailos, S., & Webb, C. (2020). Valorisation of rice straw for ethylene and jet fuel production: a technoeconomic assessment. In *Food Industry Wastes* (pp. 201-221). Academic Press.

Nikoloutsopoulos, N., Sotiropoulou, A., Kakali, G., & Tsivilis, S. (2021). Physical and mechanical properties of fly ash based geopolymer concrete compared to conventional concrete. *Buildings*, *11*(5), 178.

Panagiotopoulou, C., Perraki, T., Tsivilis, S., Skordaki, N., & Kakali, G. (2008). A study on alkaline dissolution and geopolymerisation of hellenic fly ash. In *Ceramic Engineering and Science Proceedings* (Vol. 29, No. 10, p. 165).

Rao, G. M., & Venu, M. (2020). Mix design methodology for fly ash and GGBS-based geopolymer concrete. *Adv Struct Eng. Springer, Singapore*, 173-181.

Roselló, J., Soriano, L., Santamarina, M. P., Akasaki, J. L., Monzó, J., & Payá, J. (2017). Rice straw ash: A potential pozzolanic supplementary material for cementing systems. *Industrial Crops and Products*, *103*, 39-50.

Ryu, G. S., Lee, Y. B., Koh, K. T., & Chung, Y. S. (2013). The mechanical properties of fly ash-based geopolymer concrete with alkaline activators. *Construction and building materials*, *47*, 409-418.

Verma, S., & Kumar, M. (2018). Behaviour of fly ash and rice husk ash based geopolymer concrete. In *Key Engineering Materials* (Vol. 775, pp. 596-602). Trans Tech Publications Ltd.

Vignesh, P., & Vivek, K. (2015). An experimental investigation on strength parameters of flyash based geopolymer concrete with GGBS. *International Research Journal of Engineering and Technology*, *2*(2), 135-142.

Wallah, S., & Rangan, B. V. (2006). Low-calcium fly ash-based geopolymer concrete: long-term properties.

Wijaya, A. L., & Ekaputri, J. J. (2017). Factors influencing strength and setting time of fly ash based-geopolymer paste. In *MATEC Web of Conferences* (Vol. 138, p. 01010). EDP Sciences.

Xie, T., Visintin, P., Zhao, X., & Gravina, R. (2020). Mix design and mechanical properties of geopolymer and alkali activated concrete: Review of the state-of-the-art and the development of a new unified approach. *Construction and Building Materials*, *256*, 119380.

Yuan, Q., Pump, J., & Conrad, R. (2014). Straw application in paddy soil enhances methane production also from other carbon sources. *Biogeosciences*, *11*(2), 237-246.

Proc. 3rd International Conference on Structural Engineering Research (iCSER 2022)
27-30 Nov 2022, Sydney, Australia
ISBN: 978-0-6456692-1-3

Effect of Rice Straw Ash on Compressive Strength of Fly Ash Based Geopolymer Mortar Cured at Elevated Temperature

Md. Ashraful Habib[1*], Jani Ahammad[1], S.M. Priok Rashid[1], Md. Rakibul Islam[1], Md. Ahnaf Abid Basunia[1], Md. Ibrahim Mostazid[1]

[1] *Department of Civil Engineering, Hajee Mohammad Danesh Science & Technology University, Dinajpur, Bangladesh*

**Corresponding author, E-mail: ashrafulcivilhstu@gmail.com*

ABSTRACT

The cement industry accounts for about 8% of global anthropogenic CO_2 emissions. Therefore, it is necessary to find another eco-friendly, sustainable binding material. As a result, over the past decades, institutional and business interest in using geopolymer materials in construction has increased. In geopolymer, cement is entirely replaced by another aluminosilicate rich materials activated by alkali solutions. As the abundantly produced rice straw ash is silica-rich and performs the function like a mineral admixture, therefore, the objective of this study is to investigate the effect of rice straw ash (RSA) on fly ash (FA) based geopolymer mortar (GPM) characterised by density and compressive strength. RSA was incorporated to the binder (FA) in the percentages of 0 wt.%, 10 wt.%, 20 wt.%, 30 wt.%, and 40 wt.%, respectively to produce 50 mm × 50 mm × 50 mm mortar cube. Sodium hydroxide (NaOH) and sodium silicate (Na_2SiO_3) solutions were used as alkaline activator. The specimens were cured at 65 ℃ temperature for 24 hours. The experimented results of the GPM mixes showed that addition of RSA reduces both the dry density and compressive strength. The maximum compressive strength and dry density at 28 days were found 25.13 MPa and 1904 kg/m^3 for 100% FA, where 40% incorporation of RSA yielded a lower strength of 4.1 MPa and density of 1541 kg/m^3.

***Keywords**: Geopolymer mortar; Fly ash; Rice straw ash; Density; Compressive strength*

1. INTRODUCTION

Cement is a widely used binding material for aggregates in the production of concrete and mortar. Every year, huge amounts of natural resources such as limestone, fuel, are required to manufacture cement. However, these are non-renewable resources, and their availability is decreasing day by day. Again, from the calcination of limestone, an extensive amount of CO_2 emits to the environment (Singh, 2018). Therefore, researchers are now focusing more on developing sustainable binding materials. "Geopolymer binder" is currently thought to be the sustainable binder sought by researchers (Rajan and Kathirvel, 2021). In geopolymer, aluminosilicate materials namely fly ash (FA), ground granulated blast furnace slag (GGBFS) are used as precursor. Alkali activation of silica and alumina-rich source materials produces geo-polymer, where an inorganic polymer forms with polymeric Si-O-Al-O linkages (Daniel et al., 2017). Sodium hydroxide (NaOH), sodium silicate (Na_2SiO_3), potassium hydroxide (KOH) solutions are generally used as alkali activator (Singh et al., 2015). Researchers found that the physical properties of fly ash based geopolymer mortar are comparable to those of cement-based mortar as suggested by Thang (2016), Radhakrishna et al (2011), Dutta and Ghosh (2013).

Shinde and Kadam (2015) studied the effect of different parameters (like- alkali solution to fly ash ratio, sodium silicate to sodium hydroxide ratio, curing temperatures) on the strength of fly ash based geopolymer mortar. They found a maximum compressive strength of 38.65 MPa in 0.5 activator to precursor ratio, 1.5 Na_2SiO_3/NaOH ratio, and a curing temperature of 80 °C for 24 h. Hardjito et al (2008) found that the

compressive strength of low calcium FA geopolymer mortar increased with increasing NaOH molarity. In addition, they observed that compressive strength varied with curing temperatures and time, and maximum strength attained after 24 hours of curing at 65 ℃.

Every year, a large volume of rice straw is generated all over the world (Singh et al., 2016). Managing rice straw is a problem for most of the countries. Open air burning of rice straw emits greenhouse gases, while natural decomposition aids methane gas production (Yuan et al., 2014). A recent study revealed that rice straw ash exhibits the same pozzolanic properties as FA or GGBFS (Roselló et al., 2017). A number of studies are available on the effect of GGBFS, or RHA (rice husk ash) in FA based GPM (Lau et al., 2019), (Saloma et al., 2017), however, the effect of RSA in FA based GPM is yet to be investigated. These facts draw the attention of the authors of this study to investigate the effect of RSA in FA based GPM to observe its effect on density and compressive strength.

2. MATERIALS AND METHODS

2.1. Fly Ash

Fly ash is an industrial by-product produced in a coal-fired power station. Fly ash was used as a base material because it shows better strength in reaction with alkali activator. Fly ash (class F) was collected from Barapukuria Coal-fired Thermal Power Plant, Dinajpur, Bangladesh. The chemical composition of Barapukuria fly ash presented in Table 1 as investigated by Khan et al (2013). X-ray fluorescence (XRF) was used to determine the chemical composition of the FA.

2.2. Rice Straw Ash

The conversion of rice straw to ashes offers the chance of reusing it in cementing process as rice straw ash is rich in SiO_2. After burning, rice straw produces about 15% of ashes, thus for every 1000 kg of rice straw burning, 150 kg of ash is produced (El-Sayed and El-Samni, 2006). Rice straw was collected from local market of Gopalganj, Dinajpur, Bangladesh. After collection, the straw was dried in sun rays for around 7-9 h to remove excess moisture, later it was burnt at about 600-800 ℃ temperature and left to cool it naturally. After that, the RSA was grounded manually so that all the particles passed through 100 μm sieve.

Fig. 1. Fly ash

Fig. 2. Rice straw ash

2.3. Fine Aggregate

Natural river sand was utilized as fine aggregate. It was collected from Dhepa river near Hajee Mohammad Danesh Science and Technology University (HSTU), Dinajpur, Bangladesh. Table 2 shows the properties of fine aggregate.

2.4. Alkali Activator

Sodium hydroxide and sodium silicate solutions were used as alkaline activator. NaOH with 99% purity in the pellets form and Na_2SiO_3 in liquid form was supplied by Al-Arafa Scientific and Surgical, Hatkhola, Dhaka, Bangladesh. NaOH pellets were dissolved in distilled water to produce 10 M solution and then mixed with Na_2SiO_3.

Fig. 3. NaOH solution

Fig. 4. Na_2SiO_3 solution

Table 1. Chemical composition of FA sample determined by XRF analysis (Khan et al., 2013)

Composition	Content (%)	Composition	Content (%)
SiO_2	50.20	P_2O_5	0.66
Al_2O_3	40.10	SO_3	0.45
Fe_2O_3	3.32	MnO	0.05
TiO_2	2.38	NiO	0.01
CaO	1.29	CuO	0.0158
MgO	0.20	ZnO	0.0068
Na_2O	0.06	PbO	0.0073
K_2O	0.93	Loss on ignition	2.00

Table 2. Properties of fine aggregate

SL. No.	Test Conducted	Test Results
1	Specific gravity	2.63
2	Water absorption (%)	1.73
3	Bulk density (kg/m^3)	1562
4	Fineness modulus (FM)	2.46

2.5. Preparation of geopolymer mortar

Table 3 shows the mix proportion of RSA impregnated GPM. The binder-to-aggregate ratio was set at 1:1. Four (4) distinct replacement levels of RSA replacing FA were used, namely F90R10 (10%), F80R20 (20%), F70R30 (30%), and F60R40 (40%). Plain FA based geopolymer mortar was used as a control mixture (F100). The GPM mixes used alkaline solution to binder ratio as 0.5, and NaOH to Na_2SiO_3 ratio was 0.4. At first all the solid ingredients were mixed properly for 3-4 min, then the alkaline solution was added, and mixing continued for another 5 min as per BIS 10890. After mixing, the fresh mortar was poured

into greased metal molds of 50 × 50 × 50 mm and then tamped 25 times in two layers. Later, the molds were subjected to vibration for 30s. Finally, the molds were kept in an oven at a temperature of 65 ℃ for 24 h. After initial curing, the molds were demolded and left in open air until the testing ages.

Table 3. Mix proportions of mixes for (50 mm × 50 mm × 50 mm) cube specimen

Mix	Binder		Fine aggregate (gm)	NaOH (gm)	Na_2SiO_3 (gm)
	Fly ash (gm)	Rice straw ash (gm)			
F100	200	00	200	28.57	71.43
F90R10	180	20	200	28.57	71.43
F80R20	160	40	200	28.57	71.43
F70R30	140	60	200	28.57	71.43
F60R40	120	80	200	28.57	71.43

Fig. 5. GPM specimens

Fig. 6. Compressive strength test

2.6. Testing of specimens

The dry density of the specimens was measured in accordance with ASTM C138 / C138M-17a. The compressive strength of the cube mortar specimens was measured after 7 and 28 days using a universal testing machine at a loading rate of 10 N/s. [JIS A 1108:2018].

3. RESULTS AND DISCUSSION

3.1. Density

Fig. 7 presents that the density of RSA incorporated GPM mix (with 10% addition of RSA) achieved the maximum 1805 kg/m^3 among all other RSA mixes. On the other hand, impregnation of 40 wt.% RSA of FA (total binder) possessed a minimum value of 1541 kg/m^3 than all other GPM mixes. The control mix (F100) yielded the highest density of 1904 kg/m^3. Comparing with the control mix (F100), the reduction in the density of the mixes for F90R10, F80R20, F70R30, and F60R40 was found 5.2%, 11.1%, 14.7%, and 19.1%, respectively due to the lightweight of binding agents of RSA.

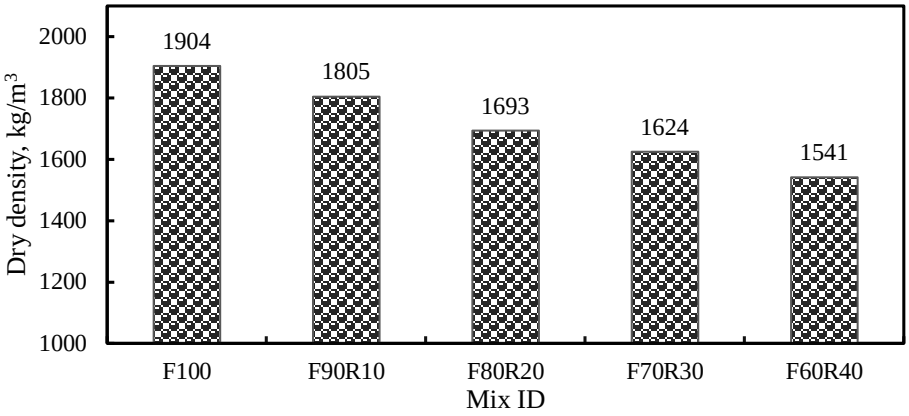

Fig. 7. Dry density of GPM after 28 days of curing

3.2. Compressive Strength

The compressive strength of geopolymer mortar produced with five different percentage substitutions of FA by RSA (0-40%) was performed at 7 and 28 days of curing are presented in Table 4. From Table 4 it can be seen that strength increased with an increase in the curing time. The mix (F100) had a higher strength of 25.13 MPa than other RSA impregnated GPM mixes. However, the mix F60R40 had a lower strength of 4.1 MPa. The GPM specimens have shown lower strength of 30% (F90R10), 62.5% (F80R20), 79.7% (F70R30), and 83.6% (F60R40) at 28 days than the control mix. 100% FA incorporated GPM is reported to yield 10 MPa strength at 28 days (Islam et al., 2014), which is significantly lower than the obtained strength for F100 of this study.

Table 4. Compressive strength of GPM cube specimens

Mix ID	7 days (MPa)	28 days (MPa)
F100	17.5	25.13
F90R10	10	17.6
F80R20	4.5	9.4
F70R30	3	5.1
F60R40	1.9	4.1

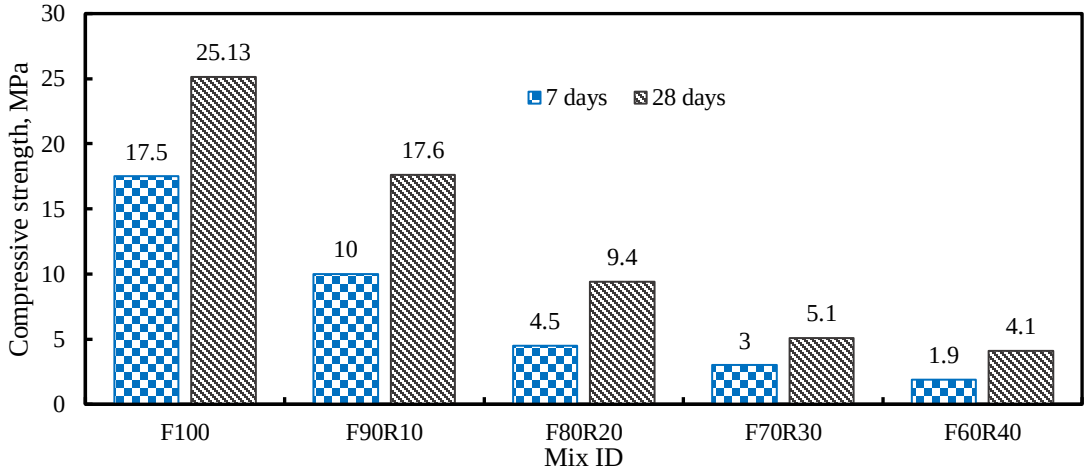

Fig. 8. Compressive strength test results of GPM specimens

4. CONCLUSION

The following conclusions are made:

- The strength gradually decreased with increasing the RSA content in the geopolymer mix.
- At 10% substitution of FA with RSA provided desirable compressive strength of 17.6 MPa.
- The maximum compressive strength of GPM was found to be 25.13 MPa for mix F100 at 28 days of curing.
- At 28 days, the compressive strength of mixes F90R10, F80R20, F70R30, and F60R40 fell by 30%, 62.6%, 79.7%, and 83.7%, respectively, as compared to the mix F100 (100% FA).
- 100% FA possessed the ultimate dry density, whereas other mixes exhibited a reduction in density due to the lightweight of RSA.

ACKNOWLEDGMENTS

The authors are grateful to the Department of Civil Engineering, Hajee Mohammad Danesh Science and Technology University, Bangladesh for providing laboratory facilities during experimentation.

REFERENCES

Daniel, A. J., Sivakamasundari, S., & Abhilash, D. (2017). Comparative study on the behaviour of geopolymer concrete with hybrid fibers under static cyclic loading. *Procedia engineering*, *173*, 417-423.

Dutta, D., & Gosh, S. (2013). Strength and durability of fly ash geopolymer blended with lime stone dust. *Int. J. Eng. Res. Technol.*, *2*, 1-8.

El-Sayed, M. A., & El-Samni, T. M. (2006). Physical and chemical properties of rice straw ash and its effect on the cement paste produced from different cement types. *Journal of King Saud University-Engineering Sciences*, *19*(1), 21-29.

Hardjito, D., Cheak, C. C., & Ing, C. L. (2008). Strength and setting times of low calcium fly ash-based geopolymer mortar. *Modern applied science*, *2*(4), 3-11.

Islam, A., Alengaram, U. J., Jumaat, M. Z., & Bashar, I. I. (2014). The development of compressive strength of ground granulated blast furnace slag-palm oil fuel ash-fly ash based geopolymer mortar. *Materials & Design (1980-2015)*, *56*, 833-841.

Khan, M. A. A., Saha, M. S., Sultana, S., Ahmed, A. N., & Das, R. C. (2013). Coal Fly ash of Barapukuria thermal power plant, Bangladesh: Physico chemical properties assessment and utilization. *International Journal of scientific & engineering research*, *4*(11), 1456-1460.

Lau, C. K., Rowles, M. R., Parnham, G. N., Htut, T., & Ng, T. S. (2019). Investigation of geopolymers containing fly ash and ground-granulated blast-furnace slag blended by amorphous ratios. *Construction And Building Materials*, *222*, 731-737.

Radhakrishna, M. G., Giridhar, C., & Jadav, M. (2011). Strength Development in Geopolymer pastes and Mortars. *International Journal of Earth Sciences, ISSN*, 0974-5904.

Rajan, H. S., & Kathirvel, P. (2021). Sustainable development of geopolymer binder using sodium silicate synthesized from agricultural waste. *Journal of Cleaner Production*, *286*, 124959.

Roselló, J., Soriano, L., Santamarina, M. P., Akasaki, J. L., Monzó, J., & Payá, J. (2017). Rice straw ash: A potential pozzolanic supplementary material for cementing systems. *Industrial Crops and Products*, *103*, 39-50.

Saloma, Hanafiah, Elysandi, D. O., & Meykan, D. G. (2017, November). Effect of Na_2SiO_3/NaOH on mechanical properties and microstructure of geopolymer mortar using fly ash and rice husk ash as precursor. In *AIP Conference Proceedings* (Vol. 1903, No. 1, p. 050013). AIP Publishing LLC.

Shinde, B. H., & Kadam, D. K. N. (2015). Properties of fly ash based geopolymer mortar. *International Journal of Engineering Research And*, *4*(7), 203-206.

Singh, B., Ishwarya, G., Gupta, M., & Bhattacharyya, S. K. (2015). Geopolymer concrete: A review of some recent developments. *Construction and building materials*, *85*, 78-90.

Singh, N. B. (2018). Fly ash-based geopolymer binder: A future construction material. *Minerals*, *8*(7), 299.

Singh, R., Srivastava, M., & Shukla, A. (2016). Environmental sustainability of bioethanol production from rice straw in India: a review. *Renewable and Sustainable Energy Reviews*, *54*, 202-216.

Thang, X. N. (2016). Influence of Curing and Water to the Mechanical Properties of Geopolymer Mortar. *International Journal of Engineering Research & Technology (IJERT)*, 2278-0181.

Yuan, Q., Pump, J., & Conrad, R. (2014). Straw application in paddy soil enhances methane production also from other carbon sources. *Biogeosciences*, *11*(2), 237-246.

Proc. 3rd International Conference on Structural Engineering Research (iCSER 2022)
27-30 Nov 2022, Sydney, Australia
ISBN: 978-0-6456692-1-3

Effect of Discrete Basalt Fibres Length On Fresh And Mechanical Properties Of Self-Compacted Geopolymer Concrete

Mohamed Heweidak[1], Bidur Kafle[2,] and Riyadh Al-Ameri[3]

[1]PhD candidature, School of Engineering, Deakin University, Geelong, VIC 3217, Australia
[2]Lecturer in Civil Engineering, School of Engineering, Deakin University, Geelong, VIC 3217, Australia
[3]Senior Lecturer in Civil Engineering School of Engineering, Deakin University, Geelong, VIC 3217, Australia

Corresponding author's E-mail: mheweidak@deakin.edu.au

Abstract

Basalt fibres (BFs) have lately become increasingly popular in the building materials sector due to their low manufacturing cost and superior mechanical characteristics to their counterparts. Geopolymer composites containing a small amount of fibres have exhibited improved mechanical characteristics and durability. However, no research has yet been conducted to explore the influence of different basalt fibre lengths and dosages on self-compacted geopolymer concrete's fresh and mechanical characteristics (SCGC). In this study, seven mixtures were developed incorporating long 30 mm and short 12 mm basalt fibres with 1%, 1.5%, and 2% content of binder weight. Incorporating BFs in SCGC worsens the fresh properties. However, the obtained results still meet the standards required of self-compacted concrete except for SCGC mix reinforced with 30 mm BF and 2% dosage. In general, the inclusion of 12 mm BFs up to 2% in the SCGC mixture reduces the composite compressive strength contrary to indirect tensile strength, which enhances with the increase of BFs content. SCGC specimens incorporating 30 mm BFs yield better indirect tensile strength than SCGC specimens included with 12 mm BFs for the exact BFs dosage. SCGC containing 30 mm BF with a 2% dosage fraction showed the highest compressive and indirect tensile strength compared to all other mixes.

1. Introduction

With an average annual production of 1.4 m3 per capita, cementitious concrete is the world's second most widely utilised substance after water [1]. The cement production process emits up to 2.8 billion tonnes of CO2[2], accounting for 7% of global CO2 emissions [3-5], exacerbating the climate change catastrophe and causing significant damage to the environment and humans. Cement manufacturing is predicted to grow by 12% to 23% by 2050 [6], with a 4% increase in CO_2 emissions[7], in line with infrastructure expansion and population growth. In this regard, the World Green Building Councils (WorldGBCs) and the construction industry have established a net zero project to achieve decarbonisation by 2050. As a result, and to tackle the global climate change crisis, the building industry has been transitioning towards using sustainable materials such as geopolymer concrete.

Joseph Davidovits presented geopolymers as a novel binder polymer family in 1979 [8]. Extensive research has been undertaken to generate a diverse range of geopolymer resins with specific qualities to suit various aerospace, building, and automotive applications. Geopolymer concrete is mainly made by combining aluminium silicate by-products, such as fly ash, slag, metakaolin, and rice husk ash, with chemical base alkaline solutions, such as sodium hydroxide and sodium silicate solutions [9]. Many scholars have been interested in geopolymer concrete over the past two decades since it generates roughly 80% fewer CO2 emissions when compared to traditional concrete [10]. Furthermore, using aluminium-silicate by-products like fly ash and slag in geopolymer concrete production helps to prevent significant environmental and human health harm caused by waste material. Fly ash, for example, is recognised by its tiny particle size and low weight, carried by air if

not properly stored. Prolonged human exposure to airborne fly ash causes health problems such as lung cancer and respiratory illnesses [11]. Geopolymer concrete has excellent mechanical properties, including comparable compressive, splitting and flexural strength to cementitious concrete [12, 13]. Geopolymer concrete possesses better chemical sulfuric acid resistance than cementitious concrete [14]. Additionally, due to its excellent chemical stability, better durability characteristics under extreme heat are associated with geopolymer concrete compared to cementitious concrete [15]. Geopolymer concrete made of fly ash and slag has a comparable freeze-thaw resistance to cementitious concrete [16].

Despite the advantages of geopolymer concrete, its use in the construction industry is generally limited due to two significant obstacles. Alkali-activator solutions must be prepared before casting day, and their severe corrosive nature necessitates particular storage and handling techniques [17-21]. Furthermore, Geopolymer concrete must cure for 24 hours at temperatures ranging from 60°C to 85°C [22-24] to gain strength. A newly developed self-compacted geopolymer concrete (SCGC) made of fly ash, slag and micro ash as the binder materials and solid sodium hydroxide metasilicate as an alkali-activator [13]. SCGC possesses compressive and splitting tensile strength of 40 and 3 MPa, respectively [13]. SCGC has an advantage over typical geopolymer concrete in that it does not need high heat curing, and solid alkali-activator powder substitutes alkali-activator solutions, making it a potential option for general building applications.

Although the manufacturing ease of SCGC makes it more viable for in-situ applications, specific noticeable concerns regarding the mechanical characteristics of fly ash slag-based geopolymer concrete (FASGC) have been reported. FASGC has poor splitting and flexural strength and a high brittleness compared to cementitious concrete[22-24]. When slag is included at a rate of more than 30% of the binder in fly ash geopolymer concrete mixes, the chance of crack formation rises[25], lowering the concrete strength and negatively impacting its durability in the long term. Incorporating discrete basalt fibres within geopolymer concrete has shown to be an efficient technique to enhance the mixture's mechanical characteristics and ductility. Several research studies have reported that adding fibres such as steel, glass, polypropylene and PVA, etc., improves the mechanical properties and reduces the concrete mixture brittleness [26, 30-38]. Basalt fibres have piqued the interest of researchers for their use in geopolymer composites owing to their cheap production cost, sustainability[26, 27], outstanding mechanical characteristics[26, 28-31], and excellent chemical and temperature stability[28, 32-37]. According to Timakul et al. (2016) [10], adding 10% weight of basalt fibres to geopolymer concrete improves the compressive strength by 37% compared to plain geopolymer concrete. The effect of 0.5% and 1% volume fraction of BFs on the fracture toughness of geopolymer and cementitious concrete have been studied[38]. Compared to plain composites, using large volume fractions of BFs reduced cracks width and improved fracture toughness in geopolymer and cementitious concrete mixes[38]. Incorporating BFs in geopolymer composite showed a better fracture toughness than cementitious composite comprised with the same volume content. Out of 3 mm, 6 mm, 12 mm and 18 mm BFs lengths, reinforcing geopolymer concrete with 6 mm BFs showed better mechanical properties, peak load and fracture energy than geopolymer concrete reinforced with other BFs lengths [39]. While studies have shown that adding BFs to geopolymer composite may improve its mechanical characteristics, there is still a significant knowledge gap regarding the performance of BFs-reinforced geopolymer concrete, particularly self-compacted geopolymer concrete (SCGC). Therefore, in this paper, the influence of short basalt fibres (12 mm) and long basalt fibres (30 mm) with dosages of 1%, 1.5% and 2% on the fresh and mechanical properties of SCGC has been studied.

2. Materials and methods

2.1 Materials

The main by-product constituents for the manufacturing of SCGC composite are fly ash and slag in a 60:40 ratio. Cement Australia Pty Ltd supplied fly ash that met AS3582.1: 2016 standards, while Independent Cement and Lime Pty Ltd provided ground slag. Fly ash Australia Pty supplied micro ash with 3.5 m fine particle size and was added to the mixture to enhance the concrete strength and workability [40, 41]. Solid anhydrous sodium metasilicate powder was employed as an alkali-activator

to develop the geoploymerisation procedure. Water accounted for 45% of the total binder weight. 12 mm and 30 mm BFs, as shown in Figure 1, with dosages of (1, 1.5, 2) % of the total binder weight, were added to reinforce self-compacted geopolymer concrete mixes. The chemical composition of SCGC's binders and the physical properties of basalt fibres are tabulated in Tables 1 and 2, respectively. The mixture design of SCGC is presented in Table 3.

a) 12 mm b) 30mm

Figure 1. Short basalt fibres with 12 mm and 30 mm were used in SCGC [42]

Table 1. Chemical composition details of SCGC mixture [42]

Chemical composition	Fly Ash (%)	Slag (Independent Cement & Lime Pty Ltd) (%)	Micro Fly Ash (%)	Sodium Metasilicate Anhydrous (%)
SiO_2	65.75	35.19	63.09	50
CaO	--	41.47	--	--
Al_2O_3	32.87	13.66	32.26	--
MgO	--	6.32	--	--
K_2O	--	--	.83	--
MnO	--	--	--	--
SO_3	--	2.43	--	--
V_2O_5	--	.20	--	--
TiO_2	1.38	.73	1.67	--
Na_2O	--	--	.41	50
P_2O_5	--	--	.62	--
FeO	--	--	1.12	--

Table 2 Physical properties of Basalt fibres [42]

Designation	Length (mm)	Diameter (μm)	Density (g/cm3)	Elongation (%)	Elastic Modulus (GPa)	Melt temperature (°C)	Thermal conductivity (W/mK)	Tensile strength (Mpa)
BF12	12	13	2.6-2.8	2.4-3.15	80-115	1450	.031-.0038	1000
BF 30	30	13	2.6-2.8	2.4-3.15	80-115	1450	.031-.0038	1000

Table 3 Mix design of SCGC

Mix	Fly Ash (kg)	Slag (kg)	Microash (kg)	Sodium Metasilicate (kg)	Fine aggregate (kg)	Coarse aggregate (kg)
SCGC	480	360	120	96	763	677

2.2 Test procedure

Table 4 presents seven SCGC mixes, including a control mix and six basalt fibres reinforced SCGC mixes. To ensure homogeneous dispersion of fibres within the mix, coarse aggregates, fine aggregate, all binder constituents, and basalt fibres were mixed for around 4 minutes in the concrete mixer drum. Water was then added to the dry mixture, and it was mixed for approximately 9 minutes. To evaluate the influence of short and long BFs on the workability of SCGC, fresh properties tests, including slump flow, T_{500}, and J-ring tests, were performed on all mixes following AS 1012.3.5:2015 standards[43]. The flowability is calculated by averaging the two diameters of the concrete mix spread. Concrete is considered self-compacting if the slump flow exceeds the spread value diameter of 500 mm[43]. The T_{500} test was performed following AS 1012.3.5:2015[43] standards requirements, using a timer and concrete slump cone. T_{500} is the necessary time for self-compacted concrete to reach 500 mm diameter in the slump cone test. J-ring tests were performed on all mixtures following AS 1012.3.4:2015 [43] standards to explore the influence of short and long fibres on self-compacted geopolymer concrete passing ability.

the effect of short and long BFs on the mechanical characteristics (compressive strength and indirect tensile strength) of self-compacted geopolymer concrete have been investigated., Forty-two cylindrical specimens with 100 mm diameter and 200 mm height were cast. Following the completion of the fresh properties test, SCGC was poured straight into cylindrical moulds that had been internally coated with a lano foam-releasing agent. All specimens were demolded two days later and maintained in a humidity chamber for 28 days at 23 C° temperature and 49% relative humidity. The compressive strength of the mixtures was determined using 3000 KN compression testing equipment provided at Deakin University's structural laboratory. The average compressive strength was determined by applying a loading rate of .33 MPa per second to three specimens of each mix following AS 1012.14:2018 [44] standard requirements. Three samples from each mix were tested under indirect tensile stress to get the average indirect tensile strength. The indirect tensile strength test was conducted according to AS 1012.10-2000 (R2014)[45]. No test repetition was required as mechanical properties results are within 15% of the average mean value.

Table 4 Designation of mixed composition

Mixture	Fibre	
	Length (mm)	Dosage (%)
M0	0	0
M1	12	1
M2	12	1.5
M3	12	2
M4	30	1
M5	30	1.5
M6	30	2

3. Results and discussion

3.1 Fresh properties

Concrete flowability plays an essential role in determining concrete quality and consistency. In general, the flowability of concrete composites is often decreased by including fibres [47]. This reduction is further increased as the volume fraction and length of the fibres increase [46-48]. According to AS 1012.3.5:2015 [43] standards, a minimum of 500 mm diameter is required to classify concrete as a self-compacted composite. The slump flow test of the plain SCGC mixture is 750 mm, as shown in Figure 2. Figure 3 shows that increasing of BFs dosage reduces the flowability of the reinforced SCGC. M1, M2 and M3 mixes exhibited 2.60%,10.76% and 13.30%, respectively, lower flowability than plain SCGC. For 30 mm BFs, a flowability reduction of 6.66%, 22.66% and 26.66% are associated with M4, M5 and M6 mixes, respectively, compared to plain SCGC. All developed mixtures are self-compacted concrete as they maintain a flowability ranging from 500 mm to 750 mm. A higher reduction in flowability is associated with mixes reinforced with long BFs than short BFs, due to the high absorption property of long BF (30 mm) that deters the flow of the self-compacted concrete mixture.

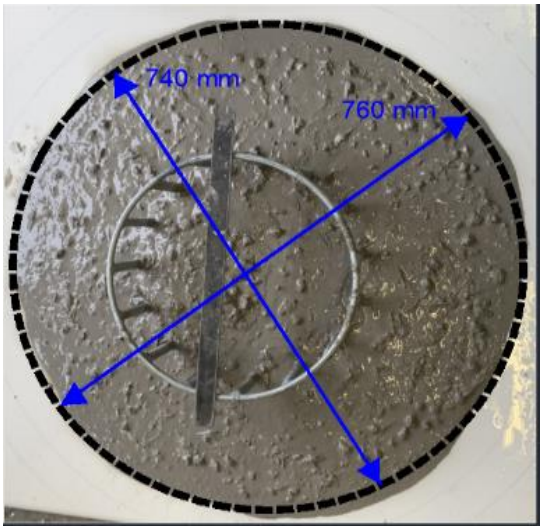

Figure 2 Slump flow diameter for SCGC [45]

Self-compacted concrete has a higher viscosity than conventional concrete, allowing for longer-term creep. The T_{500} value of self-compacted concrete ranges from 2 to 5 seconds. T_{500} values of all mixtures are shown in Figure 4. The T_{500} value of self-compacted geopolymer concrete is 2 seconds. Reinforcing SCGC with BFs increases the required time of the flowable mix to attain a spread diameter value of 500 mm. For the same dosage content of BFs, T_{500} values of SCGC mix reinforced with 30 mm BFs are higher than mixtures reinforced with 12 mm BFs. As shown in Figure 5, the T_{500} values of all developed mixes are complied with EFNRC guidelines, except for the M6 mix recorded a T_{500} value of 6 seconds. The j-ring value indicates the passing ability of self-compacted geopolymer concrete through the steel reinforcement, as shown in Figure 2. As illustrated in Figure 2, the SCGC mix flowed freely through the reinforcement of the J-ring, with no accumulation of coarse aggregate within the apparatus. Figure 5 shows the J-Ring test results for all mixes, with J-Ring values ranging from 2 mm to 10 mm, except the M6 mix, which has a J-Ring value of 15 mm.

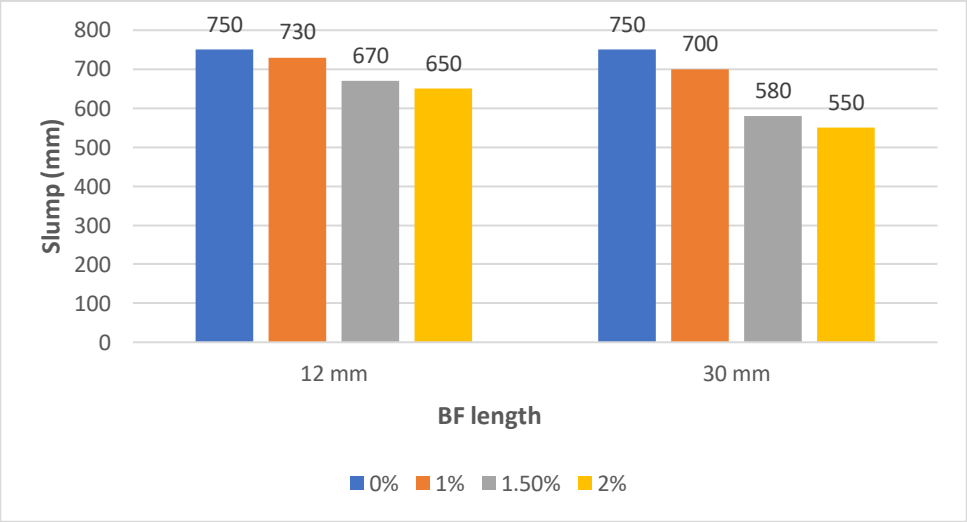

Figure 2. Effect of BF dosage and length on the flowability of SCGC

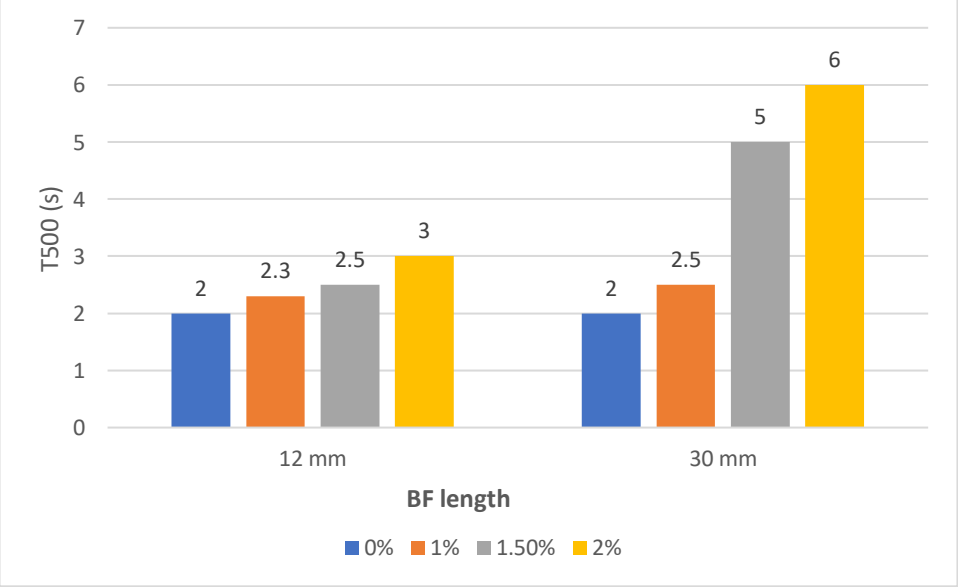

Figure 3. Effect of BF dosage and length on the viscosity of SCGC

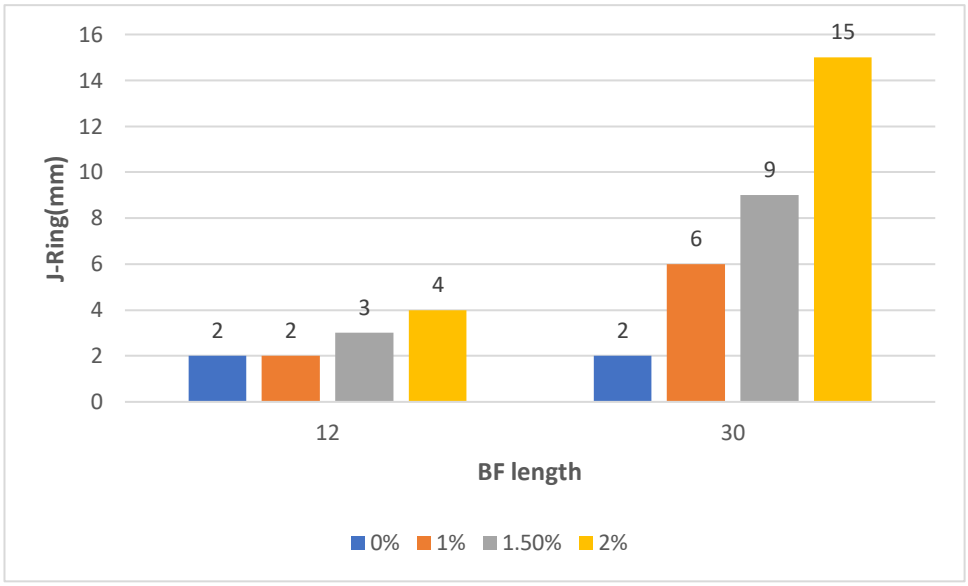

Figure 4. Effect of BF dosage and length on the passing ability of SCGC

3.2 Compressive strength

The compressive strength of developed mixes is presented in Figure 6. The average compressive strength of plain SCGC is 29.8 MPa. SCGC incorporated 12 mm BF with BFs dosages of 1%, 1.5% and 2% showed 14.5 %, 6.14% and 4% lower compressive strength than plain SCGC. Although all mixtures incorporated 12 mm BF showed lower compressive strength than plain SCGC, an increase in SCGC compressive strength with the incrementally increase of BF dosages is observed. On the other hand, the compressive strengths of fibre-reinforced SCGC with 30 mm BF length with dosages of 1.5% and 2% are 9.36% and 17.6 %, respectively, higher than SCGC's compressive strength. However, a slight decrease of 3% in the compressive strength M4 mix has been observed compared to plain SCGC compressive strength. Including 30 mm (long fibres) in SCGC composites, up to 2% dosage exhibited better compressive strength than SCGC reinforced with 12 mm (short fibres). It may return that longer BFs have a higher bridging impact and pulling-out resistance, which improves the SCGC compressive strength.

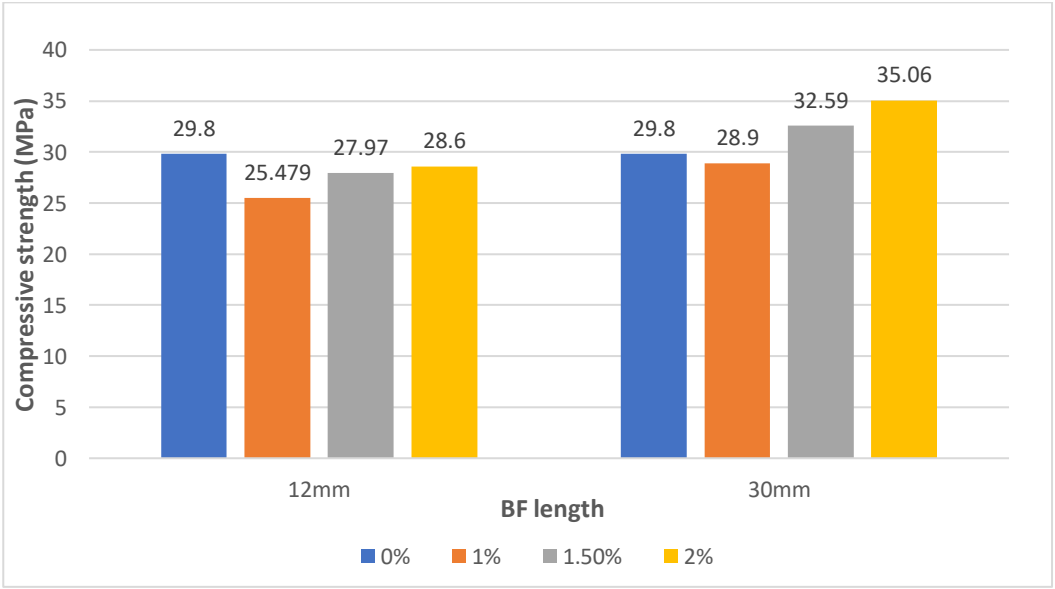

Figure 5 Effect of BF dosage on compressive strength of SCGC

3.3 Indirect tensile strength

The indirect tensile strengths of the SCGC mix reinforced with 12 mm and 30 mm BFs with different dosages are presented in Figure 7. As shown in Figure 7, incorporating both BFs lengths, 12mm and 30mm, in SCGC mixture increases the indirect tensile strength corresponding to the increase of BF dosage up to 2%. The plain SCGC has an indirect tensile strength of 2.55 MPa. 5.88 %, 13.33% and 21.96 % increase in the indirect tensile strength of SCGC reinforced with BF dosages of 1%, 1.5% and 2%, respectively, than plain SCGC. On the other hand, the addition of 30 mm BF length to SCGC composite with dosages of 1%, 1.5% and 2% exhibits an increase of indirect tensile strength of 11.76%, 31.37% and 37.65%, respectively. SCGC reinforced with 30 mm (long) BF length has better indirect tensile strength than SCGC reinforced with 12 mm (short) BF length. The study outcomes align with the Algin and Ozen (2018) [49] study, where self-compacted cementitious concrete reinforced with long chopped basalt fibres has better indirect tensile strength performance than short fibres reinforced self-compacted cementitious concrete. The dispersion of basalt fibres in the SCGC mixture creates a bridging action that efficiently restrains the development of the cracks within the composite. The increase in BF dosages and length may improve the indirect tensile strength. However, beyond a specific size and dosage, a reduction in indirect tensile strength may occur due to the balling effect, where more voids content generates in the composite and consequently restrain the bridging effect [26].

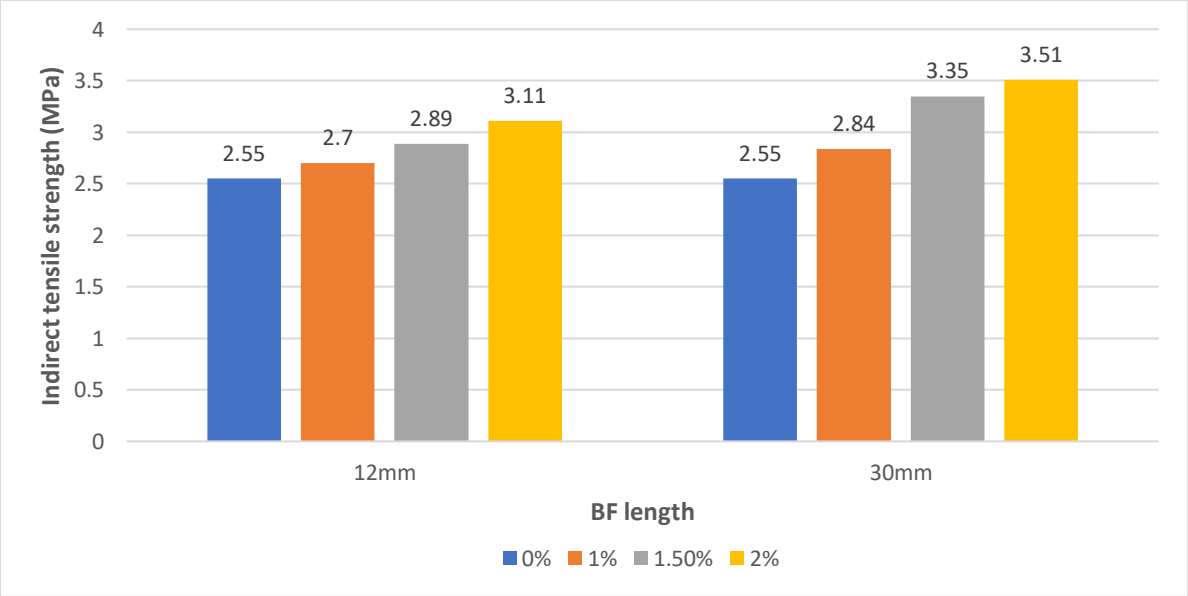

Figure 6 Effect of BF on tensile strength of SCGC

4. Conclusion

This study investigates the influence of chopped basalt fibres on the mechanical properties of self-compacted geopolymer concrete. Two different lengths, 12 mm and 30 mm, with dosage fractions of 1%, 1.5% and 2%, were used to assess the mechanical properties compared to the control specimen. Based on investigation outcomes, the following conclusion can be drawn: -

- Incorporating BFs in SCGC worsens the fresh properties. All tested mixtures have flowability greater than 500 mm, which meets Australian standards. However, the viscosity measurement and passing ability readings of the M6 mix, which had 30 mm BFs and a dosage content of 2%, were not within the acceptable range per EFNRC guidelines.
- Using 12 mm BFs with a dosage fraction between 1-2% in SCGC mixtures reduces the compressive strength compared to plain SCGC. On the other hand, SCGC mixtures with 30 mm BF behave contrarily as an increase in compressive strength is observed with the increase

of BF dosage up to 2%. M6 mix contained 30 mm BF with a 2% dosage fraction showed the highest compressive strength of 35.06 MPa.

- The indirect tensile strength of the SCGC composite increases with the addition of chopped basalt fibres to the mixture. A significant increase in indirect tensile strength for all mixtures incorporated 12 mm and 30 mm BFs with the incrementally increase of BFs dosage up to 2%. However, SCGC mixtures contained 30 mm BF show better indirect tensile strength than SCGC mixtures with 12 mm BF. M6 incorporated 30 mm BF with a 2% dosage fraction showed the highest indirect tensile strength of 3.51 MPa.

5. References

[1] L.K. Turner, F.G. Collins, Carbon dioxide equivalent (CO2-e) emissions: A comparison between geopolymer and OPC cement concrete, Construction and building materials 43 (2013) 125-130.

[2] S. Droege, Carbon pricing and its future role for energy-intensive industries, Climate Strategies (2013).

[3] D.W. Law, A.A. Adam, T.K. Molyneaux, I. Patnaikuni, A. Wardhono, Long term durability properties of class F fly ash geopolymer concrete, Materials and Structures 48(3) (2015) 721-731.

[4] P.S. Deb, P.K. Sarker, S. Barbhuiya, Sorptivity and acid resistance of ambient-cured geopolymer mortars containing nano-silica, Cement and Concrete Composites 72 (2016) 235-245.

[5] D.L. Kong, J.G. Sanjayan, Damage behavior of geopolymer composites exposed to elevated temperatures, Cement and Concrete Composites 30(10) (2008) 986-991.

[6] J. Ofosu-Adarkwa, N. Xie, S.A. Javed, Forecasting CO2 emissions of China's cement industry using a hybrid Verhulst-GM (1, N) model and emissions' technical conversion, Renewable and Sustainable Energy Reviews 130 (2020) 109945.

[7] I.E. Agency, Cement Technology Roadmap Plots Path to Cutting CO2 Emissions 24% by 2050—News. IEA, Iea, 2018, pp. 1-3.

[8] J. Davidovits, S. Cordi, Synthesis of new high temperature geo-polymers for reinforced plastics/composites, Spe Pactec 79 (1979) 151-154.

[9] C.-K. Ma, A.Z. Awang, W. Omar, Structural and material performance of geopolymer concrete: A review, Construction and Building Materials 186 (2018) 90-102.

[10] P. Timakul, W. Rattanaprasit, P. Aungkavattana, Improving compressive strength of fly ash-based geopolymer composites by basalt fibers addition, Ceramics International 42(5) (2016) 6288-6295.

[11] M. Whiteside, J.M. Herndon, Aerosolized coal fly ash: Risk factor for COPD and respiratory disease, Journal of Advances in Medicine and Medical Research 26(7) (2018) 1-13.

[12] P. Nath, P.K. Sarker, Flexural strength and elastic modulus of ambient-cured blended low-calcium fly ash geopolymer concrete, Construction and Building Materials 130 (2017) 22-31.

[13] S.K. Rahman, R. Al-Ameri, A newly developed self-compacting geopolymer concrete under ambient condition, Construction and Building Materials 267 (2021) 121822.

[14] M. Ariffin, M. Bhutta, M. Hussin, M.M. Tahir, N. Aziah, Sulfuric acid resistance of blended ash geopolymer concrete, Construction and building materials 43 (2013) 80-86.

[15] S. Luhar, D. Nicolaides, I. Luhar, Fire resistance behaviour of geopolymer concrete: An overview, Buildings 11(3) (2021) 82.

[16] R. Zhao, Y. Yuan, Z. Cheng, T. Wen, J. Li, F. Li, Z.J. Ma, Freeze-thaw resistance of Class F fly ash-based geopolymer concrete, Construction and Building Materials 222 (2019) 474-483.

[17] G.M. Zannerni, K.P. Fattah, A.K. Al-Tamimi, Ambient-cured geopolymer concrete with single alkali activator, Sustainable materials and technologies 23 (2020) e00131.

[18] R.B. Ardalan, Z.N. Emamzadeh, H. Rasekh, A. Joshaghani, B. Samali, Physical and mechanical properties of polymer modified self-compacting concrete (SCC) using natural and recycled aggregates, Journal of Sustainable Cement-Based Materials 9(1) (2020) 1-16.

[19] B. Nematollahi, J. Sanjayan, F.U.A. Shaikh, Synthesis of heat and ambient cured one-part geopolymer mixes with different grades of sodium silicate, Ceramics International 41(4) (2015) 5696-5704.
[20] S.H. Bong, B. Nematollahi, A. Nazari, M. Xia, J. Sanjayan, Efficiency of different superplasticizers and retarders on properties of 'one-Part'Fly ash-slag blended geopolymers with different activators, Materials 12(20) (2019) 3410.
[21] M. Heweidak, B. Kafle, R. Al-Ameri, Shear-Bond Behaviour of Profiled Composite Slab Incorporated with Self-Compacted Geopolymer Concrete, Applied Sciences 12(17) (2022) 8512.
[22] Z. Abdollahnejad, M. Mastali, T. Luukkonen, P. Kinnunen, M. Illikainen, Fiber-reinforced one-part alkali-activated slag/ceramic binders, Ceramics International 44(8) (2018) 8963-8976.
[23] K. Korniejenko, E. Frączek, E. Pytlak, M. Adamski, Mechanical Properties of Geopolymer Composites Reinforced with Natural Fibers, Procedia Engineering 151 (2016) 388-393.
[24] S.F.A. Shah, B. Chen, S.Y. Oderji, M. Aminul Haque, M.R. Ahmad, Comparative study on the effect of fiber type and content on the performance of one-part alkali-activated mortar, Construction and Building Materials 243 (2020) 118221.
[25] N. Lee, J.G. Jang, H.-K. Lee, Shrinkage characteristics of alkali-activated fly ash/slag paste and mortar at early ages, Cement and Concrete Composites 53 (2014) 239-248.
[26] A. Adesina, Performance of cementitious composites reinforced with chopped basalt fibres–An overview, Construction and Building Materials 266 (2021) 120970.
[27] F. Kogan, O. Nikitina, Solubility of chrysotile asbestos and basalt fibers in relation to their fibrogenic and carcinogenic action, Environmental health perspectives 102(suppl 5) (1994) 205-206.
[28] V. Fiore, T. Scalici, G. Di Bella, A. Valenza, A review on basalt fibre and its composites, Composites Part B: Engineering 74 (2015) 74-94.
[29] M. Di Ludovico, A. Prota, G. Manfredi, Structural upgrade using basalt fibers for concrete confinement, Journal of composites for construction 14(5) (2010) 541-552.
[30] L. Xin, X. Jin-Yu, L. Weimin, W. Zhi-Kun, Comparative Study of the Effect of Basalt Fiber on Dynamic Damage Characteristics of Ceramics Cement–Based Porous Material, Journal of Materials in Civil Engineering 27(8) (2015) 04014224.
[31] X. Luo, J.-y. Xu, E.-l. Bai, W. Li, Study on the effect of basalt fiber on the energy absorption characteristics of porous material, Construction and Building Materials 68 (2014) 384-390.
[32] B. Wei, H. Cao, S. Song, Tensile behavior contrast of basalt and glass fibers after chemical treatment, Materials & Design 31(9) (2010) 4244-4250.
[33] N. Bheel, Basalt fibre-reinforced concrete: Review of fresh and mechanical properties, Journal of Building Pathology and Rehabilitation 6(1) (2021) 1-9.
[34] T. Deák, T. Czigány, Chemical composition and mechanical properties of basalt and glass fibers: a comparison, Textile Research Journal 79(7) (2009) 645-651.
[35] J. Sim, C. Park, Characteristics of basalt fiber as a strengthening material for concrete structures, Composites Part B: Engineering 36(6-7) (2005) 504-512.
[36] C. Scheffler, T. Förster, E. Mäder, G. Heinrich, S. Hempel, V. Mechtcherine, Aging of alkali-resistant glass and basalt fibers in alkaline solutions: Evaluation of the failure stress by Weibull distribution function, Journal of Non-Crystalline Solids 355(52-54) (2009) 2588-2595.
[37] L. Zhu, B. Sun, B. Gu, Frequency features of basalt filament tows under quasi-static and high strain rate tension, Journal of composite materials 46(11) (2012) 1285-1293.
[38] D.P. Dias, C. Thaumaturgo, Fracture toughness of geopolymeric concretes reinforced with basalt fibers, Cement and Concrete Composites 27(1) (2005) 49-54.
[39] Y. Wang, S. Hu, Z. He, Mechanical and fracture properties of geopolymer concrete with basalt fiber using digital image correlation, Theoretical and Applied Fracture Mechanics 112 (2021) 102909.
[40] J. Zhang, H. Tan, M. Bao, X. Liu, Z. Luo, P. Wang, Low carbon cementitious materials: Sodium sulfate activated ultra-fine slag/fly ash blends at ambient temperature, Journal of Cleaner Production 280 (2021) 124363.

[41] L. Krishnaraj, P.T. Ravichandran, Characterisation of ultra-fine fly ash as sustainable cementitious material for masonry construction, Ain Shams Engineering Journal 12(1) (2021) 259-269.
[42] M. Heweidak, B. Kafle, R. Al-Ameri, Influence of Hybrid Basalt Fibres' Length on Fresh and Mechanical Properties of Self-Compacted Ambient-Cured Geopolymer Concrete, Journal of Composites Science 6(10) (2022) 292.
[43] Methods of testing concrete Determination of properties related to the consistency of concrete - Slump flow, T500 and J-ring test, Standards Australia, Australia, 2015, p. 9.
[44] AS 1012.14:2018-Methods of testing concrete Method for securing and testing cores from hardened concrete for compressive strength and mass per unit volume, Standards Australia, 2018, p. 11.
[45] AS 1012.10-2000 Methods of testing concrete Determination of indirect tensile strength of concrete cylinders ('Brazil' or splitting test) (Reconfirmed 2014), Standards Australia, 2014, p. 5.
[46] E. Güneyisi, Y.R. Atewi, M.F. Hasan, Fresh and rheological properties of glass fiber reinforced self-compacting concrete with nanosilica and fly ash blended, Construction and Building Materials 211 (2019) 349-362.
[47] M. Li, V.C. Li, Rheology, fiber dispersion, and robust properties of Engineered Cementitious Composites, Materials and Structures 46(3) (2013) 405-420.
[48] Z. Abdollahnejad, M. Mastali, M. Mastali, A. Dalvand, Comparative study on the effects of recycled glass–fiber on drying shrinkage rate and mechanical properties of the self-compacting mortar and fly ash–slag geopolymer mortar, Journal of Materials in Civil Engineering 29(8) (2017) 04017076.
[49] Z. Algin, M. Ozen, The properties of chopped basalt fibre reinforced self-compacting concrete, Construction and Building Materials 186 (2018) 678-685.

Proc. 3rd International Conference on Structural Engineering Research (iCSER 2022)
27-30 Nov 2022, Sydney, Australia
ISBN: 978-0-6456692-1-3

A Study on the Effect of Saturated Hemp Shives on the Compressive Strength of Concrete

Rahnum T. Nazmul[1], Estela O. Garcez[2], Mahmud Ashraf[3], Bre-Anne Sainsbury[3]

[1]PhD Candidate, School of Engineering, Deakin University, Victoria, Australia
[2]BCRC - Durability Consultants, Level 2, 326 Keilor Road, Niddrie, VIC 3042, Australia
[3]Professor, School of Engineering, Deakin University, Victoria, Australia

Corresponding author's E-mail: rnazmul@deakin.edu.au

Abstract

Bio-based materials are often used in concrete production to increase the sustainability of the product. Key sustainable usages include carbon sequestration, lessening natural aggregate extraction, and easier decomposition after demolition. In addition to the sustainability factor, appropriate usage of bio-based aggregates that include plant fibres, husks and chips can improve concrete properties. Current research explores the possibility of utilising the superior water absorption capacity of porous hemp shives to increase the concrete compressive strength through optimising the cement hydration process. A systemic study has been conducted with varying hemp shive particle (1.18 to 2.36 mm) percent inclusion (3%, 2% and 1% mass of binder content). The resulting compressive strengths at 1, 3, 7 and 28 days curing age were recorded and obtained results suggest that hemp shives positively impact concrete curing. Furthermore, the difference between sealed and unsealed early-age curing conditions was minimal.

Keywords: hemp shive, concrete, compressive strength, curing, water absorption.

1. INTRODUCTION

In recent years scientists have explored the possibilities of hemp as a 'green' substitute/addition to concrete (Jami, Karade, & Singh, 2019). Hemp exhibits three useful properties, namely, its superior thermal insulation capacity, high acoustic resistance and low density that make it particularly favourable as a construction element. Its first use in construction dates back to the nineties as a bio-based concrete known as 'hempcrete' (Sassoni, Manzi, Motori, Montecchi, & Canti, 2014). While hempcrete is highly favourable from acoustic and thermal insulation aspects, it is reported to offer low mechanical compressive and flexural strength (0.12 to 2 MPa and 0.06 to 1.21 MPa, respectively) compared to ordinary concrete which limits its applicability as a structural building element (Arnaud & Gourlay, 2012; Elfordy, Lucas, Tancret, Scudeller, & Goudet, 2008; Walker, Pavia, & Mitchell, 2014). The low mechanical strength is often considered as a result of the highly porous structure of hemp shives (Sáez-Pérez, Brümmer, & Durán-Suárez, 2020), poor bonding between the shive and the concrete matrix (Balčiūnas, Vėjelis, Vaitkus, & Kairytė, 2013) and substitution of a hard element within the mix (aggregate) with a relatively 'softer' material (Awwad, Mabsout, Hamad, Farran, & Khatib, 2012). While used in hempcrete, hemp shives are used as the main aggregate and mixed with a binder as lime or cement. However, the porous structure of hemp shives could also be utilised as an internal source of water if that's added partially, on a saturated state within the normal concrete. These saturated hemp shives could supply water to the concrete mass and assist in aged hydration. A technique often termed as 'internal curing. Common internal curing agents (ICA) found in the construction industry are light-weight aggregates (LWA) and super-absorbent polymer (SAP), and recycled concrete aggregates (RCA) (Li, Liu, Xiao, & Zhong, 2020). Additionally, some natural sources of ICAs were also used as eucalyptus pulp fiber (Passarin Jongvisuttisun & Kimberly) and kenaf fiber (Gwon, Choi, & Shin, 2022). The utilisation of hemp shives as internal curing is yet to be found in the existing literature.

Thus, current research explores the possibility of using saturated porous hemp shives as an additive to the cement matrix. When added to a concrete mix in saturated conditions, it is expected that the shives will dissipate their absorbed water gradually as the concrete experiences self-desiccation due to evaporation. This additional internal water supply will aid in concrete hydration to offset the water loss due to evaporation resulting in an increased strength gain of the final concrete product. Within this research, a concrete mix will be prepared where hemp shives shall be added in varying amounts. Concrete cylinders will be produced using the mix and tested for compressive strength to observe the effect of hemp addition on concrete strength.

2. EXPERIMENTAL DETAILS

Hemp shives have been added by pre-saturated mass (3%, 2% and 1%) of binder content to concrete samples which were cured under sealed and unsealed conditions. Compressive strength testing was conducted at 1, 3, 7 and 28 days of curing to monitor the effect of evaporation and performance of the hemp shive when compared to a traditional (non-hemp) concrete control mix.

2.1. Hemp shives

Hemp shives, produced and processed in Victoria, Australia, were supplied by Australian Hemp Manufacturing Company, a subsidiary of Developing Sustainable Direction Pty Ltd (DSD). The particle size of the raw shives was widely variable between 30 mm to 0.5 mm. The mean size of the particles used in this study lies in the range of 1.18 mm to 2.36 mm, as classified by a combination of sieve analysis followed by image analysis techniques. The bulk density of the particles was 86.76 kg/m^3 with an initial water content of 8.75%. The water absorption capacity of washed samples was 335% of its own weight. Desorption was measured as 96% of its absorbed moisture at a relative humidity drop to 90% (from saturated conditions) (Nazmul, Garcez, Ashraf, & Sainsbury, 2022).

2.2. Mixture and composite preparation

A control mix was prepared according to ASTM C192/C192M (ASTM C192/C192M, 2019). The mix included Type I Ordinary Portland cement, 10 mm coarse aggregate, sand, and water with a target compressive strength of 50 MPa. The water-cement ratio was selected at 0.45 to represent a standard concrete mix. Hemp shives of predetermined lengths were added to the mix under Saturated Surface Dry (SSD) conditions at the specified dosage summarised in Table 1. The amount of binder and aggregates used to prepare each mix with varying hemp shive content. This was done to observe the effect of varying saturated hemp shives on the same concrete mass. A photograph of the batch mixing process is presented in Figure 1.

Table 1. Mixture proportion with hemp shive sizes and dosage

Mix ID	Sample Repeats	Curing Time (Days)	Hemp shive sizes	Hemp (% mass of binder)	Cement (kg/m^3)	Coarse aggregate (kg/m^3)	Fine aggregate (kg/m^3)	Water (l/m^3)
Control Mix (CM)	3	1,3,7,28	-	-	556	729	806	203.26
Non-cured Mix (NC)	3	1,3,7,28	-	-	556	729	806	203.26
MHS-3P	6	1,3,7,28	1.18	3.0%	556	729	806	203.26
MHS-2P	6	1,3,7,28	to	2.0%	556	729	806	203.26
MHS-1P	6	1,3,7,28	2.36mm	1.0%	556	729	806	203.26

Figure 1 Batch mixing hemp-concrete composite

Cylinders (100 × 200 mm) were prepared for each of the mix IDs and were kept at room temperature for 24 hours prior to demoulding. Upon demoulding, samples were then subjected to three different curing scenarios.

1. Control Mix (CM) samples were cured according to ASTM C192 / C192M-19 (2019).
2. No Curing (NC) samples were cured in 'air' at room temperature.
3. Sealed (S) samples were covered in plastic wrap to ensure minimum moisture loss. Samples were cured at room temperature.

Half of the samples that included hemp shives (MHS-3P, MHS-2P and MHS-1P) were subjected to NC conditions and half were subjected to S conditions to determine the effect of curing on the mechanical strength response. The hemp shives were saturated in water for 48 hours and then dried with paper towels to bring to SSD condition prior to including in the mix. The change in mass was recorded to estimate the additional water added to the concrete mix for curing.

3. RESULTS AND DISCUSSION

The compressive strengths of each of the batch mixes and curing conditions were tested following ASTM C39/C39M (2021) after 1 day, 3 days, 7 days, and 28 days. It was observed that the compressive strength of concrete with hemp as an additive varies with both hemp dosage and curing conditions. Obtained results are presented in Table 2.

Table 2. Density and compressive strength of composites

Mix ID	Curing condition	Density (kg/m3)	Compressive strength 28 days (MPa)	Comparison to CM at 28 days
Control Mix (CM)	Water	2505.31	48.12	0%
Non-cured Mix (NC)	Air	2435.24	41.78	-13.18%
MHS-3p	Sealed	2256.90	35.71	-25.79%
	Unsealed	2339.70	31.81	-33.89%
MHS-2p	Sealed	2305.73	44.31	-7.92%
	Unsealed	2388.54	39.33	-18.27%
MHS-1p	Sealed	2307.86	51.49	+7.00%
	Unsealed	2356.69	45.46	-5.53%

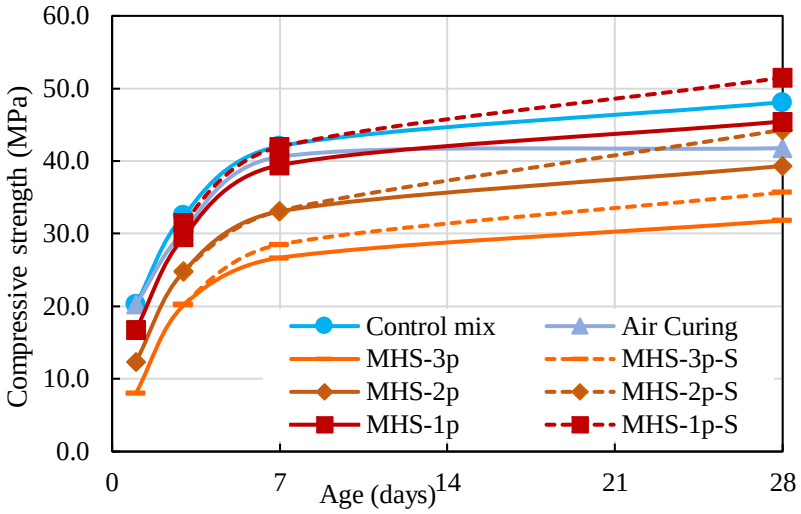

Figure 2 Compressive strength of hemp-concrete mixes under sealed and unsealed condition

The time-dependent strength gain for all samples is presented in Figure 2. There is a gradual decrease in the compressive strength of NC (air-cured) samples when compared to that of water-cured (CM) samples. This difference was initially low and increased with curing age. Thus, it can be confirmed that in the absence of proper curing, the mechanical strength may be reduced by about 13.18% after 28 days. In this case, seemingly evaporation in the absence of curing water limits the concrete from gaining its maximum strength.

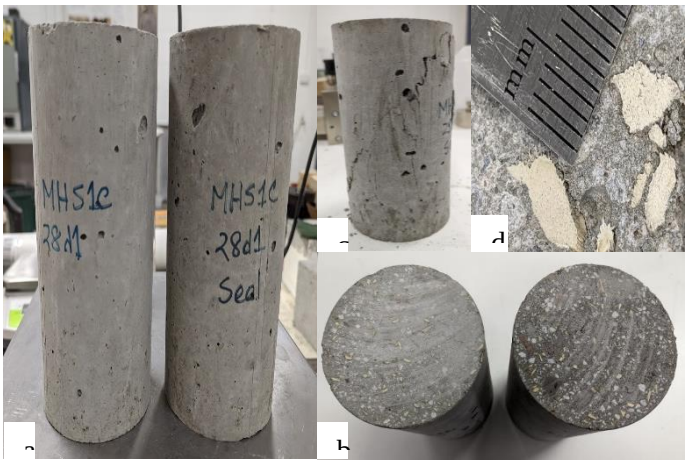

Figure 3 Image of a) Unsealed and Sealed hemp-concrete samples b) top view of sealed and unsealed samples c) cracked sample on 28 days d) magnified image of hemp shives in concrete

In the current experimental study, sealed conditions represent the case where the total water supplied by the hemp shives should be available for the hydration of self-desiccating concrete. Whereas in the unsealed condition samples, the effect of evaporation is observed on the available water for hydration. Therefore, the significant amount of water that can be supplied by porous hemp shives is more than sufficient to meet the need for both evaporation and cement hydration. This could also be observed in Figure 3 where the sealed specimen demonstrates to have a darker appearance compared to the unsealed specimen, which has dried to the exposure to air. Thus, it was observed for a particular percentage of hemp shives, the compressive strength of the sealed sample was higher than the unsealed cylinders.

As the proportion of saturated hemp shives was increased from 1 to 3% by mass into the concrete mix, there was a clear reduction in compressive strength, respectively 5.53-33.89% less than the control mix. It should be noted that the mass-wise increase of hemp shives proportionally increases the volume percentage of hemp shives with respect to the total concrete volume. Thus, the strength reduction could be attributed to the volume wise increase of hemp shives containing porous and soft intrinsic structure. The porous hemp shives replace stronger concrete elements and leave a negative effect on concrete compressive strength. Nevertheless, this effect can be optimised, as seen from the results of the mixes with 1% hemp shives. In this mix, the strength of the concrete is not undermined by excessive hemp inclusion. Rather the hemp inclusion promotes full uniform hydration of the cement providing a stronger product when compared to the control mix under ideal curing conditions.

Of note, in the test results, the 1% shive mix that was cured under sealed conditions reported a result that is 7% higher than the 28 days strength of the control mix. It can be observed in Figure 3 that the strength gain of the mix MHS-1p (when cured under sealed conditions) is far greater than the air-cured samples without shives. This can be simply explained as the relative humidity inside self-desiccating concrete drops below 93%, and self-desiccation starts to take place (presumably sometime after 3-7 days). The hemp shives release their absorbed moisture and aid in internal curing. Considering that no admixtures were used in these mixes, the reduction in relative humidity was natural – possibly due to self-evaporation and/or concrete hydration.

Seemingly, the internal curing water supplied by the soaked hemp shives was more beneficial at later stages of curing (7-28 days) for concrete hydration. However, in the early stages (i.e., 3 days - 7 days) it may be that due to the presence of sufficient water in the samples already, it is assumed that hemp shive could not release their absorbed water. Instead, the hemp left a negative effect on concrete compressive strength since their poor mechanical properties were only mobilised and not their hydration superpower.

It should be noted that this experimental program could not identify the optimum percentage of hemp shives which could maximise the compressive strength of concrete by supplying internal curing water. As the lowest percentage of hemp shives by mass was 1% of binder mass, it is possible that the inclusion of hemp shives at a lower percentage might yield a higher strength of concrete by internal curing yet maintaining a stronger structure of the concrete mass.

4. CONCLUSION

The research documents the effect of curing cementitious materials dosed with various volumes of saturated hemp shives. The followings findings are reported from the study.

1. The compressive strength of hemp-concrete composites decreases with an increase in hemp dosage.

2. Water stored in hemp shives aids in developing concrete compressive strength and is shown to be more effective with increased curing ages (e.g., 7-day +).

3. Restricting the effect of evaporation positively contributes to the compressive strength development of concrete by retaining the available moisture. Therefore, sealed cured samples perform better in compressive stress than unsealed samples.

4. At 1% dosage of hemp shives, under sealed conditions, the strength reduction due to the inclusion of the porous hemp structure is minimised to such an extent that the compressive strength is compensated by the effect of internal curing/hydration. In fact, in this case, at 29-days the sealed 1% hemp inclusion samples exceeded the compressive strength of the control mix by 7%.

These preliminary results suggest that a small, distributed volume of hemp shives in cement mixes provides positive strength benefits when long-term (28-day+) strength are considered.

REFERENCES

Arnaud, L., & Gourlay, E. (2012). Experimental study of parameters influencing mechanical properties of hemp concretes. *Construction and Building Materials, 28*(1), 50-56.

ASTM C39/C39M. (2021). Standard Test Method for Compressive Strength of Cylindrical Concrete Specimens. In. West Conshohocken, PA: ASTM International.

ASTM C192 / C192M-19. (2019). Standard Practice for Making and Curing Concrete Test Specimens in the Laboratory. In. West Conshohocken, PA: ASTM International.

ASTM C192/C192M. (2019). Standard Practice for Making and Curing Concrete Test Specimens in the Laboratory. In. West Conshohocken, PA: ASTM International.

Awwad, E., Mabsout, M., Hamad, B., Farran, M. T., & Khatib, H. (2012). Studies on fiber-reinforced concrete using industrial hemp fibers. *Construction and Building Materials, 35*, 710-717. doi:https://doi.org/10.1016/j.conbuildmat.2012.04.119

Balčiūnas, G., Vėjelis, S., Vaitkus, S., & Kairytė, A. (2013). Physical Properties and Structure of Composite Made by Using Hemp Hurds and Different Binding Materials. *Procedia Engineering, 57*, 159-166. doi:https://doi.org/10.1016/j.proeng.2013.04.023

Elfordy, S., Lucas, F., Tancret, F., Scudeller, Y., & Goudet, L. (2008). Mechanical and thermal properties of lime and hemp concrete ("hempcrete") manufactured by a projection process. *Construction and Building Materials, 22*(10), 2116-2123. doi:https://doi.org/10.1016/j.conbuildmat.2007.07.016

Gwon, S., Choi, Y. C., & Shin, M. (2022). Internal curing of cement composites using kenaf cellulose microfibers. *Journal of Building Engineering, 47*, 103867. doi:https://doi.org/10.1016/j.jobe.2021.103867

Jami, T., Karade, S. R., & Singh, L. P. (2019). A review of the properties of hemp concrete for green building applications. *Journal of Cleaner Production, 239*, 117852. doi:https://doi.org/10.1016/j.jclepro.2019.117852

Li, Z., Liu, J., Xiao, J., & Zhong, P. (2020). Internal curing effect of saturated recycled fine aggregates in early-age mortar. *Cement and Concrete Composites, 108*, 103444. doi:https://doi.org/10.1016/j.cemconcomp.2019.103444

Nazmul, R. T., Garcez, E. O., Ashraf, M., & Sainsbury, B.-A. (2022). A Critical Evaluation of Hemp as an Internal Curing Agent in Concrete Materials. *Construction and Building Materials (Under Review)*.

Passarin Jongvisuttisun, C. N., & Kimberly, E. K. Efficiency of Eucalyptus Pulps for Internal Curing. *ACI Symposium Publication, 290*. doi:10.14359/51684172

Sáez-Pérez, M. P., Brümmer, M., & Durán-Suárez, J. A. (2020). A review of the factors affecting the properties and performance of hemp aggregate concretes. *Journal of Building Engineering, 31*, 101323. doi:https://doi.org/10.1016/j.jobe.2020.101323

Sassoni, E., Manzi, S., Motori, A., Montecchi, M., & Canti, M. (2014). Novel sustainable hemp-based composites for application in the building industry: Physical, thermal and mechanical characterisation. *Energy and Buildings, 77*, 219-226. doi:https://doi.org/10.1016/j.enbuild.2014.03.033

Walker, R., Pavia, S., & Mitchell, R. (2014). Mechanical properties and durability of hemp-lime concretes. *Construction and Building Materials, 61*, 340-348. doi:https://doi.org/10.1016/j.conbuildmat.2014.02.065

Proc. 3rd International Conference on Structural Engineering Research (iCSER 2022)
27-30 Nov 2022, Sydney, Australia
ISBN: 978-0-6456692-1-3

Studies on Anwar Ispat Waste Cement Sheet Powder (C.S.P) as Partial Replacement of Sand in Concrete Block Production.

Sajjad Hossain[1], Md. Ashraful Alam[2], Md. Motaher Hossain[3], Ismail Hossain[4]

[1]Research Fellow, Housing & Building Research Institute, Dhaka, Bangladesh
[2]Director General, Housing & Building Research Institute, Dhaka, Bangladesh
[3]Joint Secretary, Ministry of Housing and Public Works, Dhaka, Bangladesh
[4]Research Officer, Housing & Building Research Institute, Dhaka, Bangladesh

Corresponding author's E-mail: sajjad.civil4389@gmail.com

Abstract

The increasing search for sustainable and green materials in the construction industry has led to research on the partial replacement of conventional concrete components by waste materials. These materials are commonly used in residential access roads, paving and curbs, walls, house foundations and gutter applications. Solid waste management is a major environmental concern for the country at this time. The possibility of using cement sheet powder as fine aggregate cannot be overlooked in order to transform waste cement sheet powder (into an environmentally friendly resource and save the environment from pollution. This research aims to investigate the feasibility of reusing waste cement sheet powder as a partial replacement of sand in concrete block production. Compressive strength and density tests of concrete block are conducted at different replacement percentages (0%, 20%, 40%, 60% and 80% by weight) of sand by waste cement sheet powder. The concrete block design strength of mix ratio 1: 4 (cement: sand) *and 0.56 w/c ratio was used for the experiment. The compressive strength of mortar is tested on the cube specimens (51 x 51 x 51)* mm *at 7, 14 and 28 days, respectively and density of the concrete block specimens were determined. The results showed that the compressive strength of the concrete block decreased with an increase in the percentage of replacement of the cement sheet powder. The results also showed a decrease in the unit weight of concrete blocks with an increase in the percentage replacement of cement sheet powder. The average compressive strength of mortar measured at 28 days of (0%, 20%, 40%, 60% and 80%) of waste cement sheet powder is 11.17, 11.15, 7.87, 7.00, and 6.85 MPa w/c ratio was 0.56 respectively. The mortar made with waste cement sheet powder has a lower density as compared to the specimens made without waste cement sheet powder. It can be inferred from this research that cement sheet powder wastes are not suitable materials that can be used to enhance the development of compressive strength in the matrix of concrete blocks, but they can be used in the production of lightweight concrete blocks in construction.*

Keywords: *Waste cement sheet powder; Recycling; Lightweight concrete block; Compressive strength; Dry density.*

1. INTRODUCTION

Asbestos-free fiber-cement is a relatively new building material: the first fiber-cement products were used in construction about 30 years ago. The fiber-cement composite material is composed of cement, cellulose fibers, admixtures, and water. Every year, the cutting of fiber-cement panels during the manufacturing process produced hundreds of tons of waste (Müller et al., 2011). These wastes contain a high concentration due to hydration cement, which has hydraulic properties. The activity could be used in the production of mortar or concrete. Furthermore, valorizing these wastes may reduce the environmental cost of construction materials. This can be accomplished by increasing the recycling of waste products in construction materials, which are currently only used as fillers (Tam et al., 2007). Today, the recovery of such wastes is a cost-effective option for a variety of applications, but they must meet the same quality and performance standards as traditional materials. Despite extensive

research on recycled concrete materials over the last few decades (Hoffmann et al., 2012), (Maier & Durham, 2012), (Soutsos et al., 2011) and (Stehlík, 2013), there have been very few studies concerning the formulation of mortars or concretes which incorporate waste fiber-cement. Recently, (Müller et al., 2011) conducted a study on the use of crushed asbestos-free fiber-cement waste as aggregate base layer for road structures. Their findings were encouraging, allowing the use of this type of waste in field construction.

Waste cement sheets powder is one of the few materials available having good mechanical strength combined with lightweight and low thermal conductivity. It can be produced in a wide range of densities and properties, which can be varied to suit particular requirements. Waste cement sheets and powder blocks are lighter than concrete & brick, respectively.

The primary purpose of this research is to conduct experiments to improve the qualities of concrete blocks as well as lightweight blocks by waste cement sheets powder. To achieve this goal, the following objectives have been identified:

- To know the effect of waste cement sheets powder on the compressive strength and density of concrete blocks.
- To provide an alternative lightweight material.
- Compare the strength and density of lightweight concrete blocks with normal concrete blocks.

The use of waste cement sheets powder can lead to the improvement in the properties of cement concrete in addition to providing a proper solution for the disposal of this natural waste. The purpose of this study is to compare the qualities of waste cement sheets powder concrete to those of conventional concrete or bricks.

2. MATERIALS AND METHODOLOGY

2.1. Materials

The materials used in making concrete blocks were sand, cement and waste cement sheets powder. The waste cement sheets powder collected from Anwar Ispat LTD, Targach, Konia, Mymensingh, Gazipur, Bangladesh as shown in Fig 1. A concrete block mix was designed to achieve the ratio of 1:4. The experiment was done by taking an additional 0%, 20%, 40%, 60%, and 80% of sand (by weight) of waste cement sheets powder.

2.2. Cement

Locally available Anwar Cement of Bangladesh CEM - II/A.M (S.V.L) 42.5 N purchased commercially from the local market and used in case of control mix. The physical properties and specifications of the cement were obtained from different tests as per BS 12:1991 and ASTM standard. The test was conducted in HBRI laboratories and results are summarized below as shown in Table -1

2.3. Dredged sand

Because of being a riverine country, the dredged sand is abundant. Dredged sand is a naturally occurring granular material as well as fine aggregate composed of finely divided rock and mineral particles (TAIWO & OLAMOJU, 2019). The composition of dredged sand is highly variable, depending on the local rock sources and conditions. The Dredged sand was collected from the river named Kopotakkho, Satkhira, Bangladesh and used as fine aggregate. The sand were clean, sharp, less amount of clay and organic matter and well graded, the properties with the test results are shown in Table 2.

2.4. Water

Water is the most important and least expensive ingredient of concrete .In the process of creating the binding matrix, which holds the inert aggregate suspended until the matrix has hardened, hydration of cement uses a portion of the mixing water. The remaining water provides permanent workability by acting as a lubricant between the fine and coarse aggregate. Impurities in the mixing water cause concrete to lose some of its strength and durability. Concrete must be mixed with clean water that contains no harmful levels of oils, alkalis, salts, organic compounds, or other contaminants that could harm the concrete. In this study drinking water have been used in mixing of concrete which is supplied from deep tube well of Housing & Building Research Institute (HBRI) and is known to have no unusual impurities.

2.5. Waste cement sheets powder (C.S.P)

Waste cement sheets (asbestos) mining existed more than 4,000 years ago, but large-scale mining began at the end of the 19th century when manufacturers and builders began using Waste cement sheets (asbestos) for its desirable physical properties: sound absorption, average tensile strength, resistance to fire, heat, electricity, and affordability. It was used in such applications as electrical insulation for hotplate wiring and in building insulation. When asbestos is used for its resistance to fire or heat, the fibers are often mixed with cement or woven into fabric or mats. These desirable properties made (waste cement sheets) asbestos very widely used. Waste cement sheets (Asbestos) use continued to grow through most of the 20th century until public knowledge (acting through courts and legislatures) of the health hazards of waste cement sheet (asbestos) dust outlawed asbestos in mainstream construction and fireproofing in most countries.

Waste cement sheets (Asbestos) are taken from Anwar Ispat LTD, Targach, Konia, Mymensingh, Gazipur, Bangladesh. Sample pictures of waste cement sheets powder are shown on Figure 1 and Table 3 shows the physical properties of waste cement sheets powder .

(a) Waste Cement Sheets Powder (b) Sand (c) Cement

Figure 1. Raw materials of concrete block

Table 1 Physical properties of cement

SL.No	Test Conducted	Test Results
1	Normal Consistency	25 %
2	Initial Setting Time	125 min
3	Final Setting Time	185 min
4	Compressive Strength	3 days – 13.69 MPa 7 days-20.62 MPa 28 days- 28.56 MPa
5	Fineness	99.4%
6	Specific Gravity	3.14

Table 2 Properties of sand

SL.No	Test Conducted	Test Results
1	Fineness Modulus (FM)	1.02
2	Specific Gravity	2.86
3	Bulk Density	1313 kg/m^3
4	Percentage voids in sand	54%
5	Water Absorption	2.31%
6	Silt Content	3.63%

Table 3 Properties of waste

SL.No	Test Conducted	Test Results
1	Specific Gravity	2.14
2	Bulk Density	446 kg/m^3
3	Water Absorption	4.16%
4	Color	Off white

2.5 Mix Design

The volume ratio between cement and sand in the mixture is 1: 4, while the percentage of waste cement sheet powder (C.S.P) in the mixture is 0%, 20%, 40%, 60% and 80%. The water-cement ratio used is 0.56; the material composition for each variation of the mixture is presented in Table 4.

Table 4 Mix Proportions of Mixes for (51 x 51 x 51) mm cube

Mix ID	Waste cement sheets powder (gm)	Sand (gm)	Cement (gm)	Water (ml)	W/C
C.S.P 0%	0	1360	340	190	0.56
C.S.P 20%	340	1020	340	190	0.56
C.S.P 40%	680	680	340	190	0.56
C.S.P 60%	1020	340	340	190	0.56
C.S.P 80%	1360	0	340	190	0.56

2.6. Mortar Mixing and Casting of Specimens

In this experiment, mortar is manually mixed for the casting of cube according to mix design. To ensure the quality strength, the following format followed sequentially for mixing concrete block. For cube compressive strength test (51 x 51 x 51) mm size cubes were cast. First properly mixed sand then mixed binding materials (PPC), water and different percent of waste cement sheets powder for the replacement of 0%, 20%, 40%, 60%, and 80% of natural sand (by weight) waste cement sheets powder mix with proportion of mix design. Finally mix all ingredients by mixture machine and hand for the casting of cube specimens.

3. RESULTS AND DISCUSSION

In 2013, research was conducted into the production of concrete containing recycled aggregates from crushed light structural and non-structural concrete (Bogas et al., 2015). This research has shown that it is possible to produce recycled lightweight structural concrete from crushed, structural and non-structural LWC with densities lower than 2000 kg/m3. Table 5 shows the cube compressive strength and density of waste cement sheets powder concrete blocks after 28 days of curing. For each type of waste and percentage, average test results for compressive strength and density concrete blocks are reported.

3.1. Compressive Strength

The compressive strength tests result for the concrete block mixes of the 0% (control), 20%, 40%, 60%, and 80% replacements are presented in Figure 2, while the compressive strength of curing for 28 days. The results reveal that as the waste cement sheet powder content increases in mixes the propensity of the strength values decreases below that for the plain mix up to 39% at 28 day curing period for 80% replacement level, as shown in Table 5. Similarly, for 40% and 60% replacement of the fine aggregate (sand) with cement sheet powder waste (Table 5) at curing of 28 days, 30% and 37% reduction in strength was recorded when compared to 0% replacement also curing at 28 days. However, for 20% replacement of the fine aggregate (sand) with cement sheet powder waste (Table 5) at curing of 28 days, 0.18% reduction in strength was recorded when compared to 0% replacement also curing at 28 days. This reduction in compressive strength can be attributed to the decrease in adhesion or bond strength between the cement sheet powder aggregate and the cement paste.

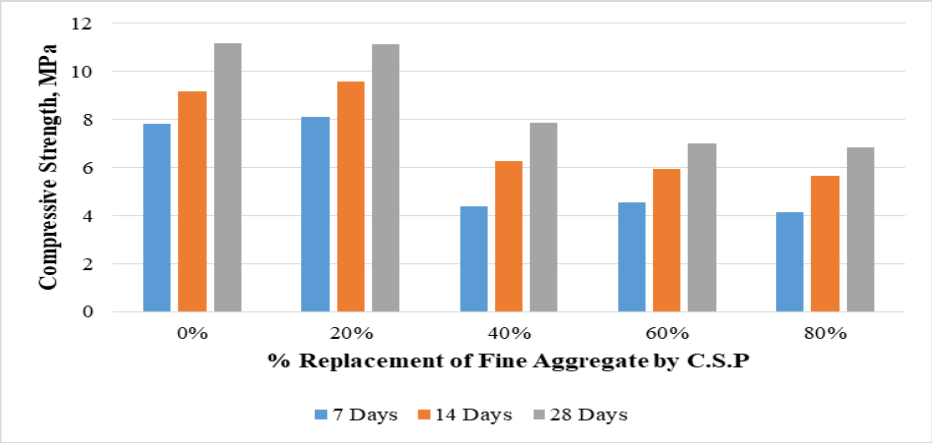

Figure 2. Compressive strength of concrete blocks with various mix percentages

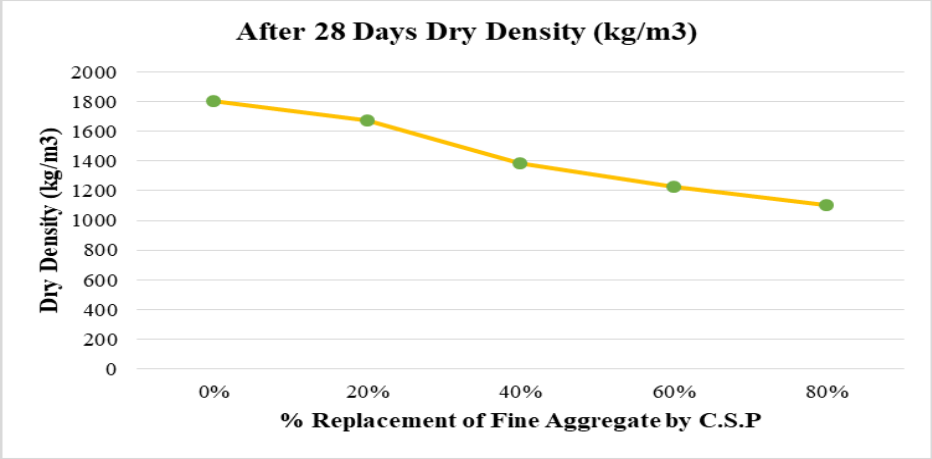

Figure 3. Density of concrete blocks with various mix percentages

3.2. Dry Density

The dry density of mortar was measured using the same mortar cubes that were used for compressive strength tests. The average dry density of concrete blocks measured at 28 days is presented in Figure 3. It was shown that as the percentage of sand replaced by waste cement sheets powder increased, the dry density of concrete blocks decreased (see Figure 3). At 28 days, the average dry density of

concrete blocks made with 0%, 20%, 40%, 60% and 80% waste cement sheets powder was 1805 kg/m3, 1676 kg/m3, 1382 kg/m3, 1230 kg/m3 and 1102 kg/m3, respectively. It shows that the density of normal concrete blocks with zero percent mixed waste cement sheets powder was the highest (1805 kg/m3) of all samples tested. On the other hand, the replacement of 80% sand mixed with a concrete block had the lowest value (1102 kg/m3) of all samples. The decrease in the dry density can be attributed to the lower density (446 kg/m3 for C.S.P and 1313 kg/m3 for sand) of waste cement sheets powder compared to sand.

Table 5 Compressive strength and density of cement blocks

Mix ID	Compressive Strength (MPa)			Density (kg/m^3)	W/C
	7 Days	14 Days	28 Days	28 Days	
C.S.P 0%	7.82	9.16	11.17	1805	0.56
C.S.P 20%	8.11	9.59	11.15	1676	0.56
C.S.P 40%	4.40	6.29	7.87	1382	0.56
C.S.P 60%	4.55	5.95	7.00	1230	0.56
C.S.P 80%	4.14	5.65	6.85	1102	0.56

4. CONCLUSION

The following conclusions can be made based on the scope of the current research.

- The waste cement sheet powder can be used to replace the fine aggregate in a concrete block mixture as it contributes to reducing the unit weight (density) of the concrete, due to the low density of cement sheet powder (C.S.P) as compared to the density of fine aggregates. The product is useful in applications requiring non-bearing lightweight concrete as concrete panels.

- 40%, 60%, and 80% of waste cement sheets powder replaced for concrete blocks gave a good low-weight structural concrete. The low density of waste cement sheets powder reduces the overall weight of waste cement sheets powder concrete block. Effectively, it can be used as structural lightweight blocks.

- The compressive strength of the concrete block decreased with an increase in the percentage of replacement of the cement sheet powder.

- The use of cement-based composite cement sheet powder waste can significantly reduce construction costs by fully or partially replacing fine aggregates (sand).

- Lightweight concrete can be used as floor tiles, roofing materials, walls or partitions in multi-storey buildings due to its lightweight, non-corrosive and weatherproof weight.

- The application of waste cement sheets powder as an ingredient in concrete blocks reduces density and therefore reduces the weight of the final component.

- Finally, the study found that cement sheet powder waste is not a good material to enhance the compressive strength of the concrete block. The lightweight concrete block should not be used for load-bearing wall where high compressive strength is required.

ACKNOWLEDGMENTS

The authors gratefully acknowledge the financial support from the Housing and Building Research Institute (HBRI), Dhaka, Bangladesh.

REFERENCES

Bogas, J. A., de Brito, J., & Figueiredo, J. M. (2015). Mechanical characterization of concrete produced with recycled lightweight expanded clay aggregate concrete. *Journal of Cleaner Production*, *89*, 187-195.

Bouharoun, S., Leklou, N., & Mounanga, P. (2015). Use of asbestos-free fiber-cement waste as a partial substitute of Portland cement in mortar. *Materials and structures*, *48*(6), 1679-1687.

Mustika, W., Kadir, A., Ngii, E., & Nurdin, M. (2021). Properties of concrete paving blocks made with nickel slags. IOP Conference Series: Earth and Environmental Science,

Sule, J., Emmanuel, S., Joseph, I., Ibhadobe, O., Alfred, B. Y., Waziri, F. I., & Sunny, E. (2017). Use of waste plastics in cement-based composite for lightweight concrete production. *Int. J. Res. Eng. Technol*, *2*(5), 44-54.

Hoffmann, C., Schubert, S., Leemann, A., & Motavalli, M. (2012). Recycled concrete and mixed rubble as aggregates: Influence of variations in composition on the concrete properties and their use as structural material. *Construction and Building Materials*, *35*, 701-709.

Maier, P. L., & Durham, S. A. (2012). Beneficial use of recycled materials in concrete mixtures. *Construction and Building Materials*, *29*, 428-437.

Müller, A., Schnellert, T., & Seidemann, M. (2011). Material utilization of fibre cement waste. *ZKG Int*, *64*, 60-72.

Soutsos, M. N., Tang, K., & Millard, S. G. (2011). Use of recycled demolition aggregate in precast products, phase II: Concrete paving blocks. *Construction and Building Materials*, *25*(7), 3131-3143.

Stehlík, M. (2013). Testing the strength of concrete made from raw and dispersion-treated concrete recyclate by addition of additives and admixtures. *Journal of Civil Engineering and Management*, *19*(1), 107-112.

Sule, J., Emmanuel, S., Joseph, I., Ibhadobe, O., Alfred, B. Y., Waziri, F. I., & Sunny, E. (2017). Use of waste plastics in cement-based composite for lightweight concrete production. *Int. J. Res. Eng. Technol*, *2*(5), 44-54.

TAIWO, S. A., & OLAMOJU, A. M. (2019). Effect of river sand and land excavated sand on the compressive strength of hollow concrete block.

Tam, V. W., Tam, C. M., & Wang, Y. (2007). Optimization on proportion for recycled aggregate in concrete using two-stage mixing approach. *Construction and Building Materials*, *21*(10), 1928-1939.

Proc. 3rd International Conference on Structural Engineering Research (iCSER 2022)
27-30 Nov 2022, Sydney, Australia
ISBN: 978-0-6456692-1-3

Utilization of Waste Iron Slag As The Fine Aggregate (Sand) Material In Concrete Block For Low Cost Application

Sajjad Hossain[1], Md. Ashraful Alam[2], Md. Motaher Hossain[3], Ar. Md. Nafizur Rahman[4] and Ahsan Habib[5]

[1]Research Fellow, Housing & Building Research Institute, Dhaka, Bangladesh
[2]Director General, Housing & Building Research Institute, Dhaka, Bangladesh
[3]Joint Secretary, Ministry of Housing and Public Works, Dhaka, Bangladesh
[4]Principal Research Officer, Housing & Building Research Institute, Dhaka, Bangladesh
[5]Senior Research Officer, Housing & Building Research Institute, Dhaka, Bangladesh

Corresponding author's E-mail: sajjad.civil4389@gmail.com

ABSTRACT

Bangladesh has a lot of environmental problems because of the production of industrial waste. The biggest problem Bangladesh faces is utilizing the massive by-products produced as a result of industrialization. Iron slag is one of the industrial wastes from the iron and steel manufacturing processes. Therefore, many studies eventually point to a variety of waste management strategies that involve both eco-efficient parameters. In the row, recent studies have been paid for their emphasis on construction materials that include fine aggregates. The majority of the studies that have been done focused on the replacement for these construction aggregates, but there is still potential for further research. The purpose of this study is to determine the effect of using replacements for fine aggregates. This paper presents the results of an experimental investigation on the properties of the concrete block using iron slag as a partial replacement of fine aggregate (sand). Compressive strength, density and water absorption tests of concrete block are conducted at different replacement percentages (0%, 10%, 20%, 25%, 30%, 40%, 50%, 60%, 70% and 80% by weight) of sand by waste iron slag. The compressive strength of mortar is tested on the cube specimens (50.8 x 50.8 x 50.8) mm at 7 and 28 days with a water-to-cement ratio of 0.45. The results indicate that the compressive strength for the mortar cubes is gradually decreasing with an increasing percentage of iron slag in the concrete block but the exception is the 25% iron slag. The average compressive strength of mortar measured at 28 days of (0%, 10%, 20%, 25%, 30%, 40%, 50%, 60%, 70% and 80%) of waste iron slag is 22.37, 20.87, 19.21, 26.87, 21.02, 20.17, 18.18, 16.45, 13.13 and 12.65 MPa, respectively. The optimal value of compressive strength is achieved at 25% replacement as the iron slag percentage of the concrete block increases rapidly. After 25% replacement, the strength decreases. The mortar made with waste iron slag has a higher density as compared to the specimens made without waste iron slag.

***Keywords**: Waste iron slag; Recycling; Compressive strength; Water absorption; Density*

1. INTRODUCTION

Concrete production cannot be completed without aggregates. They are generally inert, used to reduce costs, eliminate shrinkage and creep, and enhance the overall mechanical strength of concrete (Mehta & Monteiro). As a result, securing the supply of good quality aggregates is important for building concrete. So the material should also be affordable, eco-friendly, and sustainable (Deselnicu et al., 2018). However, the supply of river aggregates is declining due to increasing demand in the Netherlands, for instance, which has increased the need for alternate sources, such as the use of concrete waste as an aggregate (Nedeljković et al., 2019). On the other hand, certain islands lack access to natural aggregates and are investigating the use of marine coral reef aggregates in the construction of concrete (Wang et al., 2019).

In this context, the construction industry can play a significant role. In the current situation, iron slag

waste is not yet at a high level of utilization in a country like Bangladesh. The possible reason for this is the lack of research on how to use this by-product steelmaking industry. However, high levels of utilization of iron slag in some developed countries raise hopes and lessons for developing countries like Bangladesh. Therefore, appropriate research should be conducted in Bangladesh on the sustainable use of iron slag waste. To ensure that iron slag can be used as fine aggregate in the manufacturing of concrete blocks, it is also necessary to figure out a way to recycle it as a more valuable commodity.

Bangladesh is in the process of developing. Massive construction projects are going on throughout the whole country. As a result, there is a substantial rise in demand for both steel and concrete on a daily basis. Steel industries generate large amounts of waste, such as iron slag. Bangladesh's total steel production is estimated to be 8 million tons per year, with slag production ranging from 120,000 to 160,000 tons per year (Nieri, 2013). However, it is not being used properly, which means that there is no long-term use for this iron slag in Bangladesh. However, prior effort must be made for waste reuse and recycling in modern society, which is also important in terms of the environment (Martínez-Lage et al., 2012). Various research studies have already identified the various uses of iron slag. However, a limited number of studies to date have looked into the long-term use of iron slag in concrete block production. As a result, it is essential to figure out how to use iron slag in concrete block production in a sustainable manner.

The European Slag Association EUROSLAG has been conducting surveys among its members (European steelworks and processing companies) every two years since 2000. From these surveys, it is known that in 2008, 45.6 million tons of ferrous slag were produced and that more than 400 million tons of iron and steel slag are produced annually in the world. These findings are in accordance with a survey conducted by En Safe, Inc. (2002).

If iron slag can be used as a partial replacement for fine aggregate, coarse aggregate, or cement, future fine aggregate supply shortages and the problem of a slag disposal site can be reduced. A very interesting idea is to utilize iron slag aggregate in replacement of fine aggregates in concrete (Raza et al., 2014). Waste iron slag powder can also be harmful to human health because it is so simple to inhale. Studies have revealed that Waste iron slag powder might be used to partially replace natural sand in the manufacturing of concrete. For instance, Ghannam et al. investigated the results of replacing some of the sand in concrete with iron powder. Their research demonstrated that the compressive and flexural strengths of concrete could be maintained when up to 20% of the sand was replaced by waste iron slag powder (Ghannam et al., 2016).

Similarly, found that when 20% of the fine aggregate was replaced with waste iron slag, compressive and flexural strength improved (Ismail & Al-Hashmi, 2008). Compressive and flexural strengths increased by 17% and 28% (compared to the reference concrete), respectively. According to some researchers, iron fillings can replace even higher percentages of fine aggregate in concrete without impairing its structural integrity. For example, concrete constructed with 100% iron filings has a 26% higher compressive and splitting tensile strength than concrete made with 100% natural fine aggregate (Helmand & Saini, 2019).

The objective of this fine aggregate replacement is to minimize the the total cost of construction, established waste iron slag utilization for various building materials and making environment friendly concrete block by using slag as a replacement of fine aggregate, solving the dumping problem of slag & observing the variation of the concrete block compressive strength, tensile strength, density as well as due to the use of slag as a replacement of fine aggregates in various proportions at different curing period.

2. MATERIALS AND METHODOLOGY

2.1. Cement

Locally available Anwar Cement of Bangladesh CEM - II/A.M (S.V.L) 42.5 N purchased commercially from the local market and used in case of control mix. The physical properties and specifications of the cement were obtained from different tests as per BS 12:1991 and ASTM standards. The test was conducted in HBRI laboratories, and results are summarized below as shown in Table 1.

2.2. Fine aggregate

Natural river sand collected from (Someshwari river, Durgapur, Netrokona, Bangladesh with coordinate code (25.1415800, 90.6729327)) is used. Various Tests are carried on sand to find the properties as per IS: 2386 (part-2). The sand has a coefficient of curvature of 1.15 and a coefficient of uniformity of 3.96; hence, it is poorly graded sand.

2.3. Water

Water is the most important and least expensive ingredient of concrete. In the process of creating the binding matrix, which holds the inert aggregate suspended until the matrix has hardened, the hydration of cement uses a portion of the mixing water. The remaining water provides permanent workability by acting as a lubricant between the fine and coarse aggregate. Impurities in the mixing water cause concrete to lose some of its strength and durability. Concrete must be mixed with clean water that contains no harmful levels of oils, alkalis, salts, organic compounds, or other contaminants that could harm the concrete. In this study, drinking water has been used to mix concrete supplied from the Housing & Building Research Institute (HBRI) deep tube well and is known to have no unusual impurities.

2.4. Iron slag

Iron slag is an industrial waste material. It is a by-product of the production of iron and steel. Steel is made either by melting scrap to make steel in an electric arc furnace (EAF) or by converting iron to steel in a basic oxygen furnace (BOF). It was obtained from Anwar Ispat LTD, Targach, Konia, Mymensingh, Gazipur, Bangladesh. Sample pictures of waste iron slag are shown in Figure 1 and Table 3 shows the physical properties of iron slag. The waste iron slag has a coefficient of curvature of 0.72 and a coefficient of uniformity of 3.55; hence, it is poorly graded sand.

Figure 1.Waste Iron Slag

Table 1 Physical properties of cement

SL.No	Test Conducted	Test Results
1	Normal Consistency	25 %
2	Initial Setting Time	135 min
3	Final Setting Time	185 min
4	Compressive Strength	3 days – 13.69 MPa 7 days-20.62 MPa 28 days- 28.56 MPa
5	Fineness	99.4%
6	Specific Gravity	3.14

Table 2 Properties of fine aggregate

SL.No	Test Conducted	Test Results
1	Fineness Modulus (FM)	3.12
2	Specific Gravity	2.40
3	Bulk Density	1485 kg/m3
4	Water Absorption	1.01%
5	Bulking of Sand	14.28%
6	Silt Content	Nil
7	Salinity	88.5 ppm
8	TDS	111.6 ppm
9	pH	10.62

Table 3 Properties of iron slag

SL.No	Test Conducted	Test Results
1	Fineness Modulus (FM)	2.25
2	Specific Gravity	2.86
3	Bulk Density	1653 kg/m3
4	Water Absorption	1.52%
5	Bulking of Iron Slag	21.21%
6	Salinity	45.9 ppm
7	TDS	61.9 ppm
8	pH	9.06

2.5. Methodology

The industrial wastes iron slag and fine aggregate has been tested, and their properties are compared as a result. Firstly, physical tests of materials are performed with cement, fine aggregates and iron slags. As well various tests were performed on fine aggregates and iron slag. These tests are sieve analysis (FM), specific gravity, bulk density, water absorption, bulking of sand, silt content, salinity, TDS and pH. Then, their results have been compared and it is concluded that fine aggregate could be replaced by iron slag. Mortar cubes of (50.8 x 50.8 x 50.8) mm dimension were cast for 1:4 concrete blocks to determine strength characteristics with different percentages of iron slag. The replacement of 0%, 10%, 20%, 25%, 30%, 40%, 50%, 60%, 70% and 80% of fine aggregate by waste iron slag and studied for compressive strength and water absorption as well as density for the curing periods of 7days and 28 days. For each percent replacement & curing period, 2 samples are prepared & 3 samples for the compressive strength test.

2.6. Mix proportion

For concrete block, the mix design ratio for 1:4, respectively with water cement (W/C) ratio of 0.45. The mixture proportions of the mortar mixes for (50.8 x 50.8 x 50.8) mm cube are summarized in Table 4

Table 4 Mix Proportions of Mixes for (50.8 x 50.8 x 50.8) mm cube

Mix ID	Cement (gm)	Fine aggregate (gm)	Waste iron slag (gm)	Water (ml)
WIS 0%	340	1360	-	153
WIS 10%	340	1190	170	153
WIS 20%	340	1020	340	153
WIS 25%	340	880	510	153
WIS 30%	340	850	680	153
WIS 40%	340	680	850	153
WIS 50%	340	510	880	153
WIS 60%	340	340	1020	153
WIS 70%	340	170	1190	153
WIS 80%	340	-	1360	153

2.7. Mortar Mixing and Casting of Specimens

In this experiment, mortar is manually mixed for casting of cube according to the mix design. For the cube compressive strength test, (50.8 x 50.8 x 50.8 mm) size cubes were cast. First properly mixed fine aggregate then mixed binding materials (PPC), water and different percent of waste iron slag for the replacement of 0%, 10%, 20%, 25%, 30%, 40%, 50%, 60%, 70% and 80% of natural fine aggregate (by weight) iron slag mix with a proportion of mix design. Finally, mix all ingredients by mixture machine and hand for the casting of cube specimens.

3. RESULTS AND DISCUSSION

3.1. Compressive Strength

The compressive strength of mortar made with ten different percentage replacements (0%, 10%, 20%, 25%, 30%, 40%, 50%, 60%, 70% and 80%) of fine aggregate by waste iron slag was conducted at 7 and 28 days are shown in Table 5. Compressive strength increases up to the replacement of 25% iron slag when waste iron slag is added to the control mixt.

Table 5 Compressive Strength (MPa)

Days	compressive Strength in MPa obtained after adding iron slag									
	0%	10%	20%	25%	30%	40%	50%	60%	70%	80%
7	17.98	16.29	15.56	24.94	19.10	16.42	15.33	13.42	11.14	10.00
28	22.37	20.87	19.21	26.87	21.02	20.17	18.18	16.45	13.13	12.65

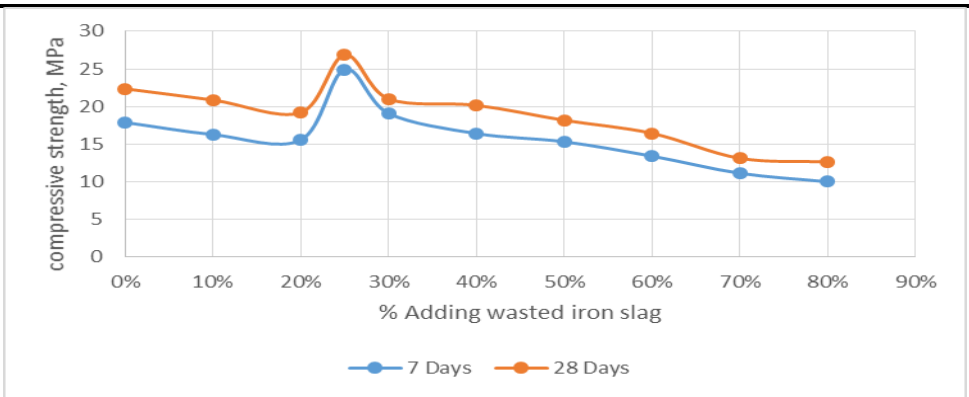

Figure 2. Compressive Strength Test results of cubes with and without waste iron slag

3.2. Density

It shows that the density of blocks for mixed waste iron slag concrete block with 40% mixed waste iron slag was the highest (2212 kg/m^3) among all the investigated samples. On the other hand, the addition of 10% for waste iron slag mixed with a concrete block achieved the lowest value (1868 kg/m^3) among all samples. The density value of a normal concrete block has achieved the value (1907 kg/m^3).

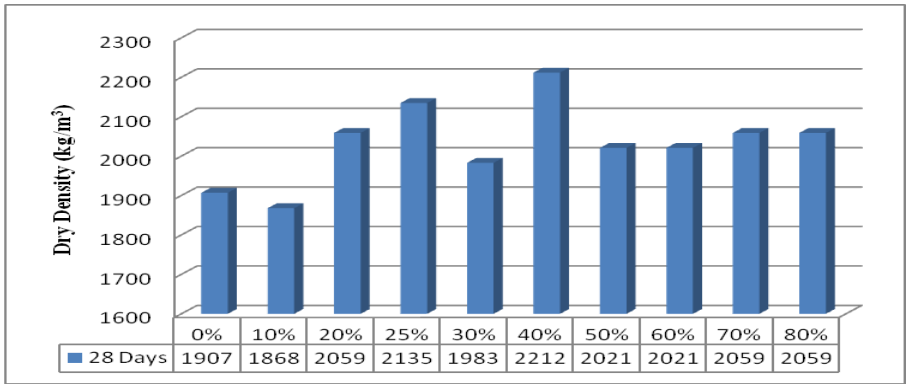

Figure 3. After 28 Days Dry density (kg/m3) concrete blocks mixed with different WIS

3.3. Water Absorption

The water absorption of concrete blocks mixed with the addition of 60% waste iron slag was found to be the highest (13.21%) among all types. The addition of 25% for waste iron slag mixed with concrete blocks achieved the lowest value (8.93%) among all samples, and the water absorption value of normal concrete block achieved value (of 10.00%).

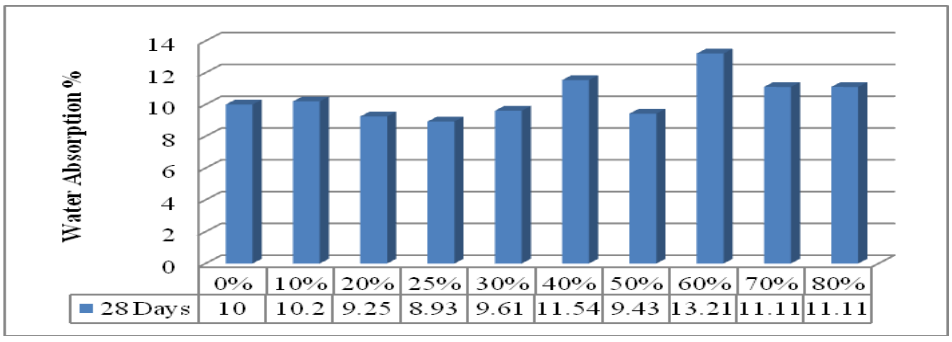

Figure 3. Water absorption (%) concrete blocks mixed with different WIS at 28 Days

4. CONCLUSION

- In the manufacturing of concrete blocks, waste iron slag may be used in replacement of fine aggregate (sand).
- At 25% replacement of fine aggregate with waste iron slag aggregate gives desirable compressive strength.
- After adding 25% waste iron slag in the mix, there is an increase of 27.91% after 7 days and 16.75% increase after 28 days as compared to the control mix and after adding (10%, 20%, 30%, 40%, 50%, 60%, 70% and 80%) waste iron slag decreases compressive strength in Concrete blocks but according to PWD schedule can be used in construction materials these percentages waste iron slag. As a result, construction can be more cost-effective.

- The use of waste iron slag in concrete block production would lead to more effective environmental waste management and profitable industrial waste utilization.

- Finally, it can be concluded that Slag from Bangladesh Steel Re–Rolling Mills (Anwar Ispat Ltd.) can be used as fine aggregate (sand) at a proportion of 25% of total fine aggregate to gain more compressive strength.

- The study indicated that the compressive strength, density and water absorption of waste iron slag were comparable with the normal concrete blocks.

Hence, it could be recommended that the waste Iron slag aggregate could be effectively utilized as fine aggregate in all concrete applications either as partial or full replacements of fine aggregate (sand).

ACKNOWLEDGMENTS

The authors gratefully acknowledge the financial support from the Housing and Building Research Institute (HBRI), Dhaka, Bangladesh.

REFERENCES

Deselnicu, D. C., Militāru, G., Deselnicu, V., Zăinescu, G., & Albu, L. (2018). Towards a circular economy–a zero waste programme for Europe. International Conference on Advanced Materials and Systems (ICAMS).

Data source from SCA (Slag Cement Association) of America.

Ghannam, S., Najm, H., & Vasconez, R. (2016). Experimental study of concrete made with granite and iron powders as partial replacement of sand. *Sustainable Materials and Technologies*, *9*, 1-9.

Helmand, P., & Saini, S. (2019). Mechanical properties of concrete in presence of Iron filings as complete replacement of fine aggregates. *Materials Today: Proceedings*, *15*, 536-545.

Ismail, Z. Z., & Al-Hashmi, E. A. (2008). Reuse of waste iron as a partial replacement of sand in concrete. *Waste Management*, *28*(11), 2048-2053.

Martínez-Lage, I., Martínez-Abella, F., Vázquez-Herrero, C., & Pérez-Ordóñez, J. L. (2012). Properties of plain concrete made with mixed recycled coarse aggregate. *Construction and Building Materials*, *37*, 171-176.

Mehta, P., & Monteiro, P. Concrete Microstructure, Properties and Materials; McGraww-Hill: New York, NY, USA, 2006. 2. *Deselnicu*, *DC*.

Miah, M. J., Ali, M. K., Paul, S. C., John Babafemi, A., Kong, S. Y., & Šavija, B. (2020). Effect of recycled iron powder as fine aggregate on the mechanical, durability, and high temperature behavior of mortars. *Materials*, *13*(5), 1168.

Nedeljković, M., Visser, J., Valcke, S., & Schlangen, E. (2019). Physical Characterization of Dutch Fine Recycled Concrete Aggregates: A Comparative Study. *Multidisciplinary Digital Publishing Institute Proceedings*, *34*(1), 7.

Nieri, M. (2013). IDLC Business Review on Steel Making. *European journal of oral implantology*, *6*, 83-84.

Qurishee, M., Iqbal, I., Islam, M., & Islam, M. (2016). Use of slag as coarse aggregate and its effect on mechanical properties of concrete. Proceedings of the 3rd International Conference on Advances in Civil Engineering, CUET.

Raza, K., Singh, A., & Patel, R. (2014). Strength analysis of concrete by using iron slag as a partial replacement of normal aggregate (coarse) in concrete. *International Journal of Science and Research (IJSR)*, *3*(10), 190-193.

Wang, A., Zhang, Z., Liu, K., Xu, H., Shi, L., & Sun, D. (2019). Coral aggregate concrete: Numerical description of physical, chemical and morphological properties of coral aggregate. *Cement and Concrete Composites*, *100*, 25-34.

Hoque, M. M., & Hosse, M. A. (2019). Sustainable Use of Steel Industry Slag (SIS) for Concrete Production: A State Art of Review. *Open Journal of Applied Sciences*, *9*(12), 841.

Proc. 3rd International Conference on Structural Engineering Research (iCSER 2022)
27-30 Nov 2022, Sydney, Australia
ISBN: 978-0-6456692-1-3

Performance Based Design (PBD) Approach on the Stability of a 16 Storey Reinforced Concrete (RC) Building

A. B. M. Golam Rabbany Palash[1] and Bulbul Ahmed[2]

[1]Structural Engineer, Advance Design & Consultancy, Dhaka, Bangladesh,
[2]PhD Candidate, School of Engineering, Design and Built Environment, Western Sydney University, Sydney, Australia, Corresponding author's E-mail: palashruet@gmail.com

Abstract

High rise RC buildings have been paid attention in recent construction due to the scarcity of land and cost of land. Seismic action is the main concern for high-rise RC buildings. To incorporate the seismic action and the lateral deflection against seismic action, a proper design approach is required. Existing linear elastic analysis cannot meet the requirements of seismic design criteria. Therefore, the advance analysis procedure needs to be carried out in the case of the structure associated with different types of loads related to frequency domain, time domain & stiffness domain etc. Linear static analysis is sufficient for simple structural system but in case of tall building, bridge or power plant dynamic analysis is mandatory. This type of structure experiences blast load, liquid load, pressure, wind load, seismic load, etc., acting in varied magnitude, direction, time, and characteristics. Performance based design (PBD) approach is getting high attention and a viable solution in the case of both economic and safety points of view. In this study, a comparative study and deviation in different analysis attempts would be made, which may help the designer about the importance of selecting the analysis method.

Keywords: Performance based design, stability, dynamic analysis, response spectrum, time history

1. INTRODUCTION

The number of high-rise RC buildings is rapidly increased in recent construction due the scarcity of land and the cost of land. For the high-rise building, seismic risk is very common (Kumar et al., 2014). Recently, the risk associated with the seismic actions have been increased on the structures (Sejal et al., 2011; Feizi et al., 2015; Hajirasouliha et al., 2016). These seismic actions can be cause of millions of deaths and huge loss of property if the high-rise buildings are not properly designed to resist the lateral actions (Bayat et al., 2017; Biradar et al., 2022). Many countries developed seismic design codes considering different factors to accommodate the hazard specifications (Biradar et al., 2022). But the recent design codes were developed based on the elastic design approach which is applicable for smaller elastic formations and weak seismic actions. For the large inelastic deformation has been occurred during strong earthquakes those codes are not applicable (Bayat et al., 2017; Zhang, 2018; Biradar et al., 2022). To ensure the safety of the buildings and the comfort of the residents during seismic action, performance-based design (PBD) is a viable solution for the recent construction of RC buildings (Kumar et al., 2014; Zhang, 2018). PBD method can achieve enhanced performance high rise RC buildings against strong seismic actions (Liao et al., 2012; Anwar, 2016). The main focus of this study to develop PBD method for high rise RC buildings and the comparative study between the linear static analysis and PBD methods. In the present study, a 16 storey RC has been considered for the analysis with Building linear static analysis and PBD methods. The numerical analysis was performed by ETABS software.

2. CONCEPT OF PBD METHOD

Performance-based design method is more advantageous than conventional methods to the performance of high-rise RC buildings against strong earthquakes (Sejal et al., 2011). This method can give opportunity to select design methods by the stakeholders with a reduced cost. But the PBD method can only be used when it meets the criteria as building performance for PBD $\geq$ prescribed procedure (Anwar, 2016). The design process typically involves different intensities of motion when dealing with an earthquake. There might have three earthquake levels as (a) service level earthquake, (b) design basis

earthquake, and (c) maximum considered earthquake (MCE). The basic objectives of PBD can be illustrated in Table 1. The green colour box is defined as basic objectives of PBD. The yellow colour means essential objectives, and the orange colour represents the safety critical objectives. The service level earthquake has a 50% probability of being exceeded in 30 years or roughly a 43-year return period. The maximum considered earthquake (MCE) might have only 2% probability of being exceeded in 50 years which would be a return period of approximately 2475 year (Anwar, 2016). Generally, it is assumed that the building remains elastic for a low-level earthquake and significant yielding of structural elements is not allowed. For this case, linear elastic response spectrum analysis can be conducted. However, for a large earthquake such as the MCE, structural elements show a significant nonlinear behaviour. The structural elements are yielded with adequate ductility so that the buildings will not lose gravity load carrying capacity or experience excessive drift or instability issues.

Table 1: Concept of performance-based design method

Earthquake design level	Return period (Yr)	Probability of occurrence in 50 yrs	Acceptance criteria (operational state)				Damage state
			Fully operational	Operational	Life safe	Near collapse	
Frequently occur	43	50%	YES	NO	NO	NO	Little damage (easy repairable)
Occasionally occurs	72	20%		YES	NO	NO	Some shear crack (more expenses to repair)
Rarely occurs	475	10%			YES	NO	Some components need reconstruction
Very Rarely occurs	2475	2%				YES	Rubbish (not repairable)

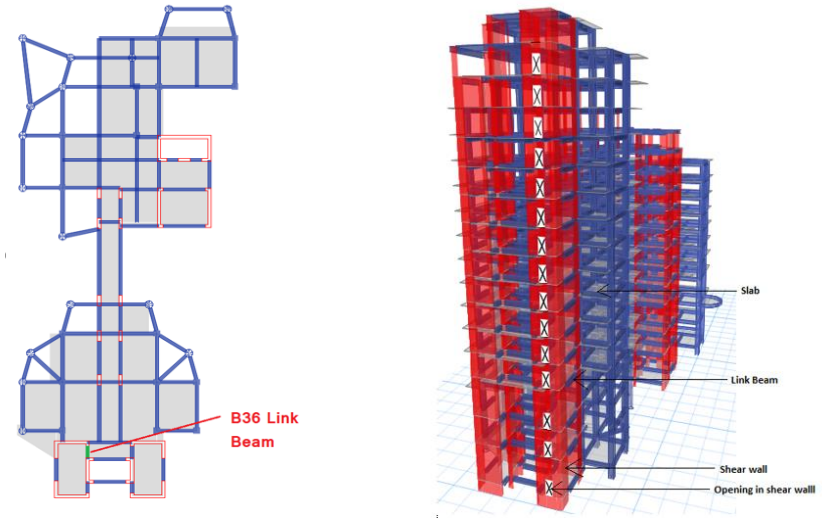

Figure 1. FE model of 16 storey RC building.

3. ANALYSIS APPROACH

3.1. FE model building

For the analysis purpose, a 16-storey high-rise RC building was taken in the present study. The building height is 59.4 m, and all floors are 3.0 m height except the ground floor and second floor. The height of the ground floor and second floor are 6 m in height. The shear wall and link beam are used in the building as deformation control elements. A typical component of the building that is discussed in this study is shown in Figure 01. Finite element (FE) analysis has been conducted in ETABS software. To increase the computational capacity, 600 × 600 mm and 450 × 450 mm mesh size is considered for floor and shear wall, respectively. The compressive strength of concrete and yield strength of steel rebar is 30

MPa and 420 MPa, respectively. The building details are shown in Figure 1. Faizan et al. (2019) method was adopted in time history analysis as a real-time seismic data in the FE analysis. Time history analysis was used to determine the seismic response of a structure under dynamic loading of representative earthquake as per Rathod et al. (2020) and Wilkinson and Hiley, (2006). The acceptance criteria were set for the nonlinear behaviour of the materials and beam rotation characteristics. A typical acceptance criterion is shown in Figure 2, depending on ASCE41-13 and the performance level (ASCE 41-13).

Figure 2. Typical acceptance criteria used in the FE analysis.

4. ANALYSIS RESULT

4.1 Result from equivalent seismic load approach

The equivalent seismic load approach (ESLA) is a static analysis procedure where the base shear is distributed throughout the structure from bottom to top. The result from linear static analysis is given in Figure 3 using the seismic load in Zone 3 (bask coefficient 0.04) as per the code where the building is being constructed. From the research of Alghuff et al. (2019) it is evaluated that the shear force, bending moment and displacement of high-rise building is more than that of analysed by dynamic analysis. The maximum deflection in the equivalent seismic load approach is 24.6 mm. Floorwise displacements are illustrated in Figure 3.

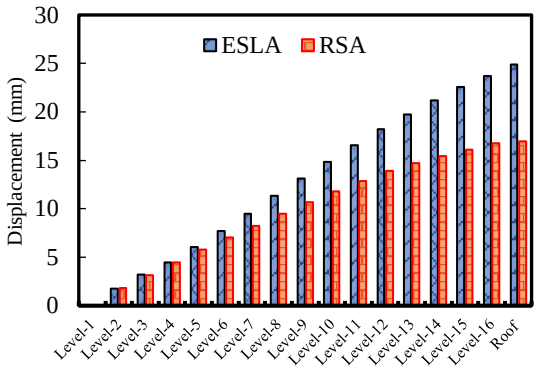

Figure 3. Displacement of building for static and dynamic load cases.

4.2 Result from response spectrum analysis

Response spectrum analysis (RSA) is a method to estimate the structural response to short, nondeterministic, transient dynamic events. Consider RSAx as response spectrum load cases in X-direction. The response spectrum analysis load case considered for this study is RSAx. Kumar et al. (2014), Mahmoud and Abdallah (2014) exposed a case study of earthquake analysis of multi-storied building, which shows that the displacement values are higher compared to dynamic analysis (Alghuff et al., 2019). The maximum deflection in response spectrum analysis is 16.95 mm. The comparison of deflections for both ESLA and RSA methods for each storey of the building is shown in Figure 3. The

comparison shows that response spectrum analysis always shows lower deflection for each storey of the building.

4.3 Result from modal analysis

Modal analysis is the study of structural dynamic characteristics to calculate natural frequency and vibration mode. From modal analysis the deformation trend of the structure under a certain natural frequency can be obtained (Ji and Li, 2014). Modal analysis can be performed based on Eigen or Ritz analysis. In this study, 950 mode numbers need to assign to obtain 90% mode participation ratio.

4.4 Result from performance-based analysis

The main objective of performance-based design is to avoid total catastrophic damage and to restrict the structural damages caused. To capture the nonlinear behaviour of beam, a moment rotation hinge is applied in some link beam to show how a beam, shear wall, or any building component behave during any seismic ground motion. As compared to the force-based approach, PBD provides a methodology for assessing the seismic performance of a building, ensuring life safety and minimum economic losses (Chaudhari and Dhoot, 2016). The present study analysed the link beam at labelled B36 for PBD consideration. For load case (Lcase1) this beam is safe from the bottom story to the top story (Figure 4(a)). But for the load case (Lcase2), the same beam fails early on seismic events, which can be illustrated in the backbone curve in Figure 4(b).

5. COMPARATIVE STUDY

In this study, only a few portions of the building are studied for PBD, whereas the whole building is studied for static and dynamic analysis. Gray colour represents the elastic range; blue colour is for immediate occupancy; aqua colour is the symbol of life safety; and green colour means collapse prevention.

From the backbone curve in Figure 4(a), the beam B36 is safe for load case 1. This can be understood from the colour of the point that travel on the blue line. The beam number B36 is located in the Figure 4. In these beam moment, rotation plastic hinges is applied to observe the significant nonlinear behaviour of the beam in different load cases. From the linear analysis, the link beam is passed, but from PBD analysis, it is seen that the beam is initially safe, but for long-duration earthquake, it will fails and that is the performance towards or against the element would be designed. This beam is safe enough from starting to the end of the service level earthquake shown in Figure 4. Figure 4(a) defines an earthquake event at the earlier stage, whereas Figure 4(b) defines the end of the earthquake events.

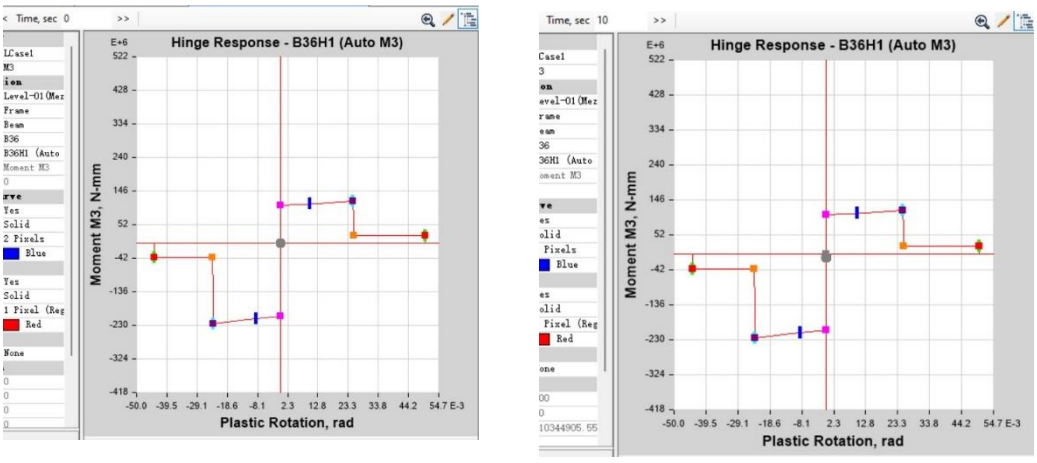

a) **b)**

Figure 4. The initial and end of the service level seismic event

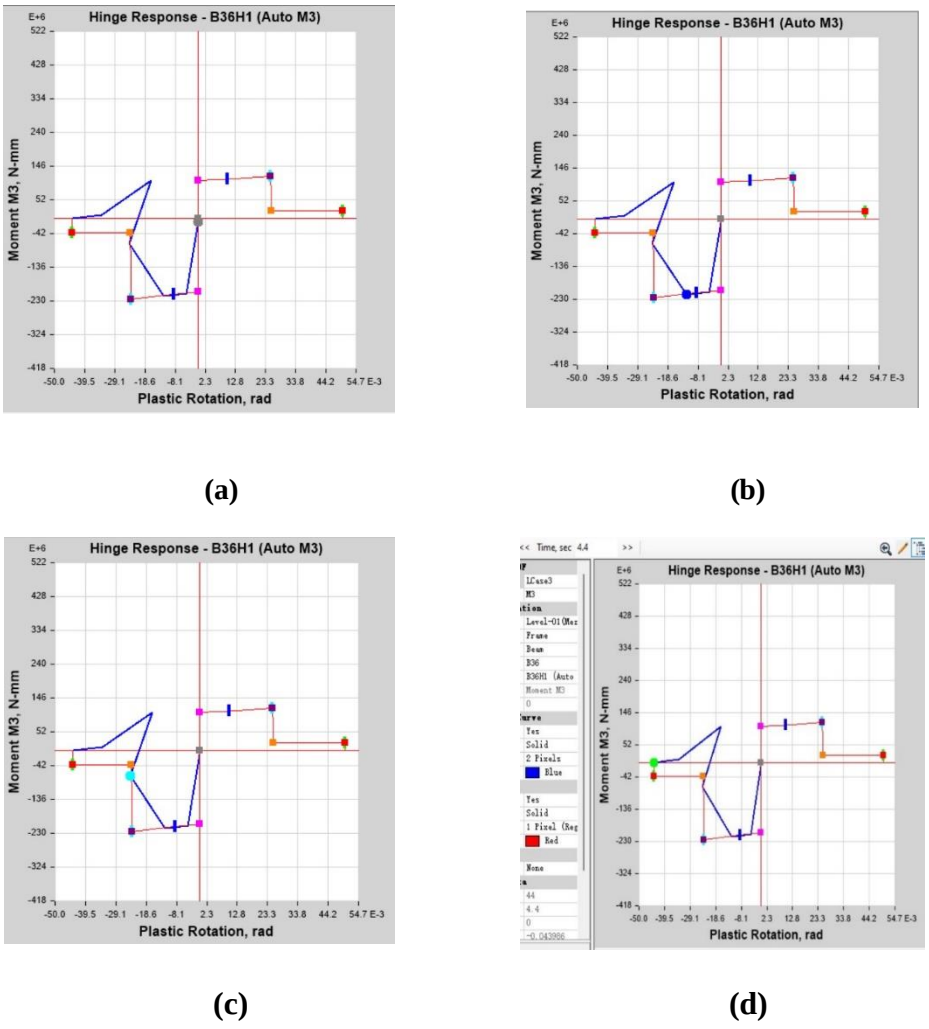

Figure 5. The backbone curve for a beam B36 in different load or earthquake event

For the same link beam after applying the fibre hinge which is denoted by B36 is at or after the collapse prevention level at the very beginning of the earthquake (T = 0.7 sec) for a recorded earthquake MCE named as HOLLISTE-1 and HOLLISTE-2. In Figure 5(a) the gray colour point marking indicates the hinge response of that beam B36 at the time of 0.1 sec. This is at the starting of the seismic event and all the responses are within elastic limit. For a time elapse 0.2 sec, 0.5 sec and 0.7 sec the point turns into blue, aqua and green colour, respectively, shown in Figures 5(b-d). The blue colour defines immediate occupancy, the aqua colour defines life safety, and the green denotes collapse prevention level and ultimate stage of nonlinear behaviour. That means for that earthquake (HOLLISTE-1 and HOLLISTE-2 or similar type) the element needs to be redesigned. Similarly, another beam, shear wall, or column susceptible to considerable nonlinear behaviour during the earthquake or past yield criteria can be evaluated from PBD analysis.

6. CONCLUSIONS

The response of a structure is a variable phenomenon which is dependent not only on material or component properties. The response varies according to its behaviour depending on the acting forces and duration of the forces. The analysis approach is also a major fact for response study and the components are assumed to have linear or nonlinear behaviour during analysis. Performance based design approach is an economical and safer option as the specific performance level of the structure is evaluated precisely. Especially for the most important structures, PBD analysis can be done to meet the design requirement and ensure the safety of structures. From this study, it is concluded that the performance of the building and other results shows better performance than the other method.

REFERENCES

Abdul Ahad Faizan, A. A. & Kirtel, O. (2019). Seismic nonlinear time history analysis of multi storied RCC residential building subjected to different earthquake ground motions using ETABS. International Journal of advances in Mechanical and Civil Engineering, 6(5).

Alghuff, A. Y., Shihada, S. M., & Tayeh, B. A. (2019). Comparative study of static and response spectrum methods for seismic analysis of regular RC buildings. Journal of Applied Sciences, 19(5).

Anwar, N. (2016). Performance based design, value engineering and peer review. Design of Tall buildings: Trends and Advancements for Structural Performance.

Bayat, M., & Zahrai, S. M. (2017). Seismic performance of mid-rise steel frames with semi-rigid connections having different moment capacity. Steel Compos. Struct, 25(1), 1-17.

Biradar, B. B., Shirkol, A. I., & Bush, R. (2022). Comparative study and performance evaluation of steel moment resisting frames design with: Force-based design and performance-based plastic design. Structures, 43, 696-709.

Chaudhari, D. J., & Dhoot, G. O. (2016). Performance based seismic design of reinforced concrete building. Open Journal of Civil Engineering, 6(02), 188.

Feizi, M. G., Mojtahedi, A., & Nourani, V. (2015). Effect of semi-rigid connections in improvement of seismic performance of steel moment-resisting frames. Steel Compos. Struct, 19(2), 467-484.

Hajirasouliha, I., Pilakoutas, K., & Mohammadi, R. K. (2016). Effects of uncertainties on seismic behaviour of optimum designed braced steel frames. Steel and Composite Structures, 20(2), 317-335.

Ji, D., & Li, L. (2014). Modal analysis of frame structure teaching building. International Conference on Mechatronics, Electronic, Industrial and Control Engineering (MEIC-14) Atlantis Press, 1724-1727.

Kumar, E. P., Naresh, A., Nagajyothi, M., & Rajasekhar, M. (2014). Earthquake analysis of multi storied residential building-A case study. International Journal of Engineering Research and Applications, 4(11), 59-64.

Liao, W. C., & Goel, S. C. (2012). Performance-based plastic design and energy-based evaluation of seismic resistant RC moment frame. Journal of Marine Science and Technology, 20(3), 9.

Mahmoud, S. & Abdallah, W. (2014). Response analysis of multi -storey rc buildings under equivalent static and dynamic loads according to Egyptian code. Int. J. Civil Struct. Eng. Res., 2, 79-88.

Rathod, K. V., & Gupta, S. (2020). A nonlinear time history analysis of ten storey RCC building. International Research Journal of Engineering and Technology, 8.

Sejal, P. D., Vasanwala, S. A., & Desai, A. K. (2011). Performance based seismic design of structure: A review. International Journal of Civil & Structural Engineering, 1(4), 795-803.

Wilkinson, S. M., & Hiley, R. A. (2006). A non-linear response history model for the seismic analysis of high-rise framed buildings. Computers and Structures, 84(5-6), 318-329.

Zhang, C. (2018). Performance-based economical seismic design of multistory reinforced concrete frame buildings and reliability assessment, Doctoral dissertation, University of Nevada, Las Vegas.

Proc. 3rd International Conference on Structural Engineering Research (iCSER 2022)
27-30 Nov 2022, Sydney, Australia
ISBN: 978-0-6456692-1-3

Structural Performance of Geopolymer Concrete with Recycled Concrete Aggregate: A review

Bahareh Nikmehr[1], Riyadh Al-Ameri[2], Bidur Kafle[3]

[1]PhD student, School of Engineering, Deakin University, Geelong, Vic 3216, Australia
[2]Senior Lecturer, School of Engineering, Deakin University, Geelong, Vic 3216, Australia
[3]Lecturer, School of Engineering, Deakin University, Geelong, Vic 3216, Australia

Corresponding author's E-mail: b.nikmehr@research.deakin.edu.au

Abstract

Geopolymer concrete (GPC) is an emerging construction material with a promising role in the industry. Recent research confirms the suitability of GPC in structural applications due to the higher compressive strength, better fire resistance, low permeability, and alkali and acid resistance compared to ordinary Portland concrete (OPC). Moreover, geopolymer concrete allows replacing the natural aggregate with more recycled concrete aggregate (RCA) than OPC. At the same time, its mechanical properties remain acceptable for structural applications. Thus, it will help waste reduction and natural resource preservation simultaneously. However, RCA adversely impacts concrete's rheological and mechanical properties, which is crucial for an optimum concrete mix. Recently, there has been a growing knowledge development on the structural applications of Portland concrete with RCA. However, there is a need to conduct a comprehensive assessment of the potential structural applications of RCA-based GPC. Hence, in the present study, previous research on various parameters that affect the structural behaviour of RCA-based GPC will be critically assessed and reviewed. These parameters include the type and content of alumina silicate materials, alkaline activator, curing regime, and RCA content. Besides, the load capacity, failure mode, and structural behaviour of composite elements with RCA-based geopolymer concrete, such as columns, beams, thin wall panels, and steel tubular columns, have been examined. Identified knowledge gap in this study area is also provided for further research.

Keywords: Recycled concrete aggregates, structural elements, structural behaviour, geopolymer concrete.

1. INTRODUCTION

Geopolymer is an environmental-friendly substitution for ordinary Portland cement, which reduces CO_2 generation and reuses industrial by-product material. Geopolymer concrete (GPC) is obtained through the reaction between alkaline activator and aluminosilicates, found in fly ash (FA), ground granulated blast-furnace slag (GGBS) and metakaolin (MK) and is available as industrial wastes (Rahman & Al-Ameri, 2021a, 2021b).

As for reducing natural resource consumption and reusing construction and demolition waste, a proper solution is using recycled concrete aggregates for developing new concrete (Tavakoli et al., 2018). GPC provides the opportunity of using more amount of RCA. Lim and Pham (2021) replaced all the aggregates with RCA, and 46.24 MPa compressive strength was achieved, which is a proper compressive strength for structural application. There exist several studies that reviewed the application of RCA in geopolymer concrete (Nikmehr & Al-Ameri, 2022), but the review on the structural application of RCA-based geopolymer has been overlooked.

Throughout this paper, the effect of RCA on the structural behaviour of geopolymer concrete will be assessed. To this end, the compressive strength and workability of the RCA-based GPC will be reviewed, and the effect of RCA on the structural performance of elements made by RCA-based

geopolymer concrete will be evaluated.

2. REVIEW OF EFFECTIVENESS OF RCA ON GPC

Although using RCA reduces overall waste and helps preserve natural resources, it may have some adverse impacts on the mechanical and rheological properties of the concrete, which should be evaluated. Furthermore, incorporating RCA in GPC on the performance of structural elements needs to be studied.

2.1. Compressive strength

RCA has a diverse effect on the compressive strength of geopolymer concrete. Compressive strength has been observed to be increased and decreased by incorporating various amounts of RCA in geopolymer concrete.

Some studies reported a drop in compressive strength by adding RCA. For example, adding 50% and 100% RCA reduces the compressive strength of FA/GGBS-based geopolymer concrete by 1.75-4.46% and 12.89-17.77%, respectively (Xie et al., 2019). On the other hand, the geopolymer concrete's compressive strength has been improved by adding RCA. For instance, adding 50% of RCA rises the compressive strength of the FA/GGBS-based geopolymer concrete from 24.27 MPa to 24.91 MPa (Liu et al., 2019). It shows that the addition of RCA affects the compressive strength of the geopolymer concrete; hence, there is a need for rigorous investigation on this topic. The reason for this contradiction is that the properties of RCA-based geopolymer concrete can be related to several parameters as follows:

- Alkali activator-related matters. For example, increasing the NaOH molarity from 8 to 12 improves compressive strength (Tho-In et al., 2017). In addition, increasing the ratio of alkali activator solution to binder materials enhances the workability and decreases the compressive strength (Le et al., 2021).

- The curing regime is another parameter that significantly affects the compressive strength of GPC. It is possible to cure GPC at ambient temperature. However, higher temperature helps accelerate the geo-polymerisation process, increasing compressive strength (Ahmed et al., 2011).

- Various treatment techniques improve the properties of RCA and the mechanical properties of concrete. Among these techniques, bio deposition, carbonation, adding nanoparticles and saturating RCA in sodium silicate or polymer emulsion reduce the porous structure of the RCA. Besides, removing old mortars can be possible by acid, mechanical methods and heating, leading to the better properties of RCA (Wang et al., 2021).

- The quality of RCA also impacts the properties of geopolymer. For example, the parent concrete with a compressive strength of higher than 50 MPa has no adverse impact on the geopolymer concrete, but incorporating RCA extracted from low to regular grade concrete decreases the compressive strength of GPC (Ohemeng et al., 2021).

- The type and amount of binding material influence the properties of the concrete. For example, increasing the amount of GGBS reduces the negative impact of using 100% RCA on the compressive strength of the geopolymer concrete (Uğurlu et al., 2021).

2.2. Workability

Adding RCA to the geopolymer concrete has a mixed effect on the slump of the geopolymer concrete. For example, using 100 % RCA reduces the slump from 117 to 106 mm in GGBS-based geopolymer concrete, as RCA has higher water absorption than natural aggregates (NA) (Parthiban & Saravana Raja Mohan, 2017). But, as illustrated in

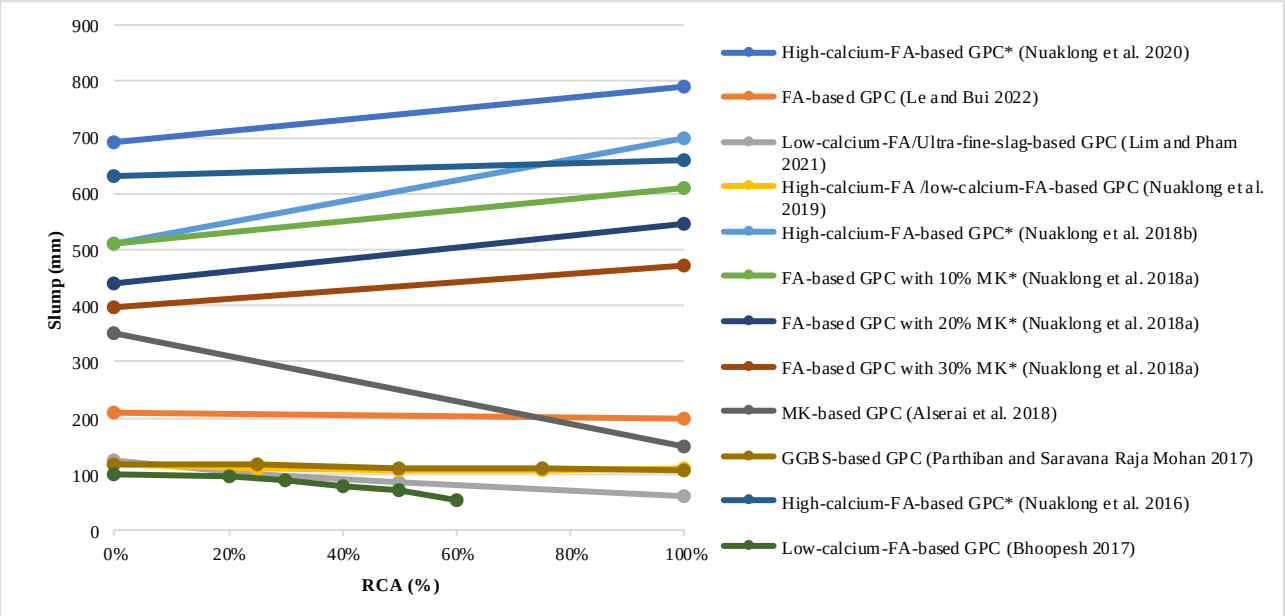

Figure 1, using RCA in saturated surface dry (SSD) form does not adversely impact the workability. For example, replacing NA with 100% RCA in SSD form in a high-calcium-FA-based GPC increases the slump by 14%, from 692 to 789. It is because further water in SSD recycled concrete aggregates increases the flowability (Nuaklong et al., 2020).

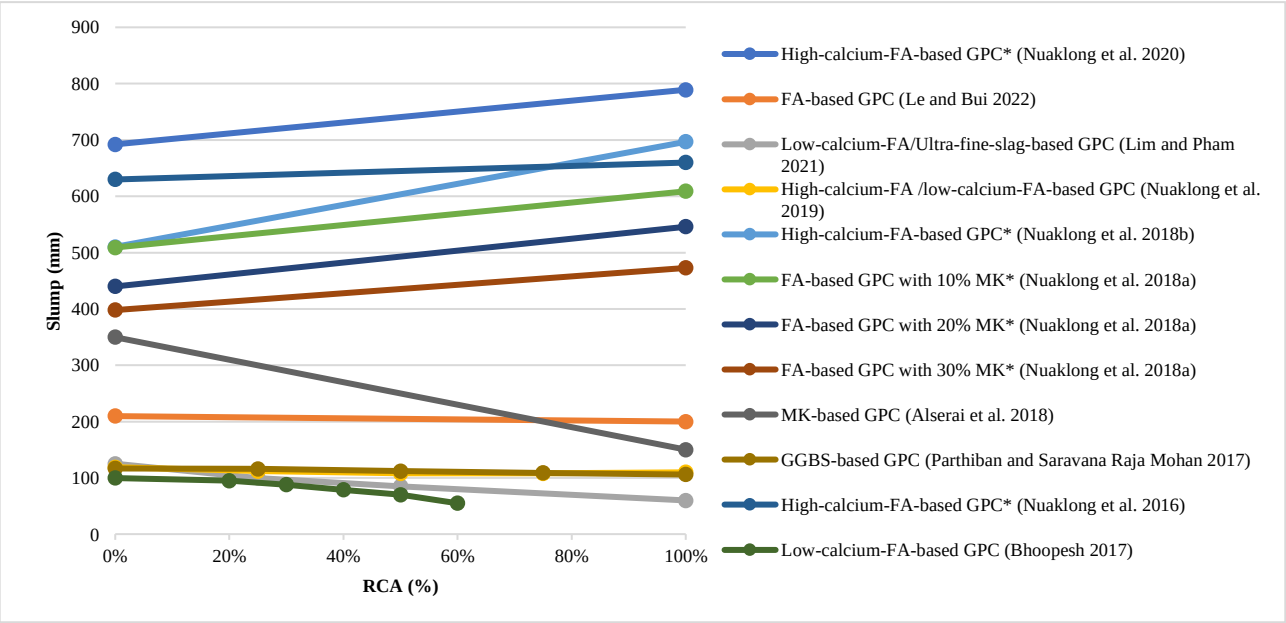

Figure 1. The link between RCA content and slump (* RCA applied in SSD form)

2.3. Structural elements

Although the research on RCA-based GPC is numerous in terms of material, minimal studies investigate the structural behaviour of RCA-based GPC, as summarised in Table 1.

Table 1. Relevant studies on the structural elements made by RCA-based geopolymer concrete

Reference	Structural element	Test	RCA content	Binder	Curing regime
(Bhoopesh, 2017)	Beam	Two-point bending	40%	FA	60 °C for 24

					hours
(Raza et al., 2021)	A column with GFRP bars	Axial loading	100% C	FA/GGBS 45:55	Ambient
(Alsaraj et al., 2019)	Wall panel	Axial eccentric uniformly distributed loading	100%	MK	Ambient
(Alalikhan et al., 2018)	Steel tubular columns	Axial loading	100% F&C	FA	Ambient
(Shi et al., 2015)	Steel tubular columns	Axial loading	0%, 50%, 100%	FA	80°C for 24 hours
(Ayub et al., 2021)	100×200 cylinder	Pull-out test	30%	FA	70°C for 24 hours
(Tho-In et al., 2017)	100×200 cylinder	Pull-out test	100%	Class C FA	60°C for 48 hours

Coarse RCA (C), Glass fibre reinforced polymer (GFRP), Fine RCA (F), Fly ash (FA), Metakaolin (MK), Ground granulated blast-furnace slag (GGBS)

2.3.1 Beams

Regarding the flexural behaviour of beams made by RCA-based GPC, Bhoopesh (2017) conducted a two-point-loading test on the reinforced beams made of GPC with 40% RCA and without RCA (with NA). The study reported that increasing the load results in flexural cracks in the bending zone. Further loading results in the widening of existing cracks for both beams with NA and RCA. However, beams with RCA-based GPC demonstrated a higher number of cracks and more crack width than the beams with NA. It might be due to the drop in tensile strength of the RCA-based GPC because of the more pores and voids in RCA. The first crack load and ultimate load of RCA-based GPC beams are less than beams with NA-based GPC by 21% and 9%, respectively. The reason contributes to the porous structure of the RCA, resulting in weaker bonds among the concrete particles.

Moreover, RCA reduces energy absorption capacity and toughness index by 15.7% and 16.82%, respectively. It is also reported that RCA reduces displacement and curvature ductility by 10.4% and 9.6%, respectively. It is due to the porous structure of RCA. However, despite decreasing the compressive strength by 20% (32.8MPa), this concrete was suggested to be used as green concrete. However, to better understand the effect of RCA on the geopolymer beams, there is a need to study the impact of various percentages of RCA on the performance of GPC reinforced beams against bending moments, shear forces, and deflections (Le & Bui, 2020).

2.3.2 Columns

As for evaluating the effect of RCA on the columns, Shi et al. (2015) pointed out that increasing the amount of RCA reduces the ultimate strength of columns grouted with GPC. A study has found that the maximum strength of steel columns filled by GPC with 100% RCA was 25% less than NA-based GPC. Besides, a higher amount of RCA increases the peak strain and improves ductility. Similarly, Alalikhan et al. (2018) used RCA-based GPC grout for steel columns and compared the performance of steel columns with those filled with OPC concrete grout. The failure load of the steel column with RCA-based GPC grout was higher than OPC concrete, although the compressive strength of OPC concrete was higher than GPC. They believe that better performance of GPC is due to the stronger bonding between GPC material and the steel column. However, the effect of RCA-based GPC was not compared with NA-based GPC in this research.

Raza et al. (2021) studied the behaviour of columns with GFRP grouted with RCA-based GPC. This research aims to optimise the number of GFRP bars and their spaces. To this aim, the columns were subjected to the axial compression test to evaluate the effects of various amounts of GFRP and the spaces between them on the ductility, crack generation and ultimate load. Although they did not compare the impact of RCA incorporation with NA, this type of column was suggested as an efficient and environmentally friendly structural element.

There is not any study on the effect of incorporating RCA on the reinforced columns made of GPC. Therefore, it is suggested to conduct a compression test on both non-cylinder and cylinder columns made with GPC with various replacing levels of RCA to evaluate the structural stiffness. The requirement for this study is crucial as RCA results drop in elastic modulus, which might decrease the ultimate resistance of the columns (Le & Bui, 2020).

2.3.3 Wall panels

The structural behaviour of wall panels made of RCA-based GPC was assessed by Alsaraj et al. (2019). They analysed the effect of aspect ratio and steel reinforcement ratio on the load-carrying capacity and lateral deflection of the walls subjected to the axial eccentric uniformly distributed loading. The results revealed that increasing the steel reinforcement enhances the load-carrying ability of wall panels and decreases their lateral deflection. They also reported that reducing the aspect ratio decreases the lateral deflection and increases the load-carrying capacity of the walls. Ultimately, they pointed out that the performance of RCA is like natural aggregates in geopolymer concrete, while RCA incorporation is economical.

2.3.4 Pull-out strength

Conducting a pull-out test revealed that geopolymer concrete with RCA demonstrates weaker bond strength than its counterpart with NA (Ayub et al., 2021; Tho-In et al., 2017). For instance, replacing 30% of the aggregates with RCA reduces the bonding strength of FA-based GPC from 5.6 to 4.15 KN/mm^2 (Ayub et al., 2021).

3 CONCLUSION

Incorporating RCA in the geopolymer concrete needs some consideration, especially for the geopolymer concrete with structural application. Based on the relevant literature, GPC has the potential to use a higher amount of RCA compared to OPC. Still, it is significant to consider the downsides of using RCA in terms of mechanical and rheological properties. The reason is that structure of the recycled concrete aggregates is weaker than the natural aggregates. Therefore, it is crucial to look for methods for improving the properties of RCA and RCA-based GPC. Removing old mortars is possible by high-temperature heating, mechanical techniques, acid, and high-pressure water washing. In addition, some materials, such as sodium silicate or polymer emulsion improve RCA by filling the pores. The type of bonding material, NaOH molarity and curing regime also influence the properties of RCA-based GPC. Added to the analysis of the effect of RCA on the mechanical and rheological properties of the GPC, it is vital to consider the structural behaviour of elements made with RCA-based GPC and try to improve them, so the following tracks need further research:

- Finding better treatment techniques for improving the quality of the RCA.
- Novice techniques should be investigated to increase the rate of replacing fine and coarse aggregates with RCA for developing GPC with the structural application.
- It is required to study the effects of various levels of replacing RCA on the GPC reinforced beams in terms of energy absorption capacity, toughness index, bending moments, ductility, shear forces, and deflections.
- The effect of RCA on the reinforced columns made with GPC needs more investigation.
- A study on the creep and fatigue of RCA-based GPC by experimental and numerical methods is also suggested.

REFERENCES

Ahmed, M. F., Nuruddin, M. F., & Shafiq, N. (2011). Compressive strength and workability characteristics of low-calcium fly ash-based self-compacting geopolymer concrete. *International Journal of civil and environmental Engineering*, *5*(2), 64-70.

Alalikhan, A. A., Habelalmateen, M. A., & Alhabbobi, A. M. (2018). STRENGTHENING OF SHORT HOLLOW STEEL COLUMNS USING GROUTED GEOPOLYMER CONCRETE WITH RECYCLED COMPONENTS. *Technology*, *9*(9), 832-841.

Alsaraj, W. K., Fadhi, S. H., & Alserai, S. J. (2019). Structural Behavior of Geopolymer Concrete Thin Wall Panels Based on Metakaolin and Recycled Concrete Aggregate. *The Open Civil Engineering Journal*, *13*(1).

Alserai, S. J., Alsaraj, W. K., & Abass, Z. W. (2018). Effect of iron filings on the mechanical properties of different types of sustainable concrete. *The Open Civil Engineering Journal*, *12*(1).

Ayub, T., Mahmood, W., & Khan, A.-u.-R. (2021). Durability performance of SCC and SCGC containing recycled concrete aggregates: A comparative study. *Sustainability*, *13*(15), 8621.

Bhoopesh, J. (2017). Strength and behaviour of recycled aggregate geopolymer concrete beams. *Advances in concrete construction*, *5*(2), 145.

Le, H.-B., & Bui, Q.-B. (2020). Recycled aggregate concretes – A state-of-the-art from the microstructure to the structural performance. *Construction and Building Materials*, *257*, 119522.

Le, H.-B., & Bui, Q.-B. (2022). Predicting the Compressive Strength of Geopolymer Concrete: An Empirical Model for Both Recycled and Natural Aggregates. In *CIGOS 2021, Emerging Technologies and Applications for Green Infrastructure* (pp. 793-802). Springer.

Le, H.-B., Bui, Q.-B., & Tang, L. (2021). Geopolymer recycled aggregate concrete: from experiments to empirical models. *Materials*, *14*(5), 1180.

Lim, Y. Y., & Pham, T. M. (2021). Effective utilisation of ultrafine slag to improve mechanical and durability properties of recycled aggregates geopolymer concrete. *Cleaner Engineering and Technology*, *5*, 100330.

Liu, C., Deng, X., Liu, J., & Hui, D. (2019). Mechanical properties and microstructures of hypergolic and calcined coal gangue based geopolymer recycled concrete. *Construction and Building Materials*, *221*, 691-708.

Nikmehr, B., & Al-Ameri, R. (2022). A State-of-the-Art Review on the Incorporation of Recycled Concrete Aggregates in Geopolymer Concrete. *Recycling*, *7*(4).

Nuaklong, P., Jongvivatsakul, P., Pothisiri, T., Sata, V., & Chindaprasirt, P. (2020). Influence of rice husk ash on mechanical properties and fire resistance of recycled aggregate high-calcium fly ash geopolymer concrete. *Journal of Cleaner Production*, *252*, 119797.

Nuaklong, P., Sata, V., & Chindaprasirt, P. (2016). Influence of recycled aggregate on fly ash geopolymer concrete properties. *Journal of Cleaner Production*, *112*, 2300-2307.

Nuaklong, P., Sata, V., & Chindaprasirt, P. (2018). Properties of metakaolin-high calcium fly ash geopolymer concrete containing recycled aggregate from crushed concrete specimens. *Construction and Building Materials*, *161*, 365-373.

Nuaklong, P., Sata, V., Wongsa, A., Srinavin, K., & Chindaprasirt, P. (2018). Recycled aggregate high calcium fly ash geopolymer concrete with inclusion of OPC and nano-SiO2. *Construction and Building Materials*, *174*, 244-252.

Nuaklong, P., Wongsa, A., Sata, V., Boonserm, K., Sanjayan, J., & Chindaprasirt, P. (2019). Properties of high-calcium and low-calcium fly ash combination geopolymer mortar containing recycled aggregate [Article]. *Heliyon*, *5*(9), Article e02513.

Ohemeng, E. A., Ekolu, S. O., & Quainoo, H. (2021). Models for predicting strength properties of recycled concretes made with non-treated CRCAs: Empirical approach. *Construction and Building Materials*, *307*, 124585.

Parthiban, K., & Saravana Raja Mohan, K. (2017). Influence of recycled concrete aggregates on the engineering and durability properties of alkali activated slag concrete. *Construction and Building Materials*, *133*, 65-72.

Rahman, S. K., & Al-Ameri, R. (2021a). The Need for a User Friendly Geopolymer Concrete-Ongoing research.

Rahman, S. K., & Al-Ameri, R. (2021b). A newly developed self-compacting geopolymer concrete under ambient condition. *Construction and Building Materials*, *267*, 121822.

Raza, A., Manalo, A. C., Rafique, U., AlAjarmeh, O. S., & Khan, Q. u. Z. (2021). Concentrically loaded recycled aggregate geopolymer concrete columns reinforced with GFRP bars and spirals. *Composite Structures*, *268*, 113968.

Shi, X.-S., Wang, Q.-Y., Zhao, X.-L., & Collins, F. G. (2015). Structural behaviour of geopolymeric recycled concrete filled steel tubular columns under axial loading. *Construction and Building Materials*, *81*, 187-197.

Tavakoli, D., Hashempour, M., & Heidari, A. (2018). Use of waste materials in concrete: A review. *Pertanika J. Sci. Technol*, *26*(2), 499-522.

Tho-In, T., Sata, V., Cao, T., & Chindaprasirt, P. (2017). Use of recycled concrete aggregate in high-calcium fly ash geopolymer concrete. Key Engineering Materials,

Uğurlu, A. İ., Karakoç, M. B., & Özcan, A. (2021). Effect of binder content and recycled concrete aggregate on freeze-thaw and sulfate resistance of GGBFS based geopolymer concretes. *Construction and Building Materials*, *301*, 124246.

Wang, B., Yan, L., Fu, Q., & Kasal, B. (2021). A Comprehensive Review on Recycled Aggregate and Recycled Aggregate Concrete. *Resources, Conservation and Recycling*, *171*, 105565.

Xie, J., Wang, J., Zhang, B., Fang, C., & Li, L. (2019). Physicochemical properties of alkali activated GGBS and fly ash geopolymeric recycled concrete. *Construction and Building Materials*, *204*, 384-398.

Proc. 3rd International Conference on Structural Engineering Research (iCSER 2022)
20-27 Nov 2022, Sydney, Australia
ISBN: 978-0-6456692-1-3

Knowledge Transfer for Structural Damage Detection using Fine-tunning based on FRF

Xutong Zhang[1], Xinqun Zhu[2] and Jianchun Li[3]
[1]PhD candidate, University of Technology Sydney, Sydney, Australia
[2]Associate Professor, University of Technology Sydney, Sydney, Australia
[3]Professor, University of Technology Sydney, Sydney, Australia
Corresponding author's E-mail: Xinqun.Zhu@uts.edu.au

Abstract

The majority of data-driven structural damage detection techniques are created based on the assumption that comprehensive labelled data is available and the underlying distribution of the training and test sets is the same, which is hard to conduct in real engineering applications. In this work, we propose an approach for structural health monitoring (SHM) based on a convolutional neural network (CNN) that uses frequency response functions (FRF) obtained from the structural response to detect structural damage. This method is capable to identify structural damage based on both severity and localisations in the real structure. Specifically, a numerical model was simulated firstly. The acceleration response was collected to process to the FRF and trained in the designed CNN model. Thus, a complete CNN model was created using the numerical data, and then the pre-trained CNN model was fine-tuned using the limited experimental data to adapt its feature distribution on the fully connected layer for the experimental data. Finally, the performance of this fine-tuned CNN was compared with the original CNN to validate the effectiveness of the proposed methods on damage detection. The results show that the proposed method is effective and accurate for structural damage detection.

Keywords: Structural health mentoring, Transfer learning, Convolutional neural network, Damage detection

1. INTRODUCTION

Civil constructions are susceptible to various damage, including corrosion and deformation brought on by unexpected environmental conditions. It could increase the deterioration of the structure and influence its severability, causing a safety risk. Therefore, detecting structural damage early is essential and avoiding building collapses (Kostic & Gul 2017).

In the data-driven based structural health monitoring (SHM) method, the main problems appear that it needs a large amount of high-quality data to train the deep learning (DP) model. Based on the numerical simulation, it could obtain a large amount of labelled data as the source domain. A robust predictor can be trained using these data. However, there are many uncertainties in practice. Very little labelled data from the real structures are accessible and that is the target domain. Recently, the transfer learning (TL) technique is used to transfer the knowledge learned from the source domain to the target domain. Some applications have been successfully applied in structural damage detection. Azimi and Pekcan (2020) used the compressed data to investigate the structural damage conducted by deep-learning models. The time history signals were used as the input of the deep neural network to extract the damage feature for structural damage detection. Dorafshan et al. (2018) conducted transfer learning based on fine-tuning AlexNet convolutional neural network (CNN) to detect the concrete crack on the structure surface using the labelled images. Wang et al. (2022) used the re-weighted adversarial domain adaptation (RADA) to address the problem of inconsistent label space across the structure's source and target domains. Thus, the damage-sensitive feature can be transferred between different systems, and the results reveal that this method is a good performance for damage detection when structural topology or operational environment changes.

This paper proposes a transfer learning-based method for structural damage detection. The numerical model is defined as the source domain and the experimental model is the target domain. A large amount of the labelled data for different damage scenarios are generated using the numerical model. The numerical simulation data are used to train the CNN model and the knowledge of the damage information is stored in the trained model. The trained model is fine-tuned with the experimental data for a few of damage scenarios. Finally, the trained model is used for predicting the damage.

2. ARCHITECTURE OF TRANSFER LEARNING NETWORKS FOR STRUCTURAL DAMAGE DETECTION

2.1 Problems Definition

Here the transfer learning is briefly introduced here. The domain and task are,

- A domain $D = \{\mathcal{X}, P(X)\}$ covers the feature $\mathcal{X}$ and a marginal distribution $P(X)$, where $X = \{x_i\}_{i-1}^{N} \in \mathcal{X}$.
- A task of this domain is defined as $\mathcal{T} = \{\mathcal{Y}, f(.)\}$, including $\mathcal{Y}$ is the label space and $f(.)$ predictive function (also considered as conditional distribution $P(y|x)$), learnt from the training data set $\{x_i, y_i\}_{i-1}^{N}$ where $y \in \mathcal{Y}$.

Transfer learning is given a source domain $D_S = \{\mathcal{X}_S, P(\mathcal{X}_S)\}$ and task $\mathcal{T}_S = \{\mathcal{Y}_S, f_S(.)\}$, and the target domain, $D_T = \{\mathcal{X}_T, P(\mathcal{X}_T)\}$ and task $\mathcal{T}_T = \{\mathcal{Y}_T, f_T(.)\}$. Generally, $D_S \neq D_T$ and $\mathcal{T}_S \neq \mathcal{T}_T$. Transfer learning is conducted to improve the target predictive function $f_T(.)$ in $\mathcal{T}_T$ transferring the knowledge learnt from D_S and $\mathcal{T}_S$. Transfer learning methods are based on whether $\mathcal{X}, P(X), \mathcal{Y}$ and $P(y|x)\}$ are consistent across the source and target domains. Fine-tunning is one of the transfer learning methods. Given a source domain D_S and task $\mathcal{T}_S$ and target domain D_T and task $\mathcal{T}_T$. It is conducted to share the part of parameters previously learnt knowledge from D_S and, then reweight the residual parameters using some labelled knowledge from D_T to improve the target prediction function , $f_T(.)$ in $\mathcal{T}_T$. Note $P(\mathcal{X}_S) \neq P(\mathcal{X}_T)$ and $P(\mathcal{Y}_S|\mathcal{X}_S) \neq P(\mathcal{Y}_T|\mathcal{X}_T)$.

For the case study conducted here, the source and target domains are presented in different but similar structures, while the task is to represent the damage data to improve damage detection. This idea comes from the inductive transfer learning method. Inductive transfer learning considers the source and target domains to be relative, in which the feature space is the same and marginal distribution is different ($\mathcal{X}_S = \mathcal{X}_T, P(\mathcal{X}_S) \neq P(\mathcal{X}_T)$). While the tasks are different but relative ($\mathcal{T}_S \neq \mathcal{T}_T$), in which the label space is the same and prediction function are different ($\mathcal{Y}_S = \mathcal{Y}_T, P(\mathcal{Y}_S|\mathcal{X}_S) \neq P(\mathcal{Y}_T|\mathcal{X}_T)$). Regarding the studies in this work, the damage condition data for the model provides the same feature space, and the marginal distribution and the conditional distribution are various from different structures forming the sources and target domains.

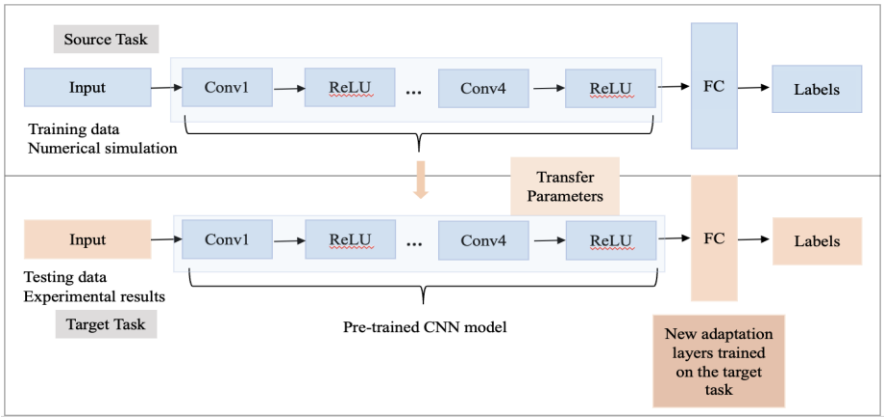

Figure 1 Overview procedure of Fine-tuning (FT) based on CNN

Once the original CNN was trained by a dataset from the three-storey model with its intact and damage scenarios, the next stage was to update and reweight the subset weight parameters for the new structural dynamic feature from the target domain. The dynamic feature of the new structure was related to the feature of the dynamic structural feature from the source domain. In this approach, the pre-trained CNN architecture shown in Figure 1 focused on the extracted feature. The weight of parameters from the first conventional layer to the last FC layer did not experience any modifications, which were initialised with pre-trained weights and kept fixed. Due to the new structural dynamic feature in the fine-tune data, only the last fully connected layer and the output layers are retrained and updated. Once the models were retrained through fine-tuning transfer learning using diverse datasets. Their performance was tested using the same data as the corresponding fine-tuned dataset.

3. DATA PREPARATION

3.1 Experiment Set-up

The basic components of a three-story building model were two identical columns with a 50 x 3 mm cross-section and a 900 mm length displayed, as well as three steel beams measuring 394 (length)*50 (width)*30 (thickness) mm. 300mm is the standard story height (Figure 2). High-strength steel with a yield stress of 435 MPa and an elasticity modulus of 20 GPa was used to construct all columns and beams. A shear-type building model might be created by considering each steel beam as a rigid beam in the horizontal direction. The masses of the first, second, and third floors were 5. 20 kg, 4.99 kg, and 4.92 kg respectively.

3.2 Numerical Modelling

The three-storey lumped mass model consists of mass blocks and columns constructed using Matlab. The three-storey is simplified as a build model composed of 3 lumped masses as shown in Figure 3.

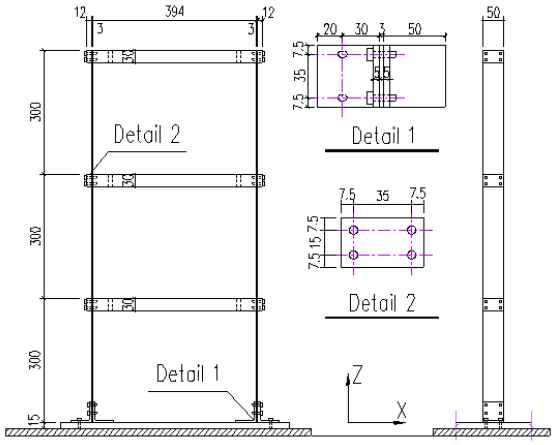

Figure 2. Configuration of the building model

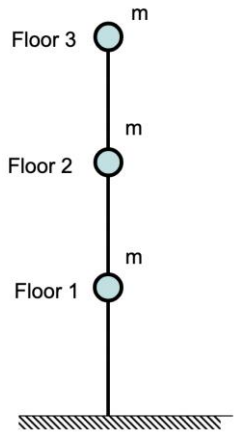

Figure 3. The lumped mass model of the three-storey building

3.3 Damage Scenario and Data Preparing

The designed damage scenarios consist of single and double damage. For experiential tests, the damage is introduced as two symmetrical saw cuts inflicting the damage scenario. There are four damage scenarios: intact, 10% & 20% damage on the second floor for the single damage scenario, and 20% & 10% damages on the second and third floor for the double damage scenario (D0, D2 and D5). Three accelerometers are installed on the building model with one sensor on one floor. The impact test is conducted to obtain the frequency response functions (FRFs). Each FRF sample is combined with three sensor responses as a 2D data sample of 3×660 to represent the entire information of structural vibrations. There are fifty-four tests

that are repeated. Totally, 648 ((3 damage scenarios +1 intact model) × 3 impact locations ×54 repeated tests) FRF samples data set is obtained from the experiment.

For the numerical simulation, it could simulate all the possible damage scenarios to feed the network, which allows the network to learn the entire features of the structural damage as the source domain data. Each of the damage scenarios inflicted damage from 0 to 30% damage in the numerical simulations. The damage locations are introduced as six different sets of damage combinations from D1 to D6. An impact force of 840 N is applied at three reference points (Floors 1, 2 and 3) on the model and the response time histories of the model are gained at three positions, which correspond to the locations of the sensors in the experimental testing. A frequency range of 0-30 Hz that covers all three vibration modes is used. Each data point in the FRF dataset has 660 spectral lines with a frequency resolution of 0.045 Hz. To summarise, the total 1701 ((6 damage scenarios +1 intact model) × 81 damage severities × 3 impact locations) FRF data sets are obtained from the simulation model.

Two regression metrics are used to show the performance of the prediction of FT for transfer learning. These indices are formed from the true labelled value Y_i and predicted value $\hat{Y}_i$. Each value being a vector has three elements to represent the damage severity of three-floor. The symmetric absolute percentage error (SAPE) is proposed to calculate the distribution of the relative error. SAPE only requires the difference between Y_i and $\hat{Y}_i$, and it requires checking the induvial relative error of each sample for each damage scenario instead of the means value of the entire sample. It is noted that the $\hat{Y}_i$ and Y_i and are only focused on the damaged floors e.g. D5 is a double damage scenario, thus the damage indices would focus on the second and third value of the three-element vector, thus the regression performance of the proposed method can be obviously shown based on these aimed floors.

$$SAPE = \frac{|\hat{Y}_i - Y_i|}{(|\hat{Y}_i| + |Y_i|)/2} \quad (1)$$

4. CASE STUDY

The transfer learner is to transfer knowledge across similar structures using the pre-built machine learners. The knowledge transfer between numerical and experimental models for single damage scenarios is provided based on methods. To achieve the aim, the transfer the knowledge of double damage scenarios from the numerical and experimental models was designed. Similar to single damage scenarios, the labels of damage scenarios on the source domain are constant from 0-30%. While the labels on the target domain are inconstant being undamaged (D0), 10% on the second floor (10D2), 20% on the second floor (20D2), and 20% & 10% on the second and third floor (20D10D5), respectively. It is noted that the double damage scenarios are introduced, being three additional damage scenarios on the source domain. In addition, the target domain labels are covered in the source domain labels, aiding in predicting the several damage scenarios on the target domain.

Figure 4 shows the latent space for both training and testing data labelled in different colours for different labels. Due to the constant labels on the source domain one, some of the samples from this domain were selected the same as the target domain damage scenarios for comparison. The feature space for source and target domains are shown as different clusters. If no domain shifts in the fully connected layers between different domains, the t-SNE subspace of one domain may expect that the t-SNE components on another domain would be well aligned. These are the conventional deep learning methods, the regressor is supposed in the t-SNE subspace for these two domains. As shown in Figure 4, the t-SNE feature spaces between these two domains have a substantial discrepancy, even though the dimension has been reduced to two dimensions. It means that the domain shifts have happened. In other words, the original data distribution has changed between source domain one and target domain one.

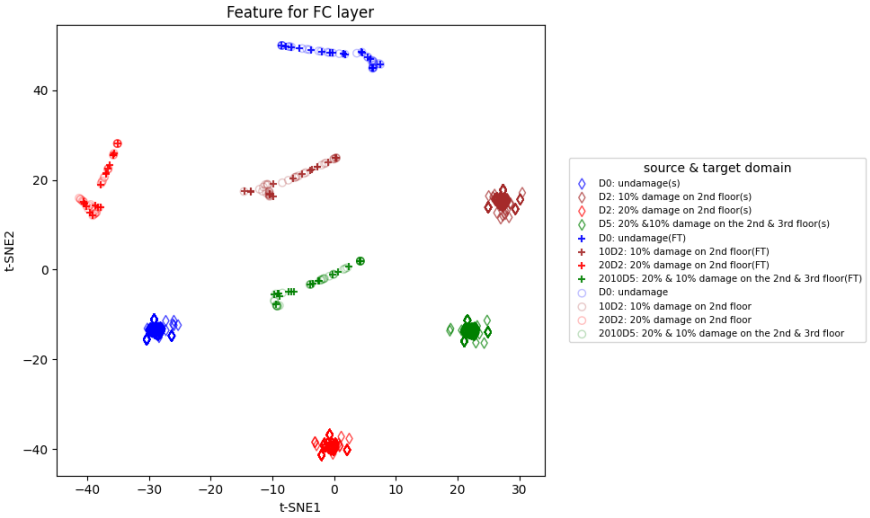

Figure 4. Feature visualization of FT the weight through t-SNE for the multiple damage case study

Fine-tuning is used to readjust the weight aims regression of damage severity on the target domains one. Figure 5 shows the comparison of predicted results (only focusing on the damaged floor) for target domain three with fine-tuning and without fine-tuning. Comparing the predicted damage severity between the original model and FT model on target domain one, the medium value for each damage scenario significantly improves from 0.025, 0.175, 0.43, 0.425 and 0.44 to 0.1, 0.2, 0.1 and 0.2 for D0, 10D2, 20D2 and of 2010D5, respectively. FT model outperforms the original model, the FT predicted results almost meet the true labels of the damages focusing on the damage locations. These results demonstrate that fine-tuning has positively transferred the labelled knowledge to the target domain one. This result is similar to the single damage case study; FT would significantly improve the accuracy of predicted damage severities when the target domain is completely labelled with every damage scenario. As for the SAPE performance, Figure 6 illustrates the FT model is more sensitive for larger damage severities i.e. 20D2 and 2010D5 on target domain one since they are closer to the distribution of -0.75% to 0.75% and -0.75 to 1%, respectively.

.

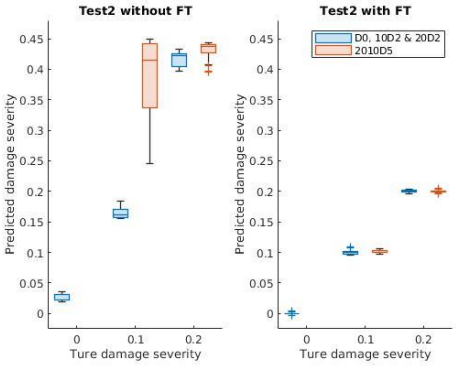

Figure 5. Box chart for predicted damage severities

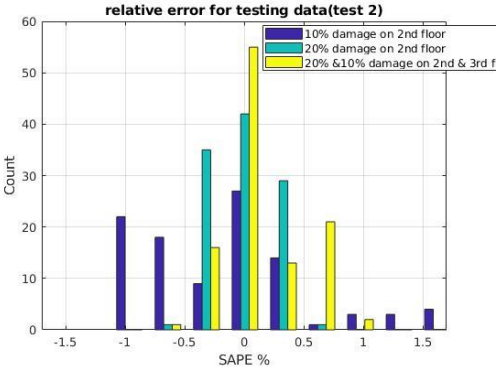

Figure 6. Histogram of SAPE (%)

5. CONCLUSIONS

A transfer learning-based method for structural damage detection has been developed in this paper. Numerical simulation and experimental tests have been carried out to verify the proposed method. The results show that the proposed method is effective and accurate for structural damage detection with limited experimental data. The numerical model, as the source domain, is used to generate a large amount of trained

data to train the deep learning model. The damage information is stored in the trained model. Through the fine-tuning, the knowledge learned in the source domain is transferred to the target domain by sharing the model parameters.

REFERENCES

Azimi, M. & Pekcan, G. 2019, 'Structural health monitoring using extremely compressed data through deep learning', *Computer-Aided Civil and Infrastructure Engineering*, vol. 35, no. 6, pp. 597-614.

Dorafshan, S., Thomas, R.J. & Maguire, M. 2018, 'Comparison of deep convolutional neural networks and edge detectors for image-based crack detection in concrete', *Construction and Building Materials*, vol. 186, pp. 1031-45.

Kostic B., Gül M. 2017, 'Vibration-based damage detection of bridges under varying temperature effects using time-series analysis and artificial neural networks', *Journal Bridge Engineering*, vol.22, no. 10, 0001085.

Wang X., & Xia Y. 2022, 'Knowledge transfer for structural damage detection through re-weight adversarial domain adaption', *Mechanical system and Signal Processing*, vol.172, 108991.

Proc. 3rd International Conference on Structural Engineering Research (iCSER 2022)
27-30 Nov 2022, Sydney, Australia
ISBN: 978-0-6456692-1-3

Transfer Learning-based Condition Assessment for Bridges

Saeid Talaei[1], Xinqun Zhu[2] and Jianchun Li[3]

[1]Phd Candidate, University of Technology Sydney (UTS), Sydney, Australia
[2]Associate Professor, University of Technology Sydney (UTS), Sydney, Australia
[3]Professor, University of Technology Sydney (UTS), Sydney, Australia

Corresponding author's E-mail: saeid.talaei@student.uts.edu.au

Abstract

Structural Health Monitoring of important civil infrastructures such as bridges is highly crucial in their long-term service life since. The early notices of damage occurrence in these structures will prevent catastrophic failures and save lives and money. Vibration-based damage detection techniques rely on measuring and analysing the structural vibration responses to assess the structural health state. The correlation between the structures vibrational responses and its health condition can be made by Machine Learning (ML) tools. Deep Learning (DL) reveals a vast area of interest while it can eliminate the needs for feature extraction. Deep learning methods (especially CNNs) are the pioneer ML techniques that make it feasible to deal with large-size data without dimension reduction or feature extraction. One of the major limitations of DL methods is the fact that they need a comprehensive dataset for training. This dataset can be generated using finite element models. There are many uncertainties in real structures and the trained model from numerical simulations cannot be used to detect the damage of the real structure accurately. This paper proposes a transfer learning-based method for the condition assessment of bridges. It provides a new framework to transfer the knowledge learned from the numerical simulation to another with deviations in input domains and output tasks. The results show that the proposed method is effective and accurate for bridge condition assessment.

Keywords: Structural Health Monitoring, Machine Learning, Deep Learning, Transfer Learning, Fine-tuning.

1. INTRODUCTION

It is crucial to monitor the health state of a bridge throughout its lifetime. Vibration-based structural health monitoring relies on changes in structural parameters due to damage. Modal parameters such as natural frequencies and mode-shapes carry the most beneficial properties of the structural dynamic response. Any changes in the structural elements, boundary conditions and joints will change these parameters (Avci et al., 2021). On the other hand, using signal-based features rather than modal parameters will reduce the data pre-processing time and costs in condition assessment process. A feature extraction method can be employed to extract the damage-sensitive feature. As an example, Principal component analysis (PCA) is a pioneering linear dimension reduction and feature extraction technique that is effectively applied in the past decade to reduce the huge size of structural responses into a few damage sensitive principal components while reducing the sensitivity of extracted features to operational and measurement errors (Khoshnoudian & Talaei, 2017).

Damage sensitive features extracted from the structural vibration response can be correlated to structural health condition using data-driven algorithms based on machine learning (ML) techniques. However, they need data for training. These data need to be labeled and cover all the desired condition scenarios. Once the model is trained to classify the structural health condition from the damage sensitive features, the trained model can be used as a black-box to receive the data as the input and return the state of the desired structure as output (Sen & Nagarajaiah, 2018).

Feature extraction is an inevitable, important part of the traditional ML models that needs to perform with most caution to extract the most reliable, damage sensitive features from the raw data. These features should have the least sensitivity to unwanted parameters such as noise pollution and

temperature deviation. A weak feature extraction will lead into sub-optimal features which can defect the classification performance. However, deep learning (DL) methods introduced a paradigm-shifting framework that can learn to automatically extract optimal features from raw data, resulting in the best classification and regression outcomes. A DL algorithm consists of multiple processing layers to learn the representation of the input data during a multi-lever abstraction (Pathirage et al., 2018). Thus the feature extraction procedure is no more a separate issue. It makes DL algorithm suitable for damage detection of structures based on the raw signal data (Krizhevsky et al., 2017). A convolutional neural network (CNN) consists of several convolutional layers each followed by a pooling layer. This part of the CNN objective is feature extraction and dimension reduction. Thus, a CNN is capable of automatically extracting high-level features from raw signals or low-level features. Fully connected layers are then employed for classification purpose (Shin et al., 2016).

There is still a gap between the numerical model which is used to generate the training dataset and the real structure that produces the real dynamic responses. Transfer learning (TL) can help to bridge the gap between these two kinds of data. TL is a ML technique that seeks to use knowledge from a source domain to carry out the task in a target domain when there are certain similarities between the source and target domains (Pan & Yang, 2010). A ML model, for instance, could be trained to find damage in a finite element model (source domain). If the transfer is successful, the knowledge learned throughout the training procedure could be applied to identify the damage on another structure or the real structure (target domain). In CNNs, the idea is to pre-train a model using data from the source domain and then fine-tune the model using data from the target domain. For fine-tuning, the hyper-parameters of a group of convolutional layers (or all of them) will be frozen based on the fact that these layers contain feature extraction-relevant data (Zhuang et al., 2021). In this study, a fine-tuning method is employed to transfer the knowledge between two models of a composite bridge. The outcome of this research shows that TL approaches can be used to transfer condition assessment and damage detection knowledge between similar structures and, thus, between a real bridge structure and its finite element model.

2. RESEARCH METHODOLOGY

The primary objective of this study is to employ TL to transfer knowledge between two distinct finite element models. A source FE model of a composite bridge is firstly built and employed to generate a large comprehensive dataset of the bridge condition scenarios. This dataset is used to train a CNN model. Secondly, a similar FE model is generated with deviations in material properties to form the target domain. This target domain is assumed to mimic the actual structure, so it is only used to generate a small amount of labelled data, which is insufficient for training a standalone DL model. A fine-tuning approach is employed to transfer the feature extraction knowledge from the source domain to the target domain to make it possible to train a classifier using the scarce labelled data in the target domain.

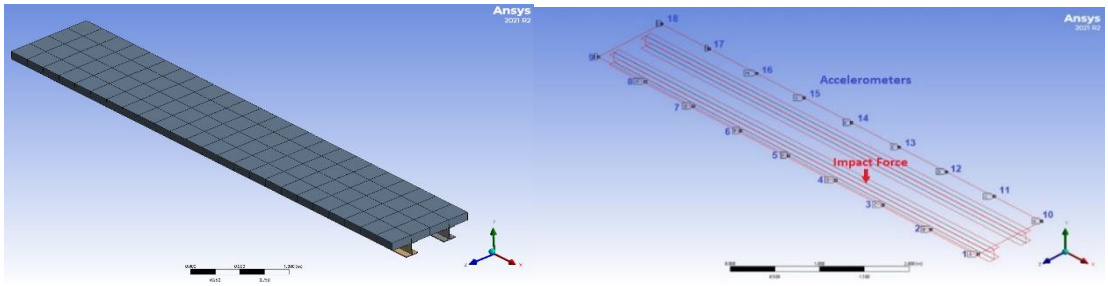

Figure 1: Finite element model of the composite bridge in ANSYS 2021

2.1. Finite Element Modelling of Composite Bridge

In this study, finite element modelling of a composite bridge deck is conducted by ANSYS 2021 R2. The bridge is composed of two 6-meter main steel girders with a cross section of 150UC 30 and a 6x1m concrete slab with 10 cm thickness. The structural elements are set as shell elements because the bridge slab's thickness is relatively thin compared to its other two dimensions. and the mesh is presented in

Figure 1. Fixed boundary conditions are defined at the bottom edges of the steel girder sections on both ends.

Eighteen accelerometers are located on the edges of the concrete slab to capture the vertical acceleration responses of the bridge, and the dynamic responses of the bridge deck under the impact force are captured. The excitation force F(t) is defined as a 100N impact force on the bridge deck (1.75 m from the short edge and 0.25 from the long edge of the concrete slab). The acceleration response X(t) is calculated for a duration of 10s with a time interval of 0.005s. The time-history acceleration responses are then used to derive the frequency response functions (FRFs), H(ω) as

$$H(\omega) = \frac{X(\omega)}{F(\omega)} = \frac{|fft(X(t))|}{|fft(F(t))|} \quad (1)$$

2.2. Mass location estimation using DL and FRF data

In this study, a condition assessment of the bridge using an added mass is conducted. The added mass is supposed to be in the range of 90 to 180 kg, which is 5% to 10% of the structures mass (1800 kg). Thirteen (13) different scenarios are defined based on the distance of the added mass from the short edge of the concrete deck. The acceleration response of the bridge for each scenario is calculated for 18 sensors located on the edges of the concrete slab. The FRF of each test is derived to form the training dataset of a CNN. Data augmentation is done by adding 2% of white Gaussian noise to the signals. Some samples of the training dataset are illustrated in Figure 2.

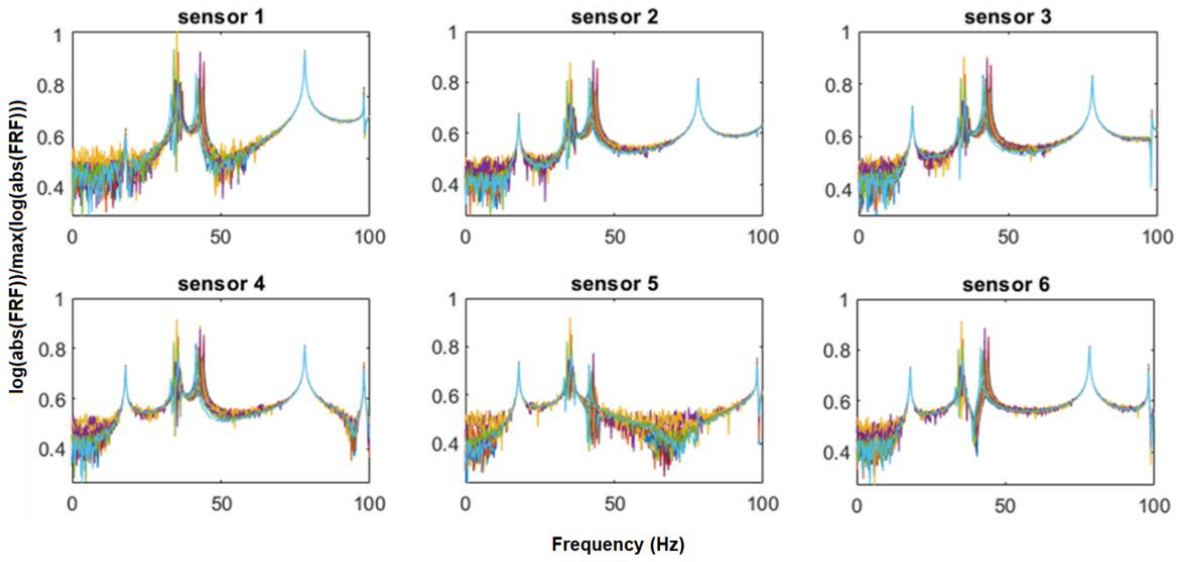

Figure 2: Noise polluted dataset of normalized FRFs

A CNN is trained using 80% of the presented data in the dataset and tested by the remained 20%. Each input data is a 500×18 matrix corresponding FRF data captured from 18 sensors with the frequency resolution of 0.2 Hz from 0 to 100Hz. This matrix is reshaped to a 100×90 matrix for a more convenient feature extraction process. The output layer contains 13 neurons corresponding to 13 scenarios. The purpose of convolutional layers is to extract damage sensitive features, while fully connected layers are used for classification.

The classification accuracy of the trained network is tested using datasets with different amount of noise added to the vibrational signals and the results are presented in Table 1.

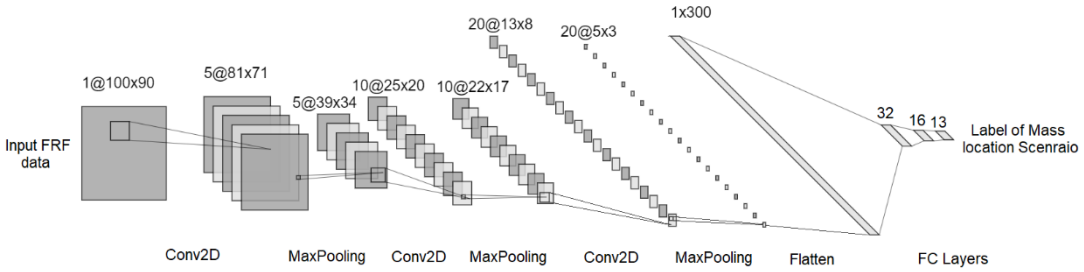

Figure 3: Structure of the trained CNN

Table 1: Classification accuracy of the trained CNN tested with different noise to signal ratios

N/S ratio	Classification Accuracy (%)
2%	100
5%	99.51
7%	97.57
10%	89.96

2.3. Fine-Tuning approach for knowledge transfer

Since the accuracy of the trained CNN is acceptable in the classification of the source domain labels, this knowledge can be transformed into a target domain. The ideal application of TL in structural condition assessment is to transfer the knowledge between FE model and the real structure. In this study, due to a lack of experimental data, the target domain in this study is specified as another FE model with the same geometry but different material properties. The material properties of the source and target domain are presented in Table 2. Samples of the FRF data corresponding to the source and target domains are compared in Figure 4. The domain shift between the source and target domains can be observed in these data.

Table 2: Material properties of the source and target domain structures

Material properties		**Source**	**Target**	**Difference (%)**
Steel	Young's Modulus (Pa)	2.00e11	2.1e11	5
	Density (kg/m^3)	7850	7845	0.06
Concrete	Young's Modulus (Pa)	1.94e10	1.5e10	22.6
	Density (kg/m^3)	2392	2000	16.4

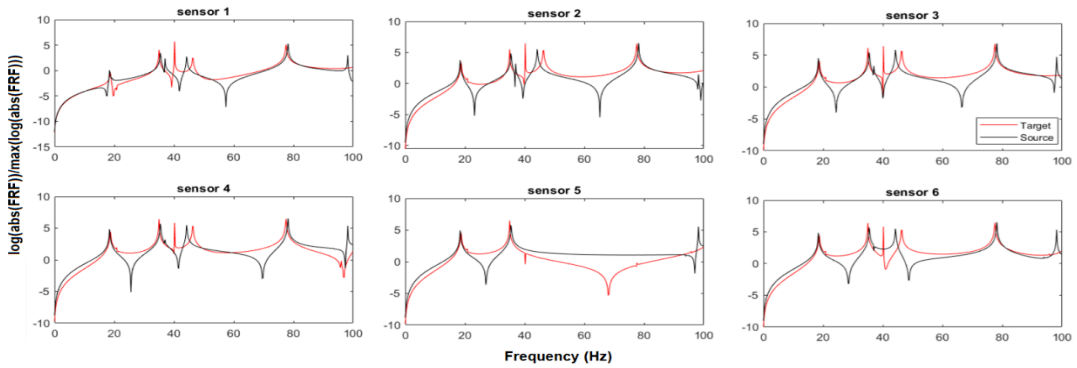

Figure 4: Domain shift between the source and the target domain FRF data

It is noteworthy that the CNN model's inputs are the FRF data. Therefore, the model trained on the source domain cannot be used effectively for the target domain due to differences in the FRF data between the source and target domains. But the knowledge of the model trained on the source domain can be transformed into another model which is fine-tuned for the target domain.

Due to the similarities between the source and target domains, all the convolutional layers are kept frozen for fine tuning. Thus, the feature extraction part of the pre-trained CNN is saved and directly employed to extract the damage-sensitive features of the target domain data. t-SNE visualization of the Damage sensitive features in the source and target domains are presented in Figure 5.

It can be observed that the damage sensitive features in the source domain (Figure 5.a) are truly divided into 13 different clusters, each referring to a mass location scenario or class. This successful feature extraction knowledge is directly used to extract the damage sensitive features of the FRF data in the target domain and it can be observed that damage sensitive features of different scenarios in the target domain are also truly distinguishable (Figure 5.b).

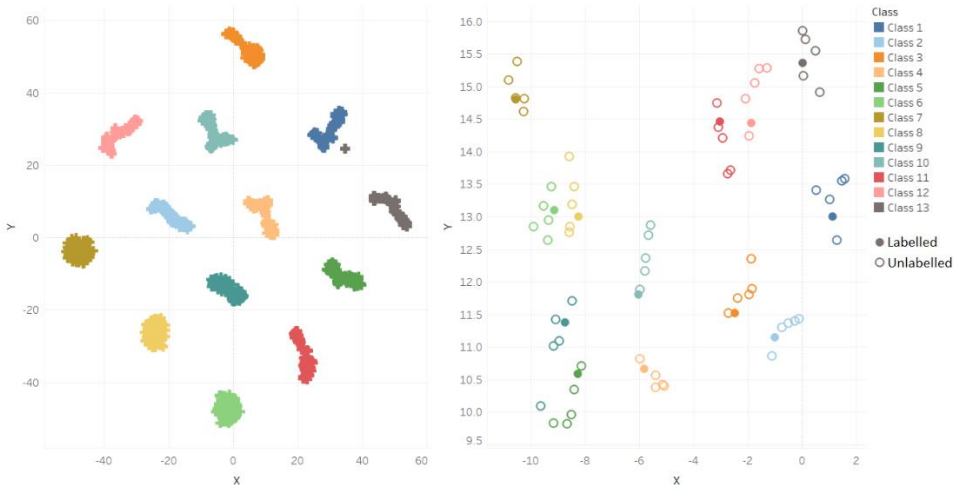

(a) Source domain (b)Target domain

Figure 5: t-SNE visualization of the source and target domain damage sensitive features

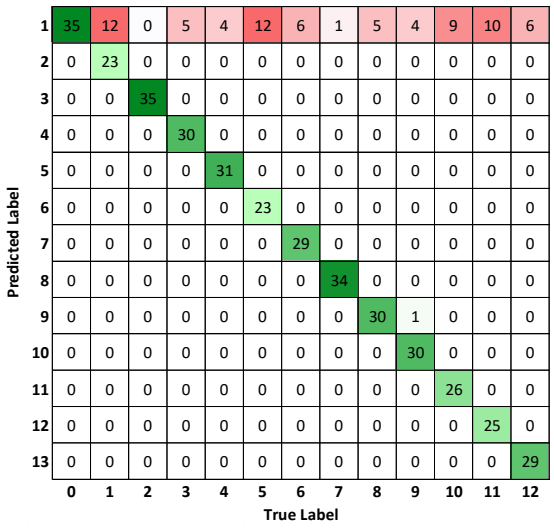

Figure 6: Confusion matrix of classification task on the target domain after fine-tuning

Among the presented data in the target domain, the FRF data corresponding to 140 kg added mass are assumed to be labelled and are used for training a classifier. The rest of data are assumed to be unlabelled and are only used for testing the fine-tuning method while they are polluted with 2% of white Gaussian noise. Finally, a "Random Forest" algorithm with 500 estimators is employed for the target classification task resulting in an accuracy of 83.56%. The confusion matrix of the classification task on the target domain data is presented in Figure 6.

3. CONCLUSIONS

It can be concluded that fine-tuning method can be employed to transfer the knowledge between the source and target domains when the domains are from the same feature space and the data in the target domain are not sufficient to train a CNN solely. In this study, a finite element model of a composite bridge was used to generate the fully labelled comprehensive dataset in the source domain and another FE model was used to generate the weak, partially labelled dataset in the target domain. In this case, a CNN was trained using the large, labelled dataset in the source domain and fine-tuned using the scarce labelled data in the target domain with acceptable performance.

REFERENCES

Avci, O., Abdeljaber, O., Kiranyaz, S., Hussein, M., Gabbouj, M., & Inman, D. J. (2021). A review of vibration-based damage detection in civil structures: From traditional methods to Machine Learning and Deep Learning applications. *Mechanical Systems and Signal Processing*, *147*, 107077.

Khoshnoudian, F., & Talaei, S. (2017). A New Damage Index Using FRF Data, 2D-PCA Method and Pattern Recognition Techniques. *International Journal of Structural Stability and Dynamics*, *17*(8), Article 1750090.

Krizhevsky, A., Sutskever, I., & Hinton, G. E. (2017). ImageNet Classification with Deep Convolutional Neural Networks. *Communications of the Acm*, *60*(6), 84-90.

Pan, S. J., & Yang, Q. A. (2010). A Survey on Transfer Learning. *Ieee Transactions on Knowledge and Data Engineering*, *22*(10), 1345-1359.

Pathirage, C. S. N., Li, J., Li, L., Hao, H., Liu, W. Q., & Ni, P. H. (2018). Structural damage identification based on autoencoder neural networks and deep learning. *Engineering Structures*, *172*, 13-28.

Sen, D., & Nagarajaiah, S. (2018). Data-driven approach to structural health monitoring using statistical learning algorithms. In *Mechatronics for cultural heritage and civil engineering* (pp. 295-305). Springer.

Shin, H. C., Roth, H. R., Gao, M. C., Lu, L., Xu, Z. Y., Nogues, I., Yao, J. H., Mollura, D., & Summers, R. M. (2016). Deep Convolutional Neural Networks for Computer-Aided Detection: CNN Architectures, Dataset Characteristics and Transfer Learning. *Ieee Transactions on Medical Imaging*, *35*(5), 1285-1298.

Zhuang, F. Z., Qi, Z. Y., Duan, K. Y., Xi, D. B., Zhu, Y. C., Zhu, H. S., Xiong, H., & He, Q. (2021). A Comprehensive Survey on Transfer Learning. *Proceedings of the Ieee*, *109*(1), 43-76.

Proc. 3rd International Conference on Structural Engineering Research (iCSER 2022)
27-30 Nov 2022, Sydney, Australia
ISBN: 978-0-6456692-1-3

Nonlinear Dynamic Characterisation of Vehicle-bridge Interaction System Using CSO-VMD

Jiantao Li[1] and Xinqun Zhu[2*]

[1]Lecturer, Zhejiang University of Technology, Hangzhou, China
[2]Associate Professor, University of Technology Sydney, Broadway, NSW, Australia
*Corresponding author's E-mail: Xinqun.Zhu@uts.edu.au

Abstract

The breathing-cracks on the bridge structure and inhere non-stationary nature of vehicle-bridge interaction (VBI) would cause complex dynamic characteristics of the bridge under moving vehicular loads. Investigation on the dynamic characteristics is important for the bridge structural condition assessment and damage detection. Variational mode decomposition (VMD) is a powerful technique to analyse the nonlinear and nonstationary dynamic signal that can decompose the signal into mono-component modes with proper parameter settings, i.e., the number of modes and the penalty factor. In this study, the Chicken-Swarm-Optimised VMD (CSO-VMD) is used to improve the identification of time-varying dynamic characteristics of the VBI system, where the parameter settings of traditional VMD is optimised with Chicken Swarm Optimization (CSO) algorithm. Firstly, a general breathing crack model is introduced to simulate the bridge damage numerically. The open-close behavior of the crack is considered using a time-dependent parameter. Secondly, the CSO-VMD is used to decompose the bridge dynamic responses due to moving vehicular loads. The decomposed bridge related components are then used to identify the instantaneous frequencies (IFs) for the dynamic characterisation. The IFs are estimated by using ridge detection on the time-frequency representation of the response components. The effects of VBI on the IFs for structural damage detection are investigated. The CSO-VMD based method successfully identifies the nonstationary and nonlinear dynamic characteristics of the bridge.

Keywords: CSO-VMD, Nonlinear characteristics, Instantaneous frequency

1. INTRODUCTION

The short- to medium-span reinforced concrete beams are widely used to the construction of highway bridges. Investigation on the dynamic characteristics of the bridge under heavy vehicle load is important to ensure the bridge operation in facing the increasing vehicle weight. The traveling vehicles on the bridge introduce extra mass and interaction effects that cause the variation of the modal parameters of the VBI system (Chang et al., 2014). In fact, the nature of the VBI dynamic responses is time-varying due to the movement of the vehicle along the bridge. Moreover, the dynamic behavior of the bridge under heavy vehicle loads is also nonlinear (Borjigin et al., 2018) that may due to the inevitable cracks in the concrete. The cracks on the concrete beam often lead to the nonlinear dynamic behaviors of the structure considering its open-close mechanism under vibration load (Neild et al., 2002). One of the commonly used crack models to simulate the behaviors of crack concrete beam includes the functions to describe a degradation in the Young's modulus of material as presented in (Abdel Wahab et al., 1999). While the crack opening/closing behavior is modelled by multiplying a time-dependent parameter to the degradation damage variable (Lee and Fenves, 1998).

The VBI leads to the complex non-stationary and nonlinear dynamic properties of the cracked concrete bridge that the time-varying dynamic properties of the bridge can reveal vital information for bridge dynamic characterisation and condition evaluation. Variational mode decomposition (VMD) methods have been proven effective in analysing the nonstationary and nonlinear dynamic responses (Dragomiretskiy and Zosso, 2014). The efficacy and accuracy of VMD based method compared to EMD, SWT has been demonstrated in (Tian and Zhang, 2020). The parameter settings of the number of modes and the penalty factor for VMD are important to the algorithm. The Chicken Swarm Optimization (CSO)

algorithm (Meng et al., 2014) has been adopted to optimise parameters for the convolutional neural network (Yu et al., 2022). The novel optimised VMD method CSO-VMD (Li et al., 2022) has been proposed to improve the parameter settings of a number of modes and the penalty factor using CSO. In the study, CSO-VMD is adopted to identify the time-varying properties of the bridge in terms of instantaneous frequencies (IFs), considering the effects of breathing cracks and VBI.

2. METHODOLOGY

2.1 Vehicle-bridge interaction modelling

The considered VBI system is modeled as a continuous uniform beam subject to a moving vehicle model as shown in Figure 1. The equation of motion of the bridge structure can be written as (Li et al., 2020)

$$\mathbf{M}_b\ddot{\mathbf{X}}_b + \mathbf{C}_b\dot{\mathbf{X}}_b + \mathbf{K}_b\mathbf{X}_b = \mathbf{HP}(\mathrm{t}) \tag{1}$$

where $\mathbf{M}_b$, $\mathbf{C}_b$, $\mathbf{K}_b$ are the mass, damping and stiffness matrices of the bridge, respectively; $\boldsymbol{P}(t)$ is the input force to the bridge at the contact points; $\mathbf{H}$ is the Hermitian cubic interpolation functions.

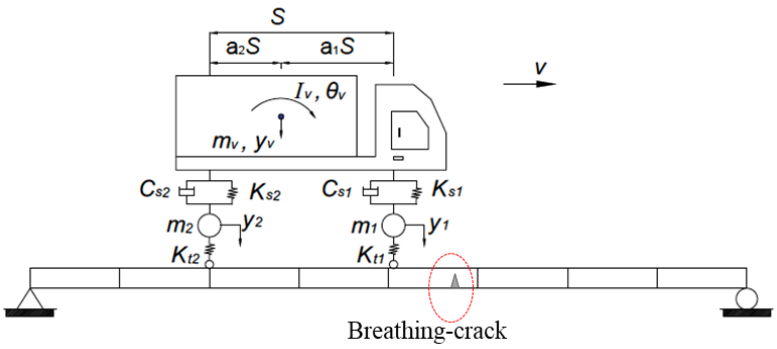

Figure 1. Vehicle-bridge interaction model

2.2 Bridge crack damage models

The local structural damage of beam is usually considered as the reduction of flexural stiffness. Different damage models have been applied to simulate the damage effect on the bridge. In this study, open and breathing crack models simulated in (Law and Zhu, 2004) are adopted. The following function is used for open crack:

$$EI(x) = E_0 I\left(1 - \alpha\cos^2\left(\frac{\pi}{2}\left(\frac{|x-l_c|}{\frac{\beta L}{2}}\right)^m\right)\right)\left(l_c - \frac{\beta L}{2} < x < l_c + \frac{\beta L}{2}\right) \tag{2}$$

where α, β, m are the damage parameters. l_c denotes the mid-point of the damage zone from the left support. β is related to the length of the damaged zone with a range between 0.0 and 1.0. α characterises the extent of damage. m represents the variation of the Young's modulus at the crack zone. E_0 is the modulus of the intact beam. The stiffness of an element with an open crack zone is

$$k_{bij} = E_0 I\left[\int_0^{l_c-\frac{\beta L}{2}} \phi_i''(x)\phi_j''(x)dx + \int_{l_c-\frac{\beta L}{2}}^{l_c+\frac{\beta L}{2}}\left(1 - \alpha\cos^2\left(\frac{\pi}{2}\left(\frac{|x-l_c|}{\frac{\beta L}{2}}\right)^m\right)\right)\phi_i''(x)\phi_j''(x)dx + \int_{l_c+\frac{\beta L}{2}}^{L}\phi_i''(x)\phi_j''(x)dx\right]/M_i \qquad (i,j = 1,2,\ldots,n) \tag{3}$$

For the complex opening closure mechanism of the breathing crack, an additional parameter, s, is used with the open crack model to describe the degradation process. It is given as

$$EI(x) = E_0 I\left(1 - s\alpha\cos^2\left(\frac{\pi}{2}\left(\frac{|x-l_c|}{\frac{\beta L}{2}}\right)^m\right)\right)\left(l_c - \frac{\beta L}{2} < x < l_c + \frac{\beta L}{2}\right) \quad (4)$$

where $s = s_0 + (1 - s_0)\sin(\pi\, vt/L)$. s_0 is the value when the beam is under its own static weight and is taken as 0.3. The parameter *vt* determines the location of the moving load on the bridge. It is related to the bending moment or the curvature at the crack location that affects the open-closing conditions of breathing-crack.

2.3 The CSO-VMD for dynamic characterisation of VBI

The decomposition performance of VMD is heavily dependent on the settings of the component number *K* and the penalty factor α for the algorithm. The recently proposed CSO-VMD (Li et al., 2022) is used to optimise the performance of VMD by incorporating the CSO to determine the optimal values of *K* and α. The bridge dynamic responses are decomposed by CSO-VMD to obtain the mono-components. The bridge-related components are then further analysed to extract the instantaneous frequencies. The wavelet transform is used to get the TFR of the bridge-related components extracted by CSO-VMD. Ridge detection in TFR of the decomposed component is adopted to estimate the IFs.

3. NUMERICAL STUDY

Numerical study is conducted to investigate the dynamic characteristics of the VBI system and verify the effectiveness of the CSO-VMD based analysis method. Considering the model described in Figure 1, the properties of the bridge and vehicle models are given as follows. Properties of the target bridge model are: $L = 40m,\ \rho = 3930\,kg/m,\ EI = 8.75 \times 10^9 Nm^2$. Parameters of the vehicle are: $m_v = 17735kg, I_v = 1.47 \times 10^5 kgm^2, S = 4.27m, a1 = 0.519, a2 = 0.481, m_1 = 1500kg, k_{s1} = 2.47 \times 10^6 N/m, k_{t1} = 3.74 \times 10^6 N/m, c_{s1} = 3.00 \times 10^4 N/m/s, c_{t1} = 3.90 \times 10^3 N/m/s, m_2 = 1000kg, k_{s2} = 4.23 \times 10^6 N/m, k_{t2} = 4.60 \times 10^6 N/m, c_{s2} = 4.00 \times 10^4 N/m/s,\ c_{t2} = 4.30 \times 10^3 N/m/s$. The first two modal frequencies of the bridge are 1.45 and 5.86Hz, respectively. The frequencies of the vehicle are 1.63, 2.30, 10.35 and 15.10Hz for the four independent degree-of-freedom, respectively. The vehicle speed is 2m/s, and the sampling frequency of the numerical simulation is 200Hz. The parameters for the damage are the crack depth ratio *a/h*=0.3 at the location of bridge midspan. The responses and response spectra of the bridge at the midspan considering no-damage, open-crack and breathing-crack cases are shown in Figure 2. It can be seen that the dominated component is related to the first bridge dynamic frequency.

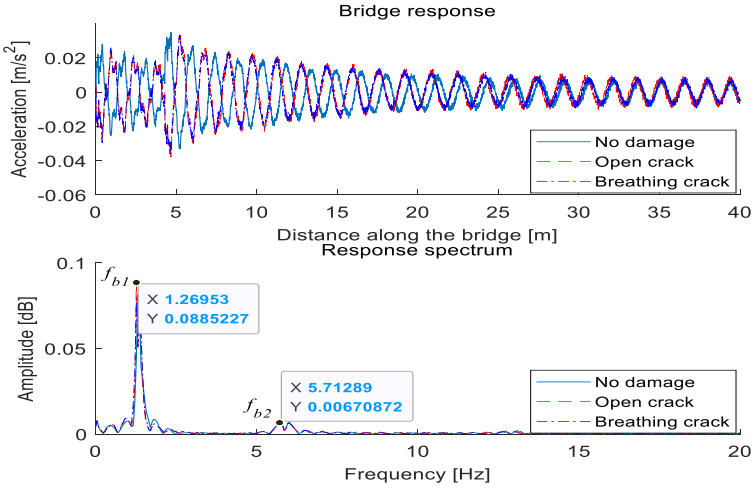

Figure 2. The responses and response spectra of the bridge

The CSO-VMD is used to decompose the bridge responses and the results are shown in Figure 3 considering different damage conditions. Two components are obtained from the responses which correspond to the bridge's first two dynamic modes. The results show that the second component is related to the first bridge dynamic mode, which dominates the response. The spectrum amplitude of the first component, which is related to the second bridge dynamic mode, is much less than the second component. The spectra of the components for different damage conditions are very close to each other. It is difficult to identify the damage states due to the effects of the VBI.

Therefore, the instantaneous frequencies of the second component for different damage conditions are extracted, as shown in Figure 4, using the abovementioned method. For the open crack condition, the identified IF is very close to the true value except at the two ends. Compared to the IFs of the no-damage case, an overall decrease of the IF curve is observed for the open-crack case. For the breathing-crack case, the decrease extent is enlarged at the crack location due to the opening of the breathing crack. From the identified IFs, three different damage conditions can easily separate from each other.

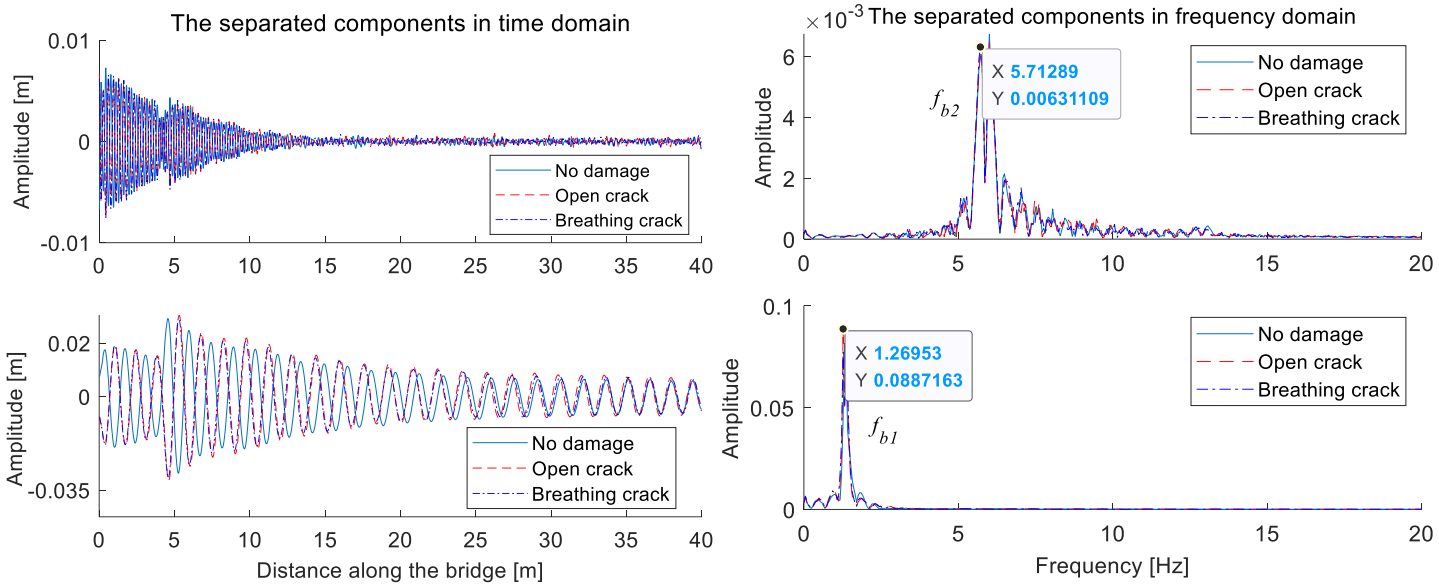

(a) The separated components (b) Spectra of the components

Figure 3. The decomposition results by CSO-VMD

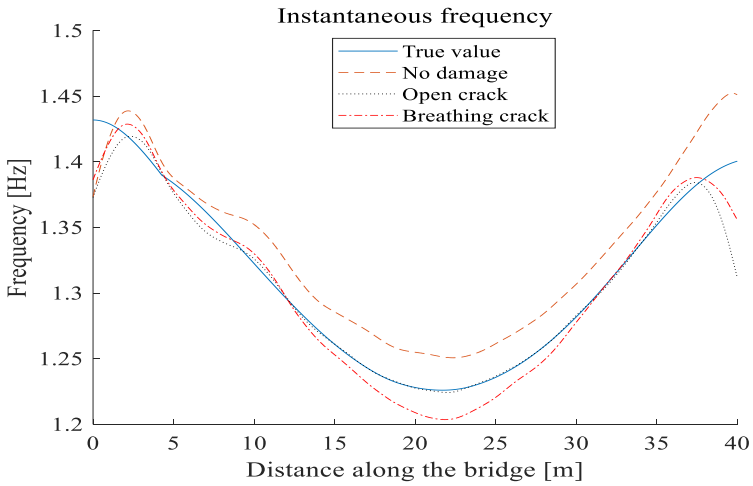

Figure 4. The identified IFs

4. CONCLUSIONS

The combined effects of vehicle-bridge interaction and the nonlinear breathing-crack cause the time-varying dynamic characteristics of the bridge under vehicle loads. Using spectral frequency may be difficult to identify the bridge damage conditions. The CSO-VMD with ridge detection is used to identify the nonlinear characteristics of the cracked bridge under moving vehicle loads. The bridge dynamic components are successfully extracted and the bridge related component is further used to identify the instantaneous frequency of bridge during the passage of the vehicle. The identified instantaneous frequencies under different damage conditions reveal important dynamic characteristics that can be used to differentiate bridge health conditions. These characteristics deserve further study to be used as future damage detection indicators.

ACKNOWLEDGMENTS

This research is supported in part by research funding of the National Natural Science Foundation of China (52108288). The financial aid is gratefully acknowledged.

REFERENCES

Abdel Wahab, M.M., De Roeck, G., & Peeters, B. (1999). Parameterization of damage in reinforced concrete structures using model updating. *Journal of Sound and Vibration*, 228(4), 717–30.

Borjigin, S., Kim, C.W., Chang, K.C., & Sugiura, K. (2018). Nonlinear dynamic response analysis of vehicle–bridge interactive system under strong earthquakes. *Engineering Structures*, 176, 500-521.

Chang, K.C., Kim, C.W., & Borjigin, S. (2014). Variability in bridge frequency induced by a parked vehicle. *Smart Structures and Systems*, 13(5), 755-773.

Dragomiretskiy, K., & Zosso, D. (2014). Variational Mode Decomposition. *IEEE Transactions on Signal Processing*, 62, 531-544.

Law, S.S., & Zhu, X.Q. (2004). Dynamic behavior of damaged concrete bridge structures under moving vehicular loads. *Engineering Structures*, 26(9), 1279-93.

Lee, J.H., & Fenves, G.L. (1998). Plastic-damage model for cyclic loading of concrete structures. *Journal of Engineering Mechanics*, 124(8), 892-900.

Li J T, Guo J, Zhu X Q, & Yu Y. (2022). Nonlinear characteristics of damaged bridges under moving loads using parameter optimization variational mode decomposition. *Journal of Civil Structural Health Monitoring*, 12:1009-1026

Li J T, Zhu X Q, Law S S, & Samali B. (2020). A two-step drive-by bridge damage detection using Dual Kalman Filter. International *Journal of Structural Stability and Dynamics*, 20(10):2042006

Meng, X. B., Liu, Y., Gao, X. Z., & Zhang, H. Z. (2014). A new bio-inspired algorithm: chicken swarm optimizationoptimisation. *International Conference in Swarm Intelligence*, Springer, 86-94.

Neild, S.A., Williams, M.S., & McFadden, P.D. (2002). Non-linear behaviour of reinforced concrete beams under low-amplitude cyclic and vibration loads. *Engineering Structures*, 24(6), 707-718.

Tian, Y.D., & Zhang, J. (2020). Structural flexibility identification via moving-vehicle-induced time-varying modal parameters. *Journal of Sound and Vibration*, 474, 115264.

Yu Y, Rashidi M, Samali B, Mohammadi M, Nguyen TN & Zhou X. Crack detection of concrete structures using deep convolutional neural networks optimized by enhanced chicken swarm algorithm. *Structural Health Monitoring*. 2022;21(5):2244-2263.

ISBN: 978-0-6456692-1-3

Authors Index

ISBN: 978-0-6456692-1-3

Authors Index

ISBN: 978-0-6456692-1-3

THE END